Development of garnet-based hybrid solid-state Li-ion conductors for advanced all-solid-state lithium batteries

Senhao Wang

260889251

Department of Mining and Materials Engineering,

McGill University

Submitted: June 2024

Abstract

Li-ion batteries (LIBs) have emerged as the key enabling technology towards electrification of transportation as the world is shifting away from carbon fuels responsible for the threat of climate change. The widespread adoption of LIBs can be attributed to their exceptional ionic conductivities and remarkable surface-wetting capabilities. Nevertheless, the liquid electrolytes often used in traditional lithium-ion batteries (LIBs) consist of extremely volatile and flammable organic solvents, namely carbonate-based electrolytes. These solvents pose significant safety risks, hence impeding the progress of LIB technology. Hence, there has been a change in research emphasis in recent years toward solid-state electrolytes (SSEs). All Solid-state lithium batteries (ASSLBs) based on solid-state electrolytes (SSEs) are considered strong candidates to overcome the energy density limitations and safety hazards of traditional Li-ion batteries. So far, several solid-state electrolytes (SSEs) has been proposed, which may be categorized into three main types: inorganic (ceramic) solid electrolytes (ISEs), solid polymer electrolytes (SPEs), and hybrid/composite electrolytes. Despite the advancements made in the development of SSEs, their application is facing many hurdles: (1) SSEs demonstrate lower levels of ionic conductivity in comparison to liquid electrolytes; (2) interfacial contact between the electrode and electrolyte results in significant interfacial resistance; (3) several of them exhibit thermodynamic instability at high potential or in contact with lithium metal. As such individual SSEs hardly fulfill all the requirements for practical application.

To address these issues, hybrid solid electrolytes (HSEs) by using a combination of two or more kinds of ISE-SPE composites are promising candidates. In this context, the present thesis describes original methods and hybrid materials that are evaluated for all solid-state lithium batteries. The core material is nanostructured garnet ($Li_{6.1}Al_{0.3}La_3Zr_2O_{12}$, c-Al-LLZO) solid electrolyte and its engineering into polymer-in-porous ceramic SSEs.

Firstly, a novel low-temperature aqueous synthesis process is developed yielding cubic phase Al-doped LLZO (c-Al-LLZO) at a temperature as low as 600 ℃, while obtaining nano-crystallites at around 100 - 200 nm. A dual-reaction mechanism is proposed to describe the process of c-Al-LLZO crystallization. The as-synthesized nanoscale c-Al-LLZO particles facilitate the densification of the solid-state electrolyte (SSE) pellets with less endowed grain boundaries (exhibiting a high relative density of 97.8%). The ionic conductivity reaches 0.42 mS cm^{-1} at 21

℃ and the activation energy is 0.17 eV (half of previously published values). Symmetric cells with Li metal exhibit excellent stability at the current density of 0.2 mA/cm^2 and 0.5 mA/cm^2, and a high critical current density (CCD) of 2.16 mA/cm^2.

Secondly, a novel HSE structure is designed featuring a polymer-infiltrated porous ceramic cubic $Li_{6.1}Al_{0.3}La_3Zr_2O_{12}$ (c-LLZO) scaffold fabricated by an integrated sintering method. The HSE structure exhibits high intrinsic ionic conductivity as well as good mechanical strength with even distribution of the polymer phase (LiTFSI-doped PEO) within the network of open pores resulting in uniform Li-ion migration flux. The infiltrated polymer solid electrolyte (PSE) (3 wt.% of HSE) forms strong molecular bonding on the interior and exterior surface of the ceramic skeleton via La-N bonds effectively lowering the interfacial impedance between the two phases. Moreover, this continuous two-phase interface provides a fast pathway for Li-ion transport. Thus, the as-designed ceramic-based HSE demonstrates high Li-ion transference number (0.71) and ionic conductivity (0.547 mS cm^{-1}) at 25 ℃. An ASSLB (Li/HSE/LFP) enabled by the novel HSE exhibits high discharge specific capacity of 163 mAh g^{-1} at 0.1 C and average Coulombic efficiency greater than 99 % after 50 cycles.

Thirdly, a highly conductive, interface-friendly, and high-voltage (4.8 V) stable composite solid electrolyte is constructed by compositing the cubic $Li_{6.1}Al_{0.3}La_3Zr_2O_{12}$ (LLZO) porous ceramic framework and poly (vinylidene difluoride) (PVDF). The ceramic-polymer two-phase 3D-continuous structure is molecularly tightly built through strong La-N and La-F bonds that promote the dissociation of Li salt to produce highly movable Li^+ for unhindered interfacial transport. These coupling effects endow the ceramic-based HSE with a high ionic conductivity (0.437 mS cm^{-1}) and lithium transfer number t_{Li^+} (0.72) at 25 ℃. The ceramic-based HSE is shown to provide interfacial stability with electrodes under high cut-off coltage. Specifically, the Li/ceramic-based HSE/Li symmetric cells stably cycle over 1000 hours at a current density of 0.5 mA cm^{-2}. Meanwhile an ASSLB featuring TiO_2-coated $LiNi_{0.6}Co_{0.2}Mn_{0.2}O_2$ cathode, Li metal anode, and the PVDF-LiTFSI-in-porous garnet HSE was cycled for over 200 times from 3 to 4.8 V exhbiting very stable performance with a Coulombic efficiency of 99.7% and no signs of lithium dendrite formation. The new porous garnet-based solid-state electrolytes and their molecularly engineerred polymer composites open new avenues towards the design and manufacturing of robust ASSLBs.

Resumé

Les batteries Li-ion (LIB) se sont imposées comme la technologie clé permettant l'électrification des transports, alors que le monde s'éloigne des combustibles carbonés responsables de la menace du changement climatique. L'adoption généralisée des batteries lithium-ion peut être attribuée à leurs conductivités ioniques exceptionnelles et à leurs remarquables capacités de mouillage des surfaces. Néanmoins, les électrolytes liquides souvent utilisés dans les batteries lithium-ion traditionnelles (LIB) sont constitués de solvants organiques extrêmement volatils et inflammables, à savoir des électrolytes à base de carbonate. Ces solvants présentent des risques importants pour la sécurité, ce qui entrave les progrès de la technologie LIB. C'est pourquoi la recherche s'est orientée ces dernières années vers les électrolytes à l'état solide (SSE). Toutes les batteries au lithium à l'état solide (ASSLB) basées sur des électrolytes à l'état solide (SSE) sont considérées comme de bons candidats pour surmonter les limitations de densité énergétique et les risques de sécurité des batteries Li-ion traditionnelles. Jusqu'à présent, plusieurs électrolytes solides ont été proposés, qui peuvent être classés en trois catégories principales: les électrolytes solides inorganiques (céramiques), les électrolytes solides polymères (SPE) et les électrolytes hybrides/composites. Malgré les progrès réalisés dans le développement des SSE, leur application se heurte à de nombreux obstacles: (1) les SSE présentent des niveaux de conductivité ionique inférieurs à ceux des électrolytes liquides ; (2) le contact interfacial entre l'électrode et l'électrolyte entraîne une résistance interfaciale significative ; (3) plusieurs d'entre eux présentent une instabilité thermodynamique à un potentiel élevé ou en contact avec le lithium métal. En tant que telles, les électrodes solides individuelles remplissent difficilement toutes les conditions requises pour une application pratique.

Pour résoudre ces problèmes, les électrolytes solides hybrides (HSE) utilisant une combinaison de deux ou plusieurs types de composites ISE-SPE sont des candidats prometteurs. Dans ce contexte, la présente thèse décrit des méthodes originales et des matériaux hybrides qui sont évalués pour toutes les batteries au lithium à l'état solide. Le matériau de base est l'électrolyte solide de grenat nanostructuré ($Li_{6.1}Al_{0.3}La_3Zr_2O_{12}$, c-Al-LLZO) et son ingénierie dans les SSE céramiques poreuses à base de polymères.

Tout d'abord, un nouveau processus de synthèse aqueuse à basse température est mis au point pour obtenir une phase cubique de LLZO dopé à l'Al (c-Al-LLZO) à une température aussi basse que

600 ℃, tout en obtenant des nanocristallites d'environ 100 à 200 nm. Un mécanisme à double réaction est proposé pour décrire le processus de cristallisation du c-Al-LLZO. Les particules de c-Al-LLZO nanométriques telles que synthétisées facilitent la densification des pastilles d'électrolyte à l'état solide (SSE) avec des joints de grains moins dotés (présentant une densité relative élevée de 97.8 %). La conductivité ionique atteint 0.42 mS cm^{-1} à 21℃ et l'énergie d'activation est de 0.17 eV (la moitié des valeurs publiées précédemment). Les cellules symétriques avec le métal Li présentent une excellente stabilité à la densité de courant de 0.2 mA cm^{-2} et 0.5 mA cm^{-2}, et une densité de courant critique (DCC) élevée de 2.16 mA cm^{-2}.

Deuxièmement, une nouvelle structure HSE est conçue avec un échafaudage céramique poreux $Li_{6.1}Al_{0.3}La_3Zr_2O_{12}$ (c-LLZO) infiltré dans un polymère et fabriqué par une méthode de frittage intégrée. La structure HSE présente une conductivité ionique intrinsèque élevée ainsi qu'une bonne résistance mécanique avec une distribution uniforme de la phase polymère (PEO dopé au LiTFSI) dans le réseau de pores ouverts, ce qui se traduit par un flux de migration des ions Li uniforme. L'électrolyte solide polymère (PSE) infiltré (3 wt.% en poids de HSE) forme une liaison moléculaire forte sur les surfaces intérieures et extérieures du squelette céramique par l'intermédiaire de liaisons La-N, ce qui réduit efficacement l'impédance interfaciale entre les deux phases. En outre, cette interface biphasée continue fournit une voie rapide pour le transport des ions Li. Ainsi, le HSE à base de céramique tel qu'il a été conçu présente un nombre de transfert d'ions Li élevé (0.71) et une conductivité ionique (0.547 mS cm^{-1}) à 25 ℃. Un ASSLB (Li/HSE/LFP) activé par le nouveau HSE présente une capacité spécifique de décharge élevée de 163 mAh g^{-1} à 0.1 C et une efficacité coulombienne moyenne supérieure à 99 % après 50 cycles.

Troisièmement, un électrolyte solide composite hautement conducteur, convivial et stable à haute tension (4.8 V) est construit en combinant la structure céramique poreuse cubique $Li_{6.1}Al_{0.3}La_3Zr_2O_{12}$ (LLZO) et le poly (difluorure de vinylidène) (PVDF). La structure biphasée 3D-continue céramique-polymère est étroitement construite au niveau moléculaire grâce à de fortes liaisons La-N et La-F qui favorisent la dissociation du sel de Li afin de produire un Li^+ hautement mobile pour un transport interfacial sans entrave. Ces effets de couplage confèrent au HSE à base de céramique une conductivité ionique élevée (0.437 mS cm^{-1}) et un nombre de transfert de lithium t_{Li^+} (0.72) à 25 ℃. Le HSE à base de céramique offre une stabilité interfaciale avec les électrodes sous une tension de coupure élevée. Plus, précisément, les cellules symétriques

HSE/Li à base de Li/céramique présentent un cycle stable de plus de 1000 heures à une densité de courant de 0.5 mA cm^{-2}. Par ailleurs, une ASSLB comprenant une cathode $LiNi_{0.6}Co_{0.2}Mn_{0.2}O_2$ recouverte de TiO_2, une anode Li métallique et le HSE à base de grenat poreux PVDF-LiTFSI a été cyclée plus de 200 fois de 3 à 4.8 V, offrant des performances très stables avec une efficacité coulombienne de 99.7 % et aucun signe de formation de dendrites de lithium. Les nouveaux électrolytes solides à base de grenat poreux et leurs composites polymères à ingénierie moléculaire ouvrent de nouvelles voies vers la conception et la fabrication d'ASSLB robustes.

Foreword

This thesis is based on a manuscript-based format that is offered by McGill University as an alternative to the traditional thesis format. Chapter 4 of this thesis has been published, whereas Chapter 5 and 6 have been submitted to peer-reviewed journals.

Authorship contributions

Senhao Wang, Hsien-chieh Chiu, George P. Demopoulos, Tetragonal phase-free crystallization of highly conductive nanoscale cubic garnet ($Li_{6.1}Al_{0.3}La_3Zr_2O_{12}$) for all-solid-state lithium-metal batteries. *Journal of Power Sources* 595 (**2024**) 234061. https://doi.org/10.1016/j.jpowsour.2024.234061.

Senhao Wang, George P. Demopoulos, High-conductive polymer-in-porous garnet solid electrolyte structure for all-solid-state lithium batteries enabled by molecular engineering. Under review. (*Submitted to Energy Storage Materials, ENSM-D-24-01008*) [under review].

Senhao Wang, Stéphanie Bessette, Raynald Gauvin, George P. Demopoulos, 4.8 V all-solid-state lithium-metal batteries enabled by high-conductive and interface-friendly garnet-based composite solid electrolytes. (*Submitted to Cell Reports Physical Science, CR-PHYS-SCI-S-24-00379-1*) [under review].

All manuscripts have been submitted for publication under the supervision of Professor Demopoulos as the corresponding author. The author of this thesis has designed the experiments, carried out materials synthesis, detailed characterization and electrochemical measurements. Dr. Hsien-chieh Chiu provided original investigation of Chapter 4. Ms. Stéphanie Bessette and Prof. Raynald Gauvin assisted with Focused-Ion-Beam and scanning electron microscopy characterization in Chapter 6.

I hereby give copyright clearance for the inclusion of above papers, of which I am corresponding author, into the Ph.D. dissertation of Senhao Wang.

Signature: _____ Date: _____

Prof. Dr. George P. Demopoulos

Department of Mining and Materials Engineering

McGill University

Montréal, Québec

Table of Contents

List of Figures

List of Tables

Acknowledgements

First and foremost, I would like to acknowledge my PhD supervisor, Professor George P. Demopoulos. His discipline and perseverance in scientific research served as a model for me throughout my life. I would also like to thank him for his trust and patience, as well as his guidance and encouragement, which provided me with the greatest support throughout my PhD period. Lastly, I hope that Professor George P. Demopoulos remains healthy and continues to shine in his scientific career.

These years in the HydroMet laboratory were the times I'll never forget. It could be much harder without you guys. I'd like to thank Rana Yekani, Han Wang, Moohyun Woo, Fan Yu, Arian Norouzi, Joon Kyung Koong, Dr. Andrea La Monaca, and Philip Gamboa. I deeply appreciate their help and support over the years. I would also like to thank the former lab members including Dr. Hsien-chieh Chiu, Dr. Marianna Uceda, Dr. Helen Zeng and Dr. Fuqiang Guo. They helped me a lot at the beginning of my PhD.

The completion of my PhD journey would not have been possible without the support of my wonderful girlfriend, Luyang Zhang, who will always be proud of my accomplishments and support me unconditionally. At the same time, her hard work and ambition is what inspires me to keep improving myself.

Above all, I would like to thank my great family who have been my biggest supporter. There are not enough words for me to ever thank them enough for the sacrifices they have had to make for me.

Lastly, I want to thanks the support from NSERC Strategic Project grant and the McGill Engineering Doctoral Award program.

Chapter 1: Introduction

1.2. Historical Progress of All-solid-state Lithium Batteries

Over nearly two centuries since the initial discovery of PbF_2 and Ag_2S, solid-state electrolytes (SSEs) have captured significant attention due to their rapid ion transport properties. As illustrated in Figure 1.1, a diverse range of SSEs has been developed for electrochemical cells. Notably, in the early 1830s, Faraday observed impressive ionic conductivities in solid PbF_2 and Ag_2S at temperatures around 177 ℃ and 500 ℃, respectively, akin to conventional metals. The 1960s marked a pivotal moment for high-ionic-conductivity materials, leading to the coining of the term "solid-state ionics". Subsequently, the progress of SSEs for practical applications advanced significantly. For instance, Ag_3SI, a novel SSE exhibiting a large Ag^+ ion conductivity of 1×10^{-2} S cm^{-1} at 20 ℃, was developed in the early 1960s and employed in a solid battery configuration $Ag/Ag_3SI/I_2$.[1,2] Additionally, in 1967, $Na_2O{\cdot}11Al_2O_3$ was reported to possess high Na^+ ionic conductivity and was utilized as the SSE for Na-S batteries, marking a pivotal moment when solid-state ionics expanded beyond inorganic materials.[3] During this period, the scope of SSEs expanded further with the discovery of ionic transport in solid polymer materials, such as poly(ethylene oxide) (PEO).[4-6] Notably, in 1973, PEO-based electrolytes impregnated with either sodium, potassium, or lithium salts were reported.[7] Concurrently, the discovery of the sodium superionic conductor (NASICON) and its crystal lattice structure emerged.[8,9] In the 1980s, Coetzer et al. achieved a breakthrough with the invention of sodium-metal-halide batteries (Na-$NiCl_2$ battery), commonly known as ZEBRA, which demonstrated high-energy-density batteries with long-term cycles and safety.[10] During this period, Armand et al. proposed solid polymeric electrolytes based on "PEO plus Li salts,"[11,12] and subsequent studies on various Li-ion conductive polymer materials, including polyacrylonitrile (PAN),[13] poly(methyl methacrylate) (PMMA),[14] and poly(vinylidene fluoride) (PVDF),[15] were extensively explored. In 1992, the inorganic lithium SSE, lithium phosphorus oxynitride (LiPON), was developed and successfully employed in assembling the first thin-film LIB by the Oak Ridge National Laboratory.[16,17] The adoption of LiPON motivated considerable research efforts into alternative inorganic solid-state electrolytes, such as perovskites, NASICON, LISICON, garnet, Li_2S-P_2S_5, Li_2S-P_2S_5, MSx, $LiBH_4$, and $Li_{1.8}N_{0.4}Cl_{0.6}$.[18-24] The 2000s witnessed an expansion of SSEs into novel LIBs, including Li-Air, Li-S, and Li-Br_2 batteries.[25] With the rapid development of solid polymer electrolytes (SPEs), lithium-metal-

polymer batteries containing SPEs found applications in vehicles. Furthermore, in recent developments, aqueous batteries with mediator-ion SSEs have emerged, wherein a mediator ion (e.g., Li^+ or Na^+) propagates in the SSE, acting as a "messenger" to regulate charge transport at the negative and positive electrodes, without direct involvement in the electrode reactions.[26] Looking ahead, in the 2020s, notable advancements continue with Solid Power, a Colorado-based battery start-up backed by BMW and Ford Motor Company, pioneering the pilot production of an innovative solid-state battery (SSB) cell. This SSB promises electric vehicle owners increased range, shorter recharging times, and cost-effectiveness.[27] The continuous progress in the development and application of SSEs holds immense potential in revolutionizing energy storage technologies, propelling the shift towards safer, higher-energy-density, and more efficient all-solid-state lithium batteries.

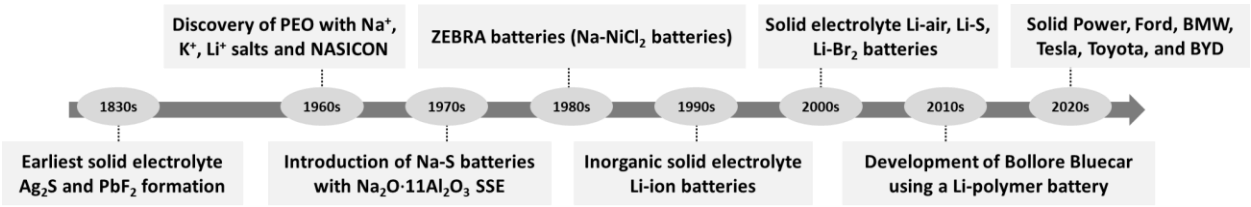

Figure 1. 1. History of development of SSEs. The timeline shows the key stages in the development of inorganic solid electrolytes (ISEs) and solid polymer electrolytes (SPEs).

1.2. Overview of the All-solid-state Lithium Batteries and Solid-state Electrolytes

The quest for high-performance and safe energy storage systems has been a driving force in research and development, especially in the field of electrochemical energy storage devices. Lithium-ion batteries (LIBs) have long dominated the portable electronic device market and have shown significant potential for electrifying the transportation sector and facilitating grid-scale energy storage. However, the reliance on liquid electrolytes in traditional LIBs presents safety concerns due to their flammability and potential for electrolyte decomposition at high voltages and temperatures. These drawbacks have motivated researchers to explore alternative solutions, leading to the emergence of all-solid-state lithium batteries (ASSLBs) as a promising candidate for next-generation energy storage technology. The primary innovation in ASSLBs lies in replacing the conventional liquid electrolytes with solid-state electrolytes (SSEs), which offer numerous advantages, including improved safety, enhanced energy density, wider operating

temperature range, and prolonged cycle life. This has ignited immense interest in the research community and the industry alike, resulting in significant progress in the development of SSEs for ASSLBs over the last two decades.

As demand for high-capacity energy storage continues to grow, the limitations of conventional LIBs become more apparent. The liquid electrolytes in LIBs pose safety hazards, particularly in high-energy applications such as electric vehicles (EVs) and grid storage. The risk of thermal runaway and electrolyte leakage may lead to catastrophic consequences, discouraging the widespread adoption of LIBs in critical applications. All-solid-state lithium batteries have the potential to overcome these drawbacks. By utilizing SSEs, ASSLBs eliminate the flammable electrolyte issue and offer increased thermal stability. Moreover, SSEs can enable the design of thinner, flexible, and lightweight battery configurations, leading to increased energy density and reduced manufacturing costs. The development of ASSLBs has thus gained substantial attention, with researchers focusing on enhancing the performance and manufacturability of SSEs.

Solid-state electrolytes serve as the critical interface between the positive and negative electrodes in ASSLBs, facilitating the transport of lithium ions during charge and discharge cycles. The ideal SSE should exhibit high lithium-ion conductivity, excellent mechanical strength, chemical stability, and wide electrochemical stability window to operate efficiently under various conditions. There are several classes of SSEs that have been extensively studied for ASSLBs:

Oxide-based SSEs: Oxide materials, such as lithium phosphorus oxynitride (LiPON), lithium garnets (e.g., $Li_7La_3Zr_2O_{12}$, LLZO), and lithium superionic conductors, have attracted significant attention due to their high ionic conductivity and chemical stability. LiPON is one of the earliest SSEs employed in ASSLBs, but challenges remain in improving its interfacial compatibility with electrode materials. LLZO, on the other hand, has demonstrated promising ionic conductivity but requires further optimization to address grain boundary resistance and manufacturing complexities.

Sulfide-based SSEs: Sulfide-based SSEs, like lithium thiophosphate (Li_3PS_4) and lithium phosphatesulfide ($Li_7P_3S_{11}$), have shown high lithium-ion conductivity at room temperature, making them attractive candidates for ASSLBs. However, issues related to air and moisture sensitivity, as well as lithium dendrite formation, must be addressed to ensure their practicality.

Polymer electrolytes: Polymers like polyethylene oxide (PEO) and its derivatives are flexible, lightweight, and can be easily processed into thin films. Their inherent ability to inhibit lithium dendrite growth and compatibility with various electrode materials make them promising SSEs for ASSLBs. However, achieving high ionic conductivity at room temperature remains a challenge, necessitating the incorporation of ceramic fillers or the development of new polymer architectures.

Hybrid ceramic & polymer solid-state electrolytes, which will be discussed in the literature review in Chapter 2.

While the progress in SSEs for ASSLBs is promising, several challenges must be addressed to realize their full potential. Some key challenges include:

Interface compatibility: SSEs must form stable interfaces with both positive and negative electrodes to prevent undesirable side reactions, interfacial resistance, and capacity loss.

Ionic conductivity: Achieving high ionic conductivity at room temperature remains a critical goal to enhance the power performance of ASSLBs.

Mechanical properties: SSEs should possess good mechanical strength and flexibility to endure mechanical stress during battery fabrication and operation.

Scalability and cost: Cost-effective and scalable manufacturing processes for SSEs are essential to enable commercialization.

Despite these challenges, the ongoing efforts and advancements in solid-state electrolytes have positioned ASSLBs as a promising energy storage technology. As the field continues to evolve, collaborative research between material scientists, electrochemists, and engineers will drive the development of SSEs and contribute to the realization of safer, higher-energy-density, and longer-cycling all-solid-state lithium batteries.

To sum up, the integration of solid-state electrolytes into all-solid-state lithium batteries (ASSLBs) has opened up new horizons in energy storage technology. By addressing the safety concerns associated with conventional liquid electrolytes, ASSLBs offer the potential to revolutionize various industries, including consumer electronics, electric vehicles, and grid storage. The development of advanced solid-state electrolytes with high ionic conductivity and superior stability is at the forefront of research, and continuous progress in this area promises a sustainable

electrified future. As researchers and industry partners continue to innovate and collaborate, all-solid-state lithium batteries will play a pivotal role in shaping the landscape of energy storage technologies for years to come.

1.3. Thesis Objectives and Organization

After this introductory chapter (Chapter 1), **Chapter 2** presents a literature review from liquid lithium-ion batteries to all-solid-state lithium batteries, classification of solid-state electrolytes, Li^+ conductive mechanism in polymer-based composite solid electrolytes, as well as interfacial stability between solid-state electrolytes and electrodes. Finally, Chapter 2 offers a comprehensive overview on the hybrid ceramic & polymer solid electrolytes. **Chapter 3** details characterization techniques and electrochemical measurements. In view of the existing limitations and challenges in garnet-type solid-state electrolytes and polymer-based hybrid solid-state electrolyte, several objectives are addressed in Chapter 4 to Chapter 6, where the original research investigations undertaken as part of this thesis are presented.

The first objective of this thesis is to address the issue of synthesis and processing of garnet-type conductors that is usually done at temperatures above 1100℃ to reach the high Li-ion conducting cubic phase resulting as a result in micron-sized particles and potential Li-loss, which are both unfavorable for manufacturing and electrode-electrolyte assembly. To address this issue, in **Chapter 4**, a novel low-temperature aqueous synthesis route is developed that achieves the crystallization of cubic phase of $Li_{6.1}Al_{0.3}La_3Zr_2O_{12}$ (c-Al-LLZO) at a temperature as low as 600 ℃, while obtaining nano-crystallites around 100 – 200 nm. As part of this development, a dual-reaction mechanism is proposed to describe the low-temperature crystallization of cubic garnet phase. The as-synthesized nanoscale cubic garnet particles facilitate the densification of solid-state electrolyte (SSE) pellets with less grain boundaries (exhibiting a high relative density of 97.8 %). The ionic conductivity reaches 0.42 mS cm^{-1} at 21 ℃ and the low activation energy is 0.17 eV. The results presented in Chapter 4 show that symmetric cells with Li metal exhibit excellent stability at current density of 0.2 mA cm^{-2} and 0.5 mA cm^{-2}, achieving an improved critical current density (CCD) of 2.16 mA cm^{-2}. **Chapter 4** is a reproduction of the original manuscript that was recently published in *Journal of Power Sources 595 (2024) 234061.*

The ceramic-based hybrid solid electrolytes (HSEs) represent excellent promise for application in next generation all-solid-state lithium metal batteries (ASSBs) due to their fast Li-ion migration, high mechanical strength, and good interfacial stability with electrodes. The second objective of this thesis is to design a novel architecture ceramic-based hybrid solid-state electrolyte based on porous cubic garnet SSE scaffold from powder synthesized in Chapter 4 and combining it with the ionic conductive polymer PEO-LiTFSI, hence providing good electrochemical performance. The novel HSE structure featuring a polymer-infiltrated porous ceramic cubic $Li_{6.1}Al_{0.3}La_3Zr_2O_{12}$ (c-LLZO) scaffold and its fabrication by an integrated sintering method is the subject of **Chapter 5**. The HSE structure exhibits high intrinsic ionic conductivity as well as good mechanical strength with even distribution of the polymer phase (LiTFSI-doped PEO) within the network of open pores resulting in uniform Li-ion migration flux. The infiltrated polymer solid electrolyte (PSE) forms strong molecular bonding on the interior and exterior surface of the ceramic skeleton via La-N bonds effectively lowering the interfacial impedance between the two phases. Moreover, this continuous two-phase interface provides a fast pathway for Li-ion transport. Thus, the as-designed ceramic-based HSE demonstrates high Li-ion transference number (0.71) and ionic conductivity (0.547 mS cm^{-1}) at 25 ℃. An ASSB (Li/HSE/LFP) built on the ceramic-based HSE exhibist high discharge specific capacity of 163 mAh g^{-1} at 0.1 C and average coulombic efficiency greater than 99 % after 50 cycles. **Chapter 5** is a reproduction of the original manuscript under peer review process in *Energy Storage Materials.*

The third objective of this thesis involves the development of ceramic-based composite solid-state electrolyte which could enable integration with high-voltage cathode materials. This effort is described in **Chapter 6**. Towards this end, a robust strategy for creating high-throughput Li^+ transport channels by coupling the conductive ceramic skeleton and polymer to overcome the low ionic conductivity and poor interfacial contact challenge of CSEs is developed. A highly conductive and interface-friendly composite solid electrolyte is constructed by compositing the cubic $Li_{6.1}Al_{0.3}La_3Zr_2O_{12}$ (LLZO) porous ceramic framework and poly (vinylidene difluoride) with a 3D-continuous structure. The ceramic-polymer two-phase composite is built tightly through strong La-N and La-F bonds promoting the dissociation of Li salt into fast moving Li^+ ions and stabilized CSE/cathode interface for highly efficient performance at high voltage.These coupling effects contribute to a high ionic conductivity (0.437 mS cm^{-1}) and lithium transfer number t_{Li+} (0.72) of the ceramic-based CSE at 25 ℃. The Li/ceramic-based CSE/Li symmetric cells stably

cycle over 1000 hours at a current density of 0.5 mA cm^{-2}. An ASSLB made of TiO_2-coated $LiNi_{0.6}Co_{0.2}Mn_{0.2}O_2$ cathode/ceramic-based CSE/Li metal anode is cycled for over 200 times from 3 to 4.8 V with the interface between ceramic-based CSE and cathode remaining ultra-stable. **Chapter 6** is a reproduction of the original manuscript that is currently considered for publication in a peer review journal. (Submitted)

At the end of each Chapter 4 and Chapter 5, a **Bridge** section is presented which connects the manuscript in each of the two chapters to the following one. **Chapter 7** connects the findings of this thesis work to the objectives laid out in Chapter 1 and topics discussed in Chapter 2, to offer a global discussion and perspective on all-solid-state lithium batteries. Finally, **Chapter 8** summarizes the major conclusions, identifies original contributions to knowledge, and outlines ideas for future work.

1.4. References

1. T. Takahashi, O. Yamamoto, The conductivity of Ag_3SI. *Denki Kagaku* **1964**, *32*, 610.
2. T. Takahashi, O. Yamamoto, The solid electrolyte cell using Ag_3SI as the electrolyte. *Denki Kagaku* **1964**, *32*, 664.
3. Y. Fang, Y. Yao, J. T. Kummer, Ion Exchange Properties and Rates of Ionic Diffusion in Beta-Alumina. *J. Inorg. Nucl. Chem.* **1967,** *29*, 2453-2475.
4. L. Yang, Preparation and Properties of PEO Complexes of Divalent Cation Salts. *Solid State Ionics* **1986,** *18*, 291-294.
5. M. F. Gray, Poly(ethylene oxide) - $LiCF_3SO_3$ - Polystyrene Electrolyte Systems. *Solid State Ionics* **1986,** *18*, 282-286.
6. W. Gorecki, C. Berthier, NMR, DSC, and Conductivity Study of a Poly(ethylene oxide) Complex Electrolyte: $PEO(LiClO_4)_x$. *Solid State Ionics* **1986,** *18*, 295-299.
7. M. P. Wright, Complexes of alkali metal ions with poly(ethylene oxide). *Polymer* **1973,** *14*, 391-397.
8. J. B. Goodenough, H. Y-P. Hong, J. A. Kafalas, Fast Na^+-ion transport in skeleton structures. *Mater. Res. Bull.* **1976**, *11*, 203–220.
9. H. Y-P. Hong, Crystal structures and crystal chemistry in the system $Na_{1+x}Zr_2Si_xP_{3-x}O_{12}$. *Mater. Res. Bull.* **1976**, *11*, 173–182.
10. R. J. Bones, R. C. Galloway, D. A. Teagle, A Sodium/Iron(ll) Chloride Cell with a Beta Alumina Electrolyte. *J. Electrochem. Soc.* **1987,** *134,* 2379.
11. M. Armand, Polymer electrolytes. *Annu. Rev. Mater. Sci.* **1986**, *16* (1), 245-261.
12. W. Gorecki, M. Jeannin, E Belorizky, C. Roux, M. Armand, Physical properties of solid polymer electrolyte PEO(LiTFSI) complexes. *J. Phys.: Condens. Matter.* **1995**, *7*, 6823.
13. B. Huang, G. Li, H. Huang, R. Xue, L. Chen, F. Wang, Lithium ion conduction in polymer electrolytes based on PAN. *Solid State Ionics* **1996,** *85*, 79-84.
14. E. Quartarone, C. Tomasi, P. Mustarelli, G. B. Appetecchi, F. Croce, Long-term structure stability of PMMA-based gel polymer electrolytes. *Electrochemica. Acta* **1998**, *43*, 1435-1439.
15. Y. Shen, Porous PVDF with $LiClO_4$ complex as solid and wet polymer electrolyte. *Solid State Ionics* **2004,** *175* (1-4), 747-750.

16. N. J. Dudney, J. B. Bats, R. A. Zuhr, C. F. Luck, Sputtering of lithium compounds for preparation of electrolyte thin films. *Solid State lomcs* **1992,** *53*, 7, 655-661.
17. J. B. Bates, N. J. Dudney, G. R. Gruzalski, R. A. Zuhr, A. Choudhury; C.F. Luck, Electrical properties of amorphous lithium electrolyte thin films. *Solid State Ionics* **1992,** *53*, 8, 647-654.
18. Y. Inaguma, L. Chen, M. Itoh, T. Nakamura, High Ionic Conductivity in Lithium Lanthanum Titanate. *Solid State Commun.* **1993,** *86*, 5, 689-693.
19. A. Martínez-Juárez, J. M. Rojo, J. E. Iglesias, J. Sanz, Reversible Monoclinic - Rhombohedral Transformation in $LiSn_2(PO_4)_3$ with NASICON-Type Structure. *Chem. Mater.* **1995,** *7*, 6, 1857-1862.
20. H. M. Kasper, A New Series of Rare Earth Garnets $Ln^{3+}{}_3M_2Li^{+}{}_3O_{12}$(M = Te, W). *Inorg. Chem.* **1968,** *8*, 3, 1000-1002.
21. J. H. Kennedy, S. Sahami, S. W. Shea, Z. Zhang, Preparation and Conductivity Measurements of SiS_2-Li_2S Glasses Doped with LiBr and LiCI. *Solid State lonics* **1986,** *18*, 4, 368-371.
22. L. Wang, Y. Wang, Y. Xia, A high performance lithium-ion sulfur battery based on a Li_2S cathode using a dual-phase electrolyte. *Energy Environ. Sci.* **2015,** *8* (5), 1551-1558.
23. J. B. Bates, N. J. Dudney, G. R. Gruzalski, R. A. Zuhr, A. Choudhury, C. F. Luck, Fabrication and characterization of amorphous lithium electrolyte thin films and rechargeable thin-film batteries. *J. Power Sources* **1993,** *43*, 8, 103-110.
24. P. Hartwig, W. Weppner, W. Wichelhaus, Fast Ionic Lithium Conductivition in Solid Lithium Nitride Chloride. *Mater. Res. Bull.* **1979,** *14*, 6, 493-498.
25. J. Castillo, L. Qiao, A. Santiago, X. Judez, A. S. de Buruaga, G. Jimenez, M. Armand, H. Zhang, C. Li, Perspective of polymer-based solid-state Li-S batteries. *Energy Mater.* **2022,** *2,* 200003-2000021.
26. X. Yu, A. Manthiram, Electrochemical Energy Storage with Mediator-Ion Solid Electrolytes. *Joule* **2017,** *1* (3), 453-462.
27. A. Unemoto, T. Ikeshoji, S. Yasaku, M. Matsuo, V. Stavila, T. J. Udovic, S. I. Orimo, Stable Interface Formation between TiS_2 and $LiBH_4$ in Bulk-Type All-Solid-State Lithium Batteries. *Chem. Mater.* **2015,** *27* (15), 5407-5416.

Chapter 2: Literature Review

2.1. From Lithium-Ion Batteries to All-Solid-State Lithium Batteries

Scientists have long recognized the necessity for the development of so-called green energy. What is relatively recent is the recognition by governments throughout the world that the development of green energy and the reduction of greenhouse gas emissions is both obligatory and urgent. The growth in the number of people in the world, along with the increase in energy consumption per person because of an increase in nominal GDP per capita at the global scale, suggests a massive increase in energy consumption in the coming years. Electrochemical energy storage has emerged as a critical issue in this setting. LIBs can tackle the intermittent challenges of sustainable energy by leveling power generation.

Rechargeable lithium-ion batteries power the portable, entertainment, computer, and telecommunications equipment that today's information-rich, mobile culture requires, and account for 63% of worldwide sales values in portable batteries. As shown in Figure 2.1, among the various existing technologies, Li-based batteries because of their high energy density and design flexibility currently outperform other systems.[1,2] Since about 30 years ago, Sony Co, commercialized the world's first lithium-ion battery (LIB), that led to revolutionization of portable electronics and an explosive increase in research interest. A lithium-ion battery consists of a cathode (coated on current collector Al foil), a liquid electrolyte (Li salts dissolved in organic solvent), a separator, and an anode (coated on current collector Cu foil), as presented in Figure 2.2. In terms of the working mechanism of a LIB, when the charging process is initiated, Li-ions are deintercalated form cathode material passing through the liquid electrolyte and separator, then intercalated into anode material. To keep the charge balanced, electrons removed from the anode material passing through the external circuit then move to cathode material. Taking the first commercial LIB as an example, where lithium cobalt oxide ($LiCoO_2$) was used as the cathode material and graphite (C) as the anode material, the redox reactions of the working mechanism are:

$$\boldsymbol{Cathode\ (oxidation)}: \boldsymbol{LiCoO_2 \rightarrow CoO_2 + Li^+ + e^-}$$

$$\boldsymbol{Anode\ (reduction)}: \boldsymbol{6C + e^- + Li^+ \rightarrow LiC_6}$$

When the discharging process happens, the above reactions are reversed. Based on these redox reactions, the LIBs can achieve the mutual conversion between chemical energy and electrical energy.

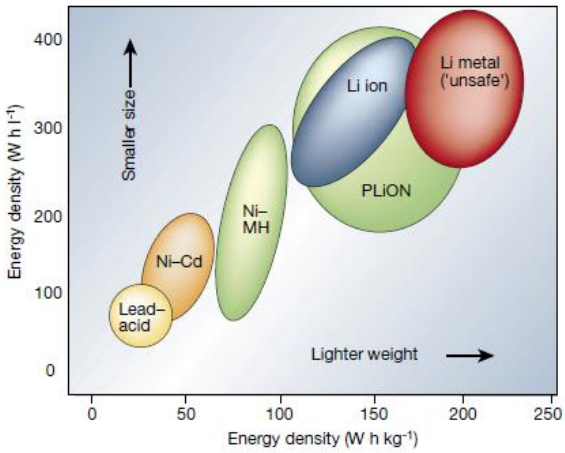

Figure 2. 1. Comparison of the different battery technologies in terms of volumetric and gravimetric energy density. Adapted with permission from Ref. [1]. Copyright (2001) Springer Nature.

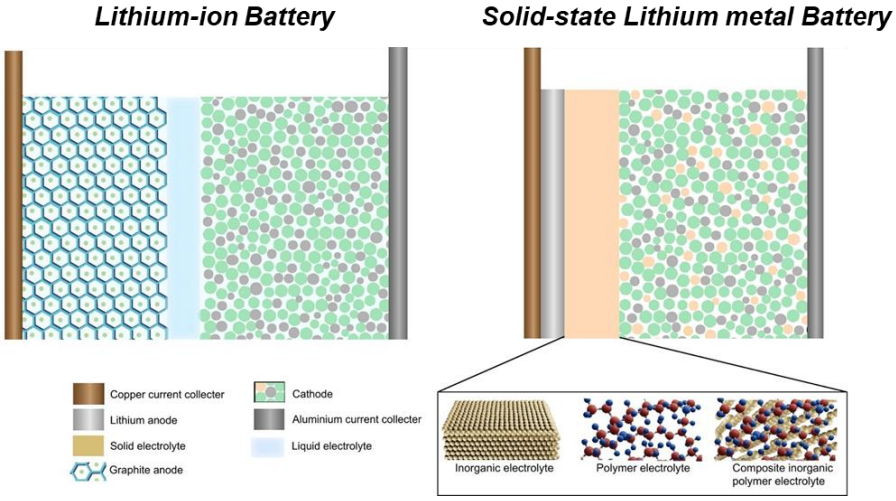

Figure 2. 2. Schematic of a lithium-ion battery and solid state lithium metal battery. Adapted with permission from Ref. [3]. Copyright (2022) Elsevier Ltd.

Lithium-ion batteries have gained significant popularity due to their notable attributes such as high energy density, extended cycle life, minimal self-discharge rate, and various other advantageous features. Lithium-ion batteries have gained widespread usage after over three decades of development, starting with Goodenough's initial introduction of $LiCoO_2$ as a cathode material in

the 1990s, followed by Sony's commercialization of the first $LiCoO_2$ cathode lithium-ion battery.[4,5] Nevertheless, conventional lithium batteries employ organic liquid electrolytes, and the interaction between the liquid electrolyte and the highly reactive lithium metal leads to undesirable side reactions. Consequently, the electrolyte decomposes and lithium dendrites form, thereby significantly compromising the battery's overall performance.[6,7] Furthermore, there exist numerous pressing challenges in the realm of lithium batteries employing liquid electrolytes. These include the inherent drawbacks of organic electrolyte solvents, namely their low boiling point and flash point, which give rise to safety concerns pertaining to flammability and explosion. Additionally, the growth of lithium dendrites penetrating through the diaphragm poses a significant risk of battery short-circuiting. The commercial utilization of lithium metal as anode to obtain high energy density is currently hindered by a significant and inescapable set of safety concerns.[8-10]

To address these challenges, individuals have sought to replace liquid electrolytes with solid electrolytes as a means of ensuring enhanced safety in battery systems and thereby enabling the use of lithium metal as anode. In contrast to liquid electrolytes, solid electrolytes possess several advantageous characteristics, including nonvolatility, high-temperature tolerance, absence of corrosion, lack of explosiveness, and significantly diminished reactivity with lithium metal. It is important to acknowledge that solid electrolytes could impede the formation of lithium dendrites, leading to significantly enhanced safety performance compared to liquid electrolytes. This characteristic plays a crucial role in facilitating the secure utilization of lithium metal batteries.[11,12]

The substitution of electrolytes and diaphragms in traditional lithium-ion batteries with solid electrolytes has emerged as a prominent area of investigation among researchers aiming to develop lithium metal batteries that are both safe and possess high energy density. Despite the numerous advantages of solid electrolytes, there has yet to be a single electrolyte that possesses a comprehensive set of properties. The utilization of inorganic oxide electrolytes with notable characteristics such as high ionic conductivity, exceptional mechanical properties, and a broad electrochemical stability range has been proposed to enhance the energy density of batteries when combined with high-voltage cathode materials.[13-15] Nevertheless, the fabrication procedure for inorganic solid electrolytes is intricate, involving challenging powder pressing techniques and necessitating high-temperature sintering. The application of sintered electrolyte sheets on a large scale is limited due to their hardness, brittleness, and high energy consumption.[16,17] Furthermore,

the significant impedance issue that arises from the contact interface between inorganic solid electrolytes and electrode materials has yet to be adequately resolved. This challenge has emerged as a crucial factor impeding the practical implementation of this technology.[18,19]

The process of preparing polymer electrolytes is relatively straightforward and does not require high-temperature sintering. The polymer also possesses the benefits of excellent flexibility and low weight, enabling it to establish a more intimate connection with electrode materials. This facilitates the reduction of interface impedance between the electrolyte and electrode, thereby satisfying the demands of high energy density batteries.[20,21] Nevertheless, the room temperature conductivity of lithium-ion in polymer electrolytes is relatively low, ranging from 10^{-8} to 10^{-5} S cm^{-1}. This limited conductivity, coupled with a low migration number of lithium ions, can result in the localized buildup of lithium ions. Consequently, concentration polarization occurs, leading to the formation of lithium dendrites. These dendrites can penetrate the polymer electrolyte membrane, which possesses inadequate mechanical strength, ultimately causing a short circuit in the battery. The polymer electrolytes typically exhibit a relatively narrow electrochemical stability window, thereby imposing restrictions on the potential enhancement of battery energy density.[22]

The performance requirements of batteries pose a significant challenge for single-component solid electrolytes, thereby impeding the advancement of solid electrolyte applications. The development of solid electrolytes is facilitated by the combination and adjustment of various types of electrolytes through structural design, thereby harnessing the complementary benefits of their components. In pursuit of this objective, the present study endeavours to furnish a comprehensive review on composite solid electrolytes by means of component manipulation and structural configuration. This overview comprises the impact of fillers, film-forming structures, component interactions, and specific processes on electrolytes. Additionally, it defines approaches to enhance the ionic conductivity, lithium-ion migration number, mechanical properties, and thermal stability of electrolytes.

2.2. Classification of Solid-State Electrolytes

In general, solid-state electrolytes (SSEs) are classified into polymer-based solid electrolytes (PSEs), inorganic solid electrolytes (ISEs) including oxide-type and sulfide-type solid electrolytes,

and organic-inorganic composite (or hybrid) solid electrolytes (CSEs or HSEs).[23] There are several requirements that need to be met in order to use the SEs in solid-state batteries. The practical application of single-ion conductors is hampered by low ionic conductivity at room temperature and poor interfacial contact with electrodes. Due to this, extensive research has been carried out recently among industrial and scientific communities to speed up innovation in this field, and although advances have been made, the large-scale application of solid-state electrolytes still faces numerous problems ranging from fundamental understanding to industrial manufacturing. For example, the mechanism of Li-ion transport remains controversial and has been fiercely debated by researchers, especially around issues associated with Li-ion transport across the interface of anodes, solid-state electrolytes, and cathodes.

2.2.1. Oxide-Type Solid Electrolytes

Perovskite-Type

Based on the best bulk ionic conductivities among different solid electrolytes, perovskite (ABO_3)-type Li-ion conductors and structurally related variants have recently received a lot of attention. Numerous studies have reported varying ionic conductivities through the replacement of A and B sites with different ions, with ionic conductivities being able to reach 10^{-3} S cm^{-1} after optimization. $Li_{3x}La_{(2/3)-x}TiO_3$ (LLTO) is the general formula for perovskite-type lithium lanthanum titanate solid-state electrolytes, with x values ranging from 0.07 to 0.13 and activation energies between 0.3 and 0.4 eV, as illustrated in Figure 2.3. Researchers have shown that cation deficiencies at A sites, which are constituted by four adjacent TiO_6 octahedra, might let Li cations move more easily across bottlenecks, explaining why LLTOs have such a high concentration of A-site vacancies.[24] In general, various perovskite-like compounds with a variety of crystal structures, including cubic, hexagonal, orthorhombic, and tetragonal, may be produced by different synthesis techniques with heterogeneous lattice vacancies. Additionally, it is crucial to investigate the LLTO's crystal structure and ionic conduction mechanism in order to develop all-solid-state electrolytes. For instance, Bohnke et al.[24] verified that the tilting and/or rotation of BO_6 octahedra as driven by either rising temperature or increasing vacancy number in the structure was included into the ionic conduction mechanism of LLTOs. The migration route of the Li-ion conductor $La_{0.62}Li_{0.16}TiO_3$ was also explored by Yashima et al.[25] They discovered that at 77 K, Li cations may move from the

2*c* site on the (002) La-deficient layer to the 2*c*-4*f*-2*c or* 2*c*-2*d*-2*c* tie line to increase conductivity. Based on their adequate electrochemical windows and acceptable ionic conductivities, perovskite-type conductors are generally regarded as viable candidates for all-solid-state electrolytes; nonetheless, the reactivity of Ti with lithium metal severely limit practical implementation.

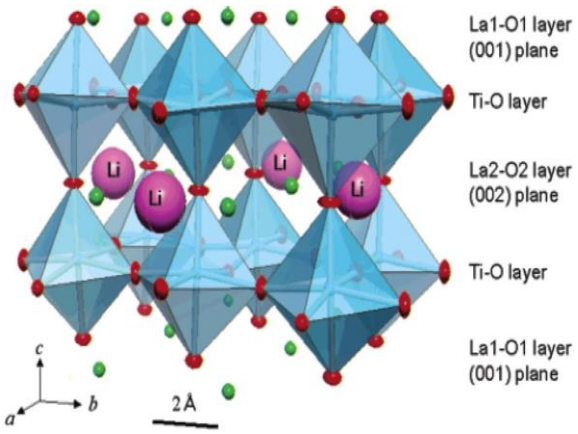

Figure 2. 3. Crystal structure of $La_{0.62}Li_{0.16}TiO_3$. Pink, green and red spheres represent Li, La and Ti atoms, respectively, red ellipsoids represent oxygen ions, and TiO_6 octahedrons are depicted as blue squares. Adapted with permission from Ref. [25]. Copyright (2005) American Chemical Society.

Anti-Perovskite-Type

In 2012, Zhao et al.[26] proposed a new strain of anti-perovskites (LiRAPs) that were "electronically inverted" as compared with standard perovskite-type electrolytes and reported that this novel class of electrolytes can be referred to as anti-perovskites because although they share similar structures with standard perovskite-type electrolytes, the ions of the anti-perovskites in the corresponding lattice sites can undergo electronic inversion. For instance, in typical ABX_3 perovskite structures with highly electronegative C anions, A (monovalent) and B (divalent) may act as metallic cations, but A, B, and X all have reversed charges in LiRAP. Chalcogens^{2-} (O^{2-}, S^{2-}) occupy B sites in the octahedral centre of LiRAP, and any halogens (F, Cl, Br, I) may function as dodecahedral centres (A sites). The ionic conductivity of LiRAP may exceed 10^{-3} S cm^{-1} at room temperature with activation energies of 0.2–0.3 eV, and these researchers also noted that the LiRAPs had excellent stability even at high temperatures. Researchers have also shown that Li^+ conduction in anti-perovskites may be easily controlled by chemical replacement. For instance, according to Zhang

et al.[26], the depletion of LiA (samples: $Li_{2.95}OCl_{0.95}$, $Li_{2.90}OCl_{0.90}$, $Li_{2.85}OCl_{0.85}$ and $Li_{2.80}OCl_{0.80}$) can optimize superionic conductivity, in which the conductivity of $Li_3OCl_{0.5}Br_{0.5}$ at room temperature can increase to 6.05×10^{-3} S cm^{-1}. Additionally, thermal treatments (such as pressing, heating, and cooling) can also affect conductivity. For example, Figure 2.4 shows that after being annealed in vacuum for 24 hours, the ionic conductivity of Li_3OCl, Li_3OBr, and $Li_3OCl_{0.5}Br_{0.5}$ can be significantly increased by 2 orders of magnitude at room temperature.[27] Zhang et al.'s investigation of the Li^+ transport mechanism in LiRAP revealed that anti perovskites (Li_3OCl, Li_3OBr, and their mixed composite $Li_3OCl_{0.5}Br_{0.5}$) were thermodynamically metastable but electrochemically stable.[27] This was supported by phase diagrams and electronic structure predictions. Additionally, it was discovered via the use of ab initio molecular dynamic simulations that an increase in structural irregularities and Li vacancies may result in an increase in Li ion transport. Another anti-perovskite is $Li_{3x}M_xHalO$, which was first described by Braga et al.[28] as a novel class of glassy electrolytes based on LiRAP that can exhibit extremely quick ionic conduction (25 mS cm^{-1} at 25 °C). M stands for divalent cations such as Mg^{2+}, Ca^{2+}, or Ba^{2+}, and Hal stands for halides such as Cl, I, or a mixture. These innovative glassy electrolytes are likely to hold promise in the future for applications where higher valence dopants may lead to better conductivities because of their advantages such as lightweight, non-flammability, nonpolluting, thermal and electrochemical stability, etc.

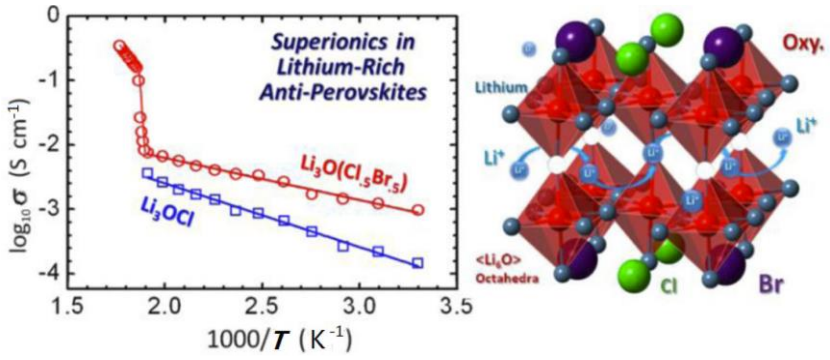

Figure 2. 4. Left plot denotes the logarithm of the ionic conductivity of Li_3OCl and mixed composite $Li_3OCl_{0.5}Br_{0.5}$ versus 1000/T (K^{-1}). The right schematic depicts the structure of $Li_3OCl_{0.5}Br_{0.5}$. Adapted with permission from Ref. [27]. Copyright (2013) Purpose-Led.

NASICON-Type

The NASICON-type conductors ($Na_{1+x}Zr_2P_{3x}Si_xO_{12}$), which are generated from $NaZr_2(PO_4)_3$ when P is replaced with Si due to the weak ionic conductivity of P, are promising rapid ion conductors with high conductivity. There are three factors that contribute to the increased conductivity of $Na_{1+x}Zr_2P_{3x}Si_xO_{12}$: the increased mobility of Na^+ ions within the structure; the higher density of the sintered pellets; and the more hospitable environment for Na^+ ion migration through the 3D structure with larger tunnel sizes. Iso-structural $LiM_2(PO_4)_3$ (M = Zr, Ti, Hf, Ge or Sn) was one of these NASICON-type conductors that was initially described in 1977. Its skeletons consisted of MO_6 octahedra and PO_4 tetrahedra sharing oxygen atoms (Figure 2.5).[29] $LiM_2(PO_4)_3$ (M = Ti, Ge) with rhombohedral symmetry and $LiM_2(PO_4)_3$ (M = Zr, Hf, or Sn) with a triclinic phase and lower symmetry are two further subgroups of this $LiM_2(PO_4)_3$ series.[30] In this case, it is anticipated that alkaline ions will occupy two crystallographic sites where M1 sites are surrounded by six oxygens and M2 sites are situated between two neighbouring M1 locations with tenfold oxygen coordination. Regarding the triclinic phase, structural distortions in a fourfold coordination at the intermediate M12 sites are what drive Li cations. Additionally, because to its ideal lattice size for Li^+ ion conductivity, researchers have shown that $LiTi_2(PO_4)_3$ outperforms other $LiM_2(PO_4)_3$ (M = Zr, Ge, or Hf) materials in terms of conductivity. Researchers have also noted that the replacement of partial Ti^{4+} cations in $Li_{1+x}R_xTi_{2x}(PO_4)_3$ by trivalent cations such Al^{3+}, Sc^{3+}, Ga^{3+}, Fe^{3+}, In^{3+}, and Cr^{3+} may improve conductivity. For example, $Li_{1.3}Al_{0.3}Ti_{1.7}(PO_4)_3$ (LATP) can achieve an improved ionic conductivity of 7×10^{-4} S cm^{-1}. Additionally, the lattice constants of $LiM_2(PO_4)_3$ (M = Ge, Hf, or Zr) may be affected by the ionic radius of M^{4+}cations, which can further affect the tunnel size for Li^+ diffusion (Fig. 2.6).[31] Ionic conductivity in NASICON-type conductors may be improved by increasing densification, raising the mobile ion content inside the structure, and lowering the activation energy caused by the inclusion of trivalent ions.[32] In a different study, Arbi et al.[31] also looked into the role of cation miscibility in the optimization of the transport properties of the $Li_{1+x}Ti_{2x}Sc_x(PO_4)_3$ ($0 < x < 0.5$) series and reported that in Sc-poor samples, NASICON phases with rhombohedral symmetry were identified while in Sc-rich structures, the existence of secondary TiO_2 and LiS was detected. The addition of secondary Li compounds such as Li_2O, Li_3PO_4, and Li_3BO_3 to serve as fluxes to promote crystallization and form conductive components at the grain boundary was also suggested by Aono et al.[30] as a method

to increase conductivity. The addition of 20% Li_2O into $LiTi_2(PO_4)_3$ results in a constant conductivity of 5×10^{-4} S cm^{-1}.

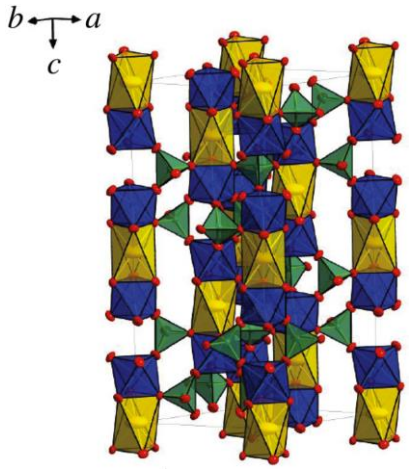

Figure 2. 5. Unit cell of $LiTi_2(PO_4)_3$. Li^+, Ti^{4+} and P^{5+} occupy yellow octahedra, blue octahedra and green tetrahedra, respectively. Adapted with permission from Ref. [29]. Copyright (2017) American Chemical Society.

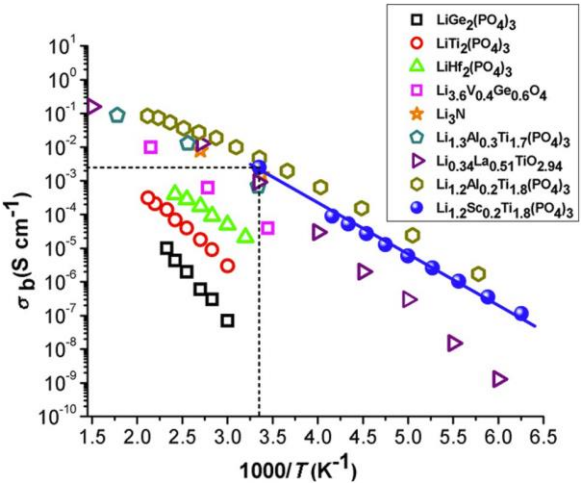

Figure 2. 6. Ionic conductivity of NASICON-type Li-ion solid electrolytes. Adapted with permission from Ref. [31]. Copyright (2017) American Chemical Society.

Garnet-Type

Thangadurai et al.[32] proposed a novel family of Li-ion electrolytes in 2003 with a garnet-like structure and a nominal composition of $Li_5La_3M_2O_{12}$ (M = Nb, Ta), which has since gained

growing attention due to its distinctive crystal structures, high conductivities, and wide electrochemical stability windows. In comparison to LiPON, Li_9AlSiO_8, and Li-alumina, the ionic conductivity of these garnet-type conductors is much higher. The Ta members ($Li_5La_3Ta_2O_{12}$) were further chemically inert to moisture and molten Li.

Orthosilicate garnets are among these garnet-type conductors, and they have the formula $A_3^{II}B_2^{III}(SiO_4)_3$, where A and B correspond to 8- and 6-coordinated cation sites, respectively. By substituting other elements for silicon, it has been discovered that different complex oxides can crystallize in garnet-like conductors with the general formula $A_3B_5O_{12}$ (A = Ca, Mg, Y or Ln = La, or rare-earth elements; B = Al, Fe, Ga, Ge, Mn, Ni, V), leading to a 3D structure made up of BO_4 tetrahedra and BO_6 octahedra sharing corners with each other. Neutron diffraction studies,[32] in which $Li(I)O_6$ was substantially more distorted than $Li(II)O_6$, indicated that Li-ions reside on both the octahedral and tetrahedral sites in the crystal structure of $Li_5La_3M_2O_{12}$ (M=Nb, Ta) (Figure 2.7), where La and Ta ions occupy the 8- and 6- coordination sites. Furthermore, according to studies, strong Li-ion conduction may be achieved by combining 6 LiO_6 octahedra with 2 open sites for Li-ions around MO_6 octahedra[32]. Thangadurai's method[33] of partially substituting K^+ for La^{3+} and In^{3+} for Nb^{5+} also improved the ionic conductivity of garnet-like $Li_5La_3Nb_2O_{12}$. Additionally, according to the findings of this group, high sintering temperatures may reduce grain boundary resistances and produce big grain size microstructure with improved conductivity. Furthermore, Thangadurai et al.[34,35] created novel garnet-like conductors by substituting alkaline earth elements for La in later studies. They also reported that ionic conductivity decreased as the ionic radius of alkaline earth ions decreased in various conductors, with Ba compound $Li_6BaLa_2Ta_2O_{12}$ exhibiting the best ionic conduction performances (4×10^{-5} S cm^{-1} at room temperature with activation energy of 0. 40eV). Additionally, these researchers discovered that Y and Li co-doping may improve the ionic conductivity of parent compound $Li_5La_3Nb_2O_{12}$, resulting in a unique Li rich $Li_{5+2x}La_3Nb_{2x}Y_xO_{12}$ structure where trivalent ions like Y^{3+} outperformed other dopants like M^{2+} (alkaline earth ions), In^{3+}, and Zr^{4+}.[36] Another garnet-like structure, cubic $Li_7La_3Zr_2O_{12}$ (LLZO) presented in Figure 2.8, was originally reported by Murugan et al.[37] It is a promising all-solid-state ion conductor with a greater overall conductivity (3×10^{-4} S cm^{-1}) than any other Li garnet-like materials previously described (Figure 2.9). According to this study's findings, Li-ions are dispersed across the octahedral 48*g*, tetrahedral 24*d*, and 96*h* Li(2) sites in cubic LLZO.[38] Another LLZO polymorph of the tetragonal type with low-temperature tetragonal

symmetry was also observed, but its conductivity value of 10^{-6} S cm^{-1} was substantially lower due to the well-ordered placement of Li-ions at its octahedral 16*f* and 32*g* sites and tetrahedral 8*a* sites.[39-40] To stabilize cubic structures in garnet-type conductors, several investigations have been focused on either raising Li vacancy concentrations or lowering Li content. For instance, Rangasamy et al.[41] showed that substituting Al for Li may increase the amount of Li vacancies created and looked into the ideal Al to Li ratio to create attractive LLZOs.

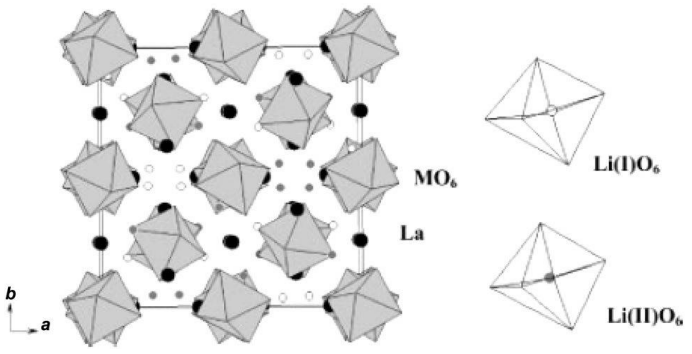

Figure 2. 7. Crystal structure of $Li_5La_3M_2O_{12}$(M = Nb, Ta). Adapted with permission from Ref. [32]. Copyright (2003) American Chemical Society.

The Li-ion diffusion process in garnet-type conductors is debatable as well, deeper comprehension of Li^+ transport mechanisms need sophisticated characterisation methods to pinpoint the precise position of Li-ions. As an illustration, Thangadurai et al.[42] used the bond valence sum method to investigate the distinctive structure of $Li_5La_3M_2O_{12}$ and confirmed potential ion transport pathways through a minimization procedure of bond valence mismatch, where the obtained results revealed that Li ions only occupied octahedral sites. Cussen et al.[43] later refuted this conclusion and proposed that Li-ions were present in both octahedral and tetrahedral sites in the structure of $Li_5La_3M_2O_{12}$ (M=Ta, Nb), with Li^+ in the octahedral sites being a mobile species while Li^+ in the tetrahedral sites was thought to be trapped and immobile. Using cutting-edge NMR techniques, Wüllen et al.[44] likewise came to same result. Furthermore, since the mobility of Li-ions is susceptible to Li-ion migration, researchers have also discussed the relevance of final annealing temperatures. For instance, increasing the number of Li-ions at octahedral sites during annealing at high temperatures might enhance ionic conductivity. The migration mechanism of LLZOs is typically governed by the imposed restrictions of occupied site-to-site interatomic isolation, which

only permits 48*g*/96*h*-24*d*-48*g*/96*h*, and the temporal stay of Li^+ at the 24*d* site, which can promote ion mobility and reorganize nearby Li neighbours[38]. The nudged elastic band (NEB) approach is used by Xu et al.[45] to determine the least energy route for Li diffusion in $Li_{3+x}La_3M_2O_{12}$(x = 0, 2, 4), which is another advantage of simulation methods for better understanding migration processes.

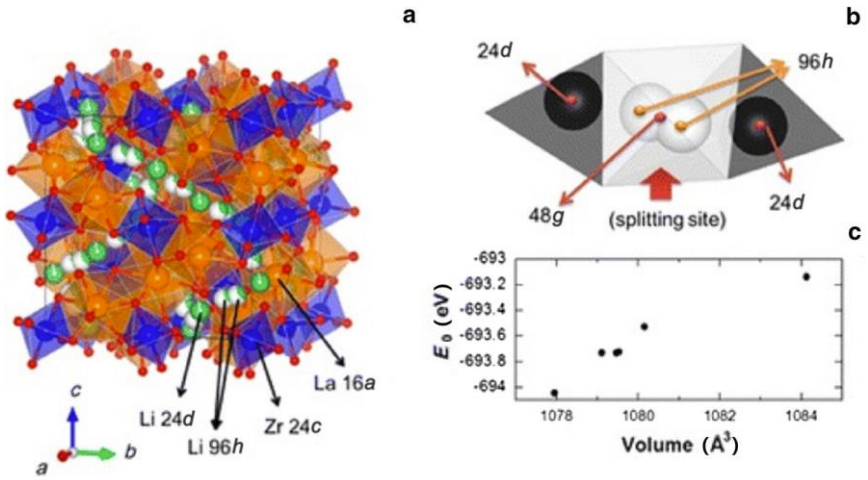

Figure 2. 8. Crystal structure of cubic LLZO. Li-ions distributed over the octahedral 48g, tetrahedral 24d Li(1) and 96h Li(2) sites. Adapted with permission from Ref. [37]. Copyright (2007) Wiley-VCH GmbH.

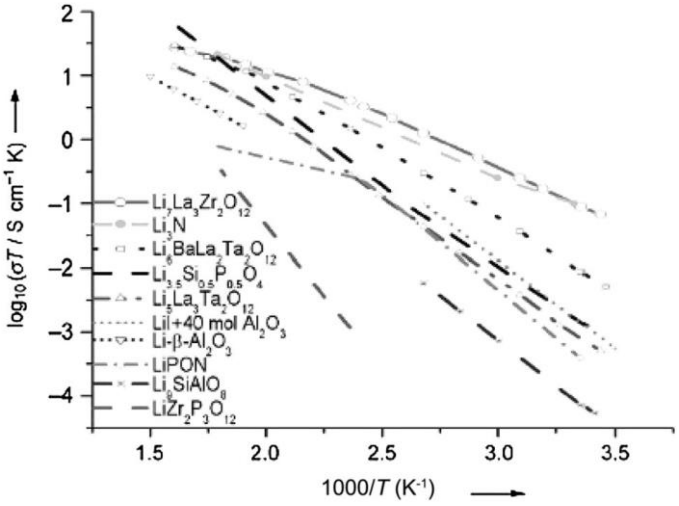

Figure 2. 9. Comparison of the total conductivity of $Li_7La_3Zr_2O_{12}$ and other Li-ion conductors. Adapted with permission from Ref. [39]. Copyright (2009) Elsevier Ltd.

2.2.2. Polymer-Based Solid Electrolytes (PSEs)

Lithium salts, polymer matrices, and additives make up PSEs. Typically, an ideal polymer-based electrolyte provides the following benefits: (1) Salt dissociation: an interaction between the polymer and the cation that has the benefit of causing ions to jump between different sites; a high dielectric constant encourages lithium salt dissociation and raises the concentration of charge carriers; a highly flexible backbone lowers the energy barrier for bond rotation and encourages block motion of the polymer chain.[46] (2) Functional groups: Thanks to molecular design, functional groups may be tailored to the requirements of various PSEs applications.[47] (3) Physical characteristics: simple film production, excellent elasticity, and light weight. (4) Safety: control of thermal runaways and dendrites.[48,49] The relationship between electrolyte structures and intrinsic qualities has been studied in the case of several polymer electrolyte materials, including polyethylene oxide (PEO),[50] polyacrylonitrile (PAN),[51] and polyvinylidene fluoride (PVDF).[52] The use of PSEs in ASSBs with various architectures is summarized in Table 1.

Table 2. 1. Summary of polymer-based solid-state electrolytes

Electrolyte composition	Functional group	Ionic conductivity (S cm^{-1})	Cycling performance	Electrochemical window (vs. Li^+/Li) (V)	Ref.
PEO/LLZO-FEC-SN-LiTFSI	EO	1.6×10^{-4}, 25℃	0.25 mA cm^{-2}, 600h, 50℃	3.9	62
PAN-PEO-LiTFSI	CN	~10^{-4}, 60℃	0.30 mA cm^{-2}, 600h, 60℃	3.7	178
PVDF-$LiNSO_2$(LiTFSI)	PVDF	1.3×10^{-4}, 25℃	0.50 mA cm^{-2}, 100h, 25℃	4.8	100
P(VDF-TrFE)-LPSC	PVDF	1.2×10^{-3}, 25℃	6 mA cm^{-2}, 200h, 25℃	3.7	143
PEGDME-LiTFSI	EO	1.5×10^{-4}, 60℃	0.20 mA cm^{-2}, 2500h, 60℃	4.3	72
PEGDA-UpyMA-LiTFSI	EO	3.4×10^{-4}, 20℃	0.20 mA cm^{-2}, 2500h, 20℃	5.2	75

Note: PEO: polyethylene oxide; PAN: polyacrylonitrile; PVDF: polyvinylidene fluoride; EO: ethylene oxide; LiTFSI: lithium bis(trifluoromethansulfonyl)imide; SN: succinonitrile; PEGDME: poly (ethylene glycol) dimethyl ether; UPy: physically crosslinking uracil; CN: cyanide; P(VDF-TrFE): poly(vinylidene fluoride cotrifluoroethylene).

In general, there are two ways that lithium ions migrate through a solid electrolyte: first, they move via vacancies and gaps; second, they fracture and create an amorphous coordination link when local polymer segments move.[53] Ionic conductivity specifically relates to ionic charge, ionic mobility, and ionic concentration.[54] The following is the general definition formula for ionic conductivity in solid electrolytes:

$$\sigma = \sum u_i \cdot q_i \cdot c_i$$

where u_i is the ion mobility, q_i is the ion charge, and c_i is the carrier concentration. The glass phase change of the polymer in the amorphous phase is connected to the ion mobility u_i in the solid electrolyte system. Lithium ions may conduct more easily via solid electrolytes with lower glass transition temperatures (T_g) and more amorphous states. Additionally, increasing the carrier concentration, or c_i, is a complicated process that primarily focuses on three areas: Lithium ion concentration in the polymer; Lewis acid-base interaction between salt and polymer; and salt's plasticizing impact on the host polymer, which lowers the crystallinity of the polymer body (plasticizer, vacancy).[55] As a result, the complicated interaction between the lithium ion and polymer functional groups as well as the ionic conductivity of solid electrolytes are affected by the glass transition temperature, lithium salt concentration, and other factors.

For solid electrolytes, the voltage range that can be maintained without redox breakdown during charge and discharge is known as the electrochemical stability window. The HOMO maximum orbital potential of the polymer/inorganic filler, lithium salt, and additive in the solid electrolyte must be lower than the cathode material for the cathode-electrolyte interface side. A solid electrolyte's anion framework and capacity to lose electrons, which are constrained by the anion ionization potential, dictate its high voltage stability.[56] The charge and discharge processes for a high-voltage lithium metal battery are more difficult. A component of the cathode material comprises transition metal ions, which, during redox, might cause interfacial parasitic reactions by jumping from their greatest molecular orbital potential to a lower orbital.[57] The solid electrolyte's capacity to take electrons determines the stability of the lithium metal anode. The contact between a lithium metal electrode and an electrolyte is primarily separated into two parts: Uneven ions deposition brought on by chemical parasitic processes causes issues at the lithium metal interface during charge-discharge, as well as the creation of dendrites, punctures, and crack extensions.[58,59] Rugged components would use lithium metal if the local distribution of impurity particles from

solid electrolytes is not uniform at the lithium metal contact. Insufficient electrode-electrolyte interface contact results from the subsequent interface parasitic reaction of solid electrolyte components.[60] The lithium/electrolyte contact is also problematic with the fracture propagation of lithium dendrite at the grain. For solid-state electrolyte coupling effects, lithium dendrite development and dendrite piercing should generally be considered.

Poly(ethylene oxide) (PEO)-based PSEs

Due to its stable contact with a lithium anode, low cost, and relatively high ionic conductivity compared to other polymers, PEO is the most used polymer electrolyte material. Its chemical name is H-(O-CH_2-CH_2)n-OH.[61,62] In PEO electrolytes, the segmental motion of the ethylene oxide (EO) unit from the PEO chains is connected to the transit of Li^+ (from lithium salts), which may produce free space for the lithium-ion hopping from one coordinating site to another.[50] PEO has a high glass transition temperature (T_g) and significant Li^+ dissociation ability from lithium salt, enabling continuous lithium ion hopping. However, PEO-based electrolytes have two significant problems: (1) the strong ionic bond (C-O) coordinated between the O atom and the lithium ions in PEO chains limits the ionic conductivity (10^{-7} S cm^{-1}) and lithium-ion transference number at room temperature; (2) the higher glass transition temperature results in high crystallinity at room temperature, which restricts the movement of chain segments; and (3) the limited electrochemical window stability below 4 V. Because they not only enhance ionic conductivity and lithium salt dissociation but also use microphase separation to balance the two opposing characteristics of ion transport and mechanical stiffness, PEO derivatives with block copolymers have drawn particular interest.[63,64] Nanostructured block copolymer electrolytes (BCE) have promising applications in the design of polymer electrolytes, such as the polystyrene block-poly(ethylene oxide) (SEO) block, which provides mechanical stiffness, and the PEO block, which dissolves lithium salt and transports derived ions from lithium bis(trifluoromethansulfonyl)imide (LiTFSI).[65] To measure the conductivity and ion dynamic transport mechanism in the PEO-based bulk copolymer electrolyte, Danie et al. developed polystyrene-block-poly(ethylene oxide) (SEO-LiTFSI) and PEO-LiTFSI.[66] Figure 2.10 (a and b) illustrates how ion conductivity changes by adjusting the ratio of EO: Li, the latter modifying concentration and ionic properties (such ion solvation, correlation, and ion dispersion). The conductivity of SEO-LiTFSI is constant even if the PEO-LiTFSI has already reached its maximum at the solvation site, meaning that the ratio of composite and straight EO

units stays constant. Moreover, the solvation and transport properties of the conductive component over the whole bulk may be impacted by the presence of non-conductive components in the periodic structure of the block copolymer electrolyte (SEO-LiTFSI).

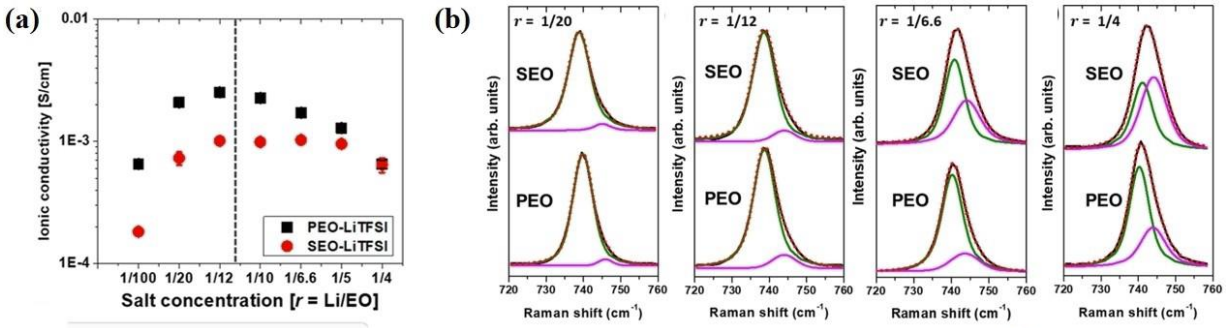

Figure 2. 10. a) PEO-LiTFSI and SEO-LiTFSI as a function of salt concentration-conductivity at 100°C; b) Raman spectra for SEO-LiTFSI and PEO-LiTFSI films at different salt concentrations (r=Li/EO) [The dissociated "free" ion species are in green and the associated ones in purple]. Adapted with permission from Ref. [66]. Copyright (2021) American Chemical Society.

By boosting the number of amorphous phases and lowering the glass transition temperature (Tg), plasticizers may act as organic solid fillers and alter crystallization behaviour.[67] It is commonly known that succinonitrile (SN) is one of the common plasticizers.[68] Ionic liquids and low molecular weight polymers are also used to inhibit the formation of PEO crystalline phase. For instance, Ran et al. used a solution casting technique to crosslink a hydrolyzed polymaleic anhydride (HPMA) low-molecular polymer plasticizer with PEO and lithium salt as shown in Figure 2.11.[69] The PEO's crystalline and amorphous phase were weakened by physical entanglement between HPMA and PEO, and the HPMA's -COOH group was able to increase ionic conductivity. Although the ionic liquid often facilitates interfacial ion diffusion, it is necessary to take the liquid flammable plasticizer's safety into consideration.

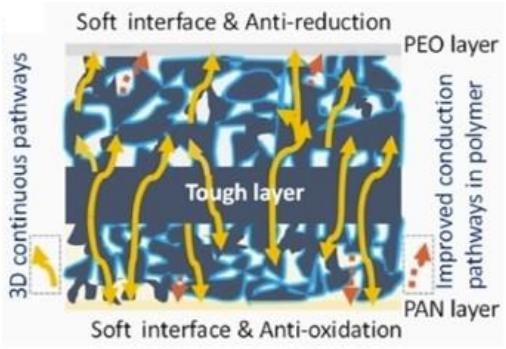

Figure 2. 11. Schematic diagram of polymer sandwich structure solid electrolyte. Adapted with permission from Ref. [69]. Copyright (2021) Elsevier Ltd.

PEO/Ceramic or PEO/Polymer SE Mixtures

The Li^+ diffusion route from polymer to inorganic particle to polymer is discontinuous, hence the physical mixing of polymer materials and inorganic filler has no impact on PEO electrolyte conductivity. To achieve high ionic conductivity, it is crucial to include extra lithium-ion routes between inorganic fillers and polymers. Lithium salt and cyclodextrins (CDs) are added to the polymer matrix, which weakens the interaction between the ether groups in PEO and allows for faster Li^+ migration across the matrix. It also creates a route for Li^+ high-speed diffusion from the PEO matrix to the $Li_7La_3Zr_2O_{12}$ (LLZO) fillers and back to the PEO matrix.[70] The intermolecular interaction between vinyl carbonate (EC) and the active inorganic filler Ta-doped LLZTO in $P(EO)_{15}$LiTFSI was ingeniously engineered by He et al. to address the issue of the low room temperature conductivity of the PEO based polymer electrolyte as shown in Figure 2.12.[71] As a result of the LLZTO-initiated ring opening reaction of EC, oligomers with ether oxygen chains are created, adding another fast Li^+ conduction channel. Additionally, it works as a destructor of the PEO chain, increasing the amorphous phase area of Li^+ migration in PEO and having a conductivity of 1.43×10^{-3} S cm^{-1} at ambient temperature.

When PEO polymer is oxidized at the voltage range of 4.05 to 4.3 V, the terminal hydroxide groups (-OH) are what are restricting the reaction. Poly (ethylene glycol) dimethyl ether (PEGDME), a crosslinked copolymer composed of conductive branched segments and a rigid matrix that can balance conductivity and mechanical properties, is created by esterifying the unstable end group -OH of PEO. PEGDME provides a satisfactory solid electrolyte membrane.[72] These conductive branched chain polymers are excellent building blocks for composite solid electrolyte structures

made of other polymers. By physically crosslinking uracil (UPy) and PEGMA having brush polyethylene glycol chain, Zhou and his colleagues creatively created a self-healing and highly tensile three-dimensional network to address the issue of fracture in polymer electrolytes.[73] In addition to suppressing lithium dendrite (stable operation for more than 500 hours at polarization current 1 mA), the cross-linked hydrogen bond network, electrolyte, and electrode contact also produce high solid-state battery performance (0.1 C, 80 cycles, capacity retention 91.6%). Similarly, Yao et al. created PE film as a 10 µm thick PEGMA composite solid electrolyte membrane that was supported by a substrate. Over 1500 hours at 0.1 mA/cm^2, the Li/PEGMA electrolyte/Li symmetric cell run steadily.[74] With a shorter backbone and two C=C terminal bonds to add monomer for polymerization, PEGDA is another polyethylene glycol (PEG) derivative with ether groups (-C-O-C-) on the chains. This results in bigger crosslink polymer network.[75] By using solvent-controlled evaporation, Wang and Dukjoon created poly(vinylidene fluoride), which was then randomly mixed with the PEGDA oligomer. With the PEO-PPO-PEO copolymers, PEGDA acts as curing agent to create an interpenetrating network that facilitates mechanical strength and ensures electrochemical stability up to 4.5 V.[76,77]

Figure 2. 12. The interaction mechanism of LLZTO with EC in PEO. Adapted with permission from Ref. [71]. Copyright (2021) Wiley-VCH GmbH.

He and coworkers looked into the effects of two MW PEGDA polymer types with variable SN-LiTFSI concentration according to the ternary phase diagram in Figure 2.13 in order to enhance their ionic conductivity and thermal stability.[78]

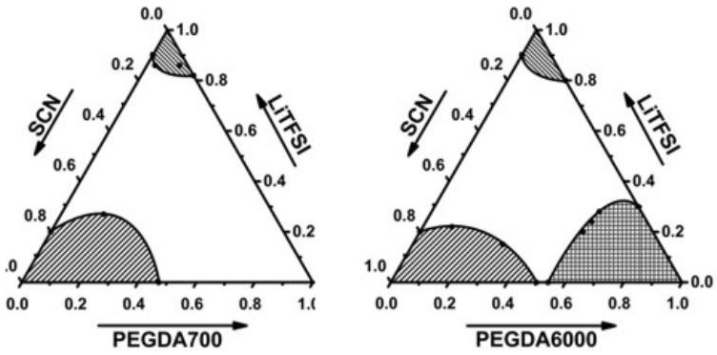

Figure 2. 13. Ternary phase diagram of PEGDA700 and PEGDA6000 blends at 25°C. Adapted with permission from Ref. [78]. Copyright (2016) Elsevier Ltd.

The cross-linking point of the polymer process is lowered when PEGDA's molecular weight is raised from 700 to 6000 g mol^{-1}, resulting in a material with better ionic conductivity and flexibility. In addition, the immediate physical cross-linking of ion-polyether oxygen coordination bonds and the chemical cross-linking of the PEGDA network cause the glass transition temperature (T_g) to rise as the concentration of lithium salt increases (Figure 2.14).[79] The ether oxygen link in the complex network is saturated when its concentration reaches 30 wt.%, which equals the threshold concentration of solution, while T_g lightly rises.

The ion transport mechanism and interfacial stability of polymer-based SSEs are greatly influenced by the chemical make-up and structure of lithium salt. Perfluoroimide lithium salts with fluorosulfonyl groups, such as LiTFSI, LiFSI, and LiFTFSI, are the most prevalent types of lithium salts. The effects of three lithium salts on PEO-based electrolytes were thoroughly examined by Zhang et al., who also established that LiTFSI had the greatest ionic conductivity and lowest crystallinity.[80] Because of the stable LiF layer that forms at the interface between LiFSI and Li metal after cycling, LiFSI exhibits steady cycling performance. Meng et al. dispersed high-concentration LiTFSI in polyvinyl acetal (PVFM) to create a novel "salt-with-salt" double lithium salt boron-based single ionic conductor polymer solid electrolyte (LiPVFM).[81] LiPVFM with a six-membered ether ring is advantageous for dissociating the ions in lithium salt, and an electrolyte with a stiff backbone has a lower Tg. In addition, lithium difluorooxalate borate (LiDFOB), which is often included as an additive to polymer-based SSE, has a broad electrochemical window and good conductivity. LiDFOB was introduced into SPEs by the Cui group; in addition to serving as a source of lithium, it also helped to create an interfacial stable layer.[82]

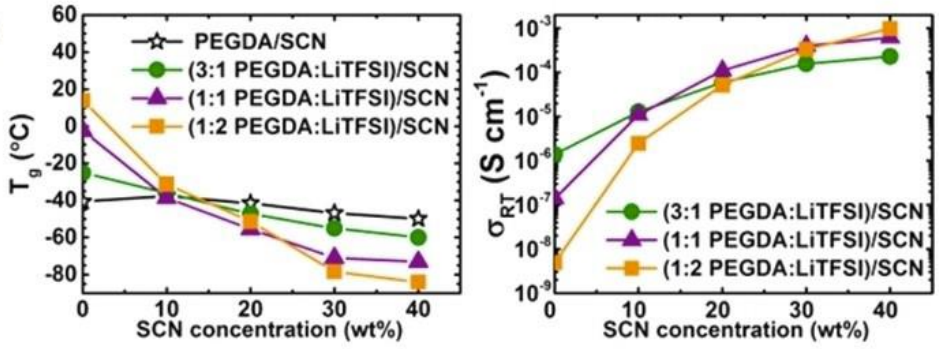

Figure 2. 14. T_g and room temperature ionic conductivity of various plasticized PEM systems. Adapted with permission from Ref. [79]. Copyright (2016) American Chemical Society.

Poly(acrylonitrile) (PAN)-based PSEs

Materials made of poly (acrylonitrile) feature a stiff bond termed cyanide (-CN) that has a rich electron polar group and may increase mechanical strength and thermal stability.[83, 84] The cathode-electrolyte interface (CEI) and solid electrolyte interphase (SEI) are two examples of interfacial phases that may be constructed and evolved at the negative electrode/electrolyte interface thanks to the functional group nitrile of polyacrylonitrile (PAN).[85-88] PAN is often utilized as the polymer substrate for extended electrochemical windows or stiff skeletons. Zhang described a sandwich membrane made of PVDF-HFP and PAN as a solid electrolyte supporting the skeleton without the need of solvents.[89] In general, PAN is semicrystalline at room temperature, which results in extremely poor ionic conductivity in PAN electrolytes.[90] Effective Li^+ conductive channels and a better carrier were given by the well-fabricated PAN polymer materials, which were also integrated with high-load ceramic electrolytes or specific molecular structure polymer materials. As opposed to pure PAN electrolyte, PAN and metal-organic framework (MOF) particles are synthesized as a composite solid electrolyte with high ionic conductivity (2.8×10^{-4} S cm^{-1}) and thermal stability.[91] PAN/MOF helps to provide structural strengthening by constructing a 3D continuous linked ion conductive channel (Figure 2.15a).[92] To boost ionic conductivity, PAN is properly molecularly modified with additional polymer components. Thus, conventional polyacrylonitrile-based composite electrolyte was reversed as follows by Wang et al.[93] Triacrylonitrile diacrylate cross-linked polyacrylonitrile-polyethyleneimine (PAN-PEI) was employed as a nanofiber membrane (Figure 2.15b).[94] The amidation processes involved combining the nitrile groups from PAN with PEI, which additionally contributes an acidic site in the solvent. The branch PEI of the flexible

skeleton is used in this particular crosslinking structure, which also serves to enhance the mechanical characteristics of the fibre-structured membrane. The improved PAN-PEI solid electrolyte membrane has a tensile strength of 9.36 MPa and an ionic conductivity of 3.39×10^{-4} S cm^{-1} at room temperature.

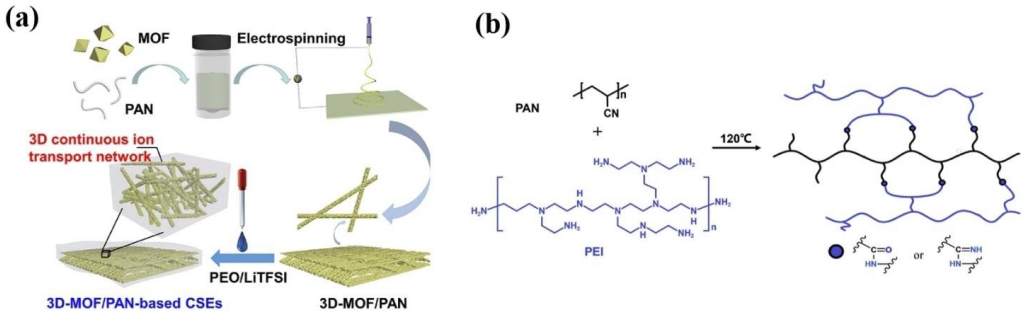

Figure 2. 15. a) Schematic procedure to fabricate 3D interconnected MOF-based CSEs. The 3D interconnected MOF/PAN network was prepared by electrospinning the mixture solution of MOFs and PAN. Adapted with permission from Ref. [92]. Copyright (2022) Elsevier Ltd. b) The schematic diagram of the crosslinking reaction between PAN and PEI. Adapted with permission from Ref. [94]. Copyright (2021) Elsevier Ltd.

The -CN group due to its strong electronegativity may draw transition metal ions from cathode materials as well as Li^+ from lithium salts. PAN is a crucial polymer for coating layer materials because of its viscosity and resistance to oxidation. According to Chen et al., the solvothermal reaction method produced a thin-film coating of PAN on the LLZTO particle surface.[95] The thin-film solid electrolytes produced by PAN were uniformly nanocoated, resulting in an enhanced Li^+ transference number of 0.66 and a satisfactory ionic conductivity of 1.1×10^{-4} S cm^{-1}. The cyclization process that results from heating PAN to 300°C produces cyclized PAN (c-PAN), whose delocalized bonds are encouraged to form a link with cathode particles.[96,97] A coating layer with high conductivity, dense regularity, and ion permeability was created by Wang et al.[98] The PAN is deposited on the NCM811 particle surfaces, and rock salt acts as a bridge layer, transitioning from the surface layer phase with charging/discharging cycles. It offers a fresh method for addressing the electrochemical-mechanical deterioration of NCM cathode particles over extended periods of time. Liang et al. synthesized single-crystalline $LiNi_{0.6}Co_{0.2}Mn_{0.2}O_2$ (SNCM622) cathode particles coated with nanoscale $Li_{1.4}Al_{0.4}Ti_{1.6}(PO_4)_3$ (LATP) and cyclized PAN (c-PAN) as shown in Figure 2.16.[99] A prolonged electrical contact between SNCM622

particles and a homogeneous coating layer, particularly PAN with a delocalized bond, resulted in high electrochemical performance for capacity retention (72.7% over 500 cycles, at 0.5 C).

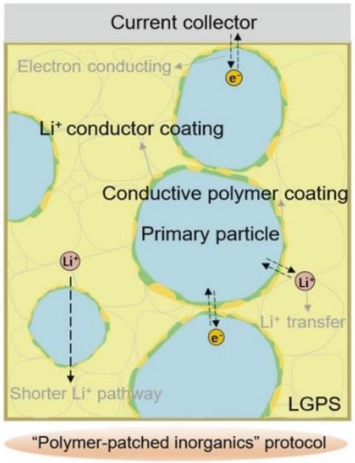

Figure 2. 16. Carbon conformation transition diagram of PEO, and SN-PEO of SPEs. Adapted with permission from Ref. [99]. Copyright (2022) Wiley-VCH GmbH.

Poly(vinylidene fluoride) (PVDF)-based PSEs

PVDF, which stands for poly(vinylidene fluoride), and its copolymers are semi-crystalline structural polymers that may be categorized by their α, β, and γ-phase.[92] PVDF and its copolymers as solid electrolytes, provide strong mechanical strength, a broad electrochemical window, and thermal stability.[52] Its good electrolyte performance is due to its exceptional chemical stability and dielectric constant. PVDF may be used in different solvent mixture formulations. For example, the solvent employed like N, N-dimethylformamide (DMF) may affect considerably the lithium transport, interface stability, and battery performance of PVDF as polymer electrolyte. The impact of DMF concentration on the chemical reaction mechanism and ionic conductivity of PVDF was examined by Nan's group (Figure 2.17).[100]

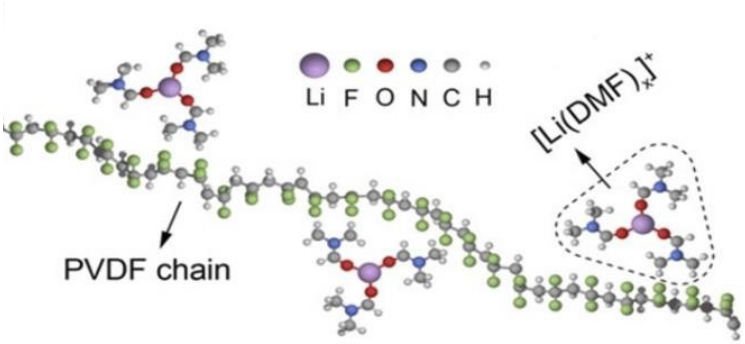

Figure 2. 17. $[Li(DMF)_x]^+$ ($x \leq 3.29$) in the PVDF-LiFSI electrolyte. Adapted with permission from Ref. [100]. Copyright (2020) Wiley-VCH GmbH.

The effect of Li salt (LiFSI) concentration in PVDF-DMF system is shown in Figure 2.18. There is an interaction between $[Li(DMF)_x]^+$ and PVDF chains that affect ion transport. With no free solvent present, the DMF is complexed with Li ions in the PVDF-DMF solution. Lithium-ion conductivity may be increased by adjusting the fillers and polymer function group composition of PVDF-based electrolytes. $Li_{29}Zr_9Nb_3O_{40}$ (LZNO) active fillers were added by Chen et al. to the PVDF electrolyte.[101] The ionic conductivity was increased at room temperature from 1.26×10^{-4} S cm^{-1} to 2.34×10^{-4} S cm^{-1} because to the high dielectric constants of PVDF and Y^{3+}. The poly (styrene sulfonic acid) (PSSA) chains grafted onto the PVDF porous electrolyte membranes were studied by Tsai et al.[102] The PVDF porous electrolyte membranes had a greater ionic conductivity when ion conductor-containing chains are present because the in-situ polymer at the surface created Li^+ conductivity routes and electrochemical stability rather than plain PVDF support.

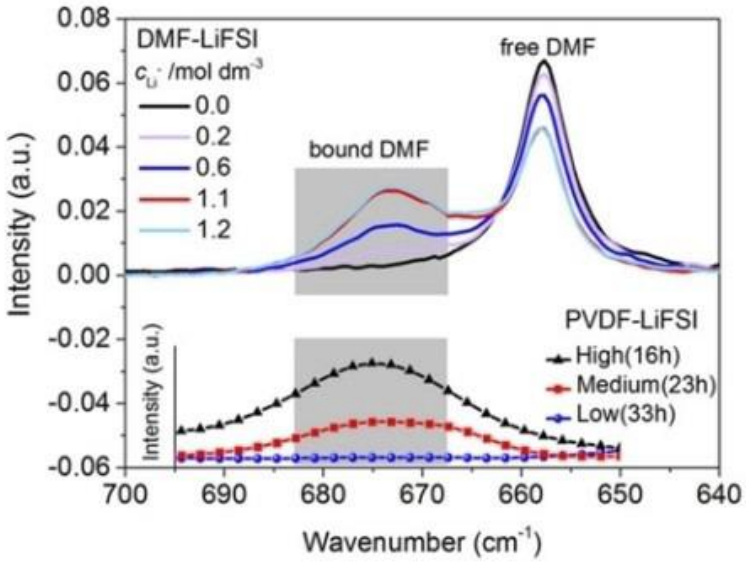

Figure 2. 18. FTIR spectra observed for DMF-LiFSI solutions with various salt concentrations and different vacuum drying times. Adapted with permission from Ref. [101]. Copyright (2022) Elsevier Ltd.

When compared to PVDF, mixture of PVDF with HFP (HFR: hexafluoropropylene) has superior flexibility and a dielectric constant of up to 8.4. This is so because of the inclusion of HFP the polymer is rendered semi-crystalline, enjoying significant more lithium salt dissociation hence enhanced ionic conductivity.[93] Li et al. created bipolar SSBs by combining the PVDF-HFP (as a solid matrix) with LLZO, LiTFSI, triglyme, and triethyl phosphate (Figure 2.19).[103]

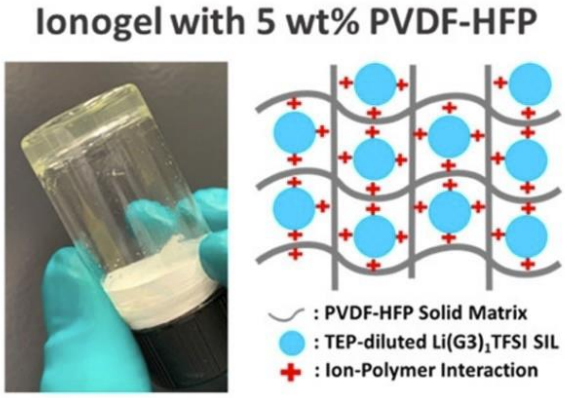

Figure 2. 19. Ionogel with 5 wt. % PVDF-HFP. Adapted with permission from Ref. [103]. Copyright (2022) American Chemical Society.

The ionic polymer gel formed with PVDF-HFP (Figure 2.19) exhibits exceptional ionic conductivity of 2.61×10^{-3} S cm $^{-1}$ at normal temperature. Additionally, the bipolar SSB is resistant to cutting, burning, and folding and can work steadily down to -18 °C. A 3D framework has also been built using the PVDF-HFP nanofiber, which has also been presented as a host. By electrospinning and then hot-pressing PEO and LATP particles, Yao et al. created a thin, high-performance composite solid electrolytes membrane (Figure 2.20).[104] With a 50 nm thickness and a high electrochemical window of 5.2 V, the PVDF-HFP nanofibers may interact with PEO to create an H-F bond at 60 °C moulding. At this temperature, the lithium transference number is 0.49, and after 100 cycles, the nanofibers can maintain 94.6% of their capacity at 0.1 C. All of the fluorine atoms are situated on one side of the polar chain conformation of poly(vinylidene fluoride cotrifluoroethylene) [P(VDF-TrFE)], while the hydrogen atoms are positioned on the other. Additionally, P(VDF-TrFE) is more flexible than frequently used PVDF and may be utilized to build ultra-thin, highly conductible solid electrolyte membranes by combining it with sulphide electrolytes.

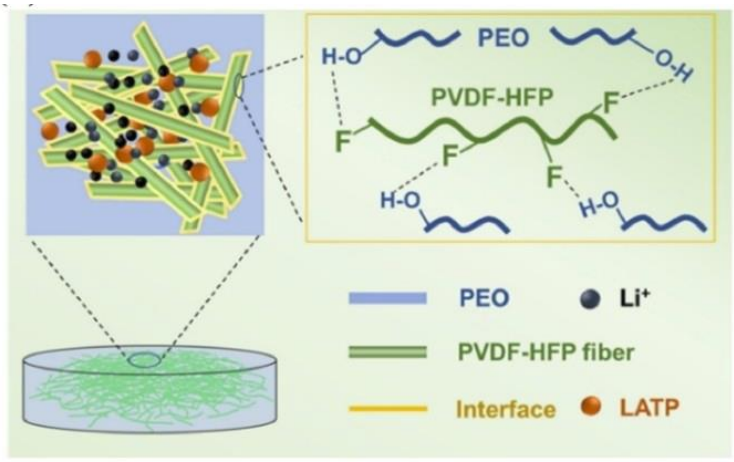

Figure 2. 20. Intermolecular hydrogen binding effect between PVD-HFP and PEO. Adapted with permission from Ref. [104]. Copyright (2022) Elsevier Ltd.

2.2.3. Sulfide-Type Solid Electrolytes

Thio-LISICON-Type

Due to its superior electrochemical performance in comparison to LISICON family conductors, the thio-LiCICONs family has been suggested as a sulfide-type Li-ion conductor[105,106]. Its nominal composition is $Li_{4x}M_{1y}M'_yS_4$ (M = Si, Ge, and M'= P, Al, Zn, Ga). Among these conductors, the

ionic conduction of $Li_{4-x}Ge_{1-x}P_xS_4$ (2.2×10^{-3} S cm^{-1} at 25 °C) outperformed every other component in terms of performance. Researchers have also discovered that the radius and polarizability of the constituted ions play a major role in their ionic conduction performance, and that the substitution of S for O can reduce the interactions between Li^+ in the sub-lattice and increase the concentration of mobile Li^+, which accounts for the higher conductivity of S-doped LISICONs compared to their oxide analogues.

Kamaya et al.[107] also developed a novel crystalline sulphide Li-ion electrolyte ($Li_{10}GeP_2S_{12}$) with outstanding electrochemical properties (exceedingly high conductivity of 1.2×10^{-2} S cm^{-1} and a wide potential window) and other advantages and reported that this material can be applied in LIBs with $LiCoO_2$ and Li-In alloy as the cathode and the anode, respectively, to achieve desirable performance. Using synchrotron radiation XRD and *ab initio* modeling, the researchers determined the crystal skeleton of $Li_{10}GeP_2S_{12}$ to consist of a 3D framework with LiS_6 octahedra and $(Ge_{0.5}P_{0.5})S_4$ tetrahedra forming 1D chains connected by a common edge, which are connected at the corners with PS_4 tetrahedra. Neutron Rietveld analysis was also employed to support the Li occupancy and content. Additionally, according to Du et al.[108], the tetrahedrally coordinated Li1 (16*h*) and Li3 (8*f*) sites facilitate ionic conduction and form a 1D tetrahedral chain along the c direction, but the octahedrally coordinated Li2 sites are unavailable for Li^+ diffusion. This implies that Li^+ diffusion paths along the c-axis are preferable to those in the a-b plane (reflecting only weak anisotropy of Li^+ diffusion) with the thermodynamic stability being studied by using as initio methods. Further in a separate study involving LGPS, the strong Coulombic link between mobile ions was assumed to induce Li-ion transport in a string-like fashion giving rise to low activation energy and exceptionally high ionic conductivity.[109]

LGPS-Type

The extraordinary ionic conductivity of $Li_{10}GeP_2S_{12}$ (LGPS), which is equivalent to that of organic liquid electrolytes (Figure 2.21), has sparked a great deal of attention since it was initially presented in 2011 [107]. The limited quantity and high cost of Ge in the electrolyte, as well as the unstable LGPS interface, must be addressed, however.[110] Given that the LGPS family may be separated into Ge-free and Ge-doped electrolytes ($Li_{10}GeP_2S_{12}$ and Li_7GePS_8), the discovery of novel LGPS-type materials is required to enhance the use of LGPS conductors.[111] Researchers

have tried to substitute homologous Si^{4+} or Sn^{4+} for Ge^{4+} to reduce the high cost of Ge, producing materials like $Li_{10}SnP_2S_{12}$,[11] $Li_{10+\delta}(Sn_ySi_{1-y})_{1+\delta}P_{2-\delta}S_{12}$,[113] $Li_{11}Si_2PS_{12}$,[113] and $Li_{9.54}Si_{1.74}P_{1.44}S_{11.7}Cl_{0.3}$.[114] Overall, researchers found that these Si- and Sn-doped materials had lower conductivities than the parent LGPS, indicating that Si-doping may, to some degree, be able to reduce conductivity and narrow tunnel widths for Li migration. Regarding the decrease in conductivity in Sn analogues, Zeier et al.'s work[115] clearly shows that Sn^{4+} substitution may cause Li^+ transport to become constrained in the z-direction, leading to stronger activation barriers.

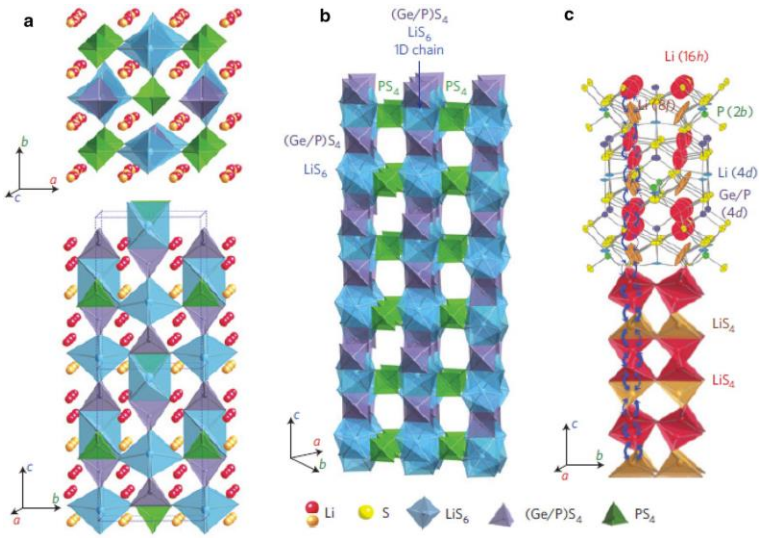

Figure 2. 21. (a) Framework structure and Li-ion environment of $Li_{10}GeP_2S_{12}$. (b) Framework of $Li_{10}GeP_2S_{12}$. (c) Conduction pathway of Li-ions in $Li_{10}GeP_2S_{12}$. Adapted with permission from Ref. [107]. Copyright (2011) Springer Nature.

Among the Ge-free LGPSs, Kato et al.[114] claimed that $Li_{9.54}Si_{1.74}P_{1.44}S_{11.7}Cl_{0.3}$ had an extremely high conductivity of up to 25 mS cm^{-1}, the greatest conductivity ever recorded for solid Li conductors (particular data shown in Figure 2.22a), and twice as much as the archetypal LGPS.[114] Here, the researchers verified 3D Li migration channels with 1D channels along the c-axis and 2D channels in the a-b plane using the anisotropic thermal displacement of Li (Figure 2.22b) and nuclear density distribution (Figure 2.22c), and they suggested that this 3D conduction pathway in the LGPS-type conductor can help to achieve the best conductivities. Additionally, these researchers noted that the LGPS-type conductor had remarkable chemical stability, particularly at 100 °C, and they ascribed this to the absence of elemental diffusion and low interfacial resistance.

Furthermore, $Li_{9.6}P_3S_{12}$ has a comparable LGPS structure to $Li_{9.6}P_3S_{12}$ and has been shown to have superior electrochemical stability and longer lifetimes under difficult cell operating circumstances. Later, Sun et al.[113] reported that by adjusting the ratio of Sn/Si and M^{4+} (Sn^{4+} and Si^{4+})/P^{5+} in the [M1/P1] (4d) site, the dual doping of the original LGPS with Sn and Si can improve ionic conduction, resulting in $Li_{10.35}(Sn_{0.27}Si_{1.08})P_{1.65}S_{12}$ with an ionic conductivity of 1.1×10^{-2} S cm^{-1} that is extremely close to that of the archetype LGPS (1.2×10^{-2} S cm^{-1}).

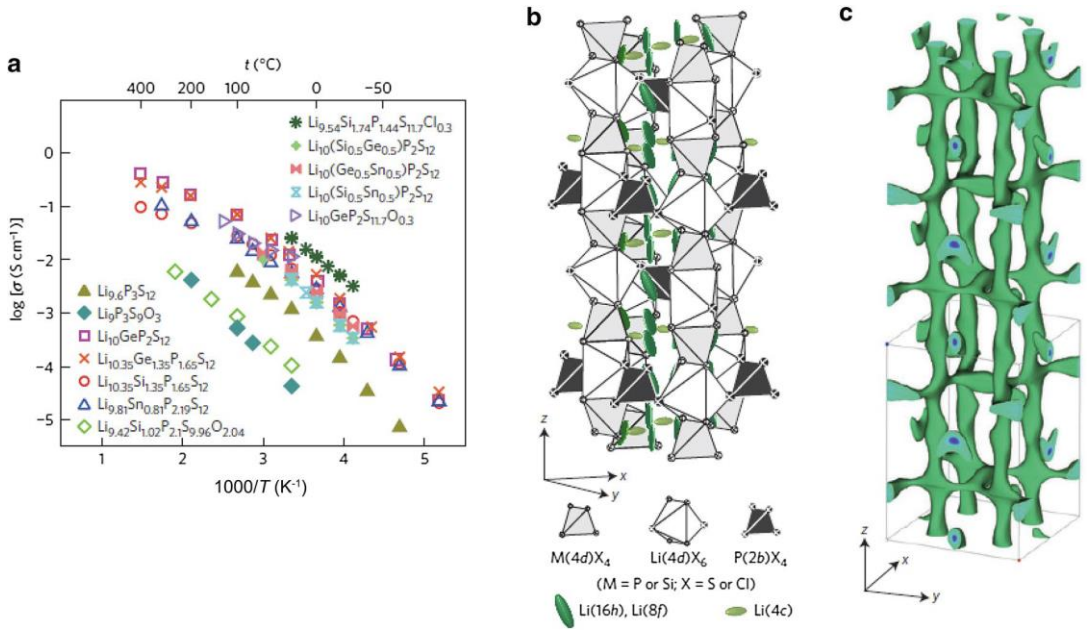

Figure 2. 22. Ionic conductivity and framework of $Li_{9.54}Si_{1.74}P_{1.44}S_{11.7}Cl_{0.3}$. (a) Arrhenius conductivity plots for the LGPS family, $Li_{9.6}P_3S_{12}$ and $Li_{9.54}Si_{1.74}P_{1.44}S_{11.7}Cl_{0.3}$. (b) Framework structure of $Li_{9.54}Si_{1.74}P_{1.44}S_{11.7}Cl_{0.3}$. (c) Nuclear distributions of Li atoms in $Li_{9.54}Si_{1.74}P_{1.44}S_{11.7}Cl_{0.3}$ at ambient temperature. Adapted with permission from Ref. [114]. Copyright (2016) Springer Nature.

Argyrodites

High ionic conductivities and excellent cation mobility are the defining characteristics of argyrodites, and fast Li-ion conducting argyrodites like Li_6PS_5X (X = Cl, Br, I) are exemplary members of this family. Whereas, Deiseroth et al.[116] observed that Li_6PS_5X may be produced by combining Li_2S, P_2S_5, and LiX at 550 °C and that Li_6PS_5Cl and Li_6PS_5Br exhibited superior conductivity than Li_6PS_5I, the addition of halides into argyrodites can also result in conductivities in the range of 10^{-2} – 10^{-3} S cm^{-1}. Regarding the Li_6PS_5X crystal structure (Figure 2.23a), the cubic

Laves topology serves as the foundation for the lattice, and the PS_4^{3-} anions are positioned in the centre of the 4*b* sites, while the other sulphur atoms occupy the 4*a* and 4*c* sites.[117] Although halogens have been used to replace the sulphur in this structure, the sulphur of PS_4^{3-} is not replaced; instead, halogens occupy the 4*a* or 4*c* sites to reveal a face-centered structure, with Li ions occupying the remaining tetrahedral interval (24*g* and 48*h* Wyckoff sites). The transition state for leaps between two 48*h* sites may also be position 24*g*, and 12 48*h* sites can form a cage structure by enclosing each 4*c* site (Figure 2.23b).

Three separate jump processes: next-neighbor leaps (48*h*-24*g*-48*h*), intra-cage jumps (48*h*-48*h* jumps inside the cage), and inter-cage jumps (48*h*-48*h* jumps across cages)—are responsible for the Li diffusion brought on by these partly occupied places.[117] Among these mechanisms, intra-cage leaps with modest jump rates may restrict diffusion whereas inter-cage jumps are thought to dominate macroscopic long-range ion transport (Figure 2.23c and d).[118,119] Additionally, the substitution of halogen for sulphur may result in vacancies, which are linked to disorder on the S^{2-}/X^{-} sublattice and can improve local Li-ion transport. For instance, Deiseroth et al.[116] found that Cl^{-1} and Br^{-1} may occupy the 4*a* and 4*c* sites in Li_6PS_5X to enable considerable halogen ion disordering, resulting in high conductivities for Li_6PS_5Cl and Li_6PS_5Br. In contrast, I^{-1} can seldom occupy 4*a* sites, and I-containing argyrodites devoid of the disorder exhibit greater activation barriers for conduction. Additionally, Kraf et al.[117] reported on the impact of lattice dynamics on ionic mobility and concluded that softer lattices result in a lower migration barrier for migrating cations.

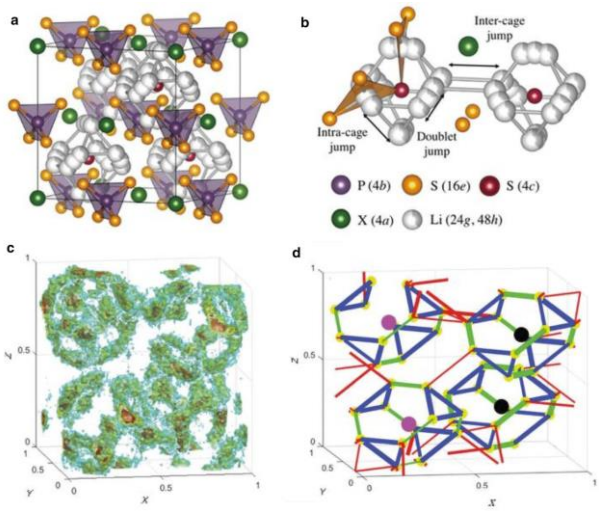

Figure 2. 23. (a) Crystal structure of Li_6PS_5X. (b) Li positions and possible jump routes. Adapted with permission from Ref. [117]. Copyright (2017) American Chemical Society. (c) MD simulation of Li-ion density in Li_6PS_5Cl Adapted with permission from Ref. [118]. Copyright (2018) Elsevier LTD. (d) MD results of jump statistics of Li_6PS_5Cl. Adapted with permission from Ref. [119]. Copyright (2016) American Chemical Society.

2.2.4. Polymer-Based Composite Solid Electrolytes

Ion transport and mechanical performance are often important factors to consider in solid electrolytes made of polymers. There are three strategies to broaden the ion transport channel for enhancing ionic conductivity, according to current research (Table 2.2): (1) Passive fillers may modify the polymer chain; (2) active fillers together with the polymer can provide a lithium-ion transport channel; and (3) metal/covalent organic frameworks can create three-dimensional skeletons or continuous phase paths.

Table 2.2. Summary of performance of organic-inorganic composite solid-state electrolytes

Filler	Polymer/Salt	Conductivity (S cm^{-1})	Electrochemical Window (vs Li^+/Li) (V)	Ref.
SiO_2	PEO/TDI	1.2×10^{-4} (25℃)	5.6	179
SiO_2 aerogel	PEGMA/PEO/LiTFSI	6.0×10^{-4} (30℃)	-	180
TiO_2-grafted NHPE	PEGMEM/LiTFSI	1.1×10^{-4} (30℃)	5.4	181
$Al2O_3$ fillers	PVDF-HFP/PEG/LiTFSI	8.3×10^{-4} (30℃)	-	182
LLZO	PEO/LiTFSI	1.1×10^{-4} (30℃)	5	183
LLTO	PVDF-HFP/LiTFSI	1.2×10^{-4} (30℃)	4.7	144
LLTO-LLZO	PVDF-PTFE	1.4×10^{-4} (30℃)	5.3	143
3D-PAN/LLZTO	PEO/LiTFSI	2.3×10^{-4} (30℃)	5.2	184
LATP/PE	PEO/LiTFSI	1.4×10^{-4} (60℃)	-	185
MOF	PAN/PEO/LiTFSI	2.9×10^{-4} (25℃)	4.7	92

PEO: polyethylene oxide; PAN: polyacrylonitrile; PVDF: polyvinylidene fluoride; LiTFSI: lithium bis(trifluoromethansulfonyl)imide; TDI: toluene diisocyanate; HFP: hexafluoropropylene; PEG: Poly(ethylene glycol); PTFE: Polytetrafluoroethylene; MOF: Metal Organic Frameworks; PEGMEM: Poly(ethylene glycol) methyl ether methacrylate.

Inert Filler

Ionic conductivity is significantly influenced by several variables, one of which being the polymer's crystallinity. It is practical to increase ionic conductivity by adding inert fillers since this lowers the polymer matrix's crystallinity and encourages the dissociation of lithium ions.[120,121] SiO_2, TiO_2, Al_2O_3, and other inert fillers may enhance the free volume of the polymer matrix and speed up the dynamics of the polymer block, which lowers polymer crystallinity and lowers the melting point of the polymer. By employing SiO_2-aerogel as the framework for polymer-based electrolytes, Lin and his colleagues conducted ground-breaking research and presented a technique to manufacture composite solid electrolytes (Figure 2.24).[122] A continuous aerogel network with

better mechanical characteristics is created by the uniform distribution of SiO_2 ultrafine particles in the polymer matrix electrolyte, which has a comparatively high specific surface area and may provide more active sites for the functional groups of organic molecules. The interaction of fillers and polymers improved the overall composite solid electrolyte's ionic conductivity and increased the dissociation of lithium ions (6×10^{-4} S cm^{-1}, 30 °C). for the practical use of polymer-based SSEs and SiO_2 filler composite. Li et al. also successfully crosslinked SiO_2 with PEO using the one-pot synthesis technique by using toluene diisocyanate (TDI) as a bridge, resulting in a polymer-inorganic crosslink.[123] The resulting electrolyte membrane has a tight link between PEO chains and SiO_2 and exhibits exceptional electrochemical performance at room temperature (1.2×10^{-4} S cm^{-1}) as a result of the anchoring of the active groups NCO on the TDI surface.

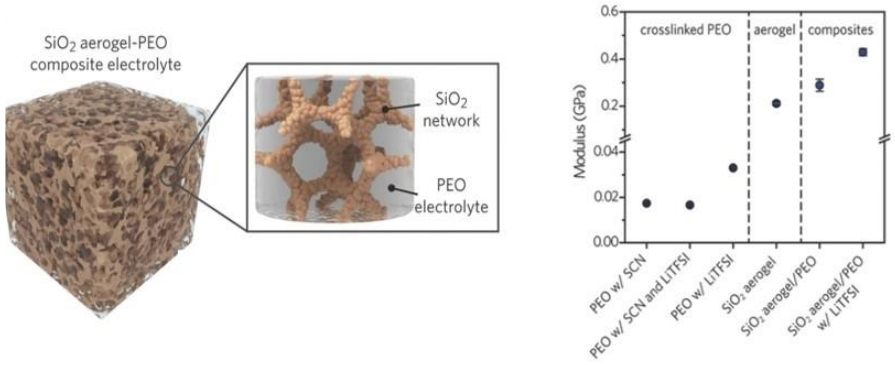

Figure 2. 24. SiO_2-aerogel as a skeleton-reinforced composite solid electrolyte and elastic modulus. Adapted with permission from Ref. [122]. Copyright (2018) Wiley-VCH GmbH.

TiO_2 is further used as a polymer electrolyte filler because of its unique form and surface characteristics.[124,125] By adding TiO_2 nanofibers to the lithium metal-LLZTO electrolyte interface recently, Chen and colleagues successfully enhanced the interface contact (Figure 2.25).[126] TiO_2 greatly lowers the interface resistance (from 374 Ω cm^{-2} to 27 Ω cm^{-2}) in comparison to the unregulated interface and enhances the cycle performance of solid-state batteries. Additionally, TiO_2 lowers the host polymer chain's crystallinity and essentially disrupts its trend of orderly stacking.

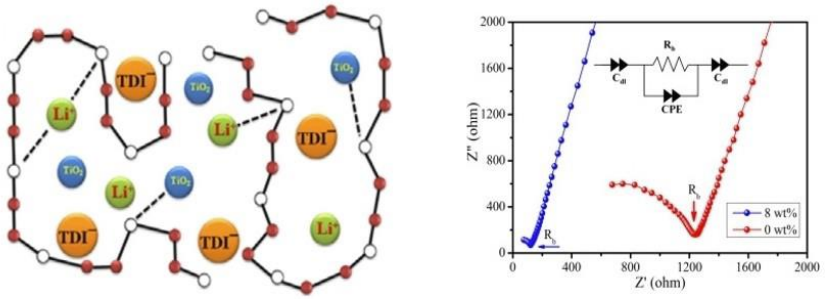

Figure 2. 25. Nyquist impedance plots of PEO_{12}-LiTDI and PEO_{12}-LiTDI-8 wt% TiO_2 electrolyte membrane at room temperature. Adapted with permission from Ref. [126]. Copyright (2016) Elsevier Ltd.

Al_2O_3 is an inorganic filler that is often used to graft polymers via the Lewis acid-base reaction, enhancing the dissociation of lithium salt and improving the wettability of the lithium metal interface. Al_2O_3 has recently been suggested as an inorganic filler for polymer electrolytes.[127] In particular, the Al_2O_3 filler addition demonstrated the anticipated ionic conductivity (5.26×10^{-3} S cm^{-1}). PVDF-HFP encases TiO_2 particles in a manner reminiscent to plasticizers being trapped in a polymer electrolyte matrix, which offers a suitable transport route for lithium ions to move through the polymer material as shown in Figure 2.26.

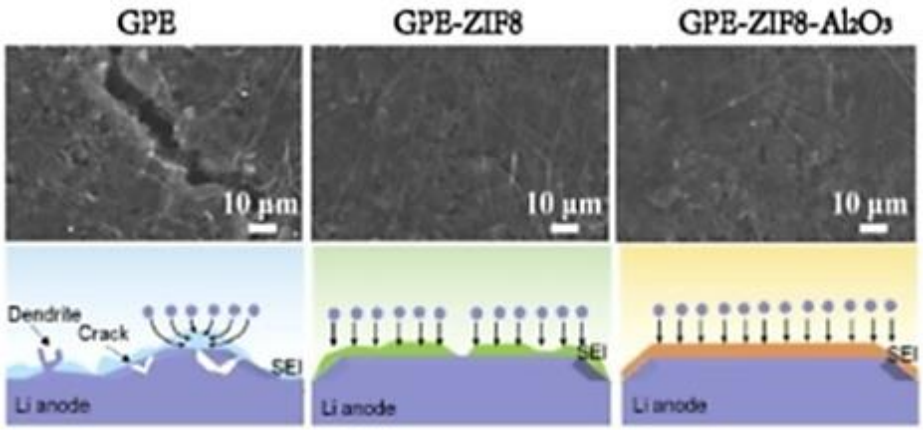

Figure 2. 26. Surface morphologies of lithium deposition, and schematic diagrams after cycling with GPE/Al_2O_3. Adapted with permission from Ref. [127]. Copyright (2020) Royal Society of Chemistry.

Although inert filler-polymer composite SSEs have made progress, the following problems still exist: 1) The inert filler is only effective in improving ionic conductivity; it has no effect on the polymer electrolyte's conductivity mechanism. 2) Nanoparticles easily aggregate or disperse due

to their poorly exposed, small active sites, making it challenging to combine with polar groups and anions. and 3) In the inert-filler particles, segmentation dynamics and ionic conductivity are blocked, resulting in lower ion transport and ion transfer numbers.

Active Ceramic Filler

Active fillers are combined with polymers to create organic-inorganic composite SSEs, which provide more lithium-ion conduction channels than inert fillers do.[128] Li^+ migration in the crystalline phase and hopping between them, creating a percolation channel, are primarily responsible for the ions transport mechanism in active filler. In particular, the grain boundary morphology of ceramics has a significant impact on the migration energy (Ea). The ionic conductivity will change with the temperature of the surroundings when polymers are the primary phase. If the primary conducting medium is made up of active fillers, then polymers serve as a binder for cross-linking and adhesion. In composite electrolytes, three separate ion transport pathways may be active.[129,130] The inorganic-organic composite SSE specifically exhibits three phases of conduction, including active filler conduction, polymer/filler interface conduction, and polymer (lithium salt) conduction.[131] As a result, increased research has concentrated on enhancing the ionic conductivity of polymer-based SSEs by adding active fillers. The cubic garnet of $Li_7La_3Zr_2O_{12}$ (LLZO) and $Li_{6.4}La_3Zr_{1.4}Ta_{0.6}O_{12}$ (LLZTO),[132] the perovskite oxide of $Li_{3x}La_{2/3-x}TiO_3$ (LLTO),[133] and the rapid ionic conductor of sodium superionic conductor (NASION) are among the active fillers that are generally being explored.[134]

Cubic garnet oxide

Lithium-ion is dispersed in the interstitial sites of the tetrahedral (24*d*), octahedral (48*g*), and octahedral (96*h*) crystal structures in garnet structure electrolytes, which have the general formula $Li_7La_3Zr_2O_{12}$(LLZO). The extra lithium cations may be accommodated by the cubic garnet crystalline structure, which results in an ionic conductivity of 10^{-4} S cm^{-1} at ambient temperature.[135] $Li_7La_3Zr_2O_{12}$ may create new conductive routes in the crystal structure, however this has an impact on the ionic conductivity at ambient temperature because its aggregation often lacks enough active sites to cross-link with the anion. Pan et al. combined $Li_7La_3Zr_2O_{12}$ fibre

material with PEO and LiTFSI salt using a silk-template technique to create a continuous conductive network (Figure 2.27).[136] At ambient temperature, the finished composite electrolyte exhibits ionic conductivity of 2.4×10^{-5} S cm^{-1}. To reduce phase transition in the air and optimize its interface stability, $Li_7La_3Zr_2O_{12}$'s air-stability must also be carefully adjusted in addition to the ion conduction route.[137]

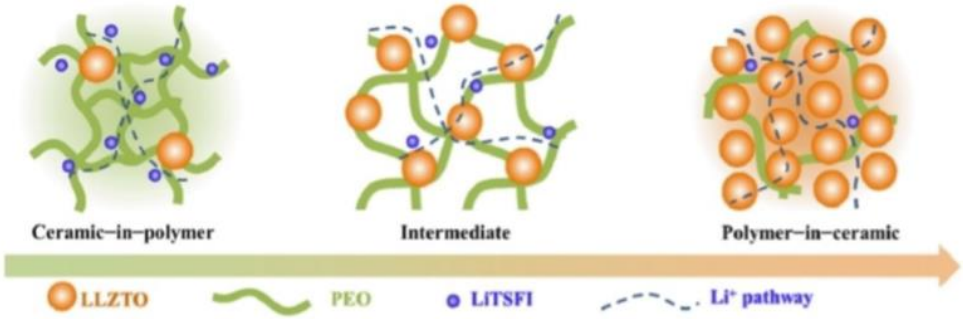

Figure 2. 27. LLZO active filler conductive network. Adapted with permission from Ref. [136]. Copyright (2018) Elsevier Ltd.

Water and oxygen may make $Li_7La_3Zr_2O_{12}$ sensitive. In a recent study, Martin Finsterbusch et al. comprehensively elucidated how $Li_7La_3Zr_2O_{12}$ hydrates in moist air.[138] Particularly, before 200 °C, the quantity of $Li_7La_3Zr_2O_{12}$ absorption rises with temperature, and once the temperature exceeds 200 °C, the water absorption stops. The surface diffusion of $Li_7La_3Zr_2O_{12}$ is constrained by $Li{\cdot}H_2O$ produced at ambient temperature, which has an impact on the interface reaction of solid-state batteries. Ta-doping of LLZO is stabilizing the surface of LLZO particles.[139] Huo et al. created the original interface, the lipophilic interface, and the three-dimensional structural interface between LLZTO and Li metals. The LLZTO was created using a three-dimensional frame using a novel acid etching procedure (Figure 2.28).[140] Acid etching not only creates a consistent pore structure in-situ but also cleans the surface contaminants and impurities from the grain boundaries. From a manufacturing standpoint, the hydrochloric acid solution concentration and etching duration regulate the thickness of the 3D skeleton, which is suitable for mass production. The 3D-LLZTO composite SSE membrane's conductivity at ambient temperature is 8.2×10^{-4} S cm^{-1}. Chen also created a gradient composite polymer electrolyte on the polymer substrate using straightforward UV curing technology in terms of interfacial ion transport.[141] The PEO layer's volume expansion

may be tolerated by the LLZTO layer's high elastic modulus, which prevents the electrolyte film from being bent or distorted.

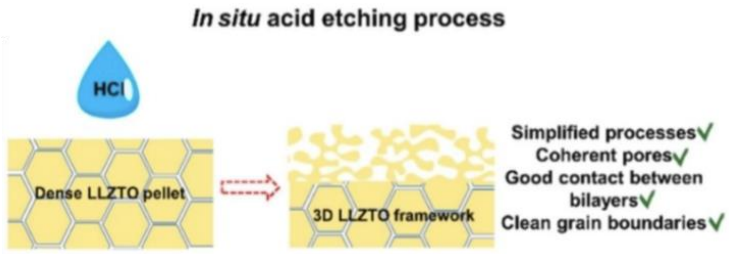

Figure 2. 28. Schematic of the in-situ acid etching process, cross-sectional and top-view SEM images of 3D-LLZTO. Adapted with permission from Ref. [140]. Copyright (2020) American Chemical Society.

Perovskite oxide LLTO

Perovskites have a cubic phase and the general formula ABO_3 with partial substitution of Li^+ for La^{3+} in $LaTiO_3$. For SSE, $Li_{3x}La_{2/3-x}TiO_3$ (LLTO) is a desirable perovskite structure. Its ionic conductivity is heavily influenced by the value of x, and its conduction mechanism is dependent on its A-site vacancy.[142] Yan created a high mechanical strain asymmetric composite SSE membrane.[143] To address unequal current distribution at the Li metal contact, LLTO is coated at the interface. The composite SSE memory material has an ionic conductivity of 1.38×10^{-4} S cm^{-1} at ambient temperature, and a Li-ion battery can cycle steadily for 2000 hours with a polarization current of 0.2 mA cm^{-2}. Similar to this, Li et al. added LLTO nanorods as a novel composite solid electrolyte to the PVDF-HFP polymer matrix. In addition to increasing free space, LLTO nanorods may provide a three-dimensional lithium-ion transport channel (Figure 2.29).[144] Additionally, the PVDF HFP polymer's great mechanical and thermal durability provide the composite solid electrolyte a high ionic conductivity (1.21×10^{-4} S cm^{-1}) at room temperature.

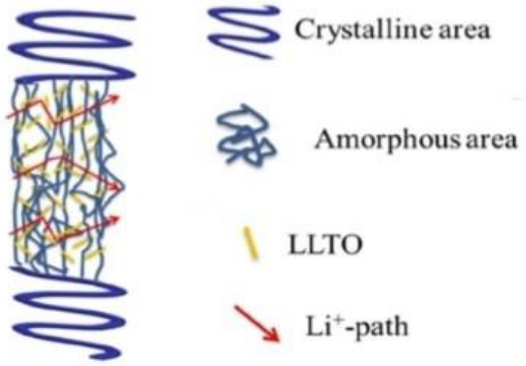

Figure 2. 29. Demonstration of the mechanism of Li^+ transmission path in the LLTO composite electrolytes. Adapted with permission from Ref. [144]. Copyright (2021) Wiley-VCH GmbH.

NASICON ionic conductors

Fast ionic conductors (NASICON), such as $Li_{1.5}Al_{0.5}Ge_{1.5}(PO_4)_3$ (LAGP) and $Li_{1.3}Al_{0.3}Ti_{1.7}(PO_4)_3$ (LATP), can be added to polymers as active fillers in addition to garnet and perovskite fillers to lessen their crystallinity, create conductive networks, and improve conductivity and lithium-ion transfer number. LATP's superior mechanical qualities and high Li^+ transfer number have been shown to make it a solid electrolyte material with good performance. Using LAGP and amorphous borosilicate glass (BG), Liu et al. created a LATPxBG thick ceramic electrolyte that showed satisfactory conductivity and mechanical qualities (conductivity 10^{-4} S cm^{-1}).[145] The authors presented a sacrificial template approach, which included the introduction of inexpensive, common sodium chloride powder into polymers as sacrificial templates, to construct a continuous 3D network of inorganic fillers in polymers. Lithium salt (LiTFSI) and polyethylene oxide (PEO) were chosen as fillers and added to 3D conductive networks.[146] First, rapid ion conductor LATP powder and sodium chloride (NaCl) were combined. Next, PTFE was used as an adhesive. Finally, the NaCl template was removed with water washing. Water can readily dissolve and remove the NaCl template, and it is simple to adjust how porous the three-dimensional conductive frame becomes. The three-dimensional LATP structure may also provide a continuous Li^+ conductive channel, enough mechanical modulus, enhanced Li^+ migration, and inhibit lithium dendrite formation. As a result, the well-designed LATP-PEO SSE demonstrates that it can function steadily at a polarization current of 0.2 mA cm^{-2} for more than 1000 hours.

In conclusion, the use of high-specific energy ASSBs may be facilitated by the combination of inorganic filler and polymer matrix via complementary control. Additionally, LAGP has gained a

lot of interest because of its properties of high electrochemical stability and conductivity at ambient temperature. Researchers suggested many LAGP composite SSE materials, including LAGP-PP membrane, LAGP-PEO composite electrolyte, and LAGP-Li_3InCl_6 composite electrolyte.[147]

2.3. Li^+ conductive mechanism in polymer-based composite solid electrolytes

2.3.1. Lewis acid-base interaction

Between the anion acceptor (Lewis acid) and the electron donor (Lewis base), there are interactions such as hydrogen bonds, positive vacancy-salt interactions, and dipole-dipole interactions that are explained by the Lewis acid-base theory.[148]

The Lewis base is introduced into the polymer chain via the inorganic filler's Lewis acid centre, creating a complicated interaction.[149] The anion has a considerable affinity for the Lewis acid centre, which makes coordination easy to form.[150,151] Lewis acid groups also coordinate with lithium salts on the surface of inorganic particles, causing higher-order dissociation of lithium salts thereby raising the concentration of free Li^+ ions. As a result, fillers containing Lewis acid centres interact with polymers via coordination bonding, which is thought to be a good candidate method for enhancing the conductivity of solid electrolytes. In a composite electrolyte, ion conduction is fast in ceramics but slow between ceramics and polymers. As a result, increasing the number of ceramic parts in a polymer matrix, or creating ceramics with a three-dimensional structure, or creating quick ion bridges between polymer and ceramic parts all contribute to boost the ionic conductivity of the polymer-based electrolyte.

Lewis acid-base interactions have the potential to significantly increase electrical conductivity, modify the ionic conductivity of polymer electrolytes, and enhance the stiffness/flexibility dynamics between polymer nanoparticles. Through strong Lewis acid-base interaction and weak hydrogen bonding, Hu and his team inventively created PEO and SiO_2 composite solid electrolytes (Figure 2.30).[152] As result of these interactions, PEO and SiO_2 filler have the following synergistic effects: (1) a decrease in the crystallinity of PEO due to chemical binding of OH group of PEO with lithium salt and SiO_2 nanoparticles; (2) enhanced molecular binding between SiO_2 nanoparticles and PEO molecular chains; and (3) suppression of deformation of polymer chains due to hydrogen bonds between SiO_2 and PEO thereby strengthening the mechanical properties of SSE.[153] Xu et al. used CaO as a strong Lewis alkaline filler combining with PEO polymers on the

basis of the Lewis acid-base interaction of oxides.[154] The results demonstrated that the calcium oxide filler had greater ionic conductivity and an additive impact on the chains of PEO polymer. A powerful Lewis acid compound, AlF_3 was utilized by Wang et al. to create PEO-based composite SSE.[155] The ionic conductivity and Li metal stability were dramatically increased (1.2×10^{-3} S cm^{-1}, over 3600 h) compared to the pure PEO-based SSE (6×10^{-4} S cm^{-1} at 60 °C, 550 h at 0.2 mA cm^{-2}).

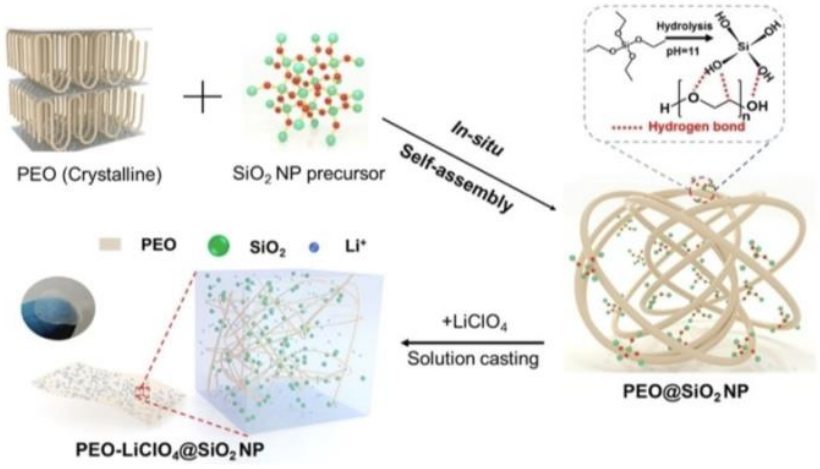

Figure 2. 30. Lewis acid-base interaction of SiO_2 and PEO-based polymers. Adapted with permission from Ref. [152]. Copyright (2020) American Chemical Society.

The open metal sites (OMSs) of MOF candidates, which may interact with Li^+ (Lewis acid), are chemically attached to Lewis bases. The ion transport gap between crystals is predicted to be reduced and the contact to be improved by the extended Lewis base long molecular chain. In accordance with molecular dynamics simulations, Brett M. Savoie et al. discovered that Lewis acidic polyborane had a higher lithium-ion mobility number than pure PEO and excellent Li^+ conductivity and lithium salt dissociation (Figure 2.31).[156]

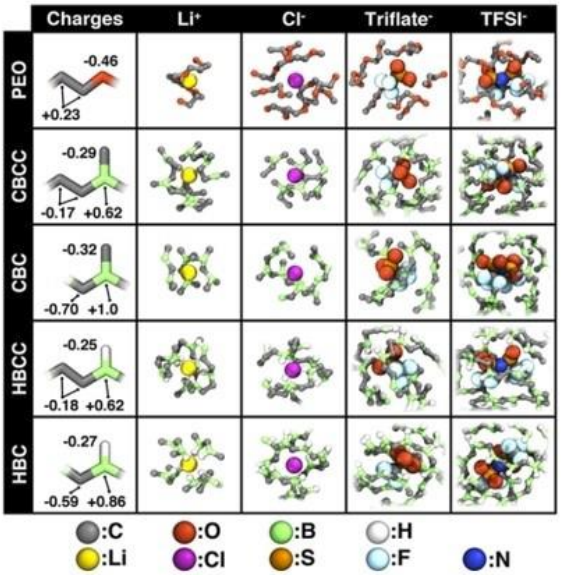

Figure 2. 31. Contrasting ion coordination behavior in Lewis-basic and Lewis-acidic polymers. Adapted with permission from Ref. [156]. Copyright (2017) American Chemical Society.

Numerous studies have been conducted on the molecular design of Lewis acid-base-centered composite SSE, particularly on sophisticated synthesis methods for metal-organic frameworks. By decorating Lewis bases on the open metal sites of MOF molecules, Li et al. effectively created a Lewis base MOF-polymer composite SSE (Figure 2.32.).[157] Li^+ transport and transition are encouraged by Lewis acid-base interaction. To facilitate Li^+ movement across the crystal gaps and enhance the electrode-electrolyte interaction, the Lewis base molecules are lengthened, and the ion transport gap between the crystals is decreased. Additionally, PEO's mechanical strength and electrical conductivity were concurrently increased, and a plan to develop a bifunctional additive was suggested. In their investigation of a solution-casting technique, Zeng et al. discovered that the addition of the bifunctional additive zinc bis(2-ethylhexanoate) ($Zn(BEH)_2$) simultaneously increased ionic conductivity and inhibited lithium dendrite growth.[158] PEO's crystallinity can be effectively decreased and the O Li^+ connection can be weakened thanks to the Lewis acid-base interaction between $Zn(BEH)_2$ and the PEO chain.

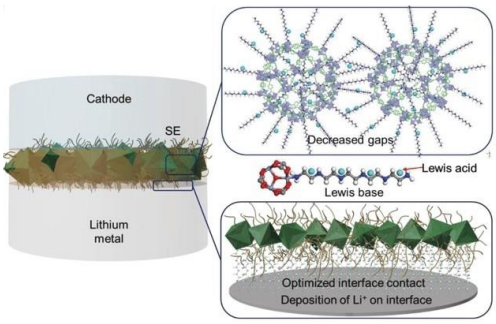

Figure 2. 32. The molecular-scale interface engineering strategy of MOF with long chain Lewis base. Adapted with permission from Ref. [157]. Copyright (2020) Wiley-VCH GmbH.

2.3.2. Vacancy

According to the conventional crystal chemistry theory, the three methods by which oxygen ion vacancies in crystals typically migrate are direct migration, incomplete occupancy, and coordinated migration.[18] In the lattice of inorganic fillers, Li^+ vacancies are often produced. In general, the active inorganic filler deviates from the initial chemical ratio, oxygen vacancies occur in the lattice, causing a significant buildup of Li^+ on the surface and ion redistribution, as well as the production of a space charge layer, which increases the electrolyte's conductivity.[132,159,160]

It has taken a lot of work to include oxide inorganic fillers into polymers to obtain oxygen ion vacancies and enhance their overall electrochemical characteristics. By electrospinning, the Cui group created a Y_2O_3-doped ZrO_2 nanowire, which afterwards was combined with PAN and $LiClO_4$ to produce a solid electrolyte. The Y_2O_3 doping process with low valence metal ions produces a high concentration of oxygen vacancies in ZrO_2, and the produced oxygen vacancies can also be used as Lewis acid sites in composite electrolytes (Figure 2.33).[161] The resultant electrolyte conductivity was enhanced from 3.65×10^{-7} S cm^{-1} to 1.07×10^{-5} S cm^{-1}, at room temperature.

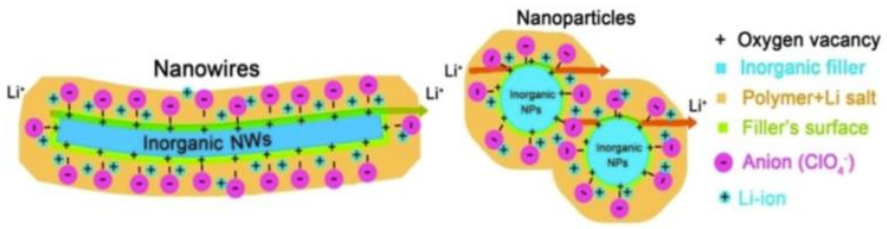

Figure 2. 33. Lithium-ion transport in composite polymer electrolyte with nanowire filler. The positively charged oxygen vacancies on the filler surface strongly interact with anions and release lithium ions. Adapted with permission from Ref. [161]. Copyright (2016) American Chemical Society.

Another method to create vacancies for SSEs is to dope high valence metal oxides with low valence ions. Using Ca-doped CeO_2 nanotubes as inorganic fillers and polyethylene oxide (PEO-LiTFSI) as a substrate, Chen et al. showed the direct injection of oxygen vacancies into SSEs (Figure 2.34).[162] When combined with PEO to create SSE, the oxygen vacancy filler considerably enhanced the electrochemical performance ($LiFePO_4$/Li battery 170 mAh g^{-1} at 0.2 C). DFT simulations investigated the cause of the enhanced discharge-specific capacity. After the incorporation of PEO, the oxygen vacancies on the surface of Ca-doped CeO_2 nanotubes interact with the anionic fraction ($TFSI^-$) of the lithium salt, which promotes its dissociation. The faster interfacial kinetic transport causes a small interfacial transfer resistance during charging and discharging.

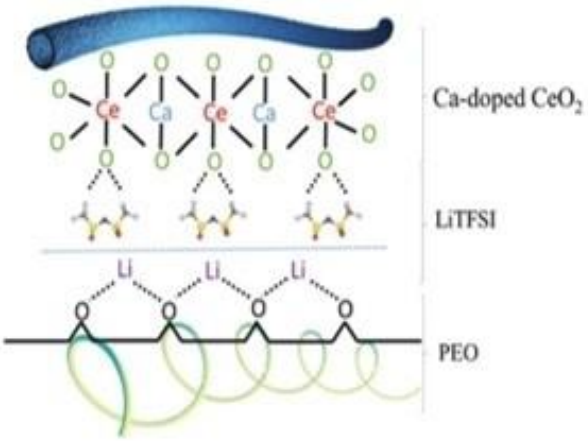

Figure 2. 34. Vacancy generation in Ca-doped CeO_2 nanotubes enhances lithium-ion transport in PEO-based electrolytes. Adapted with permission from Ref. [162]. Copyright (2020) Wiley-VCH GmbH.

In another development, Guo et al. reported a PEO-based composite solid electrolyte coated with dopamine on the surface of LLZO particles demonstrating excellent electrochemical characteristics with a room temperature conductivity of 1.15×10^{-4} S cm^{-1} (Figure 2.35).[163] After mild alkali treatment, polydopamine (PDA) was discovered to have distinctive peaks at 3550 cm^{-1} and Li_2CO_3 peaks at 1438 and 863 cm^{-1} by evaluating the Fourier transform infrared spectra (FTIR). Dopamine-induced polymerization may specifically convert Li_2CO_3 impurities on LLZTO particles into a homogenous PDA layer with a thickness of less than 15 nm. The PDA coated surface generates a space charge layer due to lithium vacancies and lithium-ion redistribution, which yields improved lithium ion transport in the composite electrolyte in comparison to the untreated LLZTO.

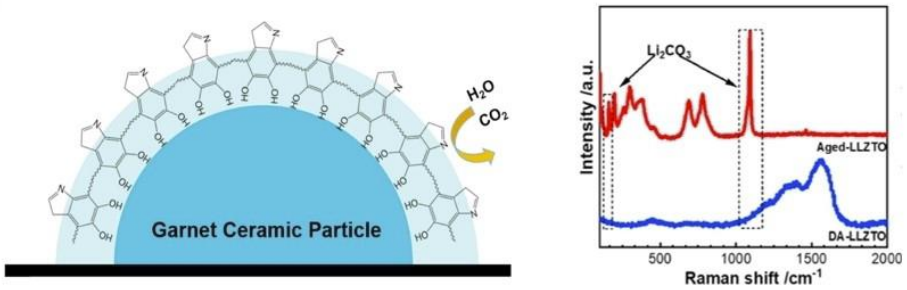

Figure 2. 35. Air-stable DA-treated garnet ceramic particles, and FTIR spectrum evidence. Adapted with permission from Ref. [163]. Copyright (2021) Elsevier Ltd.

2.4. Interfacial Stability between Solid-State Electrolytes and Electrodes

2.4.1. Compatibility of polymer-based electrolyte with high-voltage cathode

The lowest unoccupied molecular orbital (LUMO) and the highest occupied molecular orbital (HOMO) determine the electrochemical window of an ionic conductor. When lithium is being de-intercalated, the cathode material is heavily oxidized. Interfacial parasitic reactions may occur when the cathode potential is altered to a state that is lower than the HOMO of SPE.[151] The whole battery system's ionic conductivity is impacted when the solid electrolyte decomposes into by-products due to thermodynamic instability at high voltages. The electro-chemical performance of the battery is impacted by the oxidation/reduction processes that occur during charge-discharge and lead to the breakdown of active components in the electrolyte. To create high-specific-energy batteries, it is crucial to expand the electrochemical window of the solid electrolyte.

The electrochemical window of solid electrolytes made of polymers may be extended by inorganic oxides since they have a larger electrochemical window. For instance, to widen the electrochemical window of PEO, LLZNO was added into PEO as a typical organic-inorganic composite solid electrolyte (Figure 2.36),[164] and shown to increase the electrochemical window from ~4.5 to 5.2 V. In another example, enhanced stabilization of high-voltage cathode (e. g., LCO, NCM, LNMO, etc.) was achieved PMMA crosslinked PEG solid electrolyte via TiO_2 nanorod insertion into the polymer.[165] It was shown, the interface to be positively influenced (in terms of stabilization) by supramolecular interactions as well as hydrogen bonding between lithium salts and the polymer backbone. The electrochemical window may also be impacted by structural flaws, energy problems, and cathode material contact contaminants.[166]

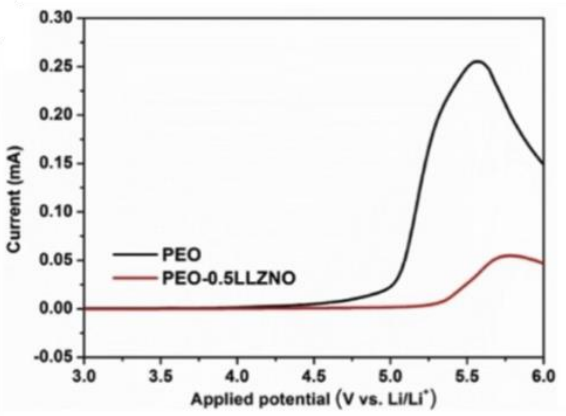

Figure 2. 36. Inorganic filler LLZNO extends the electrochemical window of PEO-based solid electrolytes. Adapted with permission from Ref. [164]. Copyright (2019) Elsevier Ltd.

Lithium salt types and polymer matrices with various primary chains and functional groups also have an impact on the electrochemical window of solid electrolytes.[167] Lithium bis(oxalate)borate (LiDFOB) is a useful lithium salt that facilitates an electrode/electrolyte interface layer that is oxidation-resistant and have low resistance. Figure 2.37 illustrates the connection between a solid electrolyte's electrochemical window and its matrix, poly (ethylene-glycol) diacrylate (PEGDA).[168] The authors discovered that crosslinking of LiDFOB with PEGDA stabilizes the high-voltage cathode in a synergistic manner, allowing for a 4 V electrochemical window.

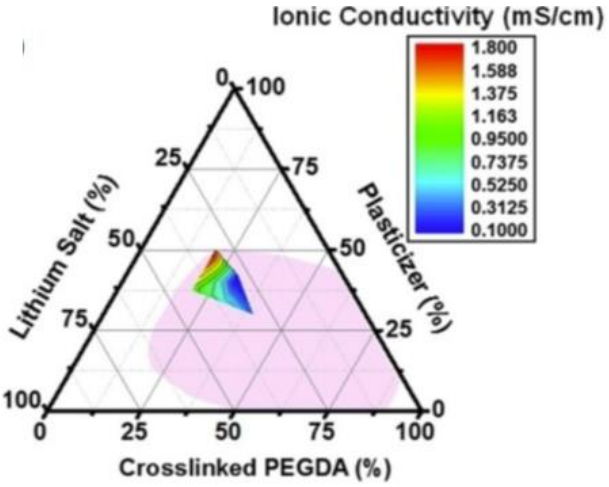

Figure 2. 37. Ternary phase diagram of ionic conductivity dependence on crosslinking degree of lithium salt. Adapted with permission from Ref. [168]. Copyright (2018) American Chemical Society.

The Sun group discovered that the terminal group's OH functional group may serve as a physical boundary for the electrochemical window of PEO-based electrolytes. The end groups of polyethylene glycol (PEG) and poly (ethylene glycol) dimethyl ether (PEGDME) are OH and OCH_3, respectively, and both contain the identical primary chain.[72] At 4.05 to 4.3 V, the terminal OH group will oxidize to form Li_2O and COOH (Li). The ether chain (COC) in the polymer will continue to oxidize when the voltage is raised over 4.3 V. According to this idea, Fang restricted hydroxyl groups to the polyethylene glycol resin's (PEG) backbone in cross-linked PEGR, raising the oxidation potential of PEG-based polymeric materials to 4.36 V (Figure 2.38a and b).[169]

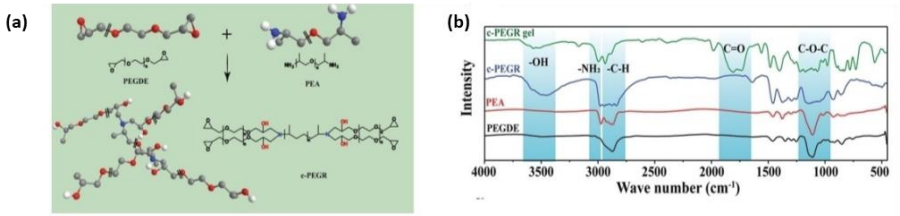

Figure 2. 38. (a) Schematic of the synthesis and (b) FITR diagram. Adapted with permission from Ref. [169]. Copyright (2021) Wiley-VCH GmbH.

A variety of composite electrolytes are often utilized in lieu of a single electrolyte for enhancing the electrochemical window of SSE. With the cathode side contacting the reduction-resistant

electrolyte and the lithium metal side contacting the oxidation-resistant electrolyte, heterogeneous layer structure electrolyte films with different compositions can specifically increase the electrochemical window of SSEs. This was studied by Luo and associates, who used solidified PAN and PEO polymer electrolytes for the different interfaces.[170] The solubility of transition metal ions may be successfully suppressed by PAN, PEGMA, and PEGDME. PAN with a C≡N group is more resistant to oxidation and has a lower energy level. A multilayer SSE membrane that has sandwich layer structure was created.[171-173]

2.4.2. Modification of interfacial stability against Li metal

Lithium metal has a strong reducing ability. If the local current is distributed unevenly during the charge-discharge process, dendrites would form on the surface of the lithium metal and spread farther along the grain boundaries, finally resulting in battery failure.[174,175] There are generally two techniques to increase the stability of the lithium-metal/SSE interface: (1) Altering the process at the lithium-metal/SSE interface to address the issue of unequal local current distribution and prevent the formation of lithium dendrites. (2) Improving the SSE's mechanical characteristics to prevent the spread of fractures and the formation of lithium dendrites.

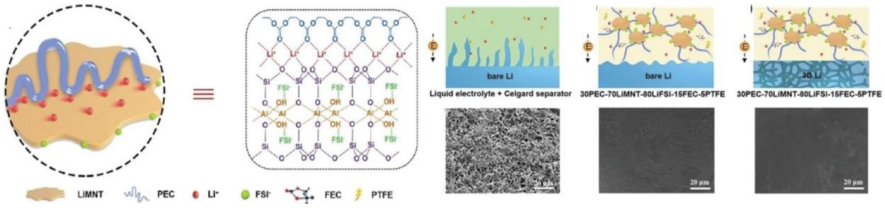

Figure 2. 39. PEC-LiMNT-CSE enhances ion transfer and optimizes Li^+ deposition. Adapted with permission from Ref. [176]. Copyright (2019) Wiley-VCH GmbH.

The issue of the local unequal current density distribution at the interface has received a lot of attention. With the help of the synergistic effects of an intercalated electrolyte, a three-dimensional lithium anode, fluoroethylene carbonate (FEC) solvent, and poly (tetra-fluoroethylene) (PTFE) adhesive, Fan et al. showed how to insert polyethylene carbonate (PEC) polymer into the interlayer of a single ion conductor made of lithium montmorillonite (LiMNT) (Figure 2.39).[176] At 0.5 mA cm^{-2}, a Li symmetric battery was cycles steadily for over 600 hours. Another method for reducing the formation of lithium dendrites and enhancing point-to-point contact at the interface between the lithium metal and LAGP electrolyte is the insertion of a buffer layer.[177] Finally, high flux

materials have been shown to enhance mechanical characteristics and interfacial connections by preventing cell failure brought on by Li dendrite development (Figure 2.40).[170]

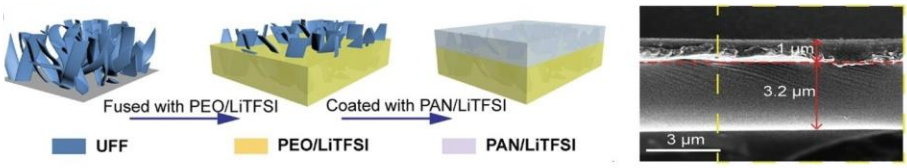

Figure 2. 40. Cross-sectional SEM image of the as-spun Vermiculite nanofibers (UFF) .170 Adapted with permission from Ref. [170]. Copyright (2021) Wiley-VCH GmbH.

2.5. References

1. J. M. Tarascon, M. Armand, Issues and challenges facing rechargeable lithium batteries. Nature, 2001, 414, 359–367.
2. P. Albertus, S. Babinec, S. Litzelman, A. Newman, Status and challenges in enabling the lithium metal electrode for high-energy and low-cost rechargeable batteries. *Nat. Energy* **2018**, *3*, 16–21.
3. V. Raj, N. P. B. Aetukuri, J. Nanda, Solid state lithium metal batteries-issues and challenges at the lithium-solid electrolyte interface. *Curr. Opin. Solid State Mater. Sci.* **2022**, *26* (4), 100999.
4. Y. Lyu, X. Wu, K. Wang, Z. Feng, T. Cheng, Y. Liu, M. Wang, R. Chen, L. Xu, J. Zhou, Y. Lu, B. Guo, An Overview on the Advances of $LiCoO_2$ Cathodes for Lithium-Ion Batteries. *Adv. Energy Mater.* **2021**, *11*, 2000982.
5. H. Wan, S. Liu, T. Deng, J. Xu, J. Zhang, X. He, X. Ji, X. Yao, C. Wang, Bifunctional Interphase-Enabled $Li_{10}GeP_2S_{12}$ Electrolytes for Lithium–Sulfur Battery. *ACS Energy Lett.* **2021**, *6* (3), 862-868.
6. Q. Yu, W. Mai, W. Xue, G. Xu, Q. Liu, K. Zeng, Y. Liu, F. Kang, B. Li, J. Li, Sacrificial Poly(propylene carbonate) Membrane for Dispersing Nanoparticles and Preparing Artificial Solid Electrolyte Interphase on Li Metal Anode. *ACS Appl. Mater. Interfaces* **2020**, *12* (24), 27087-27094.
7. X. Tian, Y. Yi, B. Fang, P. Yang, T. Wang, P. Liu, L. Qu, M. Li, S. Zhang, Design Strategies of Safe Electrolytes for Preventing Thermal Runaway in lithium-Ion Batteries. *Chem. Mater.* **2020**, *32* (23), 9821-9848.
8. M. Henriksen, K. Vaagsaether, J. Lundberg, S. Forseth, D. Bjerketvedt, Explosion characteristics for Li-ion battery electrolytes at elevated temperatures, *J. Hazard. Mater.* **2019**, *371*, 1-7.
9. B. S. Vishnugopi, F. Hao, A. Verma, P. P. Mukherjee, Double-Edged Effect of Temperature on Lithium Dendrites. *ACS Appl. Mater. Interfaces* **2020,** *12* (21), 23931-23938.
10. W. Mu, X. Liu, Z. Wen, L. Liu, Numerical simulation of the factors affecting the growth of lithium dendrites, *J. Energy Storage*, **2019**, *26*, 100921-100931.
11. S. Chen, K. Wen, J. Fan, Y. Bando, D. Golberg, Progress and future prospects of high-voltage and high-safety electrolytes in advanced lithium batteries: from liquid to solid electrolytes, *J. Mater. Chem. A* **2018**, *6*, 11631-11663.
12. Q. Wang, H. Wang, J. Wu, M. Zhou, W. Liu, H. Zhou, Advanced electrolyte design for stable lithium metal anode: From liquid to solid, *Nano Energy*, **2021**, *80*, 105516-102251.
13. S. Song, Y. Wu, Z. Dong, F. Deng, W. Tang, J. Yao, Z. Wen, L. Lu, N. Hu, J. Molenda, Multi-substituted garnet-type electrolytes for solid-state lithium batteries. *Ceram. Int.* **2020**, *46* (4), 5489-5494.
14. M. Papakyriakou, M. Lu, Y. Liu, Z. Liu, H. Chen, M. T. McDowell, S. Xia, Mechanical behavior of inorganic lithium-conducting solid electrolytes, *J. Power Sources* **2021**, *516*, 230672-230681.
15. X. Ke, Y. Wang, G. Ren, C. Yuan, Towards rational mechanical design of inorganic solid electrolytes for all-solid-state lithium-ion batteries. *Energy Storage Mater.* **2020**, *26*, 313-324.
16. S. Mu, Z. Bi, S. Gao, X. Guo, Combination of Organic and Inorganic Electrolytes for Composite Membranes Toward Applicable Solid Lithium Batteries. *Chem. Res. Chinese U.* **2021**, *37* (2), 246-253.

17. M. J. Lee, D. O. Shin, J. Y. Kim, J. Oh, S. H. Kang, J. Kim, K. M. Kim, Y. M. Lee, S. O. Kim, Y. G. Lee, Interfacial barrier free organic-inorganic hybrid electrolytes for solid state batteries. *Energy Storage Mater.* **2021**, *37*, 306-314.
18. T. Famprikis, P. Canepa, J. A. Dawson, M. S. Islam, C. Masquelier, Fundamentals of inorganic solid-state electrolytes for batteries. *Nat. Mater.* **2019**, *18* (12), 1278-1291.
19. A. Banerjee, X. Wang, C. Fang, E. A. Wu, Y. S. Meng, Interfaces and Interphases in All-Solid-State Batteries with Inorganic Solid Electrolytes. *Chem. Rev.* **2020,** *120* (14), 6878-6933.
20. A. Arya, A. L. Sharma, A. glimpse on all-solid-state Li-ion battery (ASSLIB) performance based on novel solid polymer electrolytes: a topical review. *J. Mater. Sci.* **2020**, *55* (15), 6242-6304.
21. K. Hong, J. Yuk, H. J. Kim, J. Y. Lee, S. Kim, J. L. Lee, K. H. Lee, Electrospun polymer electrolyte nanocomposites for solid-state energy storage. *Compo. B Eng.* **2018**, *152*, 275-281.
22. Z. Lin, X. Guo, Z. Wang, B. Wang, S. He, L. A. O'Dell, J. Huang, H. Li, H. Yu, L. Chen, A wide-temperature superior ionic conductive polymer electrolyte for lithium metal battery. *Nano Energy* **2020**, *73*, 104786-104795.
23. W. Zhao, J. Yi, P. He, H. Zhou, Solid-State Electrolytes for Lithium-Ion Batteries: Fundamentals, Challenges and Perspectives. *Electrochem. Energy Rev.* **2019**, *2* (4), 574-605.
24. O. Bohnke, C. Bohnke, J.L. Fourquet, Mechanism of ionic conduction and electrochemical intercalation of lithium into the perovskite lanthanum lithium titanate, *Solid State Ionics* **1996,** *91*, 21-31.
25. M. Yashima, M. Itoh, Y. Inaguma, Y. Morii, Crystal Structure and Diffusion Path in the Fast Lithium-Ion Conductor $La_{0.62}Li_{0.16}TiO_3$, *J. Am. Chem. Soc.* **2005,** *127* (10), 3491-3495.
26. Y. Zhao, L. L. Daemen, Superionic conductivity in lithium-rich anti-perovskites. *J. Am. Chem. Soc.* **2012,** *134* (36), 15042-7.
27. Y. Zhang, Y. Zhao, C. Chen, Ab initiostudy of the stabilities of and mechanism of superionic transport in lithium-rich antiperovskites. *Phys. Rev. B* **2013,** *87* (13).
28. M. H. Braga, J. A. Ferreira, V. Stockhausen, J. E. Oliveira, A. El-Azab, Novel Li_3ClO based glasses with superionic properties for lithium batteries. *J. Mater. Chem. A* **2014,** *2* (15), 5470-5480.
29. M. Giarola, A. Sanson, F. Tietz, S. Pristat, E. Dashjav, D. Rettenwander, G. J. Redhammer, G. Mariotto, Structure and Vibrational Dynamics of NASICON-Type $LiTi_2(PO_4)_3$. *J. Phys. Chem. C* **2017,** *121* (7), 3697-3706.
30. H. Aono, E. Sugimoto, Y. Sadaoka, N. Imanaka, G. Adachi, The Electrical Properties of Ceramic Electrolytes for $LiM_xTi_{2-x}(PO_4)_{3+y}$, M = Ge , Sn , Hf , and Zr Systems, *J. Electrochem. Soc.* **1993**, *140*, 1827.
31. R. Kahlaoui, K. Arbi, I. Sobrados, R. Jimenez, J. Sanz, R. Ternane, Cation Miscibility and Lithium Mobility in NASICON $Li_{1+x}Ti_{2-x}Sc_x(PO_4)_3$ ($0 \leq x \leq 0.5$) Series: A Combined NMR and Impedance Study. *Inorg. Chem.* **2017,** *56* (3), 1216-1224.
32. V. Thangadurai, H. Kaack, W. J. F. Weppner, Novel Fast Lithium Ion Conduction in Garnet-Type $Li_5La_3M_2O_{12}$ (M = Nb, Ta). *J. Am. Ceram. Soc.* **2003**, *86*, 437-440.
33. V. Thangadurai, W. Weppner, Effect of sintering on the ionic conductivity of garnet-related structure $Li_5La_3Nb_2O_{12}$ and In- and K-doped $Li_5La_3Nb_2O_{12}$. *J. Solid State Chem.* **2006,** *179* (4), 974-984.
34. V. Thangadurai, W. Weppner, $Li_6ALa_2Nb_2O_{12}$ (A=Ca, Sr, Ba): A New Class of Fast Lithium Ion Conductors with Garnet-Like Structure. *J. Am. Ceram. Soc.* **2005,** *88* (2), 411-418.

35. V. Thangadurai, W. Weppner, $Li_6ALa_2Ta_2O_{12}$ (A = Sr, Ba): Novel Garnet-Like Oxides for Fast Lithium Ion Conduction. *Adv. Funct. Mater.* **2005,** *15* (1), 107-112.
36. S. Narayanan, F. Ramezanipour, V. Thangadurai, Enhancing Li Ion Conductivity of Garnet-Type $Li_5La_3Nb_2O_{12}$ by Y and Li Co-doping: Synthesis, Structure, Chemical Stability, and Transport Properties. *J. Phys. Chem. C* **2012,** *116* (38), 20154-20162.
37. R. Murugan, V. Thangadurai, W. Weppner, Fast lithium ion conduction in garnet-type $Li_7La_3Zr_2O_{12}$. *Angew. Chem. Inter. Ed.* **2007**, *46*, 4, 7778-7781.
38. R. Jalem, Y. Yamamoto, H. Shiiba, M. Nakayama, H. Munakata, T. Kasuga, K. Kanamura, Concerted Migration Mechanism in the Li Ion Dynamics of Garnet-Type $Li_7La_3Zr_2O_{12}$. *Chem. Mater.* **2013,** *25* (3), 425-430.
39. J. Awaka, N. Kijima, H. Hayakawa, J. Akimoto, Synthesis and structure analysis of tetragonal $Li_7La_3Zr_2O_{12}$ with the garnet-related type structure. *J. Solid State Chem.* **2009,** *182* (8), 2046-2052.
40. J. Awaka, A. Takashima, K. Kataoka, N. Kijima, Y. Idemoto, J. Akimoto, Crystal Structure of Fast Lithium-ion-conducting Cubic $Li_7La_3Zr_2O_{12}$. *Chem. Lett.* **2011,** *40* (1), 60-62.
41. E. Rangasamy, J. Wolfenstine, J. Sakamoto, The role of Al and Li concentration on the formation of cubic garnet solid electrolyte of nominal composition $Li_7La_3Zr_2O_{12}$. *Solid State Ionics* **2012,** *206*, 28-32.
42. V. Thangadurai, S. Adams, W. Weppner, Crystal Structure Revision and Identification of Li^+-Ion Migration Pathways in the Garnet-like $Li_5La_3M_2O_{12}$ (M = Nb, Ta) Oxides, *Chem. Mater.* **2004**, *16* (16), 2998-3006.
43. E. J. Cussen, The structure of lithium garnets: cation disorder and clustering in a new family of fast Li^+ conductors. *Chem. Commun.* **2006,** *4*, 412-413.
44. L. Wullen, T. Echelmeyer, H. W.Meyer, D. Wilmer, The mechanism of Li-ion transport in the garnet $Li_5La_3Nb_2O_{12}$. *Phys. Chem. Chem. Phys.* **2007,** *9* (25), 3298-3303.
45. M. Xu, M. S. Park, J. M. Lee, T. Y. Kim, Y. S. Park, E. Ma, Mechanisms of Li^+ transport in garnet-type cubic $Li_{3+x}La_3M_2O_{12}$(M= Te, Nb, Zr). *Phys. Rev. B* **2012,** *85* (5), 052301.
46. D. Zhou, D. Shanmukaraj, A. Tkacheva, M. Armand, G. Wang, Polymer Electrolytes for Lithium-Based Batteries: Advances and Prospects. *Chem.* **2019,** *5* (9), 2326-2352.
47. Y. Guo, S. Wu, Y. B. He, F. Kang, L. Chen, H. Li, Q. H. Yang, Solid-state lithium batteries: Safety and prospects. *eScience* **2022,** *2* (2), 138-163.
48. H. Zhang, L. Huang, H. Xu, X. Zhang, Z. Chen, C. Gao, C. Lu, Z. Liu, M. Jiang, G. Cui, A polymer electrolyte with a thermally induced interfacial ion-blocking function enables safety-enhanced lithium metal batteries. *eScience* **2022,** *2* (2), 201-208.
49. Y. Chen, Z. Wang, X. Li, X. Yao, C. Wang, Y. Li, W. Xue, D. Yu, S. Y. Kim, F. Yang, A. Kushima, G. Zhang, H. Huang, N. Wu, Y. W. Mai, J. B. Goodenough, J. Li, Li metal deposition and stripping in a solid-state battery via Coble creep. *Nature* **2020,** *578* (7794), 251-255.
50. Y. Liu, Y. Zhao, W. Lu, L. Sun, L. Lin, M. Zheng, X. Sun, H. Xie, PEO based polymer in plastic crystal electrolytes for room temperature high-voltage lithium metal batteries. *Nano Energy* **2021,** *88*, 106205.
51. Q. T. Pham, Y. H. Jheng, D. S. Tsai, J. Y. Lai, C. C. Hu, C. S. Chern, Solid acrylonitrile-based copolymer electrolytes and their potential application in solid state battery. *J. Appl. Polym. Sci.* **2022,** *139* (20), 52158-52171.
52. Y. Wu, Y. Li, Y. Wang, Q. Liu, Q. Chen, M. Chen, Advances and prospects of PVDF based polymer electrolytes. *J. Energy Chem.* **2022,** *64*, 62-84.

53. D. Chen, M. A . Mahmoud, J. H. Wang, G. H. Waller, B. Zhao, C. Qu, M. A. El-Sayed, M. Liu, Operando Investigation into Dynamic Evolution of Cathode-Electrolyte Interfaces in a Li-Ion Battery. *Nano Lett.* **2019,** *19* (3), 2037-2043.
54. D. Zhang, L. Zhang, K. Yang, H. Wang, C. Yu, D. Xu, B. Xu, L. M. Wang, Superior Blends Solid Polymer Electrolyte with Integrated Hierarchical Architectures for All-Solid-State Lithium-Ion Batteries. *ACS Appl. Mater. Interfaces* **2017,** *9* (42), 36886-36896.
55. C. Sun, J. Liu, Y. Gong, D. P. Wilkinson, J. Zhang, Recent advances in all-solid-state rechargeable lithium batteries. *Nano Energy* **2017,** *33*, 363-386.
56. J. Qiu, X. Liu, R. Chen, Q. Li, Y. Wang, P. Chen, L. Gan, S. J. Lee, D. Nordlund, Y. Liu, X. Yu, X. Bai, H. Li, L. Chen, Enabling Stable Cycling of 4.2 V High-Voltage All-Solid-State Batteries with PEO-Based Solid Electrolyte. *Adv. Funct. Mater.* **2020,** *30* (22).
57. Y. Niu, Z. Yu, Y. Zhou, J. Tang, M. Li, Z. Zhuang, Y. Yang, X. Huang, B. Tian, Constructing stable Li-solid electrolyte interphase to achieve dendrites-free solid-state battery: A nano-interlayer/Li pre-reduction strategy. *Nano Res.* **2022,** *15* (8), 7180-7189.
58. H. Liu, X. B. Cheng, J. Q. Huang, H. Yuan, Y. Lu, C. Yan, G. L. Zhu, R. Xu, C. Z. Zhao, L.-P. Hou, C. He, S. Kaskel, Q. Zhang, Controlling Dendrite Growth in Solid-State Electrolytes. *ACS Energy Lett.* **2020,** *5* (3), 833-843.
59. A. Manthiram, X. Yu, S. Wang, Lithium battery chemistries enabled by solid-state electrolytes. *Nat. Rev. Mater.* **2017,** *2* (4), 16103.
60. W. Zhou, S. Wang, Y. Li, S. Xin, A. Manthiram, J. B. Goodenough, Plating a Dendrite-Free Lithium Anode with a Polymer/Ceramic/Polymer Sandwich Electrolyte. *J. Am. Chem. Soc.* **2016,** *138* (30), 9385-9392.
61. B. Xu, X. Li, C. Yang, Y. Li, N. S.Grundish, P. H. Chien, K. Dong, I. Manke, R. Fang, N.Wu, H. Xu, A. Dolocan, J. B. Goodenough, Interfacial Chemistry Enables Stable Cycling of All-Solid-State Li Metal Batteries at High Current Densities. *J. Am. Chem. Soc.* **2021,** *143* (17), 6542-6550.
62. C. Song, Z. Li, J. Peng, X. Wu, H. Peng, S. Zhou, Y. Qiao, H. Sun, L. Huang, S.-G. Sun, Enhancing Li ion transfer efficacy in PEO-based solid polymer electrolytes to promote cycling stability of Li-metal batteries. *J. Mater. Chem. A* **2022,** *10* (30), 16087-16094.
63. C. M. Septani, O. Shih, Y. Q. Yeh, Y. S. Sun, Structural Evolution of a Polystyrene-Block-Poly(Ethylene Oxide) Block Copolymer in Tetrahydrofuran/Water Cosolvents. *Langmuir* **2022,** *38* (19), 5987-5995.
64. M. Chintapalli, T. N. P. Le, N. R. Venkatesan, N. G. Mackay, A. A. Rojas, J. L. Thelen, X. C. Chen, D. Devaux, N. P. Balsara, Structure and Ionic Conductivity of Polystyrene-block-poly(ethylene oxide) Electrolytes in the High Salt Concentration Limit. *Macromol.* **2016,** *49* (5), 1770-1780.
65. R. Bouchet, T. N. T. Phan, E. Beaudoin, D. Devaux, P. Davidson, D. Bertin, R. Denoyel, Charge Transport in Nanostructured PS–PEO–PS Triblock Copolymer Electrolytes. *Macromol.* **2014,** *47* (8), 2659-2665.
66. D. Sharon, P. Bennington, M. A. Webb, C. Deng, J. J. de Pablo, S. N. Patel, P. F. Nealey, Molecular Level Differences in Ionic Solvation and Transport Behavior in Ethylene Oxide-Based Homopolymer and Block Copolymer Electrolytes. *J. Am. Chem. Soc.* **2021,** *143* (8), 3180-3190.

67. S. Pal, R. K. Srivastava, B. Nandan, Fascinating morphology and crystallization behavior of melt miscible binary blends of crystalline homopolymers depicting nearly simultaneous melting transitions. *Polymer,* **2021,** *231,* 124119.

68. Y. Ugata, M. L. Thomas, T. Mandai, K. Ueno, K. Dokko, M. Watanabe, Li-ion hopping conduction in highly concentrated lithium bis(fluorosulfonyl)amide/dinitrile liquid electrolytes. *Phys. Chem. Chem. Phys.* **2019,** *21* (19), 9759-9768.

69. L. Ran, M. Li, E. Cooper, B. Luo, I. Gentle, L. Wang, R. Knibbe, Enhanced Safety and Performance of High-Voltage Solid-State Sodium Battery through Trilayer, Multifunctional Electrolyte Design. *Energy Storage Mater.* **2021,** *41*, 8-13.

70. Z. Lu, L. Peng, Y. Rong, E. Wang, R. Shi, H. Yang, Y. Xu, R. Yang, C. Jin, Enhanced Electrochemical Properties and Optimized Li^+ Transmission Pathways of PEO / LLZTO-Based Composite Electrolytes Modified by Supramolecular Combination. *Energy Environ. Mater.* **2024,** *7,* 12498.

71. K. He, S. H. Cheng, J. Hu, Y. Zhang, H. Yang, Y. Liu, W. Liao, D. Chen, C. Liao , X. Cheng, Z. Lu, J. He, J. Tang, R. K. Y. Li, C. Liu, In-Situ Intermolecular Interaction in Composite Polymer Electrolyte for Ultralong Life Quasi-Solid-State Lithium Metal Batteries. *Angew. Chem. Inter. Ed.* **2021,** *60* (21), 12116-12123.

72. X. Yang, M. Jiang, X. Gao, D. Bao, Q. Sun, N. Holmes, H. Duan, S. Mukherjee, K. Adair, C. Zhao, J. Liang, W. Li, J. Li, Y. Liu, H. Huang, L. Zhang, S. Lu, Q. Lu, R. Li, C. V. Singh, X. Sun, Determining the limiting factor of the electrochemical stability window for PEO-based solid polymer electrolytes: main chain or terminal –OH group? *Energy Environ. Sci.* **2020,** *13* (5), 1318-1325.

73. B. Zhou, D. He, J. Hu, Y. Ye, H. Peng, X. Zhou, X. Xie, Z. Xue, A flexible, self-healing and highly stretchable polymer electrolyte via quadruple hydrogen bonding for lithium-ion batteries. *J. Mater. Chem. A* **2018,** *6* (25), 11725-11733.

74. Z. Wang, L. Shen, S. Deng, P. Cui, X. Yao, 10 μm-Thick High-Strength Solid Polymer Electrolytes with Excellent Interface Compatibility for Flexible All-Solid-State Lithium-Metal Batteries. *Adv. Mater.* **2021,** *33* (25), e2100353.

75. H. Wang, J. Song, K. Zhang, Q. Fang, Y. Zuo, T. Yang, Y. Yang, C. Gao, X. Wang, Q. Pang, D. Xia, A strongly complexed solid polymer electrolyte enables a stable solid state high-voltage lithium metal battery. *Energy Environ. Sci.* **2022,** *15* (12), 5149-5158.

76. Y. J. Wang, D. Kim, PEGDA/PVdF/F_{127} gel type polymer electrolyte membranes for lithium secondary batteries. *J. Power Sources* **2007,** *166* (1), 202-210.

77. Y. J. Wang, D. Kim, The effect of F_{127} addition on the properties of PEGDA/PVdF cross-linked gel polymer electrolytes. *J. Membr. Sci.* **2008,** *312* (1-2), 76-83.

78. R. He, M. Echeverri, D. Ward, Y. Zhu, T. Kyu, Highly conductive solvent-free polymer electrolyte membrane for lithium-ion batteries: Effect of prepolymer molecular weight. *J. Membr. Sci.* **2016,** *498*, 208-217.

79. R. He, T. Kyu, Effect of Plasticization on Ionic Conductivity Enhancement in Relation to Glass Transition Temperature of Crosslinked Polymer Electrolyte Membranes. *Macromol.* **2016,** *49* (15), 5637-5648.

80. Y. Zhang, W. Feng, Y. Zhen, P. Zhao, X. Wang, L. Li, Effects of lithium salts on PEO-based solid polymer electrolytes and their all-solid-state lithium-ion batteries. *Ionics* **2022,** *28* (6), 2751-2758.

81. N. Meng, H. Zhang, S. Lianli, F. Lian, Salt-with-Salt, a novel strategy to design the flexible solid electrolyte membrane for highly safe lithium metal batteries. *J. Membr. Sci.* **2020,** *597,* 117768.

82. Q. Wang, T. Dong, Q. Zhou, Z. Cui, X. Shangguan, C. Lu, Z. Lv, K. Chen, L. Huang, H. Zhang, G. Cui, An in-situ generated composite solid-state electrolyte towards high-voltage lithium metal batteries. *Sci. China Chem.* **2022,** *65* (5), 934-942.

83. J. E. Lee, J. Choi, D. J. Lee, S. Lee, H. G. Chae, Radial microstructure development of polyacrylonitrile (PAN)-based carbon fibers. *Carbon* **2022,** *191*, 515-524.

84. J. Ramachandran, J. M. Serrano, T. Liu, J. Cho, P. J. Arias-Monje, M. Lu, M. H. Kirmani, J. Elliott, S. S. Jang, G. Liu, S. Kumar, Porous carbon fibers from gel-spun polyacrylonitrile and poly(methyl methacrylate)-block-poly(acrylonitrile). *Carbon* **2022,** *192*, 332-346.

85. C. He, J. Liu, J. Cui, J. Li, X. Wu, A gel polymer electrolyte based on Polyacrylonitrile/organic montmorillonite membrane exhibiting dense structure for lithium ion battery. *Solid State Ionics* **2018,** *315*, 102-110.

86. N. Meng, X. Zhu, F. Lian, Particles in composite polymer electrolyte for solid-state lithium batteries: A review. *Particuology* **2022,** *60*, 14-36.

87. D. Zhou, Y. B. He, R. Liu, M. Liu, H. Du, B. Li, Q. Cai, Q.-H. Yang, F. Kang, In Situ Synthesis of a Hierarchical All-Solid-State Electrolyte Based on Nitrile Materials for High-Performance Lithium-Ion Batteries. *Adv. Energy Mater.* **2015,** *5* (15), 1500353.

88. J. Ye, F. He, J. Nie, Y. Cao, H. Yang, X. Ai, Sulfur/carbon nanocomposite-filled polyacrylonitrile nanofibers as a long life and high capacity cathode for lithium–sulfur batteries. *J. Mater. Chem. A* **2015,** *3* (14), 7406-7412.

89. D. Zhang, X. Xu, S. Ji, Z. Wang, Z. Liu, J. Shen, R. Hu, J. Liu, M. Zhu, Solvent-Free Method Prepared a Sandwich-like Nanofibrous Membrane-Reinforced Polymer Electrolyte for High-Performance All-Solid-State Lithium Batteries. *ACS Appl. Mater. Interfaces* **2020,** *12* (19), 21586-21595.

90. Z. Xiao, T. Long, L. Song, Y. Zheng, C. Wang, Research progress of polymer-inorganic filler solid composite electrolyte for lithium-ion batteries. *Ionics* **2021,** *28* (1), 15-26.

91. L. Y. Yang, J. H. Cao, B.-R. Cai, T. Liang, D. Y. Wu, Electrospun MOF/PAN composite separator with superior electrochemical performances for high energy density lithium batteries. *Electrochim. Acta* **2021,** *382,* 138346.

92. Z. Li, S. Wang, J. Shi, Y. Liu, S. Zheng, H. Zou, Y. Chen, W. Kuang, K. Ding, L. Chen, Y. Lan, Y. Cai, Q. Zheng, A 3D interconnected metal-organic framework-derived solid-state electrolyte for dendrite-free lithium metal battery. *Energy Storage Mater.* **2022,** *47*, 262-270.

93. L. Cong, Y. Li, W. Lu, J. Jie, Y. Liu, L. Sun, H. Xie, Unlocking the Poly(vinylidene fluoride-co-hexafluoropropylene)/$Li_{10}GeP_2S_{12}$ composite solid-state Electrolytes for Dendrite-Free Li metal batteries assisting with perfluoropolyethers as bifunctional adjuvant. *J. Power Sources* **2020,** *446*.

94. X. Wang, Y. Fang, X. Yan, S. Liu, X. Zhao, L. Zhang, Highly conductive polymer electrolytes based on PAN-PEI nanofiber membranes with in situ gelated liquid electrolytes for lithium-ion batteries. *Polymer* **2021,** *230*.

95. W. P. Chen, H. Duan, J. L. Shi, Y. Qian, J. Wan, X. D. Zhang, H. Sheng, B. Guan, R. Wen, Y. X. Yin, S. Xin, Y. G. Guo, L. J. Wan, Bridging Interparticle Li^+ Conduction in a Soft Ceramic Oxide Electrolyte. *J. Am. Chem. Soc.* **2021,** *143* (15), 5717-5726.

96. S. B. Son, T. Gao, S. P. Harvey, K. X. Steirer, A. Stokes, A. Norman, C. Wang, A. Cresce, K. Xu, C. Ban, An artificial interphase enables reversible magnesium chemistry in carbonate electrolytes. *Nat. Chem.* **2018,** *10* (5), 532-539.

97. W. Zhang, M. Sun, J. Yin, E. Abou-Hamad, U. Schwingenschlogl, P. Costa, H. N. Alshareef, A Cyclized Polyacrylonitrile Anode for Alkali Metal Ion Batteries. *Angew. Chem. Inter. Ed.* **2021,** *60* (3), 1355-1363.

98. J. Wang, Q. Yuan, Z. Ren, C. Sun, J. Zhang, R. Wang, M. Qian, Q. Shi, R. Shao, D. Mu, Y. Su, J. Xie, F. Wu, G. Tan, Thermochemical Cyclization Constructs Bridged Dual-Coating of Ni-Rich Layered Oxide Cathodes for High-Energy Li-Ion Batteries. *Nano Lett.* **2022,** *22* (13), 5221-5229.

99. Y. Liang, H. Liu, G. Wang, C. Wang, D. Li, Y. Ni, L. Z. Fan, Heuristic Design of Cathode Hybrid Coating for Power-Limited Sulfide-Based All-Solid-State Lithium Batteries. *Adv. Energy Mater.* **2022,** *12* (33), 2201555.

100. X. Zhang, J. Han, X. Niu, C. Xin, C. Xue, S. Wang, Y. Shen, L. Zhang, L. Li, C. W. Nan, High Cycling Stability for Solid-State Li Metal Batteries via Regulating Solvation Effect in Poly(Vinylidene Fluoride)-Based Electrolytes. *Batter. Supercaps* **2020**, *3* (9), 876-883.

101. J. Chen, H. Zhang, H. Chen, E. Xia, Y. Wu, Z. Li, PVDF-based electrolyte decorated by $Li_{29}Zr_9Nb_3O_{40}$ Li-ion conductor and electrochemical performance of related solid-state batteries. *J. Power Sources* **2022**, *548*, 232109.

102. C. Y. Tsai, Y. Liu, Building up ion-conduction pathways in solid polymer electrolytes through surface and pore functionalization of PVDF porous membranes with ionic conductors. *J. Membr. Sci.* **2022**, *651*, 120456.

103. Z. Li, Y. Lu, Q. Su, M. Wu, X. Que, H. Liu, High-Power Bipolar Solid-State Batteries Enabled by In-Situ-Formed Ionogels for Vehicle Applications. *ACS Appl. Mater. Interfaces* **2022**, *14* (4), 5402-5413.

104. Z. Yao, K. Zhu, X. Li, J. Zhang, J. Chen, J. Wang, K. Yan, J. Liu, 3D poly(vinylidene fluoride–hexafluoropropylen) nanofiber-reinforced PEO-based composite polymer electrolyte for high-voltage lithium metal batteries. *Electrochim. Acta* **2022**, *404*, 139769.

105. R. Kanno, Synthesis of a new lithium ionic conductor, thio-LISICON–lithium germanium sulfide system. *Solid State Ionics* **2000**, *130*, (8), 97-104.

106. R. Kanno, M. Murayama, Lithium Ionic Conductor Thio-LISICON: The $Li_2SGeS_2P_2S_5$ System. *J. Electrochem. Soc.* **2001**, *148* (7), A742.

107. N. Kamaya, K. Homma, Y. Yamakawa, M. Hirayama, R. Kanno, M. Yonemura, T. Kamiyama, Y. Kato, S. Hama, K. Kawamoto, A. Mitsui, A lithium superionic conductor. *Nat. Mater.* **2011**, *10* (9), 682-686.

108. F. Du, X. Ren, J. Yang, J. Liu, W. Zhang, Structures, Thermodynamics, and Li^+ Mobility of $Li_{10}GeP_2S_{12}$: A First-Principles Analysis. *J. Phys. Chem. C* **2014**, *118* (20), 10590-10595.

109. M. Xu, J. Ding, E. Ma, One-dimensional stringlike cooperative migration of lithium ions in an ultrafast ionic conductor. *Appl. Phys. Lett.* **2012**, *101* (3), 031901.

110. S. Wenzel, S. Randau, T. Leichtweiß, D. A. Weber, J. Sann, W. G. Zeier, J. Janek, Direct Observation of the Interfacial Instability of the Fast Ionic Conductor $Li_{10}GeP_2S_{12}$ at the Lithium Metal Anode. *Chem. Mater.* **2016,** *28* (7), 2400-2407.

111. A. Kuhn, V. Duppel, B. V. Lotsch, Tetragonal $Li_{10}GeP_2S_{12}$ and Li_7GePS_8 – exploring the Li ion dynamics in LGPS Li electrolytes. *Energy Environ. Sci.* **2013,** *6* (12), 3548-3552.

112. P. Bron, S. Johansson, K. Zick, J. Schmedt auf der Gunne, S. Dehnen, B. Roling, $Li_{10}SnP_2S_{12}$: an affordable lithium superionic conductor. *J. Am. Chem. Soc.* **2013,** *135* (42), 15694-15701.

113. Y. Sun, K. Suzuki, S. Hori, M. Hirayama, R. Kanno, Superionic Conductors: $Li_{10+\delta}[Sn_ySi_{1-y}]_{1+\delta}P_{2-\delta}S_{12}$ with a $Li_{10}GeP_2S_{12}$-type Structure in the Li_3PS_4–Li_4SnS_4–Li_4SiS_4 Quasi-ternary System. *Chem. Mater.* **2017,** *29* (14), 5858-5864.

114. Y. Kato, S. Hori, T. Saito, K. Suzuki, M. Hirayama, A. Mitsui, M. Yonemura, H. Iba, R. Kanno, High-power all-solid-state batteries using sulfide superionic conductors. *Nat. Energy* **2016,** *1* (4), 16030

115. T. Krauskopf, S. P. Culver, W. G. Zeier, Bottleneck of Diffusion and Inductive Effects in $Li_{10}Ge_{1-x}Sn_xP_2S_{12}$. *Chem. Mater.* **2018,** *30* (5), 1791-1798.

116. H. J. Deiseroth, S. T. Kong, H. Eckert, J. Vannahme, C. Reiner, T. Zaiss, M. Schlosser, Li_6PS_5X: a class of crystalline Li-rich solids with an unusually high Li^+ mobility. *Angew. Chem. Int. Ed.* **2008,** *47* (4), 755-762.

117. M. A. Kraft, S. P. Culver, M. Calderon, F. Bocher, T. Krauskopf, A. Senyshyn, C. Dietrich, A. Zevalkink, J. Janek, W. G. Zeier, Influence of Lattice Polarizability on the Ionic Conductivity in the Lithium Superionic Argyrodites Li_6PS_5X (X = Cl, Br, I). *J. Am. Chem. Soc.* **2017,** *139* (31), 10909-10918.

118. Z. Zhang, Y. Shao, B. Lotsch, Y. S. Hu, H. Li, J. Janek, L. F. Nazar, C. W. Nan, J. Maier, M. Armand, L. Chen, New horizons for inorganic solid state ion conductors. *Energy Environ. Sci.* **2018,** *11* (8), 1945-1976.

119. N. J. J. de Klerk, I. Rosłoń, M. Wagemaker, Diffusion Mechanism of Li Argyrodite Solid Electrolytes for Li-Ion Batteries and Prediction of Optimized Halogen Doping: The Effect of Li Vacancies, Halogens, and Halogen Disorder. *Chem. Mater.* **2016,** *28* (21), 7955-7963.

120. Y. Choo, D. M. Halat, I. Villaluenga, K. Timachova, N. P. Balsara, Diffusion and migration in polymer electrolytes. *Prog. Polym. Sci.* **2020,** *103,* 101220.

121. E. Staunton, Y. G. Andreev, P. G. Bruce, Factors influencing the conductivity of crystalline polymer electrolytes. *Faraday Discuss discussion***, 2007,** *134*, 143-156, 215-233, 415-419.

122. D. Lin, P. Y. Yuen, Y. Liu, W. Liu, N. Liu, R. H. Dauskardt, Y. Cui, A Silica-Aerogel-Reinforced Composite Polymer Electrolyte with High Ionic Conductivity and High Modulus. *Adv. Mater.* **2018,** *30* (32), 1802661.

123. C. Li, Y. Huang, X. Feng, Z. Zhang, H. Gao, J. Huang, Silica-assisted cross-linked polymer electrolyte membrane with high electrochemical stability for lithium-ion batteries. *J. Colloid Interface Sci.* **2021,** *594*, 1-8.

124. A. L. Monaca, W. Zhu, Z. Feng, G. Bertoni, D. Campanella, G. Girard, S. Savoie, A. G. Nita, D. Clement, H. Demers, A. Vijh, F. Rosei, A. Paolella, Influence of Rutile and Anatase TiO_2 Precursors on the Synthesis of a $Li_{1.5}Al_{0.5}Ti_{1.5}(PO_4)_3$ Electrolyte for Solid-State Lithium Batteries. *J. Electrochem. Soc.* **2022,** *169* (4), 040515.

125. S. Jayanthi, S. Shenbagavalli, M. Muthuvinayagam, B. Sundaresan, Effect of nano TiO_2 on the thransport, structural and thermal properties of PEMA-NaI solid polymer electrolytes for energy storage devices. *Mater. Sci. Eng. B* **2022,** *285,* 115942.

126. A. R. Polu, H. W. Rhee, Effect of TiO_2 nanoparticles on structural, thermal, mechanical and ionic conductivity studies of PEO_{12}–LiTDI solid polymer electrolyte. *J. Ind. Eng. Chem.* **2016,** *37*, 347-353.

127. K. Huang, Y. Wang, H. Mi, D. Ma, B. Yong, P. Zhang, [BMIM]BF_4-modified PVDF-HFP composite polymer electrolyte for high-performance solid-state lithium metal battery. *J. Mater. Chem. A* **2020,** *8* (39), 20593-20603.

128. F. Chen, X. Wang, M. Armand, M. Forsyth, Cationic polymer-in-salt electrolytes for fast metal ion conduction and solid-state battery applications. *Nat. Mater.* **2022,** *21* (10), 1175-1182.

129. Y. Horowitz, M. Lifshitz, A. Greenbaum, Y. Feldman, S. Greenbaum, A. P. Sokolov, D. Golodnitsky, Review-Polymer/Ceramic Interface Barriers: The Fundamental Challenge for Advancing Composite Solid Electrolytes for Li-Ion Batteries. *J. Electrochem. Soc.* **2020,** *167* (16), 160514.

130. Y. Dong, I. W. Chen, J. Li, Transverse and Longitudinal Degradations in Ceramic Solid Electrolytes. *Chem. Mater.* **2022,** *34* (13), 5749-5765.

131. G. Cui, Reasonable Design of High-Energy-Density Solid-State Lithium-Metal Batteries. *Materials* **2020,** *2* (4), 805-815.

132. C. Wang, K. Fu, S. P. Kammampata, D. W. McOwen, A. J. Samson, L. Zhang, G. T. Hitz, A. M. Nolan, E. D. Wachsman, Y. Mo, V. Thangadurai, L. Hu, Garnet-Type Solid-State Electrolytes: Materials, Interfaces, and Batteries. *Chem. Rev.* **2020,** *120* (10), 4257-4300.

133. J. Tang, L. Wang, C. Tian, C. Chen, T. Huang, L. Zeng, A. Yu, Double-Protected Layers with Solid-Liquid Hybrid Electrolytes for Long-Cycle-Life Lithium Batteries. *ACS Appl. Mater. Interf.* **2022,** *14* (3), 4170-4178.

134. M. Lei, S. Fan, Y. Yu, J. Hu, K. Chen, Y. Gu, C. Wu, Y. Zhang, C. Li, NASICON-based solid state Li-Fe-F conversion batteries enabled by multi-interface-compatible sericin protein buffer layer. *Energy Storage Mater.* **2022,** *47*, 551-560.

135. E. J. Cussen, Structure and ionic conductivity in lithium garnets. *J. Mater. Chem.* **2010,** *20* (25), 5167-5173.

136. L. Chen, Y. Li, S. P. Li, L. Z. Fan, C. W. Nan, J. B. Goodenough, PEO/garnet composite electrolytes for solid-state lithium batteries: From "ceramic-in-polymer" to "polymer-in-ceramic". *Nano Energy* **2018,** *46*, 176-184.

137. Y. Kim, I. Waluyo, A. Hunt, B. Yildiz, Avoiding CO_2 Improves Thermal Stability at the Interface of $Li_7La_3Zr_2O_{12}$ Electrolyte with Layered Oxide Cathodes. *Adv. Energy Mater.* **2022,** *12* (13), 2102741.

138. Y. Arinicheva, X. Guo, M. T. Gerhards, F. Tietz, D. Fattakhova-Rohlfing, M. Finsterbusch, A. Navrotsky, O. Guillon, Competing Effects in the Hydration Mechanism of a Garnet-Type $Li_7La_3Zr_2O_{12}$ Electrolyte. *Chem. Mater.* **2022,** *34* (4), 1473-1480.

139. B. Wang, G. Wang, P. He, L. Z. Fan, Rational design of ultrathin composite solid-state electrolyte for high-performance lithium metal batteries. *J. Membr. Sci.* **2022,** *642,* 119952.

140. H. Huo, J. Liang, N. Zhao, X. Li, X. Lin, Y. Zhao, K. Adair, R. Li, X. Guo, X. Sun, Dynamics of the Garnet/Li Interface for Dendrite-Free Solid-State Batteries. *ACS Energy Lett.* **2020,** *5* (7), 2156-2164.

141. L. Chen, X. Qiu, Z. Bai, L. Z. Fan, Enhancing interfacial stability in solid-state lithium batteries with polymer/garnet solid electrolyte and composite cathode framework. *J. Energy Chem.* **2021,** *52*, 210-217.

142. F. Aguesse, V. Roddatis, J. Roqueta, P. García, D. Pergolesi, J. Santiso, J. A. Kilner, Microstructure and ionic conductivity of LLTO thin films: Influence of different substrates and excess lithium in the target. *Solid State Ionics* **2015,** *272*, 1-8.

143. S. Liu, Y. Zhao, X. Li, J. Yu, J. Yan, B. Ding, Solid-State Lithium Metal Batteries with Extended Cycling Enabled by Dynamic Adaptive Solid-State Interfaces. *Adv. Mater.* **2021,** *33* (12), 2008084.

144. J. Li, L. Zhu, J. Zhang, M. Jing, S. Yao, X. Shen, S. Li, F. Tu, Approaching high performance PVDF-HFP based solid composite electrolytes with LLTO nanorods for solid-state lithium-ion batteries. *Int. J. Energy Res.* **2021,** *45* (5), 7663-7674.

145. C. Liu, H. R. Wang, T. Long, Q. Ma, P. Ning, X. R. Dong, C.-S. Zhou, X.-W. Wu, X.-X. Zeng, Borosilicate Glass-Enabled Antifracture NASICON Solid Electrolytes for Lithium-Metal Batteries. *ACS Appl. Energy Mater.* **2022,** *5* (3), 3734-3740.

146. G. Wang, H. Liu, Y. Liang, C. Wang, L. Z. Fan, Composite polymer electrolyte with three-dimensional ion transport channels constructed by NaCl template for solid-state lithium metal batteries. *Energy Storage Mater.* **2022,** *45*, 1212-1219.

147. C. Zhao, J. Liang, X. Li, N. Holmes, C. Wang, J. Wang, F. Zhao, S. Li, Q. Sun, X. Yang, J. Liang, X. Lin, W. Li, R. Li, S. Zhao, H. Huang, L. Zhang, S. Lu, X. Sun, Halide-based solid-state electrolyte as an interfacial modifier for high performance solid-state Li–O_2 batteries, *Nano Energy* **2020**, *75*, 105036-105342.

148. S. H. S. Cheng, K. Q. He, Y. Liu, J. W. Zha, M. Kamruzzaman, R. L. W. Ma, Z. M. Dang, R. K. Y. Li, C. Y. Chung, Electrochemical performance of all-solid-state lithium batteries using inorganic lithium garnets particulate reinforced PEO/$LiClO_4$ electrolyte. *Electrochim. Acta* **2017,** *253*, 430-438.

149. J. Feng, L. Wang, Y. Chen, P. Wang, H. Zhang, X. He, PEO based polymer-ceramic hybrid solid electrolytes: a review. *Nano Converg.* **2021,** *8* (1), 1-12.

150. R. Chen, W. Qu, X. Guo, L. Li, F. Wu, The pursuit of solid-state electrolytes for lithium batteries: from comprehensive insight to emerging horizons. *Mater. Horiz.* **2016,** *3* (6), 487-516.

151. Q. Zhou, J. Ma, S. Dong, X. Li, G. Cui, Intermolecular Chemistry in Solid Polymer Electrolytes for High-Energy-Density Lithium Batteries. *Adv. Mater.* **2019,** *31* (50), 1902029.

152. Z. Xu, T. Yang, X. Chu, H. Su, Z. Wang, N. Chen, B. Gu, H. Zhang, W. Deng, H. Zhang, W. Yang, Strong Lewis Acid-Base and Weak Hydrogen Bond Synergistically Enhancing Ionic Conductivity of Poly(ethylene oxide)@SiO(2) Electrolytes for a High Rate Capability Li-Metal Battery. *ACS Appl. Mater. Interface* **2020,** *12* (9), 10341-10349.

153. J. Wan, J. Xie, D. G. Mackanic, W. Burke, Z. Bao, Y. Cui, Status, promises, and challenges of nanocomposite solid-state electrolytes for safe and high performance lithium batteries. *Mater. Today Nano* **2018,** *4*, 1-16.

154. L. Xu, J. Li, W. Deng, L. Li, G. Zou, H. Hou, L. Huang, X. Ji, Boosting the ionic conductivity of PEO electrolytes by waste eggshell-derived fillers for high-performance solid lithium/sodium batteries. *Mater. Chem. Front.* **2021,** *5* (3), 1315-1323.

155. L. Wang, Y. Zhong, Z. Wen, C. Li, J. Zhao, M. Ge, P. Zhou, Y. Zhang, Y. Tang, G. Hong, A strong Lewis acid imparts high ionic conductivity and interfacial stability to polymer composite electrolytes towards all-solid-state Li-metal batteries. *Sci.e China Mater.* **2022,** *65* (8), 2179-2188.

156. B. M. Savoie, M. A. Webb, T. F. Miller, Enhancing Cation Diffusion and Suppressing Anion Diffusion via Lewis-Acidic Polymer Electrolytes. *J. Phys. Chem. Lett.* **2017,** *8* (3), 641-646.

157. D. Li, J. Wang, S. Guo, Y. Xiao, Q. Zeng, W. He, L. Gan, Q. Zhang, S. Huang, Molecular-Scale Interface Engineering of Metal–Organic Frameworks toward Ion Transport Enables High-Performance Solid Lithium Metal Battery. *Adv. Funct. Mater.* **2020,** *30* (50), 2003945.

158. Z. Zeng, G. Liu, Z. Jiang, L. Peng, J. Xie, Zinc bis(2–ethylhexanoate), a homogeneous and bifunctional additive, to improve conductivity and lithium deposition for poly (ethylene oxide) based all-solid-state lithium metal battery. *J. Power Sources* **2020,** *451,* 227730.

159. S. Hu, L. Du, G. Zhang, W. Zou, Z. Zhu, L. Xu, L. Mai, Open-Structured Nanotubes with Three-Dimensional Ion-Accessible Pathways for Enhanced Li^+ Conductivity in Composite Solid Electrolytes. *ACS Appl. Mater. Interf.* **2021,** *13* (11), 13183-13190.

160. T. Wu, W. Dai, M. Ke, Q. Huang, L. Lu, All-Solid-State Thin Film mu-Batteries for Microelectronics. *Adv. Sci.* **2021,** *8* (19), 2100774.

161. W. Liu, D. Lin, J. Sun, G. Zhou, Y. Cui, Improved Lithium Ionic Conductivity in Composite Polymer Electrolytes with Oxide-Ion Conducting Nanowires. *ACS Nano* **2016,** *10* (12), 11407-11413.

162. H. Chen, D. Adekoya, L. Hencz, J. Ma, S. Chen, C. Yan, H. Zhao, G. Cui, S.Zhang, Stable Seamless Interfaces and Rapid Ionic Conductivity of Ca–CeO_2/LiTFSI/PEO Composite Electrolyte for High-Rate and High-Voltage All-Solid-State Battery. *Adv. Energy Mater.* **2020,** *10* (21), 2000049.

163. M. Jia, Z. Bi, C. Shi, N. Zhao, X. Guo, Air-stable dopamine-treated garnet ceramic particles for high-performance composite electrolytes. *J. Power Sources* **2021,** *486,* 229363.

164. K. He, C. Chen, R. Fan, C. Liu, C. Liao, Y. Xu, J. Tang, R. K. Y. Li, Polyethylene oxide/garnet-type $Li_{6.4}La_3Zr_{1.4}Nb_{0.6}O_{12}$ composite electrolytes with improved electrochemical performance for solid state lithium rechargeable batteries. *Compos. Sci. Technol.* **2019,** *175*, 28-34.

165. G. D. Salian, C. Lebouin, A. Galeyeva, A. P. Kurbatov, T. Djenizian, Electrodeposition of Polymer Electrolyte Into Porous $LiNi_{0.5}Mn_{1.5}O_4$ for High Performance All-Solid-State Microbatteries. *Front. Chem.* **2018,** *6*, 675.

166. J. B. Goodenough, Rechargeable batteries: challenges old and new. *J. Solid State Electrochem.* **2012,** *16* (6), 2019-2029.

167. C. Wang, H. Liu, Y. Liang, D. Li, X. Zhao, J. Chen, W. Huang, L. Gao, L. Fan, Molecular-level Designed Polymer Electrolyte for High-Voltage Lithium–Metal Solid-State Batteries. *Adv. Funct. Mater.* **2022,** *33* (3), 2209828.

168. W. Liang, Y. Shao, Y. M. Chen, Y. Zhu, A 4 V Cathode Compatible, Superionic Conductive Solid Polymer Electrolyte for Solid Lithium Metal Batteries with Long Cycle Life. *ACS Appl. Energy Mater.* **2018,** *1* (11), 6064-6071.

169. Z. Fang, Y. Luo, H. Liu, Z. Hong, H. Wu, F. Zhao, P. Liu, Q. Li, S. Fan, W. Duan, J. Wang, Boosting the Oxidative Potential of Polyethylene Glycol-Based Polymer Electrolyte to 4.36 V by Spatially Restricting Hydroxyl Groups for High-Voltage Flexible Lithium-Ion Battery Applications. *Adv. Sci.* **2021,** *8* (16), 2100736.

170. F. He, W. Tang, X. Zhang, L. Deng, J. Luo, High Energy Density Solid State Lithium Metal Batteries Enabled by Sub-5 microm Solid Polymer Electrolytes. *Adv. Mater.* **2021,** *33* (45), 2105329.

171. Z. Xie, Z. Wu, X. An, X. Yue, P. Xiaokaiti, A. Yoshida, A. Abudula, G. Guan, A sandwich-type composite polymer electrolyte for all-solid-state lithium metal batteries with high areal capacity and cycling stability. *J. Membr. Sci.* **2020,** *596,*117739.

172. L. Lin, K. Qin, M. Li, Y. S. Hu, H. Li, X. Huang, L. Chen, L. Suo, Spinel-related $Li_2Ni_{0.5}Mn_{1.5}O_4$ cathode for 5-V anode-free lithium metal batteries. *Energy Storage Mater.* **2022,** *45*, 821-827.

173. Y. Li, G. Wang, L. Z. Fan, Ultra-Thin Asymmetric Composite Electrolyte Addresses the Out-of-Sync Requirements of Lithium Batteries Interfaces. *Batter. Supercaps* **2022,** *5* (9), 202200212.

174. D. Cao, X. Sun, Y. Wang, H. Zhu, Bipolar stackings high voltage and high cell level energy density sulfide based all-solid-state batteries. *Energy Storage Mater.* **2022,** *48*, 458-465.

175. T. S. Wang, X. Liu, Y. Wang, L. Z. Fan, High Areal Capacity Dendrite-Free Li Anode Enabled by Metal–Organic Framework-Derived Nanorod Array Modified Carbon Cloth for Solid State Li Metal Batteries. *Adv. Funct. Mater.* **2020,** *31* (2), 2001973.

176. L. Chen, W. Li, L. Z. Fan, C. W. Nan, Q. Zhang, Intercalated Electrolyte with High Transference Number for Dendrite-Free Solid-State Lithium Batteries. *Adv. Funct. Mater.* **2019,** *29* (28), 1901047.

177. S. Xiong, Y. Liu, P. Jankowski, Q. Liu, F. Nitze, K. Xie, J. Song, A. Matic, Design of a Multifunctional Interlayer for NASCION-Based Solid-State Li Metal Batteries. *Adv. Funct. Mater.* **2020,** *30* (22), 2001444.

178. Y. Ma, J. Wan, Y. Yang, Y. Ye, X. Xiao, D. T. Boyle, W. Burke, Z. Huang, H. Chen, Y. Cui, Z. Yu, S. T. Oyakhire, Y. Cui, Scalable, ultrathin, and high-temperature-resistant solid polymer electrolytes for energy-dense lithium metal batteries. *Adv. Energy Mater.* **2022**, *12*, 2103720.

179. C. Li, Y. Huang, X. Feng, Z. Zhang, H. Gao, J. Huang, Silica-assisted cross-linked polymer electrolyte membrane with high electrochemical stability for lithium-ion batteries. *J. Colloid Interface Sci.* **2021**, *594*, 1-8.

180. D. Lin, P. Y. Yuen, Y. Liu, W. Liu, R. H. Dauskardt, Y. Cui, A silica-aerogel-reinforced composite polymer electrolyte with high ionic conductivty and high modulus. *Adv. Mater.* **2018**, *30*, 1802661.

181. C. Ma, J. Zhang, M. Xu, Q. Xia, J. Liu, S. Zhao, L. Chen, A. Pan, D. G. Ivey, W. Wei, Cross-linked branching nanohybrid polymer electrolyte with monodispersed TiO_2 nanoparticles for high performance lithium-ion batteries. *Journal of Power Sources* **2016**, *317*, 103-111.

182. Y. He, Y. Li, Q. Tong, J. Zhang, J. Weng, M. Zhu, Highly conductive and thermostable grafted polyrotaxane/ceramic hybrid polymer electrolyte for solid-state lithium-metal batteries. *ACS Appl. Mater. Interface.* **2021**,*13* (35), 41593-41599.

183. X. Zheng, T. Yang, J. Wei, C. Wang, M. Chen, Co-contribution of quenching and nanocrystallization on ionic-conductivity improvement of a composite electrolyte of polyethylene Oxide/$Li_7La_3Zr_2O_{12}$ nanofibers at 45° C for all-solid-state Li metal batteries. *J. Power Sources* **2021**, *496*, 229843.

184. Z. Zhang, G. Zhang, L. Chao, Three–dimensional fiber network reinforced polymer electrolyte for dendrite–free all–solid–state lithium metal batteries. *Energy Storage Mater.* **2021**, *41*, 631-641.

185. S. Li, J. Lu, Z. Geng, Y. Chen, X. Yu, M. He, H. Li, Solid polymer electrolyte reinforced with a $Li_{1.3}Al_{0.3}Ti_{1.7}(PO_4)_3$-coated separator for all-solid-state lithium batteries. *ACS Appl. Mater. Interface.* 2022, 14 (1), 1195-1202.

Chapter 3: Instrumentation and Methods

3.1. Electrochemical Measurements

3.1.1. Ionic Conductivity of Solid-State Electrolytes (SSEs)

Throughout this thesis, to evaluate the Li-ion transport capability of the ceramic SEs (cubic LLZO) and ceramic-based hybrid SEs (conductive polymer in porous garnet framework/scaffold) the electrochemical impedance spectroscopy (EIS) method was employed. The cubic LLZO powders were uniaxially pressed into 13 mm diameter pellets under 10-ton load for 5 min (using the press is shown in Figure 3.1). The pressed pellets were kept covered with the sacrificial mother powder (to prevent loss of Li) in the Al_2O_3 crucible and sintered typically at 1200 ℃ for 2 hours. After that heat treatment, several surface conditioning protocols, including the dry polishing (DP), and wet polishing (WP) with SiC paper (400, 600, and 1200 grit sizes) were applied to obtain a mirror-like surface followed by gold sputtering (with thickness of 50 nm on both surfaces) as block electrodes. For the hybrid solid electrolyte (HSE), stainless steel (SS) was used as blocking electrodes. The EIS measurements were carried out from 21-25 ℃ (seasonal RT) to 80 ℃ with 10 ℃ steps using an electrochemical workstation (Bio-Logic) (Figure 3.2) in potentiostatic mode between 10^6 Hz and 1Hz at an open-circuit voltage (OCV). The cells of Au | LLZO pellet | Au and SS | Ceramic-based HSE | SS were kept at each test temperature for 30 min to reach thermal equilibrium. The resistances were determined by fitting the Nyquist plot with the Equivalent Electric Circuit using the Zview-fit method provided by EC-Lab software. Equations (1) and (2) were used to calculate the ionic conductivity and activation energy of Li-ion migration.

The ionic conductivity (σ) was calculated based on the following Equation (1):

$$\sigma = L/(R \times S) \quad (1)$$

where σ ($S \cdot cm^{-1}$) is the ionic conductivity, L is the thickness of the hybrid SE (cm), R is the resistance (Ohm), and S is the area (cm^2) of the stainless steel (SS).

The Li-ion transport activation energy (E_a) of different SEs was calculated by the Arrhenius Equation (2):

$$\sigma(T) = A \exp(-E_a/RT) \quad (2)$$

where σ ($S \cdot cm^{-1}$) is the ionic conductivity, T (K) is the absolute temperature, A is the pre-exponential constant, R is the Boltzmann constant, and E_a (eV) is the activation energy for the ionic conductivity.

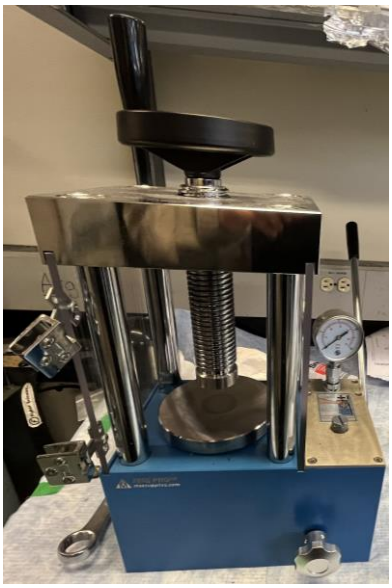

Figure 3. 1. The press employed for densification of cubic LLZO powders.

3.1.2. Li-ion Transference Number

The lithium-ion transference number is another key parameter to evaluate the Li-ion transport capability of the ion conductor, which could be calculated based on the following Equation (3):

$$t_{Li^+} = \frac{I_s(\Delta V - I_0 R_0)}{I_0(\Delta V - I_s R_s)} \quad (3)$$

where ΔV, I_0, I_s, R_0 and R_s represent the polarization potential (10 mV), the initial current (mA), steady current (mA), initial interfacial resistance (ohm), and steady interfacial resistance (ohm), respectively.

To calculate the lithium-ion transference number the Li | hybrid SE | Li symmetric cells were fabricated. The lithium-ion transference number was measured by DC polarization and AC impedance in symmetric cells using an electrochemical workstation (Bio-Logic) (Figure 3.2).

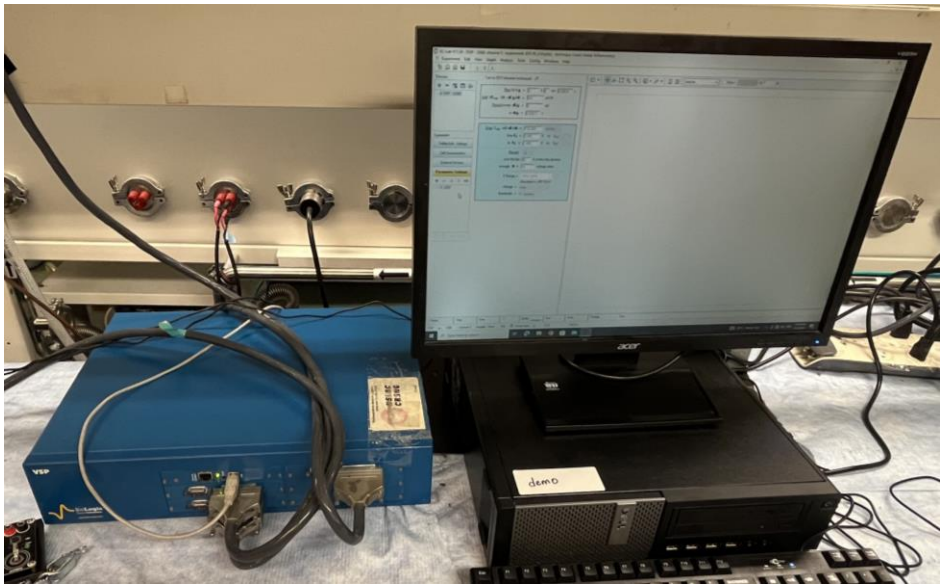

Figure 3. 2. The electrochemical workstation (Bio-Logic) employed for EIS and LSV measurements.

3.1.3. Measurements of Interfacial Stability against Li Metal

To calculate the interfacial stability against Li metal, lithium-ion stripping-plating cycling measurements were employed. The Li | LE | LLZO pellet | LE | Li, and Li | hybrid SE | Li symmetric cells were fabricated in the glovebox (Figure 3.3). The lithium stripping-plating cycling proceeded under 0.1, 0.2, 0.4, and 0.5 mA cm^{-2} current densities respectively with a period of 30 min employing an MTI battery tester (BST8-WA, MTI corporation) (Figure 3.4). EIS was conducted to measure the interfacial resistance before and after stripping-plating cycling.

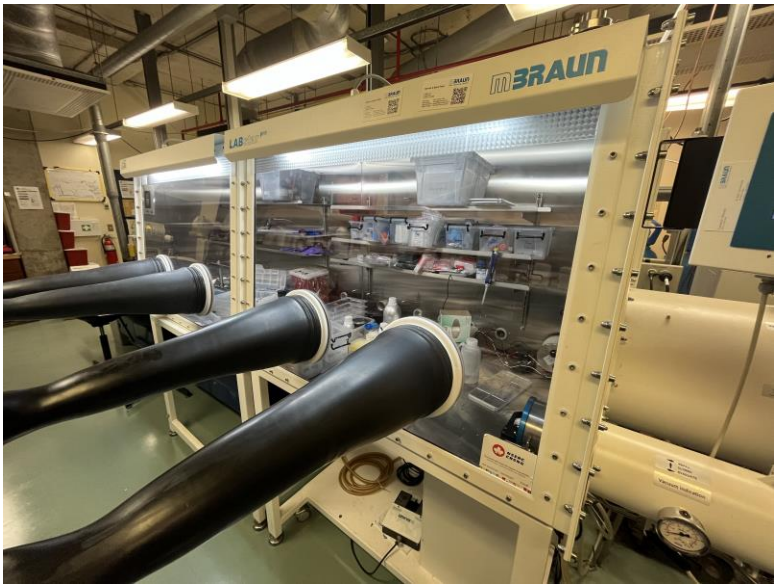

Figure 3. 3. The Argon-filled glovebox utilized for battery assembling and material preparation.

Figure 3. 4. The MTI battery tester (BST8-WA, MTI corporation) employed for battery cycling tests, including plating-stripping and charge-discharge cycling.

3.1.4. Determination of of Electrochemical Window (vs. Li^+/Li)

The electrochemical window was determined by linear sweep voltammetry (LSV) using SS | ceramic-based CSE | Li cells from 2 to 6 V (vs Li^+ / Li) at a scanning rate of 1 mV s^{-1} employing an electrochemical workstation (Bio-Logic) (Figure 3.2).

3.1.5. Charge-Discharge Cycling of All-Solid-State Lithium Batteries (ASSLBs)

For the all-solid-state batteries, two types of battery models were empolyed depending on the thickness of the as-prepared hybrid SEs. One is the Swagelok-type (Figure 3.5a), used in the case of Li | hybrid SE | LFP batteries fabricated in a glove box (Figure 3.3). Before the charge-discharge cycling, the as-fabricated cells were stored in an oven at 60 ℃ overnight then cooled down naturally to RT, so to obtain good interfacial contact between electrodes and SE. The charge-discharge cycling tests were conducted using an MTI battery tester (BST8-WA, MTI corporation) in a range of 3.0 – 4.2 V with 0.1 C rate at RT. The rate measurement of the ASSBs proceeded under 0.1 C, 0.2 C, 0.5 C, 1 C, and 2 C at RT, and rate performance at a high temperature (70 ℃) was carried under 1 C, and 2 C. EIS was employed to measure the interfacial resistance of the ASSBs under various cycling states. Another one is the coin-type (Figure 3.5b), which was used in the case of Li | Ceramic-based CSE | NMC 622 batteries fabricated in a glove box. Again before the charge-discharge cycling, the as-fabricated cells were stored in an oven at 60 ℃ overnight then cooled down naturally to RT, so to obtain good interfacial contact. The charge-discharge cycling tests were conducted using an MTI battery tester (BST8-WA, MTI corporation) in a 3.0 – 4.5, 4.6, 4.7, and 4.8 V range with a 0.2 C rate. The rate measurement of the ASSBs proceeded under 0.1 C, 0.2 C, 0.5 C, 1 C, and 2 C at 40 ℃. In addition, the ASSLB was cycled in the voltage from 3 – 4.5 V under 0.1 C at RT to compare it with a conventional battery with liquid electrolyte (LE) that was again cycled in the voltage range from 3 – 4.5 V under 0.1 C at RT.

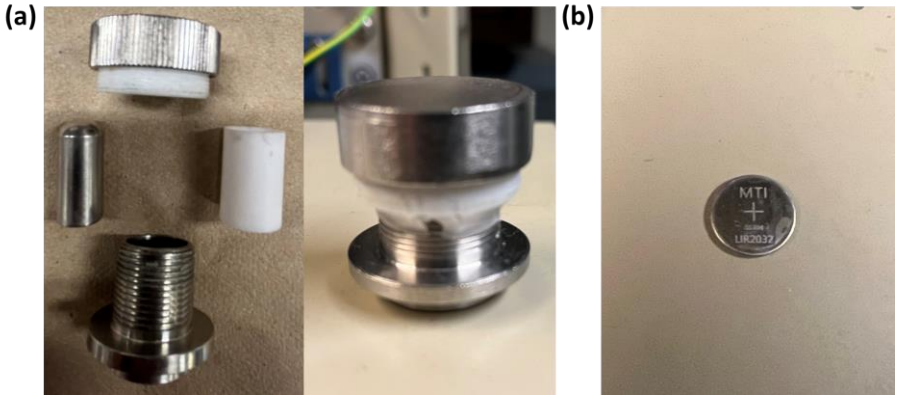

Figure 3. 5. (a) The Swagelok-type battery and (b) the coin-type battery utilized for symmetric batteries and solid-state batteries assembling.

3.2. Material Characterization

3.2.1. X-Ray Diffraction (XRD)

Throughout this thesis, XRD patterns were acquired using a Bruker D8-Advantage powder diffractometer (Figure 3.6). Cobalt source (Co-Kα) radiation with wavelength λ = 1.78892 Å was used with a voltage of 35 kV and a current of 45 mA. Scan parameters were 2θ from 5 to 120° in a step of 0.02° and 10 to 70° in a step of 0.01. The phase Rietveld refinements of the crystal structure were carried out with Fullprof suite software.

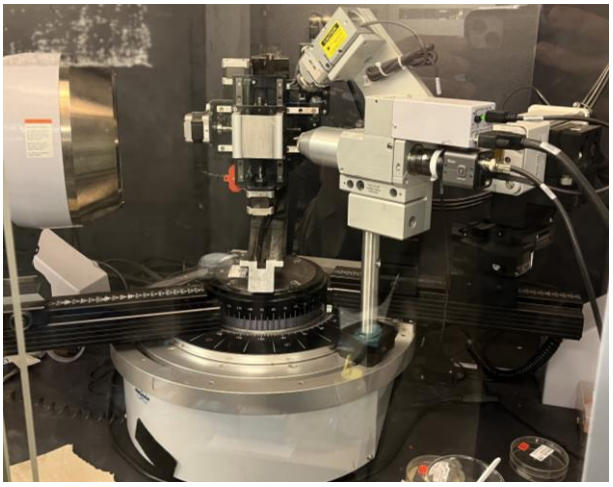

Figure 3. 6. The Bruker D8-Advantage powder diffractometer utilized for crystal structure characterization.

3.2.2. Scanning Electron Microscopy (SEM)

The morphology of the powder samples was examined with a SU8000 Hitachi (Figure 3.7a) cold-field emission scanning electron microscope (CFE-SEM), utilizing the in-lens upper secondary electron detector, and using 8mm of working distance with 30 kV acceleration voltage and emission current of 40 µA. To increase the conductivity of the LLZO powder specimen, 5 nm of gold was sputtered on them with a Quorum Q150TS sputter coater. Throughout this thesis, cross-sectional, top view SEM images as well as energy-dispersive spectroscopy (EDX) of the LLZO ceramic pellets and two types of hybrid SEs were obtained with a SU3500 Hitachi (Figure 3.7b) cold-field emission scanning electron microscope (CFE-SEM), utilizing the in-lens upper secondary electron detector, and using 8 mm of working distance with 10 kV acceleration voltage and emission current of 40 µA. The cross-sectional samples were prepared by mechanically cutting the specimen with a doctor blade. Energy dispersive X-ray spectroscopy (EDS) was performed

with a Bruker XFlash 60 standard detector at a 15mm working distance, 5kV accelerating voltage, high probe mode, and 30 µA emission current. Mappings were obtained at 15kX magnification with 15 min acquisition time using an integrated drift correction procedure to avoid drifting of the region of interest.

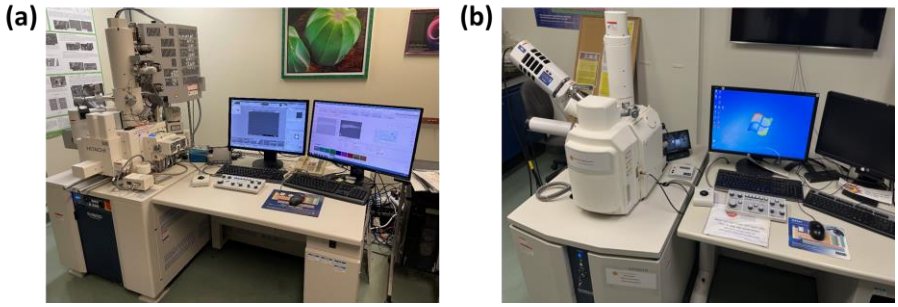

Figure 3. 7. (a) The SU8000 microscope, and (b) the SU3500 microscope utilized for obtaining SEM and EDX images.

3.2.3. Transmission Electron Microscopy (TEM)

In Chapter 4 and Chapter 6, the images of selected area electron diffraction (SAED) patterns and lattice fringe were obtained with FEI Titan Krios 300 kV Cryo-STEM (Figure 3.8) at 200 kV. A Thermo Scientific Talos F200X G2 (S) TEM microscope at 200 kV was used to acquire high-angle annular dark-field (HAADF) images. Energy dispersive X-ray (EDS) elemental mappings were acquired to determine the elemental distribution within the cubic LLZO and TiO_2-coated $LiNi_{0.6}Co_{0.2}Mn_{0.2}O_2$ particles.

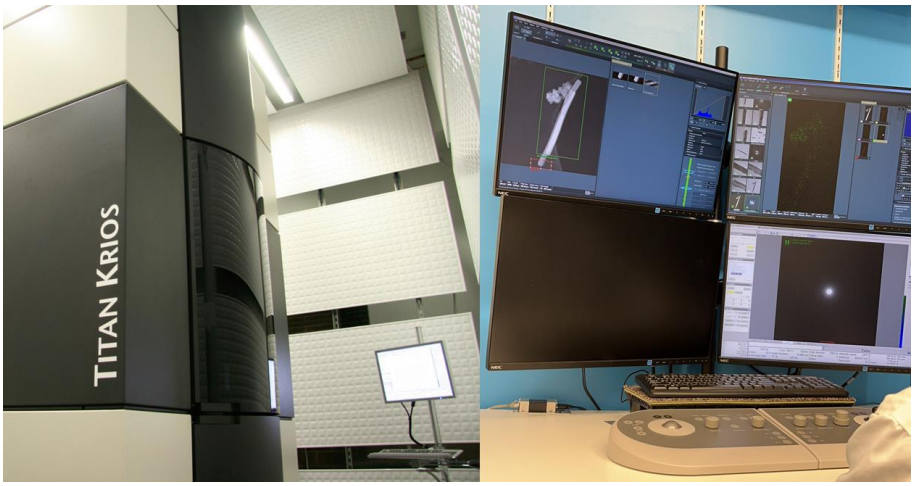

Figure 3. 8. The FEI Titan Krios 300 kV Cryo-STEM utilized for characterization of nanoscale cubic LLZO single crystals.

3.2.4. X-Ray Photoelectron Spectroscopy (XPS)

XPS spectra were collected with Nexsa G2 (Thermo Scientific) (Figure 3.9), using Al Kα radiation (1486.6 eV) and an X-ray spot size of 200 μm. The flood gun was turned on for the measurements to prevent charging effects. Samples were sealed into the sample holder inside a nitrogen-filled glovebox. For all elemental spectra, 20 scans with a dwell time of 50 ms and pass energy of 50 eV were used. Charge correction was carried out using adventitious C 1s set to a binding energy of 284.8 eV, while charge neutralization was carried out using an electron flood gun.

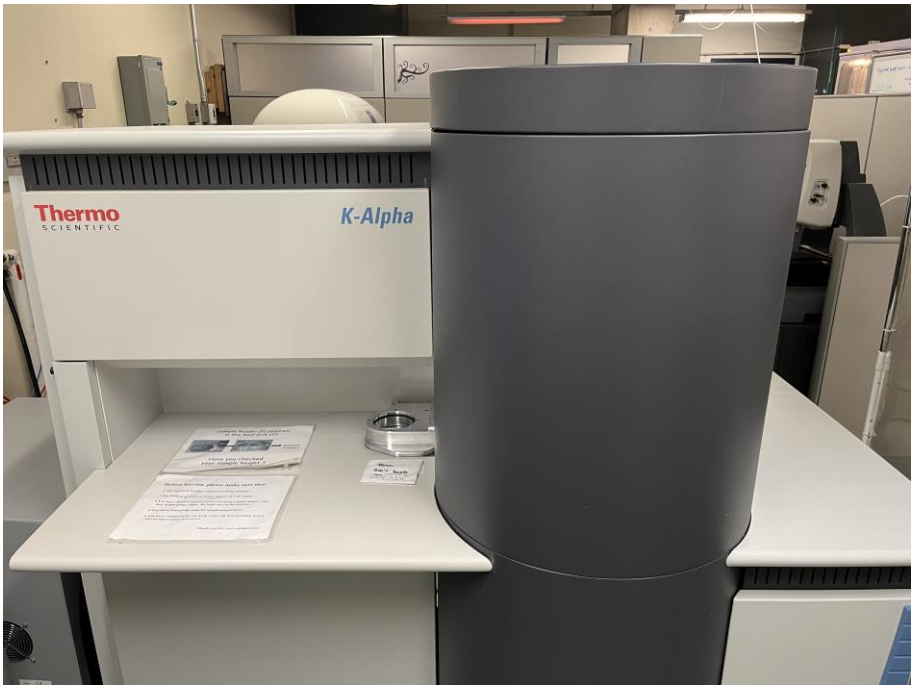

Figure 3. 9. The Nexsa G2 (Thermo Scientific) XPS utilized for chemical composition characterizations.

3.2.5. Thermogravimetric analysis (TGA)

In Chapter 4, to demonstrate the reaction mechanism of the low-temperature crystallization of cubic LLZO, TGA was examined with Discovery 5500 from TA Instruments (Figure 3.10) at a ramp rate of 3 ℃ / min from 25 to 650 ℃ under air atmosphere. The precursor sample before calcination process was exposed to isothermal TGA analysis, which was ramping up to 600 ℃ at a rate of 10 ℃ / min and keeping the system isothermally for 1 hour. In Chapters 5 and 6, TGA was conducted on two types of the as-prepared hybrid SEs with Discovery 5500 from TA

Instruments at a ramp rate of 10 ℃ / min from 25 to 700 and 800 ℃ respectively to demonstrate the ceramic-based nature and good thermal stability.

Figure 3. 10. The thermogravimetric analysis (TGA) Discovery 5500 from TA Instruments.

3.2.6. Brunauer-Emmett-Teller (BET) and Barrett-Joyner-Halenda (BJH)

In Chapter 6, to evaluate the porous structure of the as-synthesized porous cubic LLZO particles, BET and BJH pore size analysis were conducted on Micromeitics TriStar 3000 (Figure 3.11).

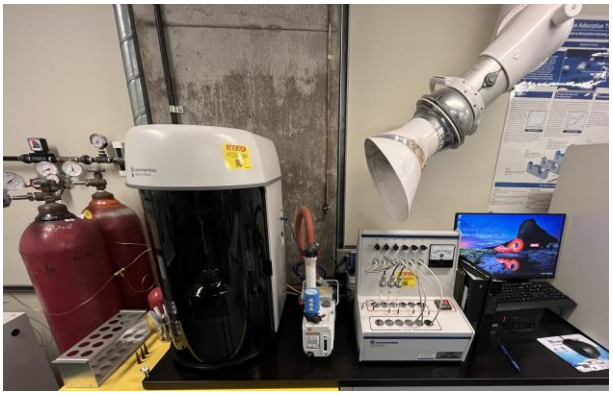

Figure 3. 11. The Brunauer-Emmett-Teller (BET) and Barrett-Joyner-Halenda (BJH) Micromeritics TriStar 3000.

3.2.7. Focused-ion and electron beam

In Chapter 6, to evaluate the cycled interface of the TiO2-coated NCM622/ceramic-based CSE/Li full solid-state batteries, Hitachi high-technologies ETHOS NX5000 focused-ion and electron-beam system was employed. (Figure 3.12)

Figure 3. 12. Hitachi high-technologies ETHOS NX5000 focused-ion and electron-beam system

3.2.7. Inductively Coupled Plasma (ICP) Optical Emission Spectroscopy

In Chapter 4, to verify whether the co-precipitation reaction was fully completed at different pH values, the suspensions were centrifuged, and the supernatants were analyzed using the Inductively coupled plasma optical emission spectroscopy (ICP-OES method (Thermo Scientific iCAP 6500 ICP spectrometer) (Figure 3.13). ICP-OES was also applied for elemental concentration analysis for the co-precipitation products.

Figure 3. 13. The inductively coupled plasma optical emission spectroscopy (ICP-OES, Thermo Scientific iCAP 6500 ICP spectrometer).

3.2.8. Porosity Measurements

In Chapters 5 and 6, the porosity of the as-prepared porous cubic LLZO frameworks/scaffolds were measured and calculated through the Archimedes method based on the following Equation (4):

$$Porosity = \left[\frac{m_{wet} - m_{dry}}{\rho_{liquid}}\right] / V_{pellet} \quad (4)$$

Where m_{wet} and m_{dry} are the weights of the pellets before and after immersion into liquid, ρ_{liquid} is the density of the liquid (n-butanol) (0.811 g/cm^3), and V_{pellet} is the volume of the as-prepared porous LLZO framework.

Chapter 4: Low-temperature crystallization of nanoscale garnet-type Li-ion conductors

This chapter addresses the 1st objective of thesis, i.e., the issue of high-temperature crystallization of cubic garnet-type solid-state electrolytes, and the reduction of the particle size from micron to nano scale to provide further flexibility in advanced all-solid-state lithium battery fabrication. This chapter has been published in *Journal of Power Sources*, with the following citation:

Senhao Wang, Hsien-chieh Chiu, and George P. Demopoulos, 2024. "Low-temperature crystallization of nanoscale garnet-type Li-ion conductors for solid-state lithium-ion batteries". *J. Power Sources 595 (2024) 234061.*

Abstract

The synthesis and processing of garnet-type conductors is usually done at temperatures above 1100℃ to reach the high Li-ion conducting cubic phase resulting in micron-sized particles and potential Li-loss, which are unfavorable for further processing and electrode-electrolyte assembly. Here, we tackle this problem and report a novel low-temperature aqueous synthesis route to stabilize the cubic phase of $Li_{6.1}Al_{0.3}La_3Zr_2O_{12}$ (c-Al-LLZO) at a temperature as low as 600 ℃, while obtaining nano-crystallites at around 100 - 200 nm. Moreover, a dual-reaction mechanism was proposed to describe the process of c-Al-LLZO crystallization. The as-synthesized nanoscale c-Al-LLZO particles facilitate the densification of the solid-state electrolyte (SSE) pellets with less endowed grain boundaries (exhibiting a high relative density of 97.8%). The ionic conductivity reaches 0.42 mS cm^{-1} at 21 ℃ and the low activation energy (half of the published values) is 0.17 eV. The results presented here show that symmetric cells with Li metal exhibit excellent stability at the current density of 0.2 mA/cm^2 and 0.5 mA/cm^2, and an improved critical current density (CCD) of 2.16 mA/cm^2. This work provides a feasible method of low-temperature crystallization of nanoscale cubic garnet SSEs with good performance for the fabrication of stable SSLBs.

4.1. Introduction

Due to their high energy density, long cycle life, and variable charge-discharge rates, automobile manufacturers favor rechargeable Li^+ batteries (LIBs) to power electric vehicles [1]. However, with the explosive demand for safe electric vehicle (EV) LIBs, current technology, and electrode

materials are insufficient to provide cost advantages and high practical energy densities necessary to extend the range of electric vehicles and, thus, enable their widespread use by eliminating consumer range anxiety [2-4]. At this stage, solid inorganic electrolytes become highly attractive because they enable the use of high-capacity electrode materials (e.g. sulphur [5], manganese [6], and vanadate-based cathodes [7]) that are not particularly stable or safe to utilize in liquid organic electrolytes for current Li^+ battery technology. Further, they allow the use of metallic Li anodes by avoiding the damage caused by dendritic Li growth [8], hence increasing realistic energy densities [9]. Additional advantages of solid inorganic electrolytes include improved thermal and chemical stability and the removal of liquids and separators in electrochemical cells [10]. Here, the development of fast Li-ion SSE materials may also be viewed as a catalyst for the development of novel types of all-solid-state thin-film micro-batteries for electronics or for the development of novel large-scale storage solutions that utilize abundant industrial waste heat to accelerate the diffusion of Li^+ in SSBs [11,12].

Among a variety of inorganic SSEs, the Li-stuffed garnet-type oxide $Li_7La_3Zr_2O_{12}$ (LLZO) has generated considerable interest as a potential solid electrolyte for SSBs due to its high ionic conductivity at room temperature and good electrochemical stability against lithium metal anode [13,14]. LLZO comprises two polymorphs: tetragonal (t-LLZO, $I4_1/acd$) [15] and cubic (c-LLZO, $Ia\bar{3}d$) [16] phases, the latter of which presents two orders of magnitude higher ionic conductivity compared to the tetragonal phase. To circumvent the emergence of the thermodynamically advantageous tetragonal phase, aliovalent doping of metal cations either at Li^+ sites with Al^{3+} [17], Ga^{3+} [18] or the Zr^{4+} sites with Ta^{5+} [19] or Nb^{5+} [20] are employed [21], through which c-LLZO can be stabilized at lower temperature. Al-doped LLZO makes an appealing candidate among all the doped derivatives, due to its excellent sinterability and cost competitiveness.

Conventionally, to obtain a conductive cubic phase, LLZO is synthesized through solid-state reaction, which requires multiple milling-calcination cycles and high calcination temperatures from 900 to 1200 ℃ [22-25]. Meanwhile, the high-temperature procedure yields micron-sized particles with significant aggregates, rendering composites of electrode-electrolyte assembly challenging [23]. Furthermore, although wet chemical routes like sol-gel, Pechini, co-precipitation, and spray pyrolysis produce fine LLZO particles at lower temperatures (700°C), they require

expensive precursors, multiple drying/calcination steps to remove water and organic solvents, and long annealing times to achieve phase pure conductive c-LLZO [26-29].

Moreover, in the further fabrication of all-solid-state lithium batteries (ASSBs), the composite cathode containing cathode active material (CAM) and solid electrolyte (SE) powders (in some cases also with a carbon additive) is necessary to obtain good interfacial contacts. [30] Due to the polycrystalline nature of LLZO-based ASSBs, there are typically more interfaces than conventional liquid-based batteries or ASSBs with soft and glassy SEs (such as polymers and sulfides). [31] Commonly, the total internal resistance of an ASSB is defined by: (1) the total electronic/ionic resistance of the cathode; (2) the homo-ionic interface resistance between the grains of active cathode and anode materials; (3) the heteronic interface resistance between the SE and the CAM and SE and anode active materials (AAM); and (4) the resistance of the SE. For the internal resistance that comes from the composite cathode, which is mostly caused by interfaces between CAM and SE particles. [32] To prepare composite cathodes, physical mixing or co-sintering is commonly employed. For both methods similar particle sizes of both components are desired, nanoscale solid electrolytes are favorable to obtaining composite cathode with lower inner interfacial resistance between cathode particles and solid electrolyte particles. Furthermore, for the co-sintering, since the conventional synthesis routes the high calcination temperatures (> 1100 ℃) to obtain the cubic LLZO phase are much higher than the crystallization temperature of cathode materials (600 to 900 ℃). The decomposition of both components and interactions between them at high temperatures cause the failure of the ASSBs.

Hence, synthesizing submicron LLZO powders at low temperatures is critical for preparing dense pellets and allowing stable interface contact between LLZO/electrodes in SSBs fabrication.

In this work, we report a novel low-temperature aqueous synthesis strategy for c-Al-LLZO through which the pure cubic garnet-type SSEs can be obtained under one-step calcination at 600 °C for 6 h. Meanwhile, it enables the synthesis of nanoscale c-Al-LLZO particles around 100 to 200 nm. Densified pellets with as-synthesized c-Al-LLZO nanoparticles attained a high ionic conductivity of 0.42 $mS \cdot cm^{-1}$ at 21℃ and a low activation energy of 0.17 eV that is almost half of the previously reported data (0.2 to 0.5 eV) [20,33-35] - a property achieved due to nanoscale particle fusion into large blocks with fewer grain boundaries during sintering (high relative density: 97.8%). The

excellent Li stripping-plating cycling performance and high critical current density (2.16 mA/cm^2) measured herald the great value of this novel synthesis strategy for practical application in SSBs.

4.2. Experimental section

4.2.1. Synthesis of cubic Al-doped LLZO

The cubic phase $Li_{6.1}Al_{0.3}La_3Zr_2O_{12}$ (c-Al-LLZO) was synthesized as described in the flowchart given in Fig. A.1. (in Appendixes: Supplementary Information for Chapter 4 A.1.) and Fig. 4.1. Lanthanum (III) nitrate hexahydrate ($La(NO_3)_3 \cdot 6H_2O$) (99.9%, Aldrich), aluminium nitrate nonahydrate ($Al(NO_3)_3 \cdot 9H_2O$) (99.99% trace metals basis, Sigma-Aldrich), and lithium hydroxide monohydrate ($LiOH \cdot H_2O$) (99.95% trace metals basis, Sigma-Aldrich) were dissolved in DI-water at room temperature, where the concentration of La must be added in excess amount stoichiometries to compensate for the solubility limitation in the elevated pH range. In this system represented as suspension A, the sociometric ratio of Li:Al:La is 6.1:0.3:3.0154. Due to the occurrence of the hydrolysis reaction, milky white precipitates are formed. Meanwhile, based on the stoichiometric, zirconyl nitrate solution ($ZrO(NO_3)_2$) (35 wt% in dilute nitric acid, ≥ 99% trace metals basis, Aldrich) was dissolved in DI-water at room temperature presented as solution B. After the hydrolysis reactions were completed in both systems, solution B was added dropwise into suspension A and mixed thoroughly (at this point, the pH value of this mixed system was around 6). To further complete the co-precipitation reaction, saturated LiOH solution (3M) was added dropwise at a rate of 1 mL / min and the pH value of the mixed phase system was set higher than pH=7 and lower than the saturation concentration of LiOH (i.e. [LiOH]= ca. 5.3M, pH=11). To determine the optimal co-precipitation pH, systems of different pH values (pH=7.5, 8.5, 9.5, and 10.5) were prepared respectively. After this co-precipitation, the suspension was directly transferred into a 100-mL autoclave, which was then heated to 200℃ for 3 hours including 1.5 hours for ramping. After this hydrothermal aging process, the wet precipitates were recovered via centrifugation (thoroughly washed with DI-water and isopropanol). Then the as-prepared precipitates were dried at 80 ℃ in the vacuum oven overnight. The dried precipitates were then mixed in isopropanol with the designated quantity of $LiOH \cdot H_2O$ powder by planetary milling in ZrO_2 container loaded with 1 mm ZrO_2 balls at 650 rpm for 10 cycles that involved 3 min grinding / 7 min resting. The total concentration of Li for calcination was 7.5 times higher with respect to the concentration of Al (i.e. [Al]), where [Al] corresponds to the stoichiometry of

$Li_{6.1}Al_{0.3}La_3Zr_2O_{12}$. Finally, the ground suspension was separated from the grinding media via a rotary evaporator at 60℃ under vacuum and dried at 80℃ in the vacuum oven overnight. The completely dry precursors were calcinated in alumina crucibles at 600 ℃ for 6 hours and the nanoscale c-Al-LLZO particles were obtained.

4.2.2. Characterization

X-ray diffraction (XRD) was conducted for the powder and pellet samples using a Bruker D8-Advantage powder diffractometer using Co-Kα radiation with wavelength λ = 1.78892 Å, 35 kV/45 mA, 2θ from 5 to 120° in a step of 0.02°. The phase Rietveld refinements of the crystal structure were carried out with Fullprof suite software. The morphology characterization of the powder samples was examined using a Hitachi SU8000 cold-field emission scanning electron microscope (CFE-SEM) (Hitachi High Technologies). Images of SAED patterns and lattice fringe were obtained with a Philips CM200 transmission electron microscope (TEM) at 200 kV. A JEM-ARM Model 200F TEM microscope at 200 kV to acquire high-angle annular dark-field (HAADF) images. Energy dispersive X-ray (EDS) elemental mapping techniques were conducted to acquire the elemental distribution of c-Al-LLZO particles. Thermogravimetric analysis (TGA) was examined with Discovery 5500 from TA Instruments at a ramp rate of 3 ℃ min^{-1} from 25 to 650 ℃ under air atmosphere. X-ray photoelectron spectroscopy (XPS) was carried out on Thermo Scientific K-Alpha at the surface of powder samples to determine the elemental state. Inductively coupled plasma optical emission spectroscopy (ICP-OES, Thermo Scientific iCAP 6500 ICP spectrometer) was applied for elemental concentration analysis for the co-precipitation products.

4.2.3. Electrochemical performance

The as-synthesized c-Al-LLZO powders were uniaxially pressed into 13 mm diameter pellets under a 10-ton load for 5 min. The pressed pellets were kept covered with the sacrificial mother powder (to prevent loss of Li) in the Al_2O_3 crucible and sintered at 1200 ℃ for 2 hours and the XRD patterns are presented in Fig. A.1.2. (in Appendixes: A.1.). After that heat treatment, several surface conditioning protocols were followed, including dry polishing (DP), and wet polishing (WP) with SiC paper (400, 600, and 1200 grit sizes) to obtain a mirror-like surface followed by gold sputtering (with a thickness of 50 nm on both surfaces) as block electrodes. Impedance measurements were carried out from 21 ℃ (room temperature) to 80 ℃ with 10 ℃ steps using an electrochemical workstation (Bio-Logic) in potentiostatic mode between 1 MHz and 1Hz at an

open-circuit voltage (OCV); the Au-LLZO-Au cells were kept at each test temperature for 30 min to reach thermal equilibrium. The resistances were determined by fitting the Nyquist plot with the Equivalent Electric Circuit by Zview-fit method provided by EC-Lab software. The Li/LE/c-Al-LLZO/LE/Li symmetric cells were fabricated in a glovebox with 10 μL liquid electrolyte (LE: $LiPF_6$ in EC: DEC = 1:1 by volume) added to both interfaces to obtain good contact between metallic lithium foil and c-Al-LLZO pellet. The lithium stripping-plating cycling was conducted at 0.2 and 0.5 mA/cm^2 current density, and the critical current density (CCD) with a 0.15 mA step using an MTI battery tester (BST8-WA, MTI corporation).

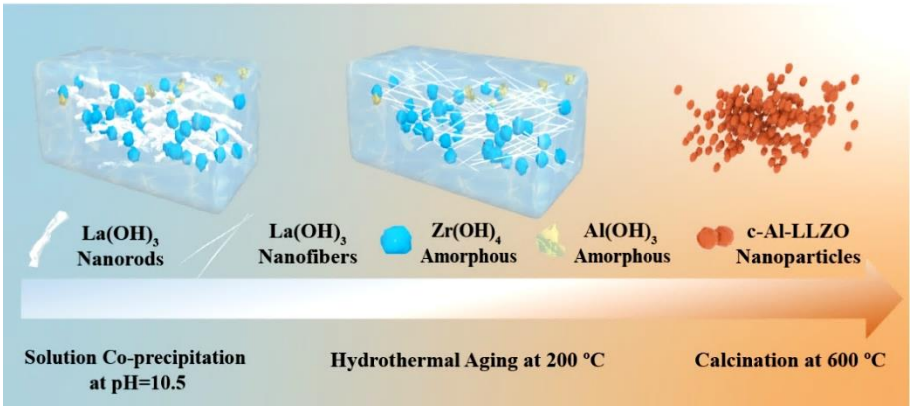

Figure 4. 1. Schematic representation of the novel three-step synthesis process for c-Al-LLZO.

4.3. Results and discussion

4.3.1. Crystallization of intermediates

The nanoscale c-Al-LLZO solid electrolyte materials were synthesized through a novel intermediate-assist three-step strategy at low calcination temperature (600℃) and the detailed procedural steps followed are described in the experimental section and Fig. A.1.1. (in Appendixes: A.1.). To investigate the intermediate-assist crystallization mechanism of c-Al-LLZO particles, products after each step, including co-precipitation, hydrothermal-aging, and calcination at different temperatures, were collected and characterized. At the beginning (*i.e.* step one: solution co-precipitation at room temperature), the drop-wise addition of diluted LiOH aqueous solution into the mixture of solution A and solution B (initial pH = ~ 6) resulted in hydrolytic co-precipitation of La^{3+}, Zr^{4+}, and Al^{3+} at different target pH values of 7.5, 8.5, 9.5, and 10.5. To verify whether the co-precipitation reaction was fully completed at different pH values, the suspensions were centrifuged, and the supernatants were analyzed using the ICP technique. As shown in Fig.

A.1.3. (in Appendixes: A.1.), in the whole pH value range, essentially no residual Al^{3+} and Zr^{4+} remained in solution, which indicates that the hydrolysis reactions of both cations were fully completed at the whole pH range. By contrast, the hydrolysis of La^{3+} progressed gradually with increasing pH at room temperature, and the reaction was completed only when reached pH = 10.5. The crystallinity of the products collected from co-precipitation at room temperature under various pH values is presented in Fig. A.1.4. (in Appendixes: A.1.). Through the characterization of the crystalline structures, only the hydrolysis product of La^{3+}, $La(OH)_3$ (PDF 00-036-1482) was identified to exist in crystalline form, whereas the precipitates of Al^{3+} and Zr^{4+} were amorphous. To be clear, the peaks of pH = 8.5 sample in Figure A.1.4. (in Appendixes: A.1.) are not related to any crystal, which is contributed from the background noise as shown in Figure A.1.5. (in Appendixes: A.1.), there are no diffraction peaks exhibits in diffraction image compared to the sample after co-precipitation at pH = 10.5.

The most adequate crystallization of $La(OH)_3$ was observed at pH = 10.5, which is consistent with the results of the ICP analysis of the supernatant aforementioned. The corresponding results in terms of crystalline morphology are presented in Fig. 4.2a. Through the SEM images, it can be deduced that the degree of crystallization of rod-shaped $La(OH)_3$ crystals improved with the rising pH environment, while the amorphous Al^{3+} and Zr^{4+} hydroxide particles are scattered around the nanorods. Consequently, the optimal pH condition for the co-precipitation at room temperature is pH = 10.5. Following step one, the suspension was transferred to an autoclave for hydrothermal aging (step two). Hydrothermal aging temperature and holding time were varied in order to determine the best conditions. The most adequate crystallization of $La(OH)_3$ as part of the intermediate was obtained at 200 ℃ and 1.5 h hydrothermal aging, as illustrated in Fig. A.1.6. and A.1.7. (in Appendixes: A.1.). Accordingly, the products of step one obtained under different pH environments were subjected to hydrothermal aging at 200℃ for 1.5 h respectively. The XRD characterization of different intermediate samples is presented in Fig. 4.2d and 4.2e. Through comparison with Fig. A.1.3. (in Appendixes: A.1.), it is evident that $La(OH)_3$ obtained from step one is more fully crystallized after step two, whilst the Al^{3+} and Zr^{4+} precipitate still remain amorphous. The characteristic peaks of the crystalline planes (210), (002), and (112) gradually showed up. Meanwhile, the characteristic peak at around 57° gradually evolved from one single low-intensity peak to stronger splitting peaks (300) and (211), as the alkaline environment of the

hydrothermal aging system rises, as shown by the amplification of the XRD patterns (Fig. 4.2e) in the 2theta range from 44° to 60°, suggesting good crystallization.

TEM characterization of the crystal morphology of the intermediates following step two provides consistent findings to the XRD results. Under the weakly alkaline hydrothermal aging environment (pH 7.5-9.5), the percentage of rod-shaped $La(OH)_3$ crystals present in the intermediate products is low, and the morphology of the crystals is heterogeneous, indicating that crystallization is not entirely completed. As the alkalinity of the hydrothermal environment increased, the $La(OH)_3$ crystals became more thoroughly crystallized, and when the pH reached 10.5, the $La(OH)_3$ crystals exhibited nanofiber morphology with uniform size, as illustrated in Fig. 4.2b. Further evaluation of $La(OH)_3$ crystal size collected from various alkaline environments presented in Fig. 4.2c reveals that as the alkalinity in the environment progressed, the crystals developed to a longer and thinner morphology (length: ~ 500 nm, thickness: ~ 20 nm). After step two, the final products contained crystalline $La(OH)_3$ nanofibers uniformly distributed within the amorphous Al^{3+} and Zr^{4+} hydroxide matrix.

The as-synthesized intermediates containing crystalline nanofibers and surrounded amorphous particles were further characterized in order to explore the effect of other cations incorporated in the hydrothermal aging environment on the crystallization of $La(OH)_3$. As shown in Fig. 4.2g, through TEM, there are two distinct particle morphologies present in the intermediates after hydrothermal aging: the amorphous particles and the crystalline nanofibers which are consistent with the XRD results (showed in Fig 4.2d and 4.2e). Fig.2h shows the TEM image of a single crystalline nanofiber (or nanorod) and its length and thickness are 261.8 nm and 29.8 nm respectively which are in line with the results shown above (Fig. 4.2c). To verify the structural composition of the crystalline nanofiber, the SAED patterns and lattice fringes obtained along [110] direction are presented in Fig. 4.2i. Comparing the lattice fringe spacing and electron diffraction pattern of the nanofiber to a reference pattern confirms that the crystal nanorod component is $La(OH)_3$. The Rietveld-refined XRD profile of the intermediate product collected after hydrothermal aging is fully matched with the $La(OH)_3$ pattern (Space group: P 63/m) as shown in Fig. 4.2f. The lattice parameters of the as-synthesized intermediate are refined to be a = b = 6.4817 Å, and c = 3.8268 Å, which are slightly smaller compared to the standard pattern (a = b = 6.547 Å and c = 3.854 Å). The phenomenon of reduced lattice parameters can be attributed to the presence

of other cations (i.e. Al^{3+} and/or Zr^{4+}) doped in $La(OH)_3$. Meanwhile, the presence of amorphous hydrolysis products of Al^{3+} and Zr^{4+} suppresses the growth of $La(OH)_3$ crystals. To further investigate the discrepancy in elemental composition between the amorphous and crystalline nanofiber parts in the intermediate product, energy dispersive X-ray spectroscopy (EDS) was conducted on the two selected areas as presented in Fig. 4.2j to 4.2n. As can be seen, the concentration of Zr and Al in the amorphous part is higher than that of La, while on the contrary, the concentration of La in the crystalline nanofiber part is higher. More confirmatory results are shown in Fig. A.1.8. (in Appendixes: A.1.). The discrepancy in the concentration of Zr and Al elements between two selected areas is significant, which is consistent with the above discussion. During the hydrothermal aging, there is a small portion of Zr^{4+} and Al^{3+}doped into $La(OH)_3$ lattice that affects crystal growth, leading to a decrease in its lattice parameters. It is also seen that there is a small amount of La in the amorphous part (area 1), which may be attributed to the elemental contamination of the sample or the presence of a very small amount of $La(OH)_3$ in amorphous form. In summary, the intermediate collected after step two is a mixture of amorphous and crystalline form, where crystalline $La(OH)_3$ nanofibers/nanorods dominate and the hydrolysis products of Zr^{4+} and Al^{3+} and a small portion of $La(OH)_3$ are present in amorphous state providing a favorable matrix for the subsequent crystallization of c-Al-LLZO upon calcination.

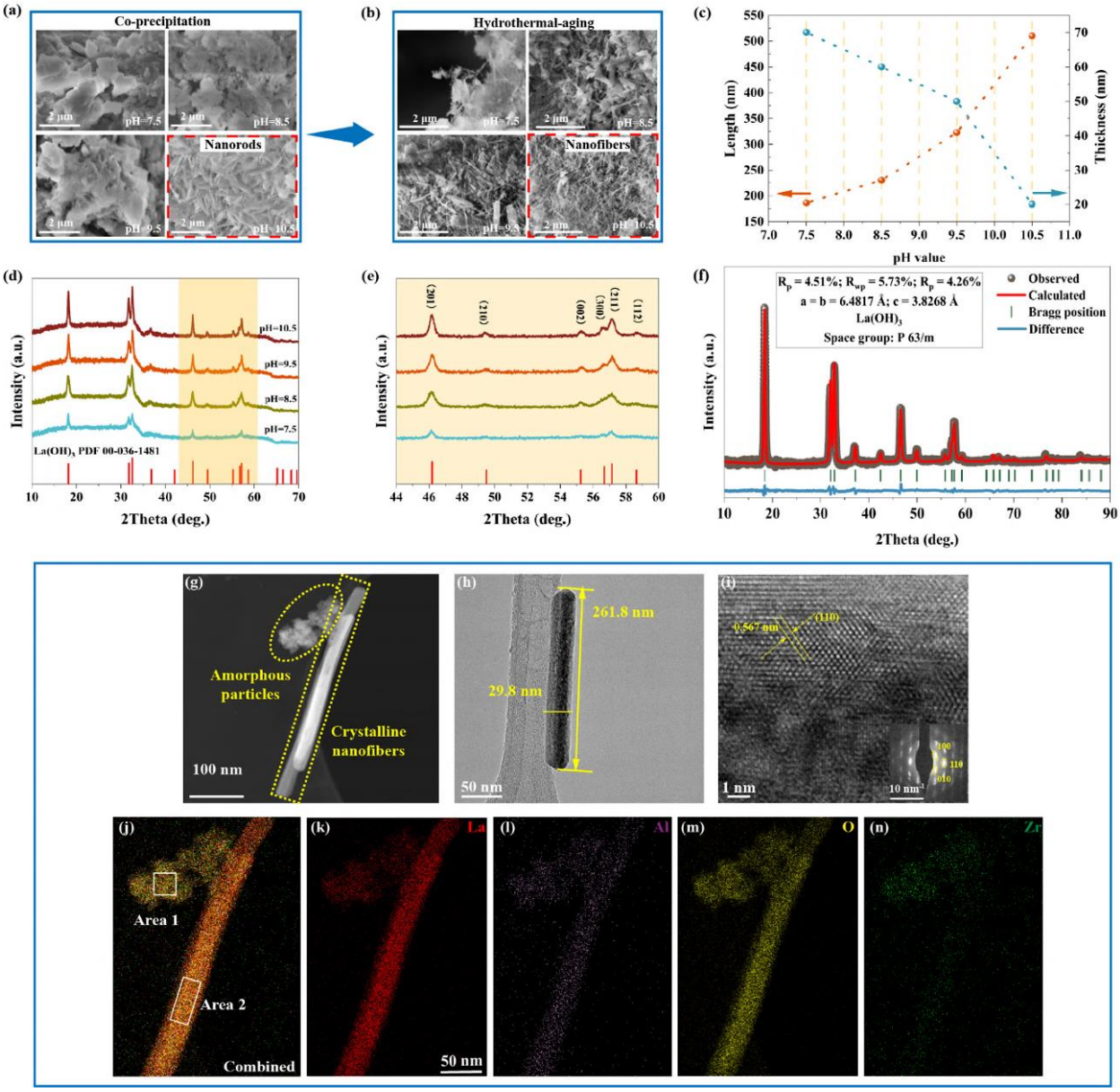

Figure 4. 2. Structure and morphology characterization of the intermediate composites after solution co-precipitation (step one) and hydrothermal aging (step two). (a) Scanning electron micrographs of samples collected after step one, and (b) after step two; (c) length and thickness evolution of synthesized intermediates after the hydrothermal aging process under different pH values; (d) X-ray diffractograms of the intermediates after step two under various pH conditions; (e) the magnification of XRD pattern from 44° to 60°; (f) Rietveld refinement on XRD pattern of the intermediate obtained at pH 10.5 after hydrothermal aging. TEM images of intermediates (pH 10.5) after hydrothermal aging: (g) both amorphous and crystalline parts; (h) single crystalline part; (i) SAED patterns and lattice fringes obtained along [110] direction. (j-n) TEM combined and individual elemental mappings of La, Al, O, and Zr.

4.3.2. Mechanism of c-Al-LLZO reactive crystallization

To induce crystallization of c-Al-LLZO, the intermediate composites are mixed with a Li source like $LiOH{\cdot}H_2O$ (using an excess amount compared to the stoichiometric ratio) via planetary-milling, collected, and dried, and then subjected to calcination (step three). The calcined products were collected and characterized by XRD. As shown in Fig 4.3a, the crystallization of $La(OH)_3$ proceeds during the co-precipitation and hydrothermal aging. When the calcination process is initiated at 400 ℃, $La_2Zr_2O_7$ forms first, and as the calcination temperature rises, the cubic phase $Li_{6.1}Al_{0.3}La_3Zr_2O_{12}$ (c-Al-LLZO) is obtained. At 550 ℃ the formation c-Al-LLZO was verified but still, the product contained a small amount of remaining $La_2Zr_2O_7$ as evident by the marked peak. The initially crystallized phase of $La_2Zr_2O_7$ was entirely transformed into c-Al-LLZO when the calcination temperature reached 600 ℃. No further phase transition occurred when the temperature was raised further, which suggests that the novel 3-step synthesis method described herein is capable of producing high-purity cubic structured c-Al-LLZO crystals at the lowest calcination temperature (600 ℃) yet reported. Moreover, the crystallization pathway did not proceed via the critical transition step from tetragonal-LLZO to cubic-LLZO, as specified in the previously published mechanism [36-38]. Interestingly it is the hydrothermal aging step that opened this new crystallization pathway. Thus, as can be seen in the XRD patterns presented in Fig. A.1.9. (in Appendixes: A.1.), direct calcination of the pH = 10.5 co-precipitated samples, without the hydrothermal aging step, yields substantially crystalline cubic garnet phase only at 900 and 1000 ℃. Thus, the intermediate composite obtained from hydrothermal aging containing $La(OH)_3$ nanocrystals embedded in a matrix of amorphous Zr-Al-La hydroxides seems to be the critical link in facilitating the direct crystallization of cubic garnet (without going through the tetragonal phase) at as low calcination temperature as 500 ℃.

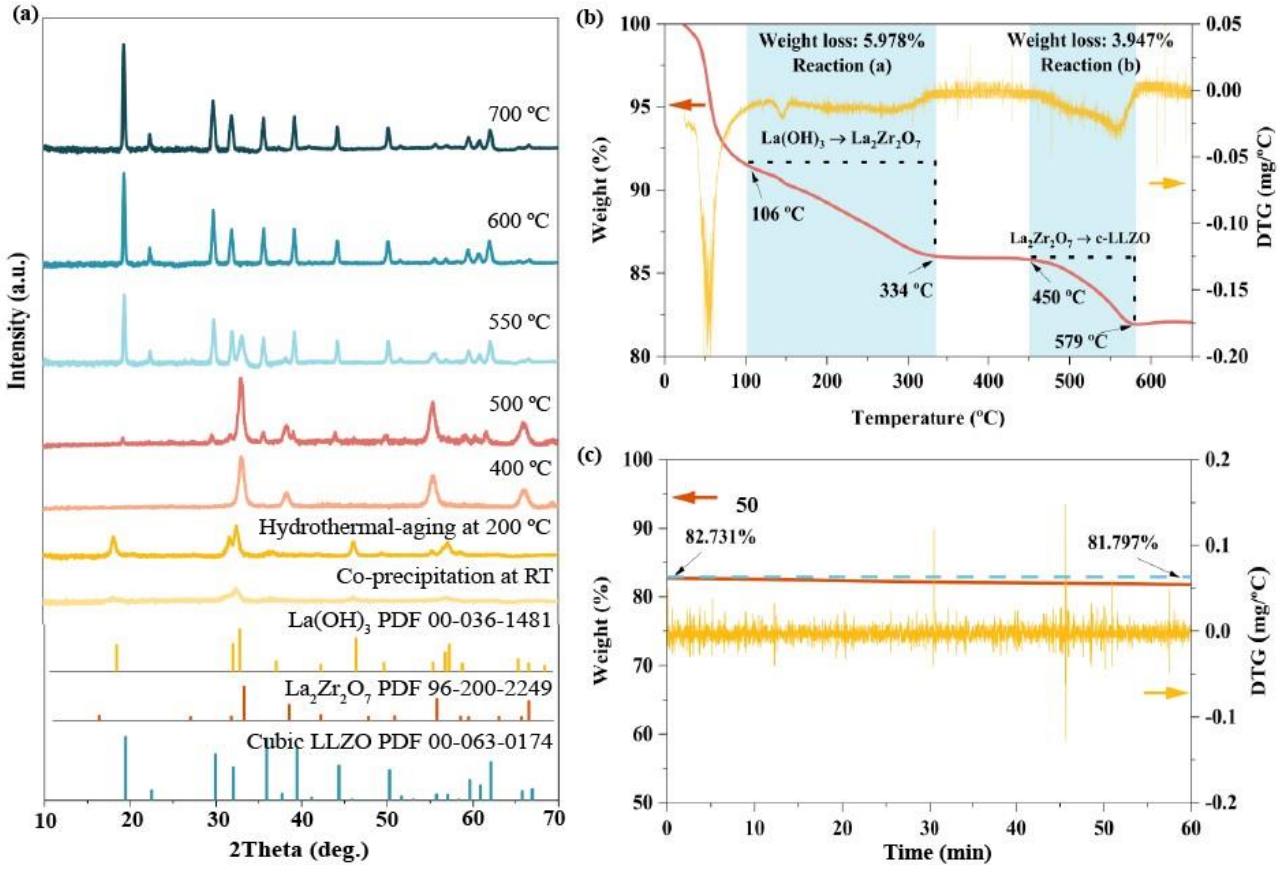

Figure 4. 3. Synthesis mechanism analysis: (a) X-ray diffraction patterns of products after solution co-precipitation at pH = 10.5, hydrothermal aging, and calcination at various temperatures from 400 ℃ to 700 ℃ for 6 h; (b) TGA and DTG curves and (c) Isothermal TGA and DTG curves of pH = 10.5 calcination precursor.

To further investigate the low-temperature synthesis reaction mechanism, thermogravimetric analysis (TGA) is employed. The TGA curve and its differential DTG curve are presented in Fig. 4.3b, where three main areas of weight loss are evident. First, when the temperature is raised to 106 ℃, which corresponds to the disappearance of residual water. Second is the transition of $La(OH)_3$ nanocrystals to $La_2Zr_2O_7$ crystals, which is completed at 334 ℃ with a weight loss of 5.98 %, which is termed as reaction (a). As the temperature rises, there is no weight loss until 450 ℃ is reached. Third is the initiation of transition from $La_2Zr_2O_7$ crystals to c-Al-LLZO crystals when the temperature hits 450 ℃, and which is ended at 579 ℃ with a weight loss of 3.95 %, referred to as reaction (b). Following that, the temperature was raised to 650 ℃, with no weight loss observed, indicating that no additional phase transition is involved. This crystal transition sequence demonstrates that cubic-LLZO can be synthesized directly via this novel three-step

$La(OH)_3$-assisted synthesis route, without the occurrence of the intermediate tetragonal phase t-LLZO and have crystallization completed at the lowest yet temperature of 600 ℃. Since the effect of the holding time factor was not considered in the above TGA analysis, the calcination precursor was also exposed to an isothermal TGA test, which was ramping at a rate of 10 ℃ / min up to 600 ℃ where it was kept isothermally for 1 hour. As shown in Fig. 4.3c, no significant weight loss occurred throughout the process, indicating that the crystallization of cubic phase LLZO was completed at 600 ℃. Based on these observations, a dual reaction mechanism for the low-temperature crystallization of c-Al-LLZO can be proposed, as shown in the following reactions:

$$(a)\ 2La(OH)_{3\,(cr)} + 2Zr(OH)_{4\,(am)} \rightarrow La_2Zr_2O_{7\,(cr)} + 7H_2O$$

$$(b)\ La_2Zr_2O_{7\,(cr)} + La(OH)_{3\,(cr)} + 0.3Al(OH)_{3\,(am)} + 6.1LiOH_{(cr)} \rightarrow Li_{6.1}Al_{0.3}La_3Zr_2O_{12\,(cr)} + 5H_2O$$

Interestingly, the ratio of weight loss corresponding to the two reactions, as derived from the TGA curves, is 5.978 % : 3.947 % which equals 1.5 : 1 molar ratio, very near to the H_2O stoichiometric ratio 1.4:1 of the two reactions (a) and (b). The crystal morphology evolution corresponding to new synthesis process is presented in Fig. 4.4.

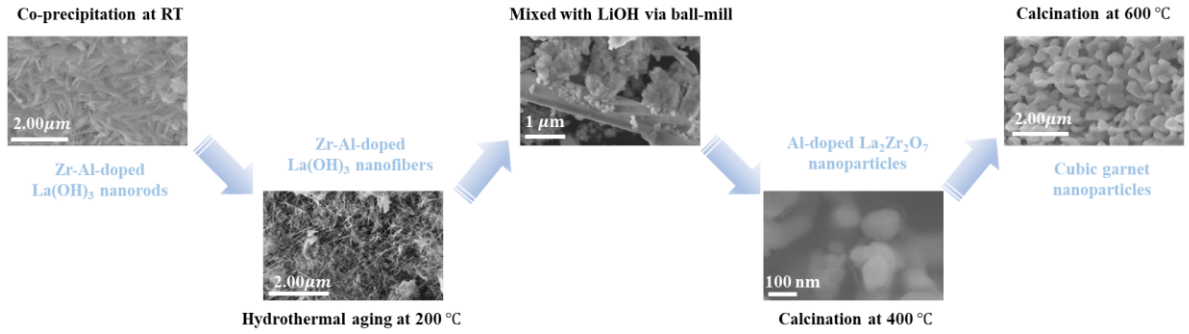

$$(a)\ 2La(OH)_{3\,(cr)} + 2Zr(OH)_{4\,(am)} \rightarrow La_2Zr_2O_{7\,(cr)} + 7H_2O$$

$$(b)\ La_2Zr_2O_{7\,(cr)} + La(OH)_{3\,(cr)} + 0.3Al(OH)_{3\,(am)} + 6.1LiOH_{(cr)} \rightarrow Li_{6.1}Al_{0.3}La_3Zr_2O_{12\,(cr)} + 5H_2O$$

Figure 4. 4. The morphology evolution of the proposed tetragonal phase free crystallization of nanoscale cubic garnet ($Li_{6.1}Al_{0.3}La_3Zr_2O_{12}$).

To further confirm the reaction mechanism from a chemical speciation perspective, X-ray photoelectron spectroscopy (XPS) was employed. The full surveys of the products after co-precipitation, hydrothermal aging, and calcination process show the presence of La, Zr, Al, Li, O,

and C as presented in Fig. A.1.10. The photoelectron O 1s spectra of products collected after the three steps are presented in Fig. 4.5a from bottom to top. From the photoelectron spectra of O 1s, it can be observed that products collected after the co-precipitation reaction consisted of characteristic peaks of water molecules and hydroxide, along the characteristic peaks of metal cation (Al^{3+}, Zr^{4+}, and La^{3+}) bonding with oxygen atoms. The ratios of the characteristic peak intensity are consistent with their concentration ratio in the system, which indicates that at the condition of pH = 10.5 and room temperature, co-precipitation of metal hydroxides was complete. From the O 1s photoelectron spectra collected from the products after hydrothermal aging at 200 ℃, similar chemical speciation and peak intensity ratios as with the co-precipitation step were obtained, except for the absence of water molecules. Finally, after the calcination process, there is no characteristic hydroxide peak detected but the four metal cations exist now as metal oxides, with their peak intensity ratios corresponding to stoichiometric ratios. In addition, the photoelectron spectra of La 3d, Zr 3d, and Al 2p are shown in Fig. 4.5 (b-d). Typically, the Zr 3d spectrum exhibits two peaks at around 181 and 184 eV which are attributed to the corresponding two spin-orbits of $3d_{5/2}$ and $3d_{3/2}$ in agreement with the reported literature [39,40]. Moreover, the shift of binding energy of two peaks to lower energy as the synthesis steps proceeded from co-precipitation to calcination suggests that the chemical environment around Zr atoms transitioned from hydroxide to oxide, consistent with the speciation evolution proposed above. Similar shifting to lower energy was also observed in La 3d and Al 2p spectra (from bottom to top), indicating the transition from hydroxide to oxide [41-43]. Generally, the speciation evolution obtained from XPS analysis supports the proposed mechanism of the dual-reaction crystallization of c-Al-LLZO at 600 ℃.

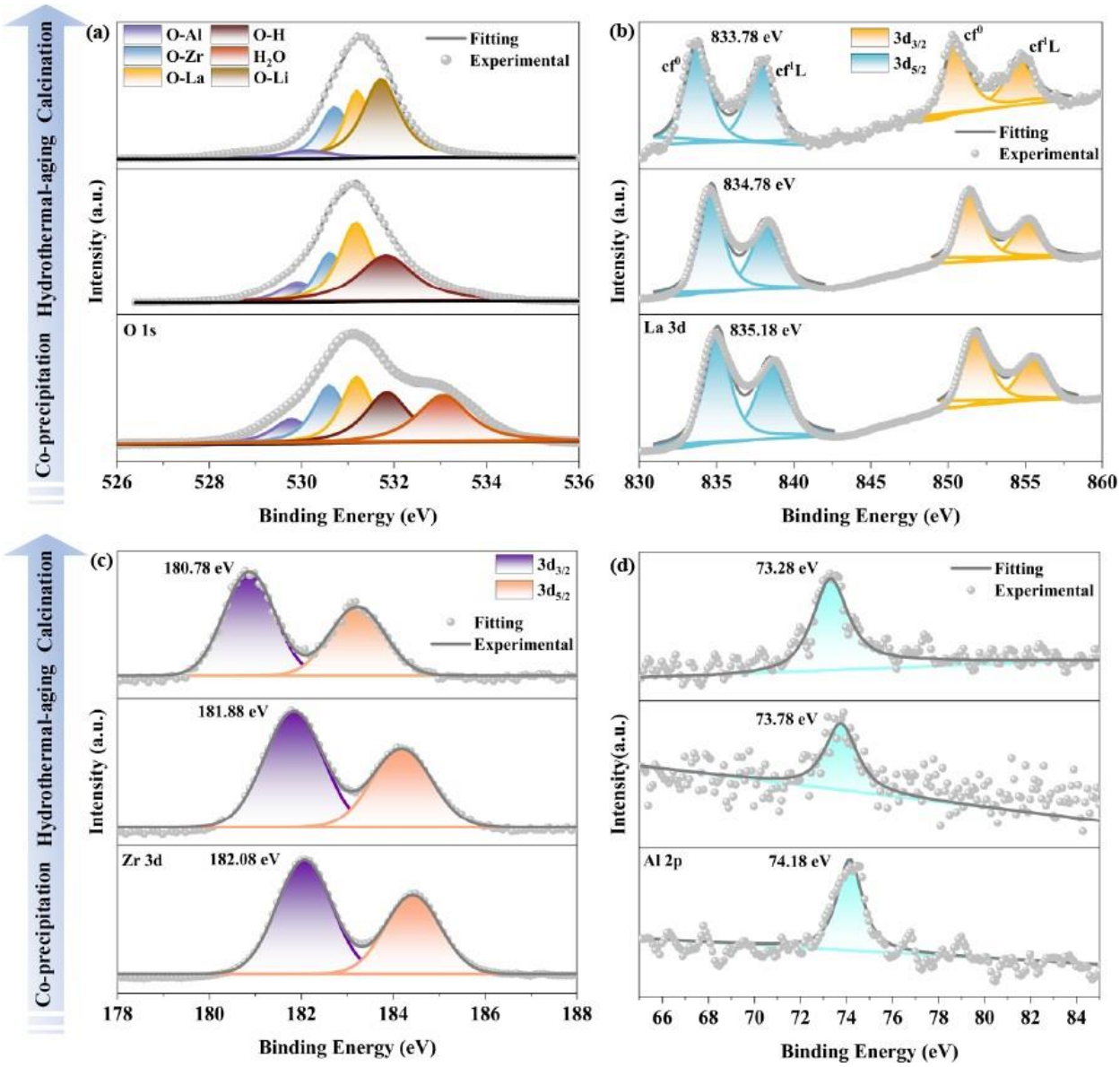

Figure 4. 5. Synthesis mechanism analysis: X-ray photoelectron spectra. (a) O 1s, (b) La 3d, (c) Zr 3d, (d) Al 2p spectra of the products collected from the three synthesis steps, co-precipitation (bottom), hydrothermal aging (middle), and calcination (top).

The XRD patterns of the calcined powders of as-synthesized c-Al-LLZO under different pH values obtained from calcination at 600 ℃ for 6 h are presented in Fig. 4.6a. Specifically, the intensity and sharpness of the XRD characteristic peaks of the product obtained at pH (7.5) are weaker than those of the other three calcined powders. Moreover, by focusing on the range of 2θ between 28 to 42 degrees (shown in Fig. 4.6b), the gradual increase in peak intensity and sharpness is noticeable, from which, it can be deduced that the crystallinity of the $La(OH)_3$ intermediate phase

has been enhanced, as indicated earlier we believe the induced growth of $La(OH)_3$ crystals by hydrothermal aging helps open the direct crystallization pathway of the cubic LLZO phase during the calcination at low temperature. Fig. 4.6d shows the representative SEM images of c-Al-LLZO powders obtained at different co-precipitation pH values. The samples show mixed morphologies of spherical shape (70 to 400 nm) and ligamentous structures. Increasing the pH led to a gradual reduction and homogenization of particle size. Specifically, the particle size distribution of the sample changes from 200 to 300 nm for the sample obtained at pH=7.5, to the range of 100 to 200 nm for the other samples. The mean size of the calcined c-Al-LLZO powders from pH = 8.5 to 10.5 were 190 to 180 nm, respectively. Thus, nearly nanoscale c-Al-LLZO phase can be obtained through the new synthesis method thanks to hydrothermal aging-enabling crystallization at a low calcination temperature of 600 ℃. This is one order reduction in particle size of c-LLZO from 2-5 μm of the powders obtained from calcination at 1000 ℃ with the same synthesis process (presented in Fig. A.1.11 a-c) and in other published works [44,45]. To verify the nano-grained structure of the as-synthesized c-Al-LLZO (pH 10.5) product, the Scherrer equation was employed determining the size of the primary crystal grains to be 29.4 nm (see Appendixes: A.1. equation 1 and the calculation data in Table A.1.1).

The Rietveld-refined XRD profile of the c-Al-LLZO (pH 10.5) sample displays the full matching with the cubic garnet structure (Space group: $Ia\bar{3}d$) as shown in Fig. 4.6c. Lattice parameters of c-Al-LLZO (10.5) are refined to be a = b = c = 13.08 Å which are a little bit larger compared to previously reported values (12.80 to 13.02 Å) [46,53-58] as presented in Fig. A.1.12. In Fig. 6f and 4.6g, the HRTEM image and selected area electron diffraction (SAED) pattern reveals that the as-synthesized c-Al-LLZO (10.5) sample possesses a cubic phase (the schematic crystal structure is presented in Fig. 4.6e) and further proves that the particles are well crystallized and structurally stable. The lattice fringes of 4.56 Å and 5.27 Å are assigned to (022) and (211) planes, respectively. This result demonstrated that the pure cubic phase of the c-Al-LLZO (10.5) sample was obtained. The elemental distribution mappings as shown in Fig. 4.6h (e-i) reveal a homogeneous elemental distribution of Al, La, Zr, and O in c-Al-LLZO (10.5) material.

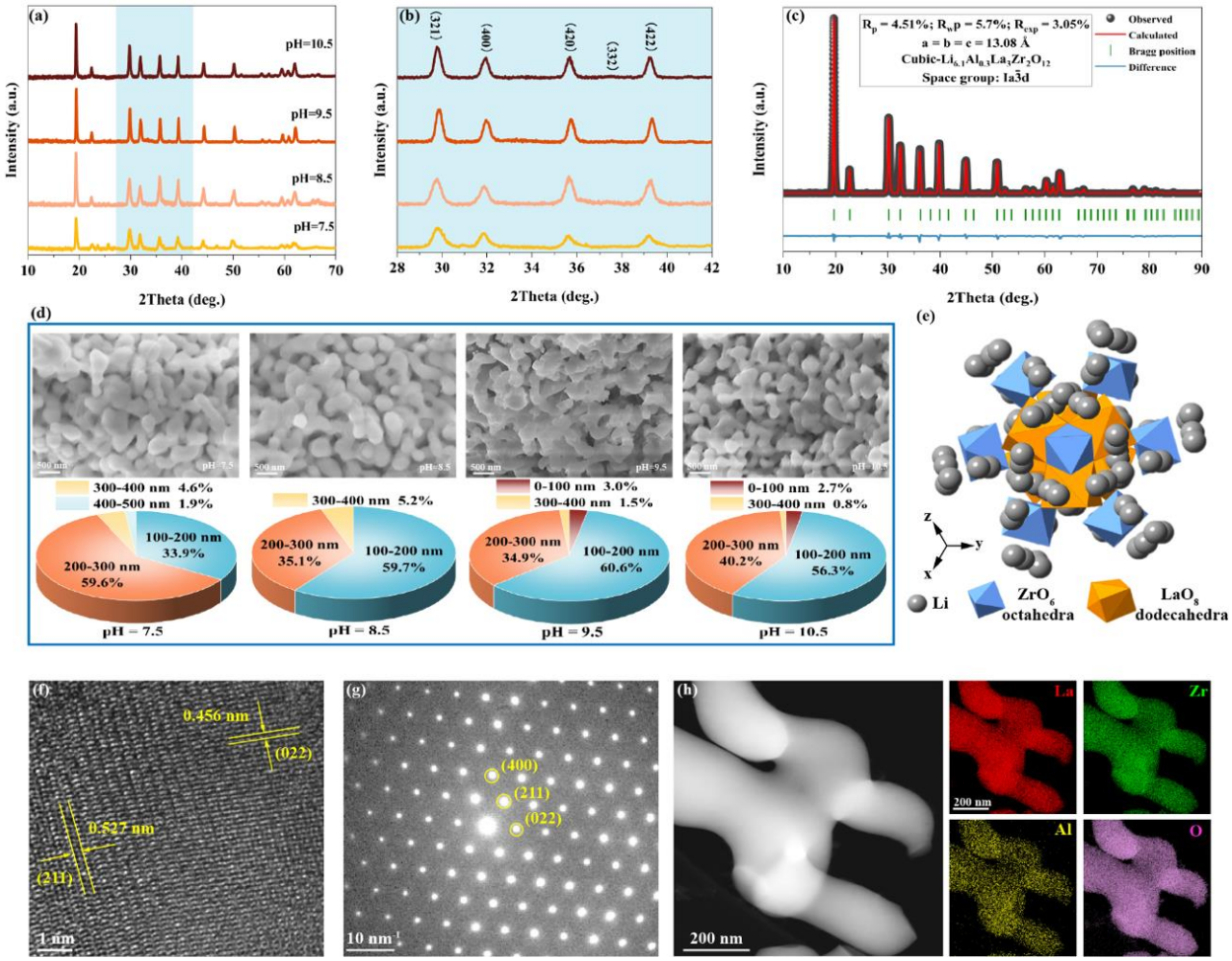

Figure 4. 6. Structure and morphology characterization. (a) X-ray diffractograms, (b) the magnification pattern of 2 theta from 28° to 42°, (c) Rietveld refinement on XRD pattern of the as-synthesized c-Al-LLZO (pH 10.5) particles; (d) the scanning electron micrographs and particle size distribution of c-Al-LLZO samples obtained at various pH values; (e) the schematic crystal structure of cubic LLZO phase; (f and g) SAED patterns and lattice fringe obtained along [001] direction; (h) TEM images and the corresponding elemental mappings of La, Zr, Al, and O, respectively.

4.3.3. Electrochemical performance

The Li-ion conductivity performance of the as-synthesized c-Al-LLZO at different pH values (7.5, 8.5, 9.5, and 10.5) measured at 21 ℃ (room temperature) is shown in Fig. 4.7a. The frequency-dependent data is quantitatively analyzed by AC impedance. A suitable equivalent circuit (Fig. 4.7b) using individual resistances and constant phase elements (CPEs) was employed to manifest the bulk and grain boundary responses. The impedance plot of c-Al-LLZO (pH 10.5) sample with fitting data is shown in Fig. 4.7b. As the pH value of the co-precipitation step increase, the

resistance reaches a minimum value of 320.4 Ω at 21 ℃ in the c-Al-LLZO (10.5) sample. As shown in insets in Fig. 4.7b, the nanoscale particles after sintering are fused into large blocks but with more homogeneous size distribution compared to the pellet obtained from the microscale c-Al-LLZO powders (calcined at 1000 ℃) as shown in Fig. A.1.11d, producing high pellet density with fewer grain boundaries. It is attributed to high relative density (~98%) as shown in Fig. 4.7e, which contributes to providing continuous Li^+ pathways. The Li-ion conductivity (calculated through equation 2 in Appendixes: A.1.) reached 0.42 $mS \cdot cm^{-1}$ at 21 ℃ (room temperature). The Nyquist plots of different c-Al-LLZO pellets measured at room temperature (21 ℃) as well as from 30 to 80 ℃ are presented in Fig. A.1.13, while the corresponding Electrochemical Impedance Spectroscopy (EIS) data are presented in Table A.1.2. The temperature dependence of the total ionic conductivity (Arrhenius plot-see equation 3 in Appendixes: A.1.) of as-synthesized c-Al-LLZO electrolytes from 21 to 80 ℃ is shown in Fig. 4.7c and 4.7d. As the pH of co-precipitation step increases, the activation energy decreases and reaches the minimum value of 0.174 eV for the c-Al-LLZO obtained at pH (10.5) corresponding to the highest ionic conductivity at 21 ℃. The decrease of the magnitude of activation energy E_a reflects an increase in lithium ionic conductivity. The lowest activation energy reported here is lower than other published data (the lowest one is 0.24 eV [47]), which may be attributed to two main reasons: one is the lattice parameter expansion of the as-synthesized c-Al-LLZO garnet, which enhances the lithium-ion transport within the cubic structure making it easier for Li^+ hopping between sites. The other reason is the nanograined structure of the as-synthesized c-Al-LLZO particles, which after compression and sintering, fuse into larger blocks with less grain boundary resistance (improved relative density). The comparison of the activation energies of the total lithium-ion conductivity of the c-Al-LLZO electrolytes with published results [47-52] is shown in Fig. 4.7f, demonstrating that the newly synthesized c-Al-LLZO garnet possesses better ionic conductivity and activation energy, and these properties are achieved remarkably at the lowest yet calcination temperature (600 ℃ for 6h).

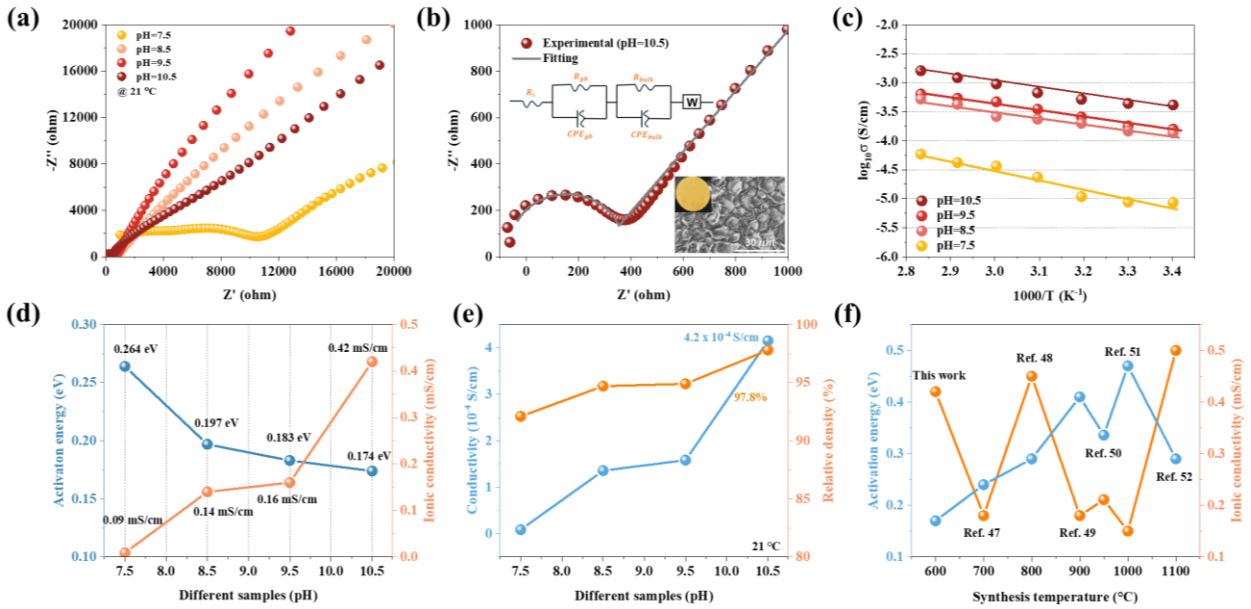

Figure 4. 7. The ionic conductivities of the as-synthesized c-Al-LLZO electrolytes: (a) the Nyquist plots of c-Al-LLZO samples synthesized at different pH (7.5, 8.5, 9.5, and 10.5) measured at 21 ℃ (room temperature); (b) the Nyquist plot of the as-synthesized c-Al-LLZO (pH 10.5) sample at the high-frequency region with fitting data and corresponding equivalent circuit, SEM image and a digital image of the sintered pellet (pH 10.5); (c) Arrhenius plots for the as-synthesized c-Al-LLZO samples; (d) a summary of ionic conductivities and activation energies; (e) relative densities of c-Al-LLZO sintered pellets and corresponding ionic conductivities; (f) comparison of ionic conductivity and activation energy with published results [47-52].

To evaluate the interfacial stability of the as-synthesized c-Al-LLZO with metallic lithium foil the electrochemical reversibility of Li plating and stripping across the interface, and critical current density, symmetric cells were prepared as the schematic presented in Fig. 4.8c. As shown in Fig. 4.8a and 4.8b, there is no pronounced voltage polarization of Li transport over 400 h cycling at a current density of 0.2 mA/cm^2, and over 200 h at a current density of 0.5 mA/cm^2 demonstrating excellent Li^+ transfer capability across the Li/c-Al-LLZO interface. A suitable equivalent circuit employing individual resistances and constant phase elements (CPEs) is used to address the EIS curves, as presented in Fig. 4.8d. Here, $R_{c\text{-}Al\text{-}LLZO}$ represents the total resistance of c-Al-LLZO solid electrolyte, $R_{interface}$ represents the resistance between c-Al-LLZO and Li metal, and $R_{electrode}$ represents the Li electrode. $CPE_{interface}$ and $CPE_{electrode}$ correspond to the constant phase elements mentioned above. The Nyquist plots of the symmetric cell before and after plating/stripping cycling at 0.5 mA/cm^2 for 200h are shown in Fig. 4.8d, indicating good stability between c-Al-LLZO and Li metal. Moreover, the images of the as-prepared c-Al-LLZO pellets' surface

morphology are inserted, exhibiting excellent stability against Li metal. Critical current density (CCD) is determined by the maximum current density of Li/c-Al-LLZO/Li symmetric cells before lithium dendrite growth occurs in solid electrolytes. Here, CCD is used to evaluate the dendrite suppression capability of c-Al-LLZO. In Fig. 4.8e, as the current increases from 0.15 mA, the voltage rises linearly until the current reaches 2.25 mA, corresponding to the current density of 2.16 mA/cm^2 at 25 ℃. This performance is attributed to the nanograined nature of the as-synthesized c-Al-LLZO particles that facilitates formation of dense structure with fewer grain boundaries yielding strengthened interfacial stability and good capability of lithium dendrite suppression.

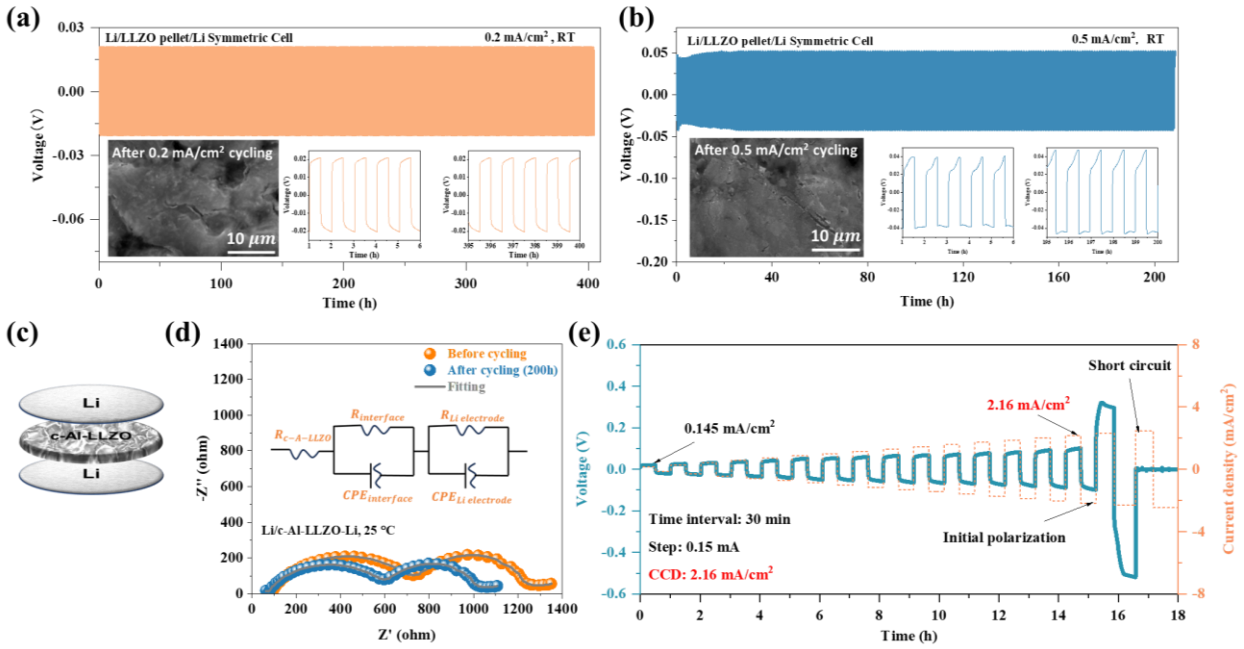

Figure 4. 8. The electrochemical performance of the symmetric cells Li/c-Al-LLZO (pH 10.5)/Li: (a and b) Li plating and stripping cycling at 0.2 and 0.5 mA/cm^2 and SEM images of cycled pellets; (c) the schematic of symmetric cell; (d) the Nyquist plots of symmetric cell before and after plating/stripping at 0.5 mA/cm^2 for 200h, and the corresponding equivalent circuit; (e) CCD test by galvanostatic cycling from 0.145 to 2.16 mA/cm^2 with a duration of 30 min for each charge/discharge process.

4.4. Conclusion

Nanoscale garnet-type cubic-Al-LLZO solid electrolyte with high Li-ion conductivity and low activation energy was successfully synthesized through a novel crystallization pathway enabled by hydrothermal $La(OH)_3$ intermediate nanocrystals in an amorphous $Zr(OH)_4$ matrix and their

calcination at only 600 ℃. The crystallization process consists of three steps: co-precipitation, hydrothermal aging, and calcination. The pH of co-precipitation step proved to be critical (optimum pH=10.5) as is the hydrothermal step in avoiding the intermediate formation of tetragonal phase hence allowing the lowering of the calcination temperature down to 600 ℃. The as-synthesized nanoscale c-Al-LLZO solid electrolyte particles with 180 nm average size were found to promote dense structure (with a relative density of 97.8%) upon compaction and sintering with fewer grain boundaries leading to high Li-ion conductivity of 0.42 $mS \cdot cm^{-1}$ at 21 ℃ and lower activation energy of 0.174 eV. Symmetric cells built with sintered pellets of the new breed of c-Al-LLZO electrolyte are characterized by very good Li plating and stripping cycling stability when tested at the high current density of 0.2 and 0.5 mA/cm^2. And the high critical current density (CCD) of 2.16 mA/cm^2 demonstrates good capability of lithium dendrites suppression.

This novel low-temperature synthesis strategy in producing nanoscale garnet-type LLZO with high Li-ion conductivity provides new possibilities for building not only dense ceramic electrolyte films but also composite cathodes for all-solid-state lithium batteries.

4.6. Reference

[1] J. B. Goodenough; K. S. Park, The Li-ion rechargeable battery: a perspective. *J. Am. Chem. Soc.* **2013**, *135* (4), 1167-1176. https://doi.org/10.1021/ja3091438

[2] M. Li; J. Lu; Z. Chen; K. Amine, 30 years of lithium-ion batteries. *Adv. Mater.* **2018**, *30* (33) 1800561. https://doi.org/10.1002/adma.201800561

[3] A. Masias; J. Marcicki; W. A. Paxton, Opportunities and challenges of lithium ion batteries in automotive applications. *ACS Energy Lett.* **2021**, *6* (2), 621-630. https://doi.org/10.1021/acsenergylett.0c02584

[4] J. Janek; W. G. Zeier, A solid future for battery development. *Nat. Energy* **2016**, *1* 16141. https://doi.org/10.1038/nenergy.2016.141

[5] X. Ji; K. T. Lee; L. F. Nazar, A highly ordered nanostructured carbon-sulphur cathode for lithium-sulphur batteries. *Nat. Mater.* **2009**, *8* (6), 500-506. https://doi.org/10.1038/nmat2460

[6] A. Semih; W. Michael; N. Reinhard; A lithium-rich compound $Li_7Mn(BO_3)_3$ containing Mn^{2+} in tetrahedral coordination: a cathode candidate for lithium-ion batteries. *Angew. Chem. Int. Ed.* **2013**, *125*, 12773-12776. https://doi.org/10.1002/ange.201307655

[7] S. Afyon; F. Krumeich; C. Mensing; A. Borgschulte; R. Nesper, New high capacity cathode materials for rechargeable Li-ion batteries: vanadate-borate glasses. *Sci. Rep*. **2014**, *4*, 7113. https://doi.org/10.1038/srep07113

[8] A. Jana; S. I. Woo; K. S. N. Vikrant; R. E. García, Electrochemomechanics of lithium dendrite growth. *Energy & Environ. Sci.* **2019**, *12* (12), 3595-3607. DOI: 10.1039/C9EE01864F

[9] J. Chen; J. Wu; X. Wang; A. Zhou; Z. Yang, Research progress and application prospect of solid-state electrolytes in commercial lithium-ion power batteries. *Energy Stor. Mater.* **2021**, *35*, 70-87. https://doi.org/10.1016/j.ensm.2020.11.017

[10] B. Zhang; R. Tan; L. Yang; J. Zheng; K. Zhang; S. Mo; Z. Lin; F. Pan, Mechanisms and properties of ion-transport in inorganic solid electrolytes. *Energy Stor. Mater.* **2018**, *10*, 139-159. https://doi.org/10.1016/j.ensm.2017.08.015

[11] H. Liu; X. Cheng; J. Huang; H. Yuan; Y. Lu; C. Yan; G. Zhu; R. Xu; C. Zhao; L. Hou; C. He; S. Kaskel; Q. Zhang, Controlling dendrite growth in solid-state electrolytes. *ACS Energy Lett.* **2020**, *5* (3), 833-843. https://doi.org/10.1021/acsenergylett.9b02660

[12] Y. Chen; Y. Jiang; S. Chi; H. J. Woo; K. Yu; J. Ma; J. Wang; C. Wang; Y. Deng, Understanding the lithium dendrites growth in garnet-based solid-state lithium metal batteries. *J. Power Sources* **2022**, *521*, 230921. https://doi.org/10.1016/j.jpowsour.2021.230921

[13] L. Xu; J. Li; W. Deng; H. Shuai; S. Li; Z. Xu; J. Li; H. Hou; H. Peng; G. Zou; X. Ji, Garnet solid electrolyte for advanced all-solid-state Li batteries. *Adv. Energy Mater.* **2020**, *11* (2), 2000648. https://doi.org/10.1002/aenm.202000648

[14] T. Krauskopf; R. Dippel; H. Hartmann; K. Peppler; B. Mogwitz; F. H. Richter; W. G. Zeier; J. Janek, Lithium-metal growth kinetics on LLZO garnet-type solid electrolytes. *Joule* **2019**, *3* (8), 2030-2049. https://doi.org/10.1016/j.joule.2019.06.013

[15] J. Awaka; N. Kijima; H. Hayakawa; J. Akimoto, Synthesis and structure analysis of tetragonal $Li_7La_3Zr_2O_{12}$ with the garnet-related type structure. *J. Solid State Chem.* **2009**, *182* (8), 2046-2052. https://doi.org/10.1016/j.jssc.2009.05.020

[16] J. Awaka; A. Takashima; K. Kataoka; N. Kijima; Y. Idemoto; J. Akimoto, Crystal structure of fast lithium-ion-conducting cubic $Li_7La_3Zr_2O_{12}$. *Chem. Lett.* **2011**, *40* (1), 60-62. https://doi.org/10.1246/cl.2011.60

[17] E. Rangasamy; J. Wolfenstine; J. Sakamoto, The role of Al and Li concentration on the formation of cubic garnet solid electrolyte of nominal composition $Li_7La_3Zr_2O_{12}$. *Solid State Ion.* **2012**, *206*, 28-32. https://doi.org/10.1016/j.ssi.2011.10.022

[18] C. Li; Y. Liu; J. He; K. S. Brinkman, Ga-substituted $Li_7La_3Zr_2O_{12}$: An investigation based on grain coarsening in garnet-type lithium ion conductors. *J. Alloys Compd.* **2017**, *695*, 3744-3752. https://doi.org/10.1016/j.jallcom.2016.11.277

[19] A. Gupta; R. Murugan; M. P. Paranthaman; Z. Bi; C. A. Bridges; M. Nakanishi; A. P. Sokolov; K. S. Han; E. W. Hagaman; H. Xie; C. B. Mullins; J. B. Goodenough, Optimum lithium-ion conductivity in cubic $Li_{7-x}La_3Hf_{2-x}Ta_xO_{12}$. *J. Power Sources* **2012**, *209*, 184-188. https://doi.org/10.1016/j.jpowsour.2012.02.099

[20] S. Ohta; T. Kobayashi; T. Asaoka, High lithium ionic conductivity in the garnet-type oxide $Li_{7-x}La_3(Zr_{2-x}, Nb_x)O_{12}$ (x=0 - 2). *J. Power Sources* **2011**, *196* (6), 3342-3345. https://doi.org/10.1016/j.jpowsour.2010.11.089

[21] L. J. Miara; W. D. Richards; Y. E. Wang; G. Ceder, First-principles studies on cation dopants and electrolyte|cathode interphases for lithium garnets. *Chem. Mater.* **2015**, *27* (11), 4040-4047. https://doi.org/10.1021/acs.chemmater.5b01023

[22] R. Murugan; V. Thangadurai; W. Weppner, Fast lithium ion conduction in garnet-type $Li_7La_3Zr_2O_{12}$. *Angew. Chem. Int. Ed. Engl.* **2007**, *46* (41), 7778-7781. https://doi.org/10.1002/anie.200701144

[23] C. Deviannapoorani; S. Ramakumar; N. Janani; R. Murugan, Synthesis of lithium garnets from $La_2Zr_2O_7$ pyrochlore. *Solid State Ion.* **2015**, *283*, 123-130. https://doi.org/10.1016/j.ssi.2015.10.006

[24] B. Xu; H. Duan; W. Xia; Y. Guo; H. Kang; H. Li; H, Liu, Multistep sintering to sinthesize fast lithium garnets. *J. Power Sources* **2016**, *302*, 291-297. https://doi.org/10.1016/j.jpowsour.2015.10.084

[25] H. Zheng; G. Li; J. Liu; S. Wu; X. Zhang; Y. Wu; H. Zhu; X. Huang; H. Liu; H. Duan, A rational design of garnet-type $Li_7La_3Zr_2O_{12}$ with ultrahigh moisture stability. *Energy Storage Mater.* **2022**, *49*, 278-290. https://doi.org/10.1016/j.ensm.2022.04.027

[26] I. Kokal; M. Somer; P. H. L. Notten; H. T. Hintzen, Sol–gel synthesis and lithium ion conductivity of $Li_7La_3Zr_2O_{12}$ with garnet-related type structure. *Solid State Ion.* **2011**, *185* (1), 42-46. https://doi.org/10.1016/j.ssi.2011.01.002

[27] N. Janani; C. Deviannapoorani; L. Dhivya; R. Murugan, Influence of sintering additives on densification and Li^+ conductivity of Al doped Sol–gel synthesis and lithium ion conductivity of $Li_7La_3Zr_2O_{12}$ with garnet-related type structure. lithium garnet. *RSC Adv.* **2014**, *4* (93), 51228-51238. DOI: 10.1039/C4RA08674K

[28] Y. Shimonishi; A. Toda; T. Zhang; A. Hirano; N. Imanishi; O. Yamamoto; Y. Takeda, Synthesis of garnet-type $Li_{7-x}La_3Zr_2O_{12-1/2x}$ and its stability in aqueous solutions. *Solid State Ion.* **2011**, *183* (1), 48-53. https://doi.org/10.1016/j.ssi.2010.12.010

[29] T. Ryohei; T. Kiyoharu; H. Akitoshi; T. Masahiro, Low temperature synthesis of Al-doped $Li_7La_3Zr_2O_{12}$ solid electrolyte by a sol-gel process. *Solid State Ion.* **2014**, *255*, 104-107. https://doi.org/10.1016/j.ssi.2013.12.006

[30] M. Balaish; J. C. Gonzalez-Rosillo; K. J. Kim; Y. Zhu; Z. D. Hood; J. L. M. Rupp, Processing thin but robust electrolytes for solid-state batteries. *Nat. Energy* **2021**, *6* (3), 227-239. https://doi.org/10.1038/s41560-020-00759-5

[31] K.V. Kravchyk; D.T. Karabay; M.V. Kovalenko; On the feasibility of all-solid-state batteries with LLZO as a single electrolyte. *Sci. Rep.*, **2022**, *12*, 1177. https://doi.org/10.1038/s41598-022-05141-x

[32] Y. Ren; T. Danner; A. Moy; M. Finsterbusch; T. Hamann; J. Dippell; T. Fuchs; M. Müller; R. Hoft; A. Weber; L. A. Curtiss; P. Zapol; M. Klenk; A. T. Ngo; P. Barai; B. C. Wood; R. Shi; L. Wan; T. W. Heo; M. Engels; J. Nanda; F. H. Richter; A. Latz; V. Srinivasan; J. Janek; J.

Sakamoto; E. D. Wachsman; D. Fattakhova-Rohlfing, Oxide-Based Solid-State Batteries: A Perspective on Composite Cathode Architecture. *Adv. Energy Mater.* **2023**, *13*, 2201939. https://doi.org/10.1002/aenm.202201939

[33] J. Awaka; N. Kijima; Y. Takahashi; H. Hayakawa; J. Akimoto, Synthesis and crystallographic studies of garnet-related lithium-ion conductors $Li_6CaLa_2Ta_2O_{12}$ and $Li_6BaLa_2Ta_2O_{12}$. *Solid State Ion.* **2009**, *180* (6-8), 602-606. https://doi.org/10.1016/j.ssi.2008.10.022

[34] H. Xie; Y. Li; J. Han; Y. Dong; M. P. Paranthaman; L. Wang; M. Xu; A. Gupta; Z. Bi; C. A. Bridges; M. Nakanishi; A. P. Sokolov; J. B. Goodenough, $Li_6La_3SnMO_{12}$(M= Sb, Nb, Ta), a family of lithium garnets with high Li-ion conductivity. *J. Electrochem. Soc.* **2012**, *159* (8), A1148-A1151. **DOI:** 10.1149/2.009208jes

[35] R. Murugan; V. Thangadurai; W. Weppner, Effect of lithium-ion content on the lithium ion conductivity of the garnet-like structure $Li_{5+x}BaLa_2Ta_2O_{11.5+0.5x}$ (x = 0-2). *Appl. Phys. A* **2008**, *91* (4), 615-620. https://doi.org/10.1007/s00339-008-4494-2

[36] B. Dong; L. L. Driscoll; M. P. Stockham; E. Kendrick; P. R. Slater, Low temperature synthesis of garnet solid state electrolytes: Implications on aluminium incorporation in $Li_7La_3Zr_2O_{12}$. *Solid State Ion.* **2020**, *350*, 115317. https://doi.org/10.1016/j.ssi.2020.115317

[37] Z. Qin; X. Meng; Y. Xie; D. Qian; H. Deng; D. Mao; L. Wan; Y. Huang, Fast Li-ion transport pathways via 3D continuous networks in homogeneous garnet-type electrolyte for solid-state lithium batteries. *Energy Stor. Mater.* **2021**, *43*, 190-201. https://doi.org/10.1016/j.ensm.2021.09.005

[38] S. Afyon; F. Krumeich; J. L. M. Rupp, A shortcut to garnet-type fast Li-ion conductors for all-solid-state batteries. *J. Mater. Chem. A* **2015**, *3* (36), 18636-18648. DOI: 10.1039/C5TA03239C

[39] M. F. Sunding; K. Hadidi; S. Diplas; O. M. Løvvik; T. E. Norby; A. E. Gunnæs, XPS characterisation of in situ treated lanthanum oxide and hydroxide using tailored charge referencing and peak fitting procedures. *J. Electron Spectrosc. Relat. Phenom.* **2011**, *184* (7), 399-409. https://doi.org/10.1016/j.elspec.2011.04.002

[40] B. Ding; C. Han; L. Zheng; J. Zhang; R. Wang; Z. Tang, Tuning oxygen vacancy photoluminescence in monoclinic Y_2WO_6 by selectively occupying yttrium sites using lanthanum. *Sci. Rep.* **2015**, *5*, 9443. https://doi.org/10.1038/srep09443

[41] H. Qiu; C. Liang; J. Yu; Q. Zhang; M. Song; F. Chen, Preferable phosphate sequestration by nano-La(III) (hydr)oxides modified wheat straw with excellent properties in regeneration. *J. Chem. Eng.* **2017**, *315*, 345-354. https://doi.org/10.1016/j.cej.2017.01.043

[42] M. Mallet; K. Barthelemy; C. Ruby; A. Renard; S. Naille, Investigation of phosphate adsorption onto ferrihydrite by X-ray photoelectron spectroscopy. *J. Colloid Interface Sci.* **2013**, *407*, 95-101. https://doi.org/10.1016/j.jcis.2013.06.049

[43] L. Zhang; Y. Liu; Y. Wang; X. Li; Y. Wang, Investigation of phosphate removal mechanisms by a lanthanum hydroxide adsorbent using p-XRD, FTIR and XPS. *Appl. Surf. Sci.* **2021**, *557*, 149838. https://doi.org/10.1016/j.apsusc.2021.149838

[44] P. J. Kumar; K. Nishimura; M. Senna; A. Duvel; P. Heitjans; T. Kawaguchi; N. Sakamoto; N. Wakiya; H. Suzuki, A novel low-temperature solid-state route for nanostructured cubic garnet $Li_7La_3Zr_2O_{12}$ and its application to Li-ion battery. *RCS adv.* **2016**, *6* (67), 62656-62667. DOI: 10.1039/C6RA09695F

[45] L. Xu; G. Li; J. Guan; L. Wang; J. Chen; J. Zheng, Garnet-doped composite polymer electrolyte with high ionic conductivity for dendrite-free lithium batteries. *J. Energy Storage* **2019**, *24*, 100767. https://doi.org/10.1016/j.est.2019.100767

[46] R. Murugan; W. Weppner; P. Schmid-Beurmann; V. Thangadurai, Structure and lithium ion conductivity of bismuth containing lithium garnets $Li_5La_3Bi_2O_{12}$ and $Li_6SrLa_2Bi_2O_{12}$. *Mater. Sci. Eng. B* **2007**, *143* (1-3), 14-20. https://doi.org/10.1016/j.mseb.2007.07.009

[47] V. Avila; B. Yoon; S. Ghose; R. Raj; L. M. Jesus, Phase evolution during reactive flash sintering of $Li_{6.25}Al_{0.25}La_3Zr_2O_{12}$ starting from a chemically prepared powder. *J. Eur. Ceram. Soc.* **2021**, *41* (8), 4552-4557. https://doi.org/10.1016/j.jeurceramsoc.2021.02.054

[48] P. Badami; S. Smetaczek; A. Limbeck; D. Rettenwander; C. K. Chan; A. N. M. Kannan, Facile synthesis of Al-stabilized lithium garnets by a solution-combustion technique for all solid-state batteries. *Mater. Adv.* **2021**, *2* (15), 5181-5188. DOI: 10.1039/D1MA00393C

[49] C. Chen; Y. Sun; L. He; M. Kotobuki; E. Hanc; Y. Chen; K. Zeng; L. Lu, Microstructural and electrochemical properties of Al- and Ga-Doped $Li_7La_3Zr_2O_{12}$ garnet solid electrolytes. *ACS Appl. Energy Mater.* **2020**, *3* (5), 4708-4719. https://doi.org/10.1021/acsaem.0c00347

[50] Z. Hu; H. Liu; H. Ruan; R. Hu; Y. Su; L. Zhang, High Li-ion conductivity of Al-doped $Li_7La_3Zr_2O_{12}$ synthesized by solid-state reaction. *Ceram. Int.* **2016**, *42* (10), 12156-12160. https://doi.org/10.1016/j.ceramint.2016.04.149

[51] K. Masashi; K. Masaki, Preparation of $Li_7La_3Zr_2O_{12}$ solid electrolyte via a sol-gel method. *Ceram. Int.* **2014**, *40* (10), 5043-5047. https://doi.org/10.1016/j.ceramint.2013.09.009

[52] L. Cheng; J. S. Park; H. Hou; V. Zorba; G. Chen; T. Richardson; J. Cabana; R. Russo; M. Doeff, Effect of microstructure and surface impurity segregation on the electrical and electrochemical properties of dense Al-substituted $Li_7La_3Zr_2O_{12}$. *J. Mater. Chem. A* **2014**, *2* (1), 172-181. DOI: 10.1039/C3TA13999A

[53] J. C. Edumud The structure of lithium garnets: cation disorder and clustering in a new family of fast Li^+ conductors. *Chem. Commun.* **2006**, *4*, 412-413. DOI: https://doi.org/10.1039/B514640B

[54] Y. Zhang; D. Luo; W. Luo; S. Du; Y. Deng; J. Deng, High-purity and high-density cubic phase of $Li_7La_3Zr_2O_{12}$ solid electrolytes by controlling surface/volume ratio and sintering pressure. *Electrochimica Acta* **2020**, *359*, 136965. https://doi.org/10.1016/j.electacta.2020.136965

[55] A. Stefan; P. R. Rayavarapu, Ion transport and phase transition in $Li_{7-x}La_3(Zr_{2-x}M_x)O_{12}$ (M = Ta^{5+}, Nb^{5+}, x = 0, 0.25). *J. Mater. Chem.* **2013**, *22*, 1426-1434. DOI: 10.1039/C1JM14588F

[56] M. Xu; M. S. Park; J. M. Lee; T. Y. Kim; Y. S. Park; E. Ma, Mechanisms of Li^+ transport in garnet-type cubic $Li_{3+x}La_3M_2O_{12}$ (M = Te, Nb, Zr). *Phys. Rev. B* **2012**, *85*, 052301. DOI: 10.1103/PhysRevB.85.052301

[57] Y. Kim; H. Jo; J. L. Allen; H. Choe; J. Wolfenstine; J. Sakamoto, The effect of relative density on the mechanical properties of hot-pressed cubic $Li_7La_3Zr_2O_{12}$. *J. Am. Ceram. Soc.* **2016**, *99*, (4), 1367-1374. https://doi.org/10.1111/jace.14084

[58] E. Rangasamy; J. Wolfenstine; J. Allen; J. Sakamoto, The effect of 24c-site (A) cation substitution on the tetragonal-cubic phase transition in $Li_{7-x}La_{3-x}A_xZr_2O_{12}$ garnet-based ceramic. *J. Power Sources* **2013**, *230*, 261-266. https://doi.org/10.1016/j.jpowsour.2012.12.076

Chapter 5: High-Conductive Polymer-in-Porous Garnet Solid Electrolyte Structure

Bridge: In Chapter 4, the synthesis of nanoscale cubic garnet (c-Al-LLZO) at a temperature as low as 600 ℃, which is characterized by high ionic conductivity (0.42 mS cm^{-1} at 21 ℃) and low activation energy 0.17 eV. Moreover, symmetric cells with Li metal found to exhibit excellent stability at the current density of 0.2 and 0.5 mA cm^{-2}, with a high critical density of 2.16 mA cm^{-2} demonstrating good capability for lithium dendrite suppression. Since, the conventional densified ceramic SSEs are known to have poor contact (point-to-point) with electrodes, they are necessary to be appropriately engineered to render them with highly conductive and stable interfaces with the anode (Li metal) and cathode composite. Use of a polymer solid-state electrolyte (PSE) or polymer-based hybrid SSE can form good contact (face-to-face) with electrodes. However, the poor mechanical strength and commonly bad electrochemical stability (narrow electrochemical window) of PSEs or polymer-based SSEs impede their application in ASSLBs. Under this realization, the work in Chapter 5 is focused on the development of a novel type of ceramic-based hybrid SSE with the capability of fast Li-ion migration, improved mechanical strength for suppression of lithium dendrites, and good interfacial contact (face-to-face) with electrodes. More specifically, in this chapter the 2nd objective of the thesis is addressed, i.e. the design of a porous ceramic-based hybrid solid-state electrolyte, using the cubic garnet SSE material synthesized in Chapter 4 and the ionic conductive polymer PEO-LiTFSI. The new HSE thanks to molecular bonding of PEO-LiTFSI on the interior pore and external surface of the garnet (c-Al-LLZO) scaffold provides high ionic conductivity, good chemical/electrochemical stability, high mechanical strength, as well as low interfacial resistance against both cathode and Li metal.

This chapter is replication of a manuscript under peer review process in *Energy Storage Materials,* with the following citation:

Senhao Wang and George P. Demopoulos. 2024. “High-Conductive Polymer-in-Porous Garnet Solid Electrolyte Structure for All-Solid-State Lithium Batteries Enabled by Molecular Engineering” (submitted).

Abstract

The ceramic-based hybrid solid electrolytes (HSEs) represent excellent promise for application in next generation all-solid-state lithium metal batteries (ASSBs) due to their fast Li-ion migration, high mechanical strength, and good interfacial stability with electrodes. Herein, a novel HSE structure is designed featuring a polymer-infiltrated porous ceramic cubic $Li_{6.1}Al_{0.3}La_3Zr_2O_{12}$ (c-LLZO) scaffold fabricated by an integrated sintering method. The HSE structure exhibits high intrinsic ionic conductivity as well as good mechanical strength with even distribution of the polymer phase (LiTFSI-doped PEO) within the network of open pores resulting in uniform Li-ion migration flux. The infiltrated polymer solid electrolyte (PSE) forms strong molecular bonding on the interior and exterior surface of the ceramic skeleton via La-N bonds effectively lowering the interfacial impedance between two phases. Moreover, this continuous two-phase interface provides a fast pathway for Li-ion transport. Thus, the as-designed ceramic-based HSE demonstrates high Li-ion transference number (0.71) and ionic conductivity (0.547 mS cm^{-1}) at 25 ℃. The ASSBs (Li/HSE/LFP) enabled by the ceramic-based HSEs exhibit high discharge specific capacities of 163 mAh g^{-1} at 0.1 C and average coulombic efficiency greater than 99 % after 50 cycles. This novel design opens new possibilities in our pursuit for next generation high-performance ASSBs.

5.1. Introduction

Li-ion batteries (LIBs) after the ushering of the mobile electronic device era, they are now propeling the proliferation of electric vehicles (EVs), drawing attention to the need for enhanced safety and energy density.[1] Lithium metal, with its high gravimetric capacity (3869 mAh g^{-1}), the lowest reduction potential (-3.04 V vs. SHE), and low density (0.534 g cm^{-3}), could greatly boost specific energy and energy density.[2] However, safety issues prevent its use in commercial batteries, due to the risk of lithium deposition and cell shorting caused by Li-dendrites in conventional batteries with flammable liquid electrolytes.[3] All-solid-state batteries (ASSBs) - in particular those based on ceramic electrolytes - are considered a potential solution for the aforementioned issues due to their high energy density and high safety when coupled with a Li metal anode.[4] As the core component in ASSBs, solid electrolytes (SEs), hold the merits of inflammability, non-leakage, and high Young's modulus, to address the long-standing challenges of liquid electrolyte Li-ion batteries.[5]

Significant efforts have been devoted to developing SEs with high electrochemical performance. Among them, the cubic garnet-type oxide (cubic $Li_7La_3Zr_2O_{12}$) is a promising SE because of its high electrochemical stability, good chemical stability in the air, excellent mechanical strength, and relatively high room temperature (RT) conductivity of nearly 1 mS cm^{-1}. Particularly, cubic garnet SEs possess excellent chemical/electrochemical stability against the Li metal anode. These prominent advantages have made the cubic garnet strong candidate in commercial applications.[6] However, the large interfacial resistance caused by their poor interfacial matching with electrodes is a major hurdle to their further application in ASSBs.[7] Meanwhile, among various types of SEs, polymer solid electrolytes (PSEs) have been widely studied because of their advantages, such as good interfacial wettability with electrodes, good filming property, and mechanical flexibility.[8] Despite these advantages, the low Li-ion conductivity, especially at RT (usually lower than 10^{-6} S cm^{-1}) limits their actual application at only high temperatures becoming a serious fire hazard.[9]

Combining ceramic and polymer electrolytes into composites, utilizing their advantages, and addressing their drawbacks, is a promising approach to solving these problems. Hybrid polymer-based SEs with ceramic fillers in the polymer matrix, are known to reduce the polymer's crystallinity and weaken the interactions between lithium ions and polymer chains, increasing Li-ion conductivity.[10] Unfortunately, the fillers' propencity to aggregate, on the other hand, limits their effectiveness for Lewis acid-base interaction, and the resulting ionic conductivity is insufficient from a battery kinetic point of view.[11] Furthermore, the fillers do not successfully form an interconnected reinforcement to improve the mechanical properties of the composites while the increased filler content may also reduce the mechanical strength of the composite electrolytes.[12] Ionic conductivity and mechanical properties are insufficient to fulfill commercial requirements. Nan et al. utilized the catalysis of La in dehydrofluorination and prepared poly(vinylidenefluoride) (PVDF)–$Li_{6.75}La_3Zr_{1.75}Ta_{0.25}O_{12}$(LLZTO) Hybrid SE whose ionic conductivity is as high as 5×10^{-4} S cm^{-1} at 25 °C, but still with polymer matrix.[13] In addition, suppression of the Li dendrite growth can be obtained through modifying the morphology of the fillers resulting in homogeneousl Li-ion migration and deposition. Ci et al. synthesized a sheet-like garnet SE and prepared the hybrid SE with introducing sheet-like garnet in Poly(ethylene oxide) (PEO) polymer matrix, which improved the interfacial stability against Li metal. But the mechanical strength and safety issues caused by the polymer matrix still remain serious limitations.[14] Another approach is to add plasticizers to Li salt/polymer blends to boost

ionic conductivity to feasible levels, however, this sacrifices rigidity and increases flammability.[15] A third recent technique blends polymer electrolytes with inorganic ion conductors, although mechanical criteria have yet to be reached despite progress in demonstrating enhanced ionic conductivity.[16] In reality, there is a clash between ionic conductivity and elastic modulus in hybrid SEs. For high ionic conductivity, low crystallinity, and high mobility polymer chains are often required, resulting in mechanically soft polymers. This paradox must be resolved in order to create feasible hybrid ceramic-based solid electrolytes capable of suppressing Li dendrites while delivering high power. So the ceramic-based hybrid SE offers the most promising option, where ceramic skeleton provides bulk ionic transport capability and high mechanical strength, and the inflitrated conductive polymer offers favorable interfacial coupling with the ellectrodes.

Herein, a hybrid ceramic-based solid electrolyte enabled by molecular engineering has been developed to resolve the above challenge. In this work, we engineer a unique porous $Li_{6.1}Al_{0.3}La_3Zr_2O_{12}$ (c-LLZO) scaffold design, which exhibits high ionic conductivity, high porosity, and, notably, high mechanical strength. By incorporating PEO-LiTFSI PSE into the strong c-LLZO porous membrane, the mechanical properties are markedly improved compared to the polymer-based hybrid SEs, allowing the electrolyte to mechanically suppress the growth of Li dendrites. The high porosity further facilitates a wide distributed occupancy of PSE within the composite to form metal-nitrogen bonding between the $TFSI^-$ groups in PSE and the La atoms in c-LLZO. The molecularly bonded polymer on the surface of garnet scaffold creates a tight interfacial contact between PSE/garnet, resulting in a low interfacial impedance while at the same time alleviating the side effects of grain boundaries on ionic conductivity. Moreover, the PSE can provide additional free lithium ions for lithium-ion transport. This synergistic effect increases the lithium-ion conductivity of this hybrid SE significantly. Furthermore, the introduced PSE could form and ultra-thin and smooth cover on the surfaces which improves the interfacial wettability with the electrodes when are assembled in ASSBs ensuring low impedance and long cycling stability (prevention of delamination). As a result, the as-designed ceramic-based HSEs exhibit good electrochemical characteristics, with a room-temperature ionic conductivity of 0.547 mS cm^{-1} and 2 mS cm^{-1} at 80 ℃. Meanwhile, the symmetric cells with the hybrid SEs have excellent long cycling stability against Li metal (over 500 h), and the assembled ASSB Li | ceramic-based HSE | $LiFePO_4$ devices also exhibit good cycling performance with 163 mAh g^{-1} after 50 cycles at RT and good rate performance at 70 ℃.

5.2.Experimental section

5.2.1.Preparation of porous c-LLZO scaffolds

The porous $Li_{6.1}Al_{0.3}La_3Zr_2O_{12}$ (c-LLZO) scaffolds were prepared as described in the schematics in Figure 1 and the flowchart given in Figure A.2.1. (In Appendixes A.2.) The synthesis route is based on our pervious research on low-temperature crystallization of nano-scale cubic garnet.[17] $La(NO_3)_3{\cdot}6H_2O$ (99.9%, Aldrich), $Al(NO_3)_3{\cdot}9H_2O$ (99.99% trace metals basis, Sigma-Aldrich), and $LiOH{\cdot}H_2O$ (99.95% trace metals basis, Sigma-Aldrich) were dissolved in DI-water at room temperature, with the amount of La added in excess of stoichiometry to compensate for its solubility limitation in the elevated pH range. More precisely, in this system represented as suspension A, the stoichiometric ratio of Li: Al: La is 6.1: 0.3: 3.0154. Due to the occurrence of the spontaneous hydrolysis reaction, a milky white precipitate forms. Meanwhile, separately a stoichiometric amount of $ZrO(NO_3)_2$ (35 wt% in dilute nitric acid, ≥ 99% trace metals basis, Aldrich) was dissolved in DI-water at room temperature. Polyethylene glycol (PEG, MW=20000) (Sigma-Aldrich) and propylene glycol (PG) (Fisher Scientific) with the molar ratio equal 2 : 0.5, were added as porous template and plasticizer respectively presented as solution B. After the dissolution and hydrolysis reactions were complete in both solutions, solution B was added dropwise into suspension A and mixed thoroughly (at this point, the pH value of this mixed system was around 6). To further promote their complete co-precipitation, concentrated LiOH solution (3M) was added dropwise at a rate of 1mL/min, to the optimal pH value of 10.5 that we have found previously to produce cubic garnet with best ionic conductivity.[17] After this co-precipitation step, the suspension was directly transferred into a 100 mL autoclave (hydrothermal aging step), which was then heated to 200 ℃ for 4 hours (h) (2 h for ramping and 2 h for holding) followed by cooling down to RT naturally. After the hydrothermal aging step, the wet precipitated solids were recovered via centrifugation and washed thoroughly with DI-water and isopropanol. Then the as-prepared precipitates were dried at 80 ℃ in the vacuum oven overnight. The dried precipitates were then mixed with the designated quantity of $LiOH{\cdot}H_2O$ by ball milling in a ZrO_2 container loaded with 1mm ZrO_2 balls at 650 rpm for 10 cycles of 10 min each (3 min grinding-7 min resting) with isopropanol as the liquid mediator. The amount of Li added was 7.5 times that of Al corresponding to the stoichiometry of $Li_{6.1}Al_{0.3}La_3Zr_2O_{12}$. Finally, the ground hydrothermal precursor solids were recovered after evaporation of the isopropanol in a rotary evaporator at 60 ℃ under vacuum and drying at 80 ℃ in the vacuum oven overnight. The completely dry precursor particles were cold-

pressed into pellets with a diameter of 13 mm and a thickness of 1.5 mm. The pellets were sintered at 400 ℃ for 2 h under the air to burn out the organic additives (polymer template and plasticizer), then were sintered at 800 ℃ for 6 h to obtain the c-LLZO phase with primary porous structure. Finally, the primary porous c-LLZO scaffolds were sintered at 1080 ℃ for 1 h under an Ar atmosphere to enhance their mechanical strength as well as their pore uniformity. Ambient air was avoided during sintering because it resulted in large loss of lithium, partial decomposition of c-LLZO and poor densification of the structure.

5.2.2.Preparation of hybrid SEs: PEO/LiTFSI in porous c-LLZO scaffolds

Poly(ethylene oxide) (PEO) (MW = 600,000, Sigma-Aldrich) and lithium bis(trifluoromethane sulfonyl)imide (LiTFSI) (≥ 98.0%, Tokyo Chemical Industry Co.) were dissolved in anhydrous acetonitrile (≥ 99.9%, Sigma-Aldrich) with a mole ratio of EO/Li = 10. Then, the mixture was stirred for 24 h at 55 ℃ in a sealed bottle to obtain the homogeneous gel. To evaluate the pristine ionic conductivity of the porous c-LALZO framework, the PEO gel without LiTFSI was prepared under the same concentration of EO as the PEO/LiTFSI gel. To prepare the ceramic-based hybrid SEs, the as-prepared porous c-LLZO scaffolds were immersed into PEO/LiTFSI and PEO gel respectively for 48 h and dried in the glove box.

5.2.3.Preparation of the composite $LiFePO_4$ electrode

The binder solution was prepared by dissolving the PVDF (HSV900 PVDF binder for Li-ion battery electrodes, MTI corporation) and PEO into N-methyl pyrrolidinone (NMP, 99.5% Sigma-Aldrich) with a ratio of 1:2, together with the LiTFSI in a ratio of EO/Li = 10, of which the solution concentration was 50 mg/mL. The $LiFePO_4$ (MSE supplies), carbon black (Super C65 carbon black conductive additive for lithium-ion battery cathode and anode, MSE supplies), and binder solution were mixed with a ratio of 70: 20: 10 and coated on an aluminum foil after stirring into a homogeneous suspension. Then the electrode was dried at 50 ℃ for 6 h and further dried in a vacuum oven at 120 ℃ overnight to remove NMP solvent. The dried electrode was punched into disks with a diameter of 9 mm, of which the mass loading is about 3 mg cm^{-2}.

5.2.4.Material characterization

X-ray diffraction (XRD) was conducted for the pellet samples using a Bruker D8-Advantage powder diffractometer using Co-Kα radiation with wavelength λ = 1.78892 Å, 35 kV/45 mA, 2θ from 10 to 70° in a step of 0.02°. The morphology characterization of the particle and pellet

samples were examined using a Hitachi SU8000 and SU3500 cold-field emission scanning electron microscope (CFE-SEM) (Hitachi High Technologies). Energy dispersive X-ray (EDS) elemental mapping techniques were conducted to acquire the elemental distribution of as-synthesized samples. X-ray photoelectron spectroscopy (XPS) was carried out on Thermo Scientific K-Alpha to determine the elemental state and the cross-section of the as-prepared hybrid SEs. Thermogravimetric analysis (TGA) was examined with Discovery 5500 from TA Instruments at a ramp rate of 10 ℃ min^{-1} from 25 to 700 ℃ under air atmosphere.

5.2.5.Electrochemical measurements

To evaluate the ionic conductivity of the as-synthesized porous c-LLZO scaffold and the hybrid SEs, two types of PSE were prepared: PEO with (Type 2) & without (Type 1) LiTFSI respectively, electrochemical impedance spectroscopy (EIS) was employed, using stainless steel (SS) as blocking electrodes. The EIS measurements were carried out from 25 ℃ (RT) to 80 ℃ with 10 ℃ steps using an electrochemical workstation (Bio-Logic) in potentiostatic mode between 10^6 Hz and 1Hz at an open-circuit voltage (OCV); the cells of SS | ceramic-based hybrid SE | SS were kept at each test temperature for 30 min to reach thermal equilibrium. The resistances were determined by fitting the Nyquist plot with an Equivalent Electric Circuit by the Zview-fit method provided by EC-Lab software. Equations (A.2.2) and (A.2.3) given in Appendixes A.2. were used to calculate the ionic conductivity and activation energy of Li-ion migration.

To calculate the lithium-ion transference number and conduct the lithium-ion stripping-plating cycling, the Li | ceramic-based hybrid SE | Li symmetric cells were fabricated. The lithium-ion transference number of the hybrid SEs was measured by DC polarization and AC impedance in symmetric cells based on equation (A.2.4) in Appendixes A.2.

The electrochemical window was determined using the linear sweep voltammetry (LSV) method in SS | ceramic-based hybrid SE | Li batteries from 2 to 6 V (vs Li^+ / Li) at a scanning rate of 1 mV s^{-1}.

The lithium stripping-plating cycling proceeded under 0.1, 0.2, 0.4, and 1 mA/cm^2 current densities respectively with a period of 30 min employing an MTI battery tester (BST8-WA, MTI corporation). Further, EIS was conducted to measure the interfacial resistance before and after stripping-plating cycling.

For evaluation of the performance of all-solid-state batteries featuring the hybrid electrolytes, Swagelok-type Li | ceramic-based hybrid SE | LFP cells were fabricated in a glove box and were stored in an oven at 60 ℃ overnight before cooled down naturally to RT, in order to obtain good interfacial contact between electrodes and ceramic-based hybrid SE. The charge-discharge cycling tests were conducted using an MTI battery tester (BST8-WA, MTI corporation) in a range of 3.0 – 4.2 V with 0.1 C rate at RT. The rate measurement of the ASSBs proceeded under 0.1 C, 0.2 C, 0.5 C, 1 C, and 2 C at RT, and rate performance at a high temperature (70 ℃) was carried under 1 C, and 2 C. Finally, EIS was employed to measure the interfacial resistance of the ASSBs under various cycling states.

5.3.Results and Discussion

5.3.1. Fabrication and characterization of porous scaffolds

Figure 5.1 illustrates the synthesis process of the ceramic-based hybrid SE and the schematic diagrams of the interfaces based on four different types of SEs, which are dense ceramic solid electrolytes, polymer solid electrolytes (PSEs), polymer-based hybrid SEs, and ceramic-based hybrid SEs, respectively. Dense ceramic SE has a reasonable lithium-ion conductivity, but its poor interfacial contact with the electrodes results in a large interfacial impedance, while the lithium dendrites generated during cycling will further lead to cracks spreading inside the dense ceramic structure. Due to the good wettability property of PSEs, they can form good interfacial contact with the electrodes, but their Li-ion conductivity is extremely low at ambient temperature, moreover due to their soft nature, they are unable to suppress the growth of lithium dendrites during cycling. When ceramic fillers are added into PSE to form composite polymer-based hybrid SE, the Li-ion conductivity is commonly increased due to the inhibited crystallization of polymer matrix, Li dendrite growth is suppressed to some extent, as well as good interfacial contact could be obtained, but the agglomeration of the ceramic fillers adversely affects ionic transport causing local dendrite growth. In this work, we report a unique ceramic-based hybrid SE with a 3D continuous c-LLZO skeleton infiltrated with PEO-LiTFSI PSE and forming ultra-thin surface layers via bonding of the N from $TFSI^-$ groups with surface La atoms. The as-prepared ceramic-based hybrid SEs achieve high Li-ion migration efficiency, while exhibiting low interfacial resistance and suppressed Li dendrite growth.

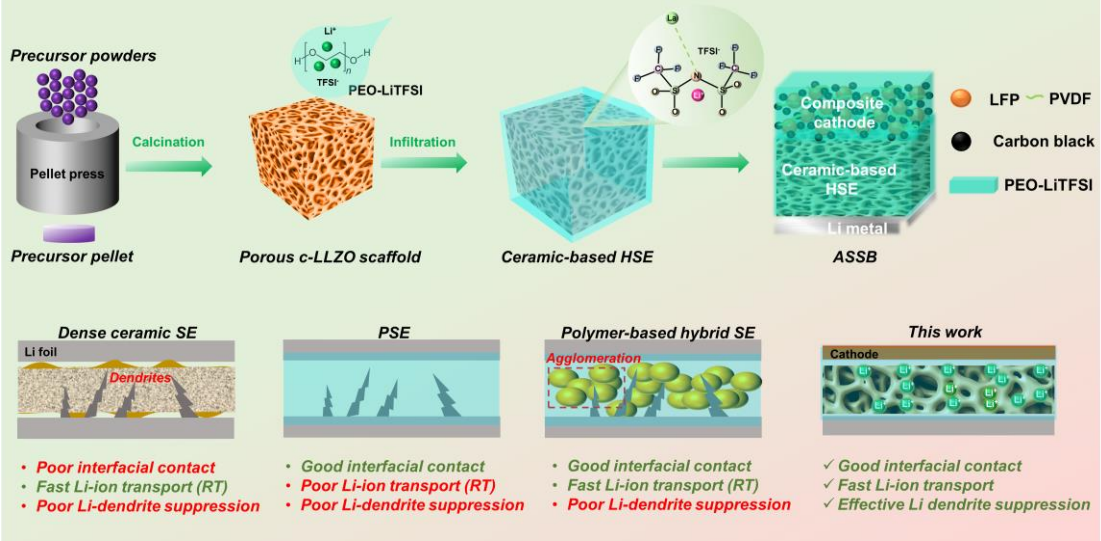

Figure 5. 1. Schematic illustration of the preparation of porous ceramic-based HSE and the schematic diagram of the interfaces based on four different types of solid electrolytes.

Precursor garnet powders

Here, the precursor powders were prepared following the first two steps of the three-step synthesis method of c-LLZO, as described in our previous paper [17] and Figure A.2.1. In the present method a modification was brought to the previous protocol by employing organic additives serving as pore template (polyethylene glycol) and plasticizer (propylene glycol). The SEM images of the precursors obtained from the first two steps (co-precipitation and hydrothermal aging) are presented in Figure A.2.2. $La(OH)_3$ nanofibers are surrounded by Zr-Al hydroxides, porous template (PEG 20000) and plasticizer (PG) components. After collecting the intermediate precipitate from hydrothermal process mixing it with Li source via ball-milling, and dried, the recovered samples are regarded as precursor powders.

Porous LLZO scaffolds

The precursor powders were pressed into pellets and then subjected to 2 steps of calcination. The calcined pellets were collected and characterized by XRD. As shown in Figure 5.2a, before the calcination process was initiated, the precursor pellet comprised only one crystalline component, $La(OH)_3$ crystals, with Zr-Al hydroxides, and porous template and plasticizer particles going unnoticed due to their amorpous nature. The first calcination step was conducted at 400 ℃ for 2h under air atmosphere to burn out the organic porous template and plasticizer components.

According to the corresponding XRD pattern, $La_2Zr_2O_7$ crystals form first at 400 ℃. As the calcination temperature is raised during the second calcination step, it can be seen the crystallization of c-LLZO to begin at 500 ℃ (6h holding time), and to have complete pure c-LLZO phase formation at 700 ℃. No further phase transition occurred at higher calcination temperature indicating the c-LLZO synthesis mechanism proceeding in stages from $La(OH)_3$ to $La_2Zr_2O_7$ and finally the cubic LLZO phase with no evidence of tetragonal phase. The standard XRD reference patterns of $La(OH)_3$, $La_2Zr_2O_7$, and c-LLZO are provided in Figure A.2.3. To investigate the morphological and chemical speciation evolution of the porous c-LLZO structure, the SEM images and XPS spectra of O 1s and C 1s are presented in Figures 5.2 (b-d). According to the SEM images, prior to calcination, the precursor pellet has a composite microstructure composed of $La(OH)_3$ crystal nanofibers within a matrix of Zr-Al hydroxides and organic components (Figure 5.2b). After the first calcination step (400 ℃-2h), the organic porous template and plastisizer components were burnt out, yielding a homogeneous porous structure as it can be observed in Figure 5.2c. Then after the second calcination step, based on the XRD results presented in Figure 5.2a, the pure c-LLZO phase is obtained at 700 ℃. The SEM of the porous c-LLZO scaffolds obtained at different temperatures (700 ℃ to 900 ℃) are presented in Figure 5.2d and Figure A.2.4. The porous structure obtained at 700 ℃ is not fully homogeneous composed of pores and particles, while that obtained at 900 ℃ is also unsatisfactory, as at that temperature fusion of pores occurs due to grain coarsening, leading to the loss of homogeneous porosity distribution. As shown in Figures 5.2d and 5.2e, the top-surface and cross-sectional SEM images obtained at 800 ℃ reveal a highly homogeneous primary porous structure corroborated by the uniform EDS element distribution results. However, as shown in the inset digital images, the porous c-LLZO scaffolds obtained after calcination at 800 ℃ have rather poor mechanical strength, an issue addressed with further heat treatment as discussed in the next section.

To further investigate the fabrication process of the as-prepared porous c-LLZO scaffold, XPS was employed to characterize its chemical speciation at different calciantion stages. The respective photoelectron spectra of O 1s and C 1s are presented in rhs of Figures 5.2 (b-d). Before the first calcination step (400 ℃-2h), the precursor powders are composed of hydroxides and organic template and plastisizer components, as evidenced by characteristic peaks of O-H observed in O 1s spectra and C-OH, C-C/C-H, and C=O observed in C 1s spectra. As the calcination temperature increased, the organic components burnt out and the hydroxides converted to oxides, as it can be

deduced from the presence of only C-O and C-C peaks caused by atmospheric CO_2 and environmental contamination. Meanwhile, there is no characteristic peak of hydroxide detected but only metal oxides, whose peak intensity ratios correspond to the stoichiometry of c-LLZO. Having achieved the formation of porous c-LLZO scaffold with homogeneous porous structure next the poor mechanical property addressed.

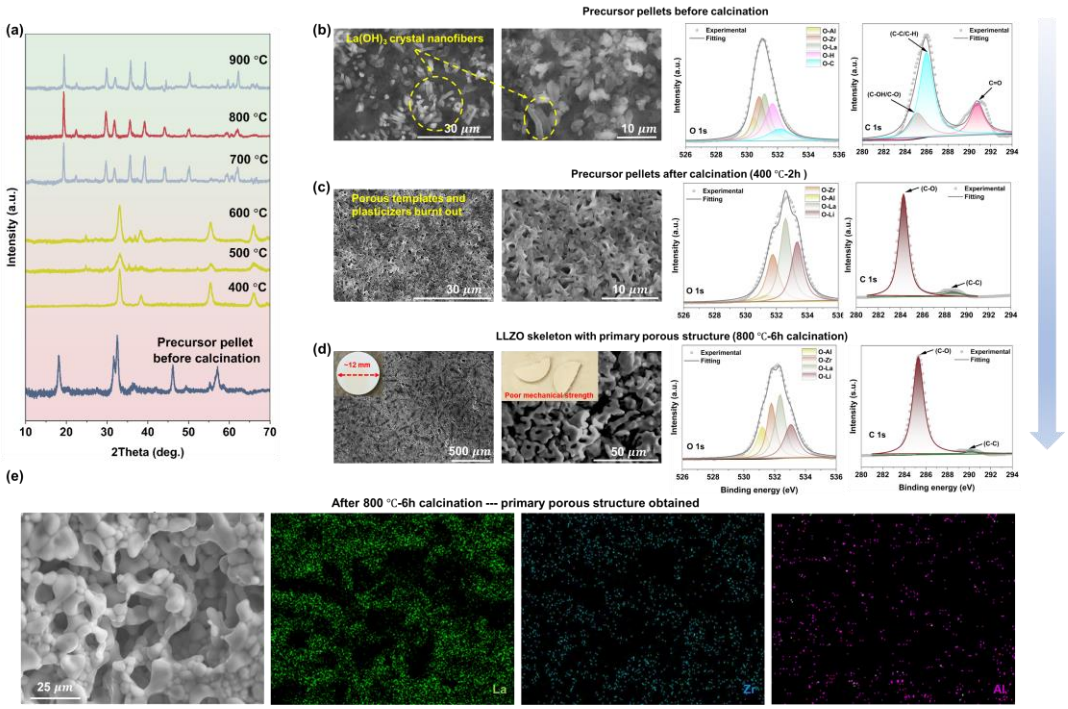

Figure 5. 2. Crystalline, morphological, and chemical speciation characterizations. (a) XRD patterns of the as-prepared porous c-LLZO scaffold before calcination, after initial calcination at 400 ℃ for 2h, and after calcination at various temperatures from 500 ℃ to 900 ℃ for 6h; (b-d) the top-surface SEM images and XPS O 1s and C 1s spectra of the as-prepared porous c-LLZO scaffold at different calcination stages. The inset shows the digital image of the primary porous c-LLZO pellet; (e) cross-sectional SEM image and EDS mapping of the porous c-LLZO scaffold.

Mechanical strengthening of porous scaffolds

To improve the mechanical strength of the as-prepared primary porous c-LLZO scaffold, another sintering treatment was conducted at 1080 ℃ for 1h under Ar atmosphere. The XRD pattern of the porous c-LLZO skeleton after sintering, shown in Figure 5.3a, has no signs of impurities while still exhibits the pure cubic garnet phase. However, the digital image of the sintered porous c-LLZO skeleton (inset in Figure 5.3a), showed a reduction in pellet diameter from initial 12 mm down to 11 mm implying certain degree of volume shrinkage. Despite this small volume shrinkage,

the scaffolds retained their porosity as can be inspected with the microscopic images of the top surface and cross-section of the porous c-LLZO skeleton shown in Figures 5.3b and 5.3c. The results show that the inner pores are continuous in three dimensions (3D), and the garnet grains are tightly connected to form a 3D conductive network. The pore channels formed are micron-level connected, which are also conducive to the infiltration of polymer electrolyte (PEO-LiTFSI) as described in the next section. Notably, the porous c-LLZO skeleton with a homogeneous distribution of pores and very good mechanical strength was obtained with a thickness of ~ 1.3 mm. The porosity of the as-prepared porous c-LLZO scaffold determined through the Archimedes method (refer to Eq. (A.2.1) in Appendixes A.2, was found to be on average 30.56% (see Table A.2.1 in Appendixes A.2).

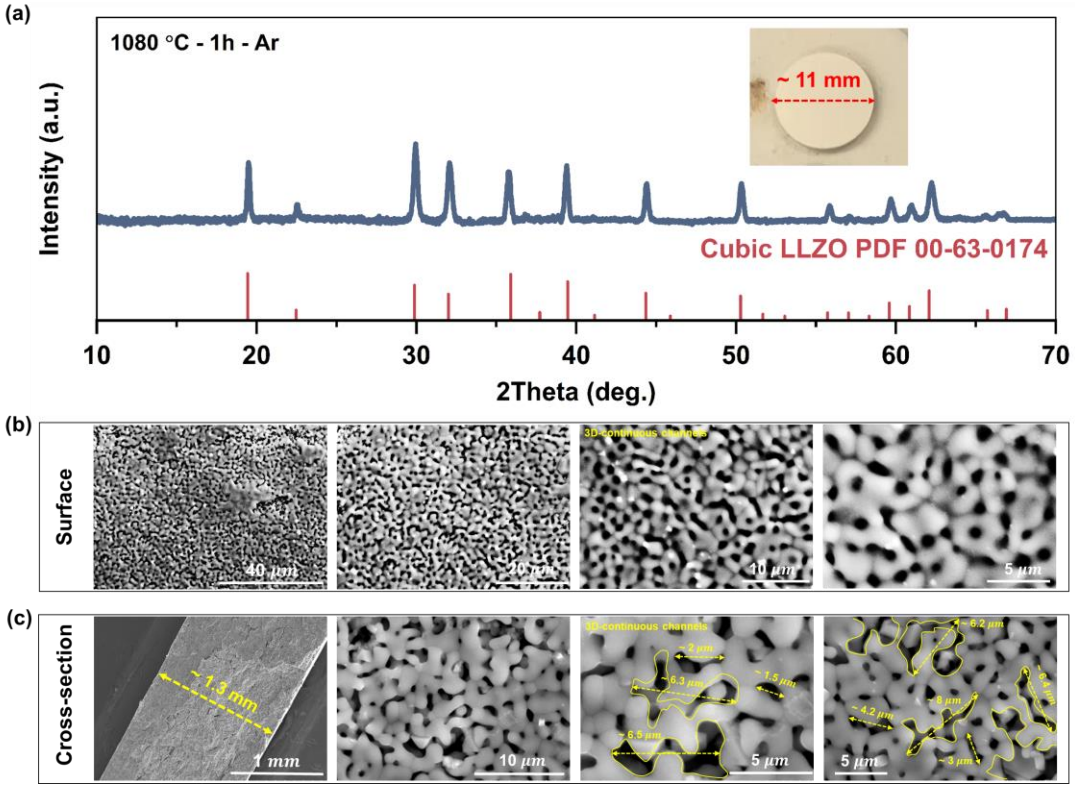

Figure 5. 3. Crystal structure and morphological characterization of as-designed porous c-LLZO scaffold. (a) XRD pattern of the porous c-LLZO scaffold after sintering at 1080℃; SEM images of (b) top surface and (c) cross-section of the sintered porous c-LLZO scaffold.

5.3.2 Preparation and Characterization of Ceramic-based Hybrid SEs

To prepare the ceramic-based hybrid SEs, the as-prepared porous c-LLZO scaffolds were infiltrated with PEO-LiTFSI gel, thus forming a continuous double-phase composite, as shown in Figure 5.4a. The newly designed ceramic-based hybrid SEs did not only feature conductive PSE inside the porous channels but also formed on the exterior an ultra-thin (less than 4 μm-thick) smooth conductive polymer surface, which facilitates low impedance interfacial contact with electrodes in ASSBs as presented in Figures 5.4b and 5.4c. The cross-sectional microscopic images of the ceramic-based hybrid SE in Figure 4d and Figure A.2.5 show its thickness to be around 1.3 mm, which could provide strong mechanical "barrier" against Li-dendrite growth. The cross-sectional EDS results of the ceramic-based hybrid SE (Figure 5.4d) and the selected area of the red dash box (Figure 5.4e) indicate highly homogeneous element distribution and continuous dispersion of PSE inside porous channels as well as on the surface. Moreover, both ceramic and organic phases are tight-connected and interspersed to form a packed polymer-in-ceramic hybrid solid electrolyte. The tight adhesive interface between the porous ceramic channel walls and PSE filler is conducive to fast transport of Li-ions, while at the same time the porous c-LLZO scaffold with a high Young's modulus can resist dendrite growth and the softer PSE can improve electrode-electrolyte interfacial contact. Notably, the color of the carbon-layered mapping (PSE distribution) and combined element mapping of the ceramic-based hybrid SE cross section (Figures 5.4d and 5.4e) clearly suggest the infiltrating PSE to be continuous, homogeneously distributed, and in modest (minor) quantity.

In order to clarify the chemical interaction between infiltrating PSE and porous c-LLZO scaffold walls, XPS analysis was performed. In Figure 5.4f, the N 1s spectrum of the PEO-LiTFSI PSE is shown to have only one signal peak, which is located at 398.88 eV ($TFSI^-$). However, for the ceramic-based hybrid SE (PEO-LiTFSI in porous c-LLZO scaffold) (Figure 5.4i), the N 1s spectrum shows a new peak at 400.38 eV corresponding to La-N bonding, indicating chemical anchoring of the $TFSI^-$ groups of PSE on the surface La atoms of c-LLZO via the principle of hard and soft acids and bases. As for the C 1s spectrum of PSE and hybrid SE shown in Figures 5.4g and 5.4j, the peaks located at 284.18, 286.18, 287.58, and 292.38 eV are attributed to ($-CH_2-$), ($-OCH_2-CH_2-$), (-COOR), and ($-TFSI^-$) of the PSE. But in the ceramic-based hybrid SE, the corresponding four peaks shift to higher binding energy by 0.4, 0.2, 0.7, and 0.2 eV respectively, indicating the interaction of some groups in PSE with metal atoms of c-LLZO scaffold. Meanwhile,

Figure 5.4h shows the La 3d spectrum of the ceramic-based hybrid SE to display two sets of peaks located at 854.68, 850.28 eV (La $3d_{3/2}$), and 837.98, 833.48 eV (La $3d_{5/2}$), which shift to low binding energy by 0.8, 1.4, 0.7, and 1.4 eV compared with the peaks of c-LLZO scaffold, respectively, indicating the formation of bonds between surface La atoms and PSE. Thus, it is proposed that the robust La-N bonding between the infiltrated PSE and porous c-LLZO scaffold results in strong and homogeneous contact of PSE inside/outside the porous structure as presented in Figure 4k. Supplementary XPS surveys of the porous c-LLZO scaffold, PSE membrane, and the ceramic-based hybrid SE are shown in Figure A.2.6a, and the F 1s spectrum of the PSE membrane and the ceramic-based hybrid SE are presented in Figures A.2.6b and A.2.6c. Thermogravimetric analysis (TGA) results in Figure A.2.7, indicate that the weight percentage of ceramic porous c-LLZO skeleton in the ceramic-based hybrid SE is over 97%, which proves that the as-prepared hybrid SE is overwhelmingly ceramic-based, ensuring good thermal stability and safety when employed in all-solid-state batteries.

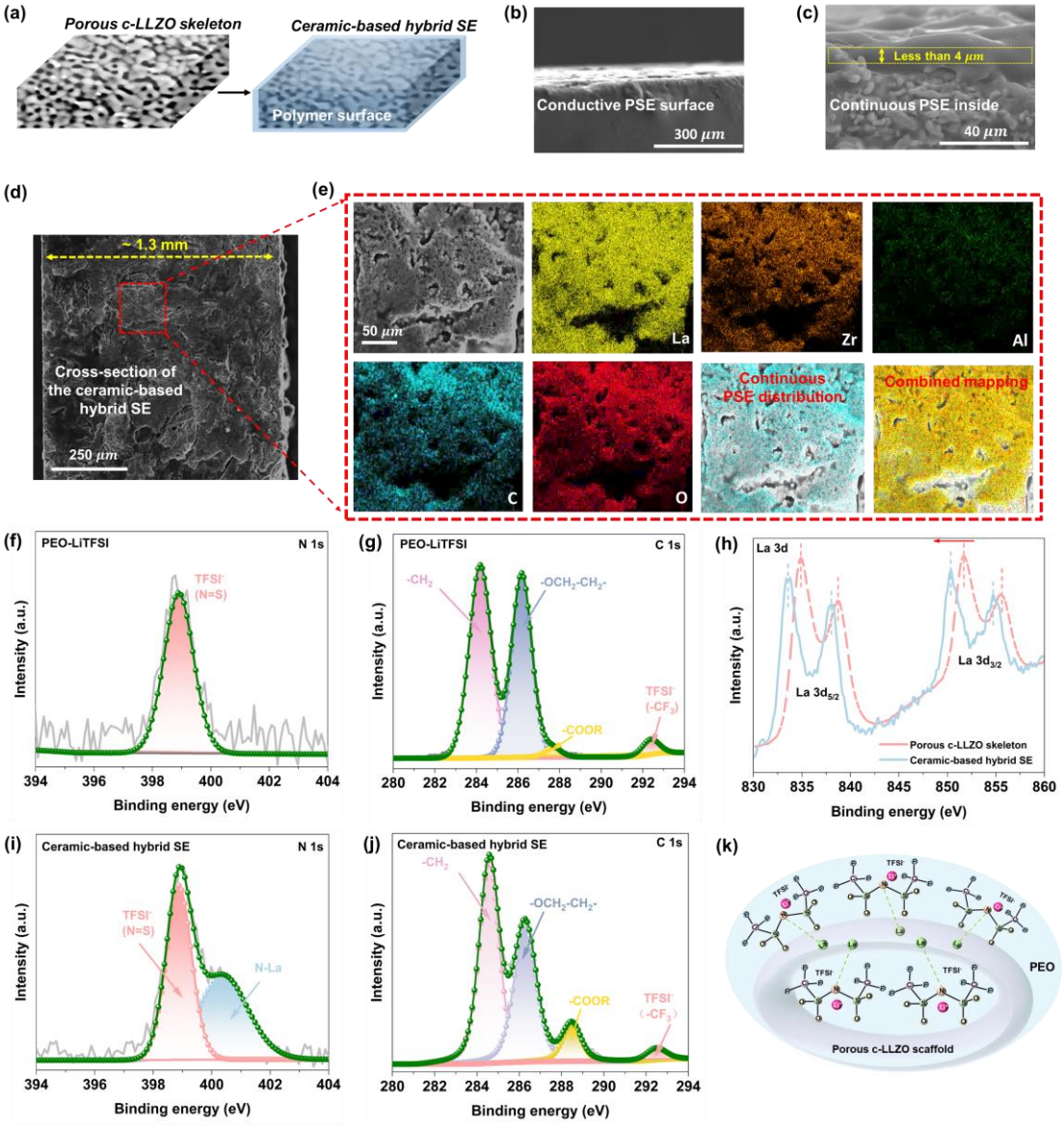

Figure 5. 4. Characterization of PEO-LiTFSI in porous c-LLZO scaffold: (a) the schematic diagram of the preparation of the ceramic-based hybrid SE; SEM images of (b) the surface, and (c) cross-section of the ceramic-based hybrid SE; (d) cross-sectional SEM image and (e) EDS maps of the ceramic-based hybrid SE; (f) and (i) the N 1s XPS spectra of PEO-LiTFSI PSE and hybrid SE; (g) and (j) the C 1s spectra of PEO-LiTFSI PSE and ceramic-based hybrid SE; (h) the La 3d spectra of porous c-LLZO scaffold and the ceramic-based hybrid SE; (k) schematic representation of the interaction between infiltrated PSE and porous c-LLZO scaffold.

5.3.3 Ionic Transport of the Ceramic-based Hybrid SE

Ionic conductivity is the key property of a solid electrolyte. This was evaluated for the as-designed ceramic-based hybrid SEs using electrochemical impedance spectroscopy (EIS). The ionic conductivity results under various temperatures of four types of electrolytes: ceramic-based hybrid SE with PEO-LiTFSI, ceramic-based hybrid SE with PEO (no Li salt dissolved), sole c-LLZO ceramic SE, and sole PEO-LiTFSI PSE are shown in Figures 5.5 (a – d). Based on equation (A.2.2) in Appendixes A.2, the ceramic-based hybrid SE with PEO-LiTFSI has the highest ionic conductivity, reaching 0.547 mS cm^{-1} at 25 ℃. The ceramic-based hybrid SE with PEO only exhibits similar ionic conductivity with the pure c-LLZO ceramic SE as 0.42 mS cm^{-1} at 25 ℃, which demonstrates the high intrinsic ionic conductivity of the porous c-LLZO scaffold. The activation energies of Li-ion migration were calculated based on equation (A.2.3) in Appendixes A.2. The hybrid SE with PEO and pure c-LLZO SE have similar values of activation energies around 0.2 eV much lower than that of PSE, indicating their low temperature dependent. Moreover, the ceramic-based hybrid SE with PEO-LiTFSI has the lowest activation energy at 0.187 eV. This good capability for Li-ion migration in the hybrid SE with PEO-LiTFSI is on one part due to the as-designed c-LLZO ceramic skeleton that possesses high intrinsic ionic conductivity and promotes the dissociation of lithium salt; and on the other part the molecular bonding of La with $TFSI^-$ groups that ensures a 3D-continuous two-phase with low interface impedance. As a consequence, fast Li-ion migration pathways open. Li-ion transference number (t_{Li^+}) is also a key property of the electrolyte. As presented in Figures 5.5e and 5.5f, and equation (A.2.4) in SI, the ceramic-based hybrid SE with PEO-LiTFSI exhibits a very high t_{Li^+} of 0.71, which is much higher than the PEO-LiTFSI PSE (~0.15) (in Figure A.2.8) and polymer-based hybrid SE (10 wt% c-LLZO particles in a polymer matrix) (~0.25) (in Figure A.2.9). The comparison of lithium-ion transfer numbers and ionic conductivities is presented in Figure 5i (four different types of SE). Among them, the as-prepared ceramic-based hybrid SE demonstrates an apparent superiority, which is mainly due to the fact that the PSE does not have ion transport selectivity, and thus it usually has low t_{Li^+}, in contrast, a ceramic electrolyte as the single ion conductor compounded with polymer usually improves the t_{Li^+} of the ceramic-based composite. High t_{Li^+} enables lower concentration polarization in practical application as well as reducing the driving force of Li dendrite growth. Figure 5.5k summarizes the ionic conductivity of PEO-LLZO hybrid SE systems (with variable ratios of each component) reported in previous research works. It could be seen that

the ionic conductivity of most PEO-LLZO hybrid SEs is lower than 10^{-4} S/cm in the temperature ranging from 20 to 40 ℃, while the ceramic-based (over 97 wt% LLZO) hybrid SE in this work exhibits a remarkable ionic conductivity higher than 0.5 mS/cm at 25 ℃.

The electrochemical window (EW) is another crucial parameter that determines the applicability of SEs in high-energy ASSBs. Figure 5.5j compares the EWs of the as-prepared ceramic-based hybrid SE with sole PEO-LiTFSI PSE in the voltage ranging from 2 to 6 V *vs.* Li/Li^+, based on the battery configuration SS / ceramic-based hybrid SE / Li and SS / PEO-LiTFSI PSE / Li (where SS is stainless steel). Their stable windows extend respectively to nearly 3.9 V and 5.2 V. The enhanced electrochemical stability exhibited by the hybrid SE is mainly due to (i) the electrochemically stable porous c-LLZO skeleton (high percentage of ceramic), (ii) the stable electrochemical interaction between porous c-LLZO skeleton and infiltrated PEO-LiTFSI PSE, and (iii) the high chemical stability of LLZO with Li metal that avoids early-stage oxidation. Therefore, the as-prepared ceramic-based hybrid SE is characterized with fast Li-ion transport and good electrochemical stability in addition to mechanical strength that makes it highly suitable for application in advanced ASSBs.

5.3.4 Li Plating-Stripping Stability and Dendrite Suppression

To evaluate the interfacial stability and lithium metal dendrite inhibition ability of the ceramic-based hybrid electrolyte structure, symmetric batteries were assembled and tested. The schematic diagram and digital image of the Li symmetric battery are shown in Figure 5l. Long-term interfacial stability is critical for the stable operation of ASSBs, and it can be analyzed by constant current cycling tests as shown in Figures 5.5m and 5.5n. The results indicate that the ceramic-based hybrid SE did not short-circuit at current densities of 0.1 and 0.2 mA cm^{-2} over 500 h. Even at a higher current density of 0.4 mA cm^{-2}, the symmetric battery still worked properly showing no increase in polarization as it can be verified with the data in Figure A.2.10. The symmetric cell only gradually starting failing after the current density was increases to 1 mA cm^{-2}, as shown in Figure S10. The SEM images and digital images (inset) in Figure 5.5l of the cycled Li symmetric batteries at 0.1 and 0.2 mA cm^{-2} over 500 h, provide proof of good interfacial contact between the ceramic-based hybrid SE and Li metal. To robust nature of the formed stable interface is further demonstrated with the EIS plots of the Li symmetric batteries before and after long-term plating-stripping cycling under different current densities that are shown in Fig. 5.5g. A suitable equivalent

circuit with individual resistances and constant phase elements (CPEs) is employed to elucidate the Nyquist plots. Here, R_{Bulk} represents the resistance of the c-LLZO bulk structure, $R_{Interface + gb}$ represents the resistance contributed from the interface between c-LLZO scaffold walls and PEO-LiTFSI PSE, as well as the grain boundaries (gb) of c-LLZO itself. R_{Bulk} and $R_{Interface + gb}$ represent the total resistance of the as-designed ceramic-based hybrid SE. $R_{Interface\ with\ Li\ electrode}$ represents the interfacial resistance between the ceramic-based hybrid SE and Li electrodes (*i.e.* the interfacial resistance of the symmetric battery). $CPE_{Interface+gb}$ and $CPE_{Interface\ with\ Li\ electrode}$ correspond to the constant phase elements. The impedance caused by the ceramic-based hybrid SE and interface against Li electrode are is measured and presented in Fig. 5.5h. After the long-term plating-stripping cycling, the interfacial impedance only slightly increased, meanwhile, the total resistance of the ceramic-based hybrid SE basically remains unchanged. Therefore, the results demonstrate excellent intrinsic stability of the ceramic-based hybrid SE itself and in interface with Li electrode, even under higher current densities, this being due to fast ionic transport, favourable interfacial contact, and good electrochemical stability. Moreover, since the cumulative cycling capacity is the product of cycling current and time in a symmetric cell, it is deduced the solid electrolyte structure to resist lithium dendrite penetration. On this basis, the as-designed ceramic-based hybrid SE is judged highly promising for building ASSBs with increased energy density and safety.

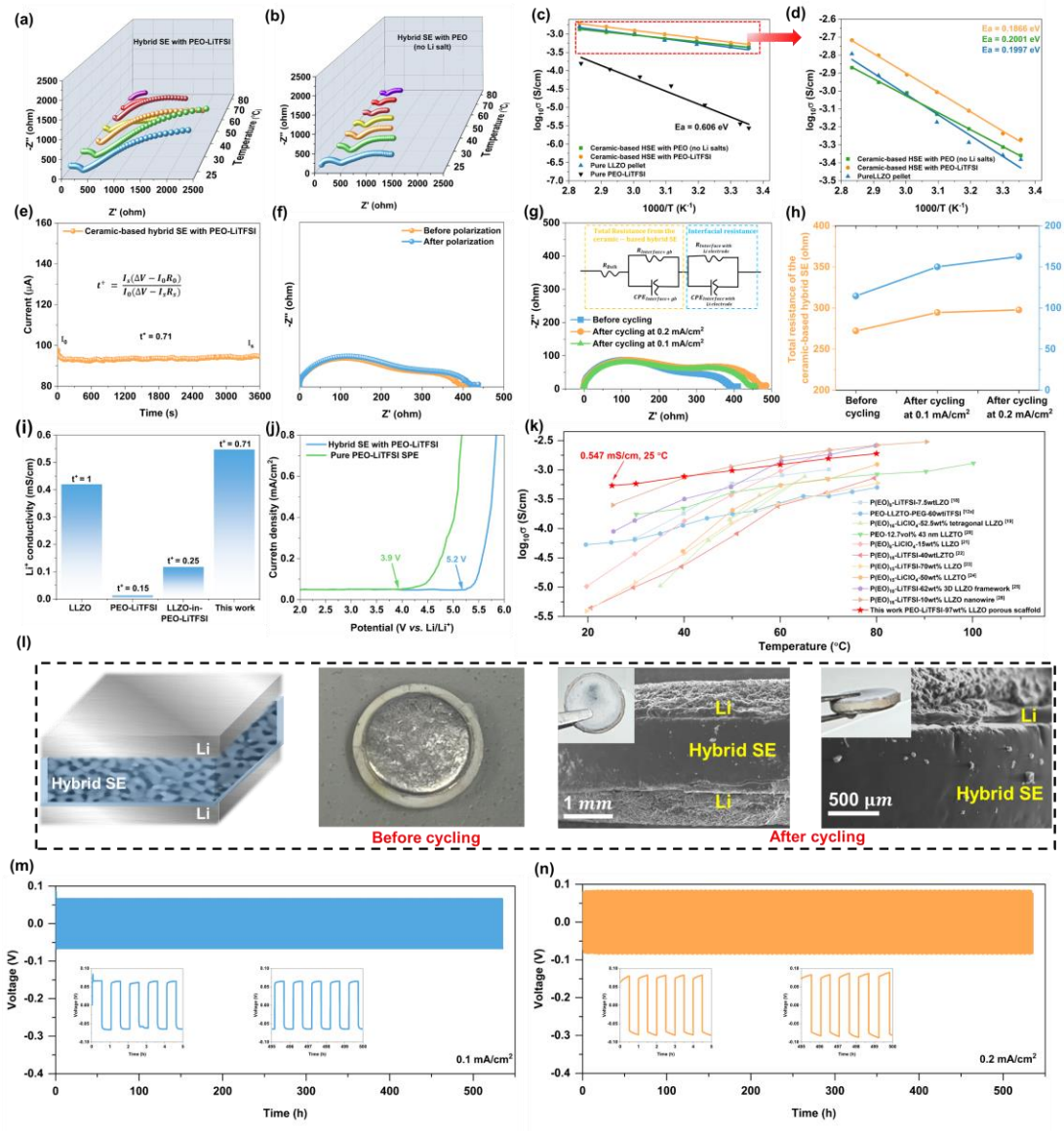

Figure 5. 5. Electrochemical characterization of ceramic-based HSE: EIS plots of two types of the ceramic-based hybrid SEs, (a) with PEO-LiTFSI and (b) with PEO only; (c and d) Arrhenius plots of four types of solid electrolytes and their magnification; (e) EIS of the symmetric battery before and after polarization; (f) polarization curve of the hybrid SE at 25 ℃; (g) EIS plots of the Li symmetric batteries before cycling and after 500 cycles at 0.1 and 0.2 mA cm^{-2} respectively, (h) the impedance caused by hybrid SE and interface; (i) comparison of Li^+ transference numbers and ionic conductivities; (j) LSV curve at room temperature with scan rate 10 mV s^{-1} from 2 to 6 V; (k) comparative ionic conductivity of (PEO & garnet)-based hybrid solid electrolytes from different refs; (l) schematic diagram of Li symmetric battery and its digital image before plating-stripping cycling plus SEM images and digital images (inset) after 500 cycles at 0.2 mA cm^{-2}; (m and n) galvanostatic curves of the Li symmetric batteries at 0.1 and 0.2 mA cm^{-2} respectively.

5.3.5 ASSB Performance Based on the Ceramic-based Hybrid SE

To demonstrate the feasibility of ceramic-based hybrid SE in practical applications, ASSBs were assembled and tested. The schematic diagram of the ASSB assembled with the hybrid SE is presented in Figure 5.1. The cathode electrode is $LiFePO_4$ and the anode electrode is lithium metal. The results of the long-term cycling of ASSB under 0.1C at 25 ℃ are shown in Figures 5.6a and 5.6b, where it can be observed that the capacity is up to 163 mAh g^{-1} and remains stable for 50 cycles, with a capacity retention rate of 98% and an average Coulombic efficiency of more than 99%. To investigate the interfacial stability of ASSB, EIS was conducted as shown in Figure 5.6f. Therein, it can be found that the cell has a large total impedance before cycling, which is due to the incomplete activation of the solid-solid interface. After the interfacial activation during the first cycle, the total impedance decreased significantly and stabilized at about 150 ohms. Hence, the as-designed ASSB delivers a favorable electrochemical performance with high capacity that is mainly attributed to stable interfaces with both electrodes enabled by the design of the polymer-in-porous c-LLZO ceramic membrane.

To further explore the stability of the as-designed ASSB under high rates, Figures 5.6c and 5.6d show the results of the rate performance test at 0.1, 0.2, 0.5, 1, and 2 C. The specific discharge capacities at 0.1, 0.2, and 0.5 C, are stable at 163.0, 162.7, and 153.7 mAh g^{-1} respectively. While there is severe specific capacity drop from 134.3 to 89.9 mAh g^{-1} at 1C cycling and no capacity delivered at 2 C charge/discharge rate. Meanwhile, when the charge/discharge rate is restored to 0.1 C after experiencing the total capacity fade at 2 C charge/discharge, the specific discharge capacities can still recover to 162.6 mAh g^{-1}, which indicates the as-designed ASSB enabled by the ceramic-based hybrid SE has good reversibility of capacity with rate change. With respect to the severe capacity drop exhibited at 1 C rate cycling and the no capacity delivery at 2 C rate cycling, this is attributed to limitation at the cathode mainly (and not the ceramic-based HSE) where PEO-LiTFSI is the electrolyte which is known to have low lithium-ion conductivity at ambient temperature (see conductivity data in Figure 5.5c), which is caused by limited chain motion and thus results in high operating temperatures of around 50 – 70 ℃.[27] To verify this assumption, the battery was tested at 70 ℃ for high-rate cycling performance, and as shown in Fig. 5.6e, the battery exhibited reasonable capacities at 1 C and 2 C cycling rates of 138 mAh g^{-1} and 130 mAh g^{-1} respectively. This suggests that the poor high-rate performance of the battery at

ambient temperature is only limited by the conductivity of the polymer electrolyte component in the cathode and is not a consequence of the breakdown of interfacial stability of the battery.

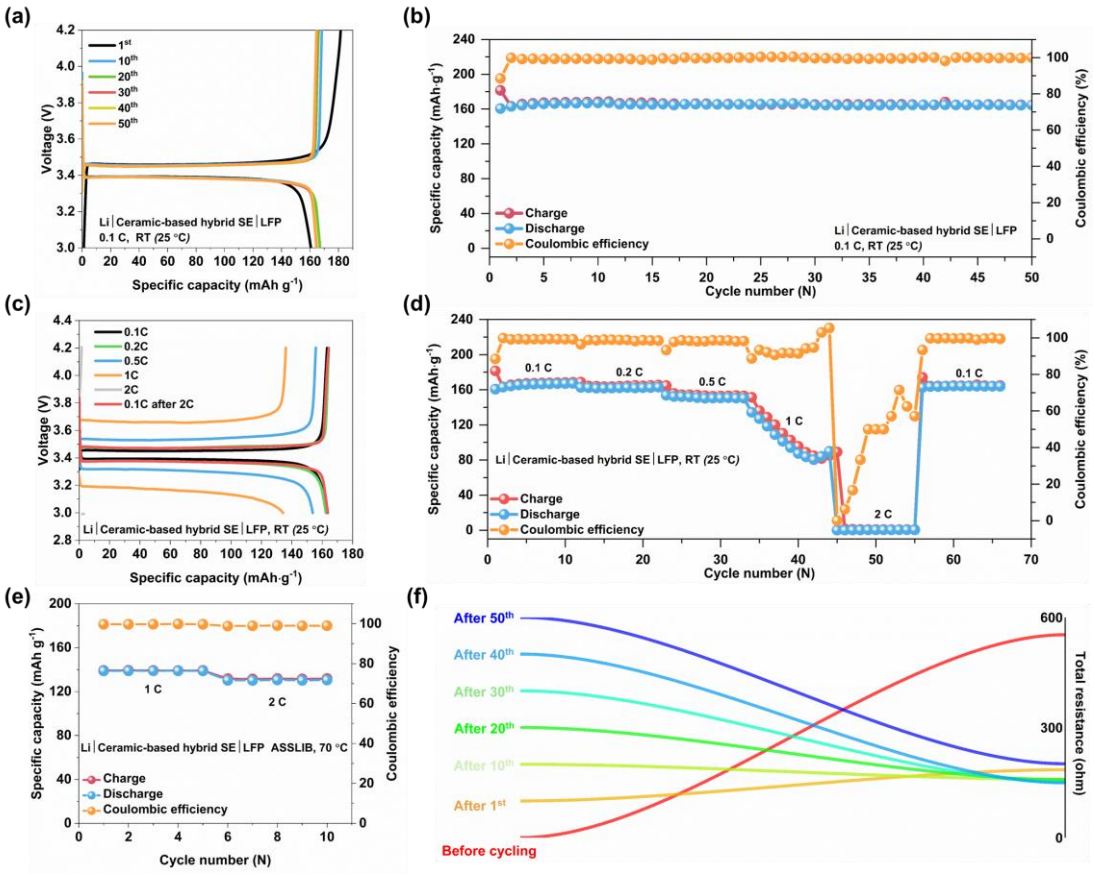

Figure 5. 6. The electrochemical performance of ASSBs. (a) charge-discharge voltage profiles at different cycles; (b) cycling stability obtained from ASSB at 0.1 C and 25 ℃; (c) charge-discharge profiles at different rates and 25 ℃; (d) the rate performance from 0.1 C to 2 C at 25 ℃; (e) the rate performance under 1 C and 2 C at 70 ℃; (f) the total resistance of the ASSB at different cycles.

5.4. Conclusion

In summary, a predominantly (97% of the SE) porous c-LLZO high-conductive scaffold with a 3D continuous percolation network was obtained through an integrated sintering strategy that upon polymer infiltration with PEO-LiTFSI provides a very robust solid electrolyte membrane. The ceramic-based hybrid SE exhibits a high ionic conductivity of 0.547 mS cm^{-1} and t_{Li^+} is 0.71 at room temperature due to the high intrinsic ionic conductivity of porous c-LLZO scaffold as well as the synergetic interaction between ceramic and PSE via La-N bonding, lowering the interfacial

resistance between two phases. Meanwhile, in the cycling test of symmetric batteries, the lithium symmetric batteries enabled by the ceramic-based hybrid SE can cycle stably for over 500 h at 0.2 mA cm^{-2}. As a result, the Li | Ceramic-based hybrid SE | $LiFePO_4$ full batteries exhibit good rate performance as well as long cycle stability (163 mAh g^{-1} after 50 cycles). The ASSB can be operated at higher rate (even at 2C) without sign of interfacial instability. The results indicate that the newly designed porous ceramic-based hybrid SE can facilitate fast Li-ion migration, excellent electrochemical stability, and favourable interfacial integration with electrodes. This strategy and designed SE structure constitute new paradigms towards high-performance and robust all-solid-state batteries.

5.5. References

1. a) Y. Ding; Z. P. Cano; A. Yu; J. Lu; Z. Chen, *Electrochem. Energy Rev.* **2019,** *2* (1), 1-28; b) Y. Tian; G. Zeng; A. Rutt; T. Shi; H. Kim; J. Wang; J. Koettgen; Y. Sun; B. Ouyang; T. Chen; Z. Lun; Z. Rong; K. Persson; G. Ceder, *Chem. Rev.* **2021,** *121* (3), 1623-1669.

2. a) M. Li; J. Lu; Z. Chen; K. Amine, *Adv. Mater.* **2018**, *30*, 1800561; b) P. Albertus; S. Babinec; S. Litzelman; A. Newman, *Nat. Energy* **2017,** *3* (1), 16-21; c) J.-M. Tarascon, M. Armand, *Nature* **2001,** *414*, 9.

3. a) Q. Zhao; S. Stalin; C. Zhao; L. A. Archer, *Nat. Rev. Mater.* **2020,** *5* (3), 229-252; b) R. Chen; Q. Li; X. Yu; L. Chen; H. Li, *Chem. Rev.* **2020,** *120* (14), 6820-6877; c) R. S. Longchamps; X. Yang; C. Wang, *ACS Energy Lett.* **2022**, 1103-1111.

4. a) X. Shen; Q. Zhang; T. Ning; T. Liu; Y. Luo; X. He; Z. Luo; A. Lu, *Mater. Today Chem.* **2020,** *18*, 100368; b) A. Banerjee; X. Wang; C. Fang; E. A. Wu; Y. S. Meng, *Chem. Rev.* **2020,** *120* (14), 6878-6933.

5. a) M. Balaish; J. C. Gonzalez-Rosillo; K. J. Kim; Y. Zhu; Z. D. Hood; J. L. M. Rupp, *Nat. Energy* **2021,** *6* (3), 227-239; b) J. C. Bachman; S. Muy; A. Grimaud; H. H. Chang; N. Pour; S. F. Lux; O. Paschos F.; Maglia; S. Lupart; P. Lamp; L. Giordano; Y. Shao-Horn, *Chem. Rev.* **2016,** *116* (1), 140-62.

6. Q. Liu; Z. Geng; C. Han; Y. Fu; S. Li; Y. He; F. Kang; B. Li, *J. Power Sources* **2018,** *389*, 120-134.

7. a) Y. Xiao; Y. Wang; S. Bo; J. C. Kim; L. J. Miara; G. Ceder, *Nat. Rev. Mater.* **2019,** *5* (2), 105-126; b) B. Zhang; R. Tan; L. Yang; J. Zheng; K. Zhang; S. Mo; Z. Lin; F. Pan, *Energy Storage Mater.* **2018,** *10*, 139-159.

8. a) W. Li; Y. Pang; J. Liu; G. Liu; Y. Wang; Y. Xia, *RSC Adv.* **2017,** *7* (38), 23494-23501; b) Y. C. Jung; M. S. Park; D. H. Kim; M. Ue; A. Eftekhari; D. W. Kim, *Sci. Rep.* **2017,** *7* (1), 17482.

9. Y. An; X. Han; Y. Liu; A. Azhar; J. Na; A. K. Nanjundan; S. Wang; J. Yu; Y. Yamauchi, *Small* **2022,** *18* (3), 2103617.

10. a) X. Yu; A. Manthiram, *Energy Storage Mater.* **2021,** *34*, 282-300; b) S. Li; S. Zhang; L. Shen; Q. Liu; J. Ma; W. Lv; Y.He,; Q. Yang, *Adv Sci (Weinh)* **2020,** *7* (5), 1903088.

11. a) Y. M. Jeon; S. Kim; M. Lee; W. B. Lee; J. H. Park, *Adv. Energy Mater.* **2020,** *10* (47), 2003114; b) J. Zhang; N. Zhao; M. Zhang; Y. Li; P. K. Chu; X. Guo; Z. Di; X. Wang; H. Li, *Nano Energy* **2016,** *28*, 447-454.

12. a) L. Chen; Y. Li; S. Li; L. Fan,; C. Nan; J. B. Goodenough, *Nano Energy* **2018,** *46*, 176-184; b) C. Bao; C. Zheng; M. Wu; Y. Zhang; J. Jin; H. Chen; Z. Wen, *Adv. Energy Mater.* **2023,** *13*, 2204028.

13. X. Zhang; T. Liu; S. Zhang X.; Huang; B. Xu; Y. Lin; B. Xu; L. Li; C. Nan; Y. Shen, *J. Am. Chem. Soc.* **2017,** *139* (39), 13779-13785.

14. J. Cheng; G. Hou; Q. Chen; D. Li; K. Li; Q. Yuan; J. Wang; L. Ci, *J. Chem. Eng.* **2022**, *429*, 132342.

15. a) L. Li; Y. Deng; G. Chen, *Journal of Energy Chemistry* **2020**, *50*, 154-177; b) G. Xi; M. Xiao; S. Wang; D. Han; Y. Li; Y. Meng, *Adv. Funct. Mater.* **2020**, *31* (9), 2007598.

16. B, Jinisha; K.M. Anilkumar; M. Manoj; V. S., Pradeep; S. Jayalekshmi, *Electrochim. Acta* **2017,** *235*, 210-222.

17. S. Wang; H. Chiu; G. P. Demopoulos, *J. Power Sources* 2024, 595, 234061.

18. F. Chen; D. Yang; W. Zha; B. Zhu; Y. Zhang; J. Li; Y. Gu; Q. Shen; L. Zhang; D. R. Sadoway, *Electrochim. Acta* **2017**, *258*, 1106-1114.

19. J. H. Choi; C. H. Lee; J. H. Yu; C. H. Doh; S. M. Lee, *J. Power Sources* **2015**, *274*, 458-463.

20. J. Zhang; N. Zhao; M. Zhang; Y. Li; P. K. Chu; X. Guo; Z. Di; X. Wang; H. Li, *Nano Energy* **2016**, *28*, 447-454.

21. X. Tao; Y. Liu; W. Liu; G. Zhou; J. Zhao; D. Lin; C. Zu; O. Sheng; W. Zhang; H. W. Lee; Y. Cui, *Nano Letters* **2017**, *17*, 2967-2972.

22. C. Zhao; X. Zhang; X. Cheng; R. Zhang; R. Xu; P. Chen; H. Peng; J. Huang; Q. Zhang, *Proc. Nati. Acad. Sci.* USA **2017**, *114*, 11069.

23. M. Keller, G. B. Appetecchi, G. T. Kim, V. Sharova, M. Schneider, J. Schuhmacher, A. Roters, S. Passerini, *J. Power Sources* **2017**, *353*, 287-297.

24. S. H. S. Cheng, C. Liu; F. Zhu; L. Zhao; R. Fan, C. Y. Chung; J. Tang; X. Zeng; Y. He, *Nano Energy* **2021**, *80*, 105562.

25. J. Bae, Y. Li, F. Zhao, X. Zhou, Y. Ding, G. Yu, *Energy Storage Mater*. **2018**, *15*, 46-52.

26. Z. Wan, D. Lei, W. Yang, C. Liu, K. Shi, X. Hao, L. Shen, W. Lv, B. Li, Q. H. Yang, F. Kang, Y. B. He, *Adv. Funct. Mater.* **2019**, *29*, 1805301.

27. a) S. Xu, Z. Sun, C. Sun, F. Li, K. Chen, Z. Zhang, G. Hou, H.-M. Cheng, F. Li, *Adv. Funct. Mater.* **2020**, *30*, 2007172; b) K. Pan, L. Zhang, W. Qian, X. Wu, K. Dong, H. Zhang, S. Zhang, *Adv. Funct. Mater.* **2020**, *32*, 2000399; c) X. Yang, Q. Sun, C. Zhao, X. Gao, K. Adair, Y. Zhao,

J. Luo, X. Lin, J. Liang, H. Huang, L. Zhang, S. Lu, R. Li, X. Sun, *Energy Storage Mater.* **2019**, *22*, 194-199.

Chapter 6: 4.8 V High-Voltage All-Solid-State Lithium-Metal Batteries

Bridge: The work described in Chapter 5 led to the development of a novel type of porous ceramic (c-Al-LLZO)-based hybrid SSE infiltrated with PEO-LiTFSI that demonstrates high Li-ion transference number (0.71) and ionic conductivity (0.547 mS cm^{-1}) at 25 ℃. The ASSLB (Li/HSE/LFP) enabled by the ceramic-based HSE exhibits high discharge specific capacity of 163 mAh g^{-1} at 0.1 C and average Coulombic efficiency greater than 99 % after 50 cycles. This novel design opens new possibilities in the pursuit for next generation high-performance ASSLBs. However, the designed hybrid SSEs have a thickness of around 1 mm, which is unfavorable for improving the energy density of the all-solid-state lithium batteries. Moreover, the PSE employed, PEO-LiTFSI, could only maintain stability up to 4.2 V (vs. Li^+/Li) during charge-discharge cycling, which motivated the work in this Chapter, to develop another type of ceramic-based hybrid SSE with reduced thickness as well as compatibility with high voltage cathode materials (4.8 V).

This chapter addresses the 3rd objective of thesis, i.e., to develop an ultra-thin ceramic-based hybrid solid-state electrolyte for high-voltage all-solid-state lithium batteries. More specific the following advances are made in this Chapter vis-à-vis the system described in Chapter 5: The synthesis of nanoscale garnet is modified with the aid of organic additives leading to production of mesoporous particles of c-Al-LLZO. The mesoporous garnet powder is engineered via sintering to a thin (~100 μm porous scaffold that is infiltrated with PVDF-LiTFSI as conductive solid polymer, which after successful testing in symmetric cells was assembled into ASSLB with Li metal as anode and TiO_2-coated NMC622 cathode capable for high-voltage operation.

This chapter is replication of a manuscript to be submitted. The citation information for this chapter is provided below:

Senhao Wang, Stephanie Bessette, Raynald Gauvin and George P. Demopoulos. 2024. "4.8 V all-solid-state lithium-metal batteries enabled by high-conductive and interface-friendly garnet-based composite solid electrolytes" (submitted).

Abstract

The garnet-type solid electrolyte (SE) presents poor wettability with electrodes, resulting in an extremely large interfacial impedance. Herein, a highly conductive and interface-friendly garnet-based composite solid electrolyte (CSE) is constructed by comprising a cubic $Li_{6.1}Al_{0.3}La_3Zr_2O_{12}$ (LLZO) porous ceramic framework and poly (vinylidene difluoride) (PVDF) with a 3D-continuous structure. The La-N and La-F bonds between ceramic-polymer two-phase promoting the dissociation of Li salt having as result the production of agile Li^+ ions giving rise to highly efficient transport across the solid electrolyte structure.These coupling effects contribute to a high ionic conductivity (0.437 mS cm^{-1}) and lithium transfer number t_{Li^+} (0.72) at 25 ℃, while simultaneously enable high electrode/electrolyte interfacial stability under high cut-off voltage. The TiO_2-coated $LiNi_{0.6}Co_{0.2}Mn_{0.2}O_2$/ceramic-based CSE/Li full solid-state batteries stably cycle over 200 times from 3 to 4.8 V with interfaces between ceramic-based CSE and cathode remaining ultra-stable.

6.1.Introduction

Rechargeable lithium-ion batteries (LIBs) have risen to leading energy storage technology due to their relatively high volumetric and gravimetric energy densities vis-à-vis other energy storage devices.[1-3] However, the drastic growth of LIB-powered electric vehicle transportation requires further increase in energy density and safety by replacing the graphite anode with lithium metal anodes. However, lithium metal is electrochemically unstable in contact with organic liquid electrolytes, but also suffers from the formation of lithium dendrites during Li^+/Li plating-stripping cycling which may pierce the separator, resulting in short-circuit and serious safety hazard.[4-6] The use of solid-state electrolytes can significantly overcome these obstacles enabling the safe use of lithium (Li) metal anodes. Generally, there are three types of solid-state electrolytes (SEs): ceramic, polymer, and composite SEs (CSEs). Among them, ceramic SEs commonly exhibit relatively high ionic conductivity at ambient temperature, good electrochemical stability, and excellent mechanical strength.[7,8] Particularly, the cubic garnet-type SSEs exhibit high ionic conductivity of approximately 1 mS cm^{-1}, a very wide electrochemical window up to 5.5 V, and very good chemical/electrochemical stability against lithium metal.[9] However, the cubic garnet-type ceramic SEs suffer from poor contact with electrodes resulting in high interfacial resistance.[10-13] Compared to ceramic SEs, polymer solid-state electrolytes (PSEs) are particularly attractive due to their

flexibility, facile preparation and low-resistance interface with electrodes.[14,15] However, unlike liquid electrolytes (LEs) with their high dielectric constant (relative permittivity) and low-viscosity solvents that facilitate the dissociation of Li salts and ion transport to achieve high ionic conductivity,[16] PSEs have a limited ability to promote the dissociation of Li salts and ion transport, leading to a quite low ionic conductivity.[17] Adding ionic conductive inorganic fillers to PSEs, thus forming composite solid-state electrolytes (CSEs), can reduce the polymer crystallinity and construct a conductive three-dimensional (3D) network for Li-ion transport.[18-20] Generally, CSEs could overcome the drawbacks of individual ceramic and polymer solid electrolytes, exhibiting high ionic conductivity at ambient temperature (10^{-3} ~10^{-4} S cm^{-1}), improved mechanical strength, chemical/electrochemical stability, as well as wettability with electrodes.[21,22] Specifically, two types of CSEs can be classified based on the matrix employed, polymer-based and ceramic-based CSEs, respectively. The polymer-based CSEs, where ceramic fillers are introduced into a PSE matrix, are known to reduce the crystallization of the PSE and lower the interactions between Li^+ and polymer chains, resulting in improved efficiency of Li^+ migration. However, their ionic conductivity can be improved only to 10^{-4} S cm^{-1} by incorporating conductive nanofillers such as $Li_7La_3Zr_2O_{12}$ (LLZO) and $Li_{0.33}La_{0.56}TiO_{3-x}$ (LLTO)-type ceramic SEs.[23,24] The low ionic conductivity of the polymer-based CSEs is attributed to low concentration of movalbe Li^+ and the space charge layer (CSL) between the polymer and inorganic fillers, which greatly blocks Li^+ transport.[25-29] Moreover, the amount of ceramic fillers within the polymer-based CSEs is limited, which implies the introduced ceramic fillers do not effectively form an interconnected reinforcement improving only modestly the mechanical strength. In fact, in the system of polymer-based CSEs, Li^+ conductivity and elastic modulus are in conflict. Polymer chains with high ionic conductivity, low crystallinity, and high mobility are commonly desired, resulting in mechanically soft strength. This dichotomy could be overcome with ceramic body-based CSEs, that are strong mechanically thus suppressing Li dendrite growth while enabling fast Li^+ migration. More particularly, building CSEs having as ceramic body, a 3D engineered scaffold infiltrated with conductive polymer has the potential of providing viable ionic transport capabilities, good chemical/electrochemical stability, low interfacial resistance, and great mechanical strength. A such SSE structure is designed and presented shown to be advantageously interfaced in all-solid-state lithium metal battery for high voltage and energy density operation.

Herein, a ceramic-based CSE with high Li^+ conductivity and wide electrochemical window is developed by compositing porous cubic LLZO framework and conductive PVDF PSE (Figure 1). The novel-designed porous cubic garnet ($Li_{6.1}Al_{0.3}La_3Zr_2O_{12}$, LLZO) ultra-thin framework (122 μm) with 3D continuous ion-conductive channels exhibits high Li^+ conductivity, high porosity (45.74 %), and particularly, wide electrochemical window (5.08 V) for pairing high-voltage cathode materals. The as-prepared ceramic CSEs possess high ceramic-mass content (~ 93%), which can mechanically suppress the growth of Li dendrites. The porous structure of the LLZO framework provides a high-volume occupancy of PVDF-LiTFSI, moreover, there are two types of metal-atom bondings formed, specifically, La from the LLZO framework with N from $TFSI^-$ groups, and F from the PVDF polymer chains, respectively. The coupled LLZO-$TFSI^-$ facilitates the dissociation of Li salts, promotes the Li^+ transport and reduces the interfacial impedance between ceramic and polymer phases, which contributes to a high ionic conductivity and Li transfer number of the ceramic-based CSE at 25 ℃ (0.437 mS cm^{-1}, and 0.72). The ceramic-based CSE is advantageously interfaced with TiO_2-coated $LiNi_{0.6}Co_{0.2}Mn_{0.2}O_2$ (TiO_2@NCM622) and Li metal shown to be characterized by uniform Li^+ transport electric field enabling homogeneous Li stripping and plating (dendrite-free). The high-voltage solid-state Li/ceramic-based CSE/TiO_2@NCM622 battery (0.2C, from 3 to 4.8 V) delivers a high capacity (110.4 mAh g^{-1} after 200 cycles) and high energy densities 398.3 and 376.1 Wh kg^{-1} at cell level (at 100 and 200 cycle, respectively) higher than the current United State Advanced Battery Consortium LLC (USABC) goals for advanced high-performance batteries for electric vehicle applications (350 Wh kg^{-1})[30] and stable cycling for 200 cycles showing excellent potential for application thanks to the porous ceramic scaffold-based CSE architecture.

6.2. Experimental section

6.2.1. Preparation of porous cubic LLZO powders

The porous cubic-phase $Li_{6.1}Al_{0.3}La_3Zr_2O_{12}$ (LLZO) powders were prepared as described in the schematic of Figure 6.1 with the flowchart given in Figure A.3.1. The synthesis route is based on our pervious research on low-temperature crystallization of nano-scale cubic garnet.[31] $La(NO_3)_3{\cdot}6H_2O$ (99.9%, Aldrich), $Al(NO_3)_3{\cdot}9H_2O$ (99.99% trace metals basis, Sigma-Aldrich), and $LiOH{\cdot}H_2O$ (99.95% trace metals basis, Sigma-Aldrich) were dissolved in DI-water at room temperature, with the amount La added in excess of stoichiometry to compensate for its solubility

limitation in the elevated pH range. More precisely, in this system represented as suspension A, the stoichiometric ratio was Li: Al: La = 6.1: 0.3: 3.0154. Due to the spontaneous hydrolysis reaction, a milky white precipitate forms. Meanwhile, separately a stoichiometric amount of $ZrO(NO_3)_2$ (35 wt.% in dilute nitric acid, ≥ 99% trace metals basis, Aldrich) was dissolved in DI-water at room temperature. Polyethylene glycol (PEG, MW= 2000, 6000, and 20000) (Sigma-Aldrich) and propylene glycol (PG) (Fisher Scientific) with various molar ratios were added as porous template and plasticizer respectively presented as solution B. After the dissolution and hydrolysis reactions were complete in both solutions, solution B was added dropwise into suspension A and mixed thoroughly (at this point, the pH value of this mixed system was around 6). To further promote their co-precipition, concentrated LiOH solution (3M) was added dropwise at a rate of 1mL / min, to the optimal pH value of 10.5 that we have found previously to produce cubic garnet with best ionic conductivity.[31] After this co-precipitation step, the suspension was directly transferred into a 100 mL autoclave (hydrothermal aging step), which was then heated to 200 ℃ for 4 hours (h) (2 h for ramping and 2 h for dwelling) followed by cooling down to RT naturally. After the hydrothermal aging step, the wet precipitated solids were recovered via centrifugation and washed thoroughly with DI water and isopropanol. Then the as-prepared precipitates were dried at 80 ℃ in the vacuum oven overnight. The dried precipitates were then mixed with the designated quantity of $LiOH{\cdot}H_2O$ by ball milling in ZrO_2 container loaded with 1mm ZrO_2 balls (with the mass ratio of powder and balls of 1:6) at 650 rpm for 10 cycles of 10 min each (3 min grinding-7 min resting) with isopropanol as the liquid mediator (4 mL). The amount of Li added was 7.5 times that of Al corresponding to the stoichiometry of $Li_{6.1}Al_{0.3}La_3Zr_2O_{12}$. Finally, the ground hydrothermal precursor solids were recovered after evaporation of the isopropanol in a rotary evaporator at 60 ℃ under vacuum and drying at 80 ℃ in the vacuum oven overnight. The completely dry precursors were sintered at 240 ℃ for 2 h under the air atmosphere to burn out the polymer additives (template and plasticizer), then were sintered at 800 ℃ for 6 h to obtain the cubic LLZO phase with primary porous structure.

6.2.2. Preparation of ultra-thin porous cubic LLZO framework

As-produced powders were first dispersed in EtOH with 2 wt.% polyacrylic acid (MW = 2000) dispersant, using an ultrasonic horn at 100 W for 30 min. The suspension was let to settle for 4 h to allow large particles to aggregate. The supernatant was decanted, and the recovered powder was dried. Collected powder, polyvinyl butyral (PVB, Sigma-Aldrich), benzyl butyl phthalate (BBP,

Sigma-Aldrich) at 7:2:1 weight ratio, and acetone were added to ZrO_2 jar and ball-milled with 3.0 mm diameter spherical ZrO_2 beads (with the mass ratio of mixture and ball of 1:6) for 1 h to homogenize the suspension. Suspensions were drop casted on Mylar substrate. Dried green films were manually peeled off the Mylar substrate and punched to selected sizes as presented in Figure A.3.11. Punched green films were placed in between graphite foils and heated to 1100 ℃ under Ar flow (100 mL min^{-1}). The graphite foil was used to maintain the integrity and avoid contamination or reaction with common ceramic crucibles. The resulting films had carbon deposits that were removed by reheating to 700 ℃ for 30 min under an air atmosphere.

6.2.3. Preparation of ceramic-based CSEs: PVDF/LiTFSI in porous cubic LLZO frameworks

Poly(vinylidene fluoride) (PVDF) (MW = ~ 543000, Sigma-Aldrich) and lithium bis(trifluoromethane sulfonyl)imide (LiTFSI) (≥ 98.0%, Tokyo Chemical Industry Co.) with a weight ratio of 3:1 were dissolved in N-methyl pyrrolidinone (NMP, 99.5% Sigma-Aldrich) with a polymer concentration of 15%. Then, the mixture is stirred for 24 h at 55 ℃ in a sealed bottle to obtain the homogeneous gel. To prepare the ceramic-based composite solid electrolytes (CSEs), the as-prepared porous cubic LLZO frameworks were immersed into PVDF/LiTFSI gel for 48 h and dried in the vacuum oven at 60 ℃ for 24 h to remove any residual NMP solvent.

6.2.4. Preparation of the TiO_2 coated NMC622 cathode

Tetrabutyl titanate (TBOT) as Ti source (0.1918 g corresponds to 1.5 wt.% TiO_2) was added into 40 mL ethyl alcohol and stirred for 1 h, then 3 g $LiNi_{0.6}Co_{0.2}Mn_{0.2}O_2$ (NCM 622) (MSE supplies) powder was added into the mixed solution and continually stirred for another 2 h. Next, 0.4 mL ammonium hydroxide (NH_4OH) were slowly added into the solution under stirring for another 2 h. Afterwards, the residual powder was collected by centrifugation and washed with ethyl alcohol and deionized water thoroughly, then dried under vacuum at 120 ℃ overnight. The final product was obtained by annealing the dried powder at 500 ℃ under air atomsphere for 5 h.[32-34] The obtained TiO_2 coated NCM622 powder, carbon black (MSE supplies), and PVDF (HSV900 PVDF binder MTI corporation) with LiTFSI (weight ratio 3:1), are mixed in NMP solvent with a weight ratio of 8:1:1 and coated on an aluminum foil after stirring into a homogeneous suspension. Then the electrode was dried at 50 ℃ for 6 h and further dried in a vacuum oven at 80 ℃ overnight to

remove NMP solvent. The dried electrode is punched into disks with a diameter of 9 mm, of which the mass loading is about 13 mg cm^{-2}.

6.2.5. Material characterization

X-ray diffraction (XRD) was conducted for the samples using a Bruker D8-Advantage powder diffractometer using Co-Kα radiation with wavelength λ = 1.78892 Å, 35 kV/45 mA, 2θ from 10 to 70° in a step of 0.02°. BET (Brunauer-Emmett-Teller) and BJH (Barrett-Joyner-Halenda) pore size analysis were conducted on Micromeritics TriStar 3000. The morphology characterization of the samples was examined using Hitachi SU3500 and SU8000 cold-field emission scanning electron microscopes (CFE-SEM) (Hitachi High Technologies). Energy dispersive X-ray (EDS) elemental mapping was conducted to acquire the elemental distribution in as-synthesized samples. X-ray photoelectron spectroscopy (XPS) was carried out on Thermo Scientific K-Alpha to determine the elemental state of samples. Thermogravimetric analysis (TGA) was examined with Discovery 5500 from TA Instruments at a ramp rate of 10 ℃ min^{-1} from 25 to 700 ℃ under air atmosphere. Images of SAED patterns and lattice fringes were obtained with a Thermo Scientific Talos F200X G2 transmission electron microscope (TEM) at 200 kV. A JEM-ARM Model 200F TEM at 200 kV to acquire high-angle annular dark-field (HAADF) images. EDS was conducted to acquire the elemental distribution of TiO_2-coated NCM622 particles before and after cycling. Hitachi high-technologies ETHOS NX5000 focused-ion and electron-beam system was employed to analyze the cycled ASSBs.

6.2.6. Electrochemical measurements

To evaluate the ionic conductivity of the as-prepared ceramic-based CSEs, electrochemical impedance spectroscopy (EIS) was employed, using stainless steel (SS) as blocking electrodes. The EIS measurements were carried out from 25 ℃ (RT) to 80 ℃ with 10 ℃ steps using an electrochemical workstation (Bio-Logic) in potentiostatic mode between 10^6 Hz and 1Hz at an open-circuit voltage (OCV); the cells of SS | Ceramic-based CSE | SS were kept at each test temperature for 30 min to reach thermal equilibrium. The resistances were determined by fitting the Nyquist plot with the Equivalent Electric Circuit using the Zview-fit method available in EC-Lab software. Equations (A.3.2) and (A.3.3) in Appendixes A.3. (supplemental information for Chapter 6) were used to calculate the ionic conductivity and activation energy of Li-ion migration respectively.

To calculate the lithium-ion transference number and conduct the lithium-ion stripping-plating cycling, Li | Ceramic-based CSE | Li symmetric cells were fabricated. The lithium-ion transference number of the ceramic-based CSE was measured by DC polarization and AC impedance in symmetric cells based on equation (S4) in SI.

The electrochemical window was determined using the linear sweep voltammetry (LSV) method in SS | ceramic-based CSE | Li batteries from 3 to 6 V (vs Li^+ / Li) at a scanning rate of 1 mV s^{-1}.

The lithium stripping-plating cycling was conducted under 0.1 and 0.5 mA cm^{-2} current densities with a period of 30 min employing an MTI battery tester (BST8-WA, MTI corporation). Further, EIS was conducted to measure the interfacial resistance before and after stripping-plating cycling.

For the all-solid-state batteries, the coin-type Li | Ceramic-based CSE | TiO_2@NCM622 batteries were fabricated in a glove box. Before the charge-discharge cycling, the as-fabricated batteries were stored in an oven at 60 ℃ overnight then cooled down naturally to RT, to obtain good interfacial contact between electrodes and ceramic-based CSE. The charge-discharge cycling tests were conducted using an MTI battery tester (BST8-WA, MTI corporation) from 3.0 V to 4.5, 4.6, 4.7, and 4.8 V with a 0.2 C rate at 40 ℃. The rate measurements of the Li | Ceramic-based CSE | TiO_2@NCM622 batteries were made under 0.1 C, 0.2 C, 0.5 C, 1 C, and 2 C from 3 to 4.5, 4.6, 4.7, and 4.8 V at 40 ℃. The charge-discharge cycling of the Li | Ceramic-based CSE | TiO_2@NCM622 and Li | liquid electrolyte (LE) | TiO_2@NCM622 batteries were conducted from 3.0 to 4.5 V with a rate of 0.2 C at RT as comparsion.

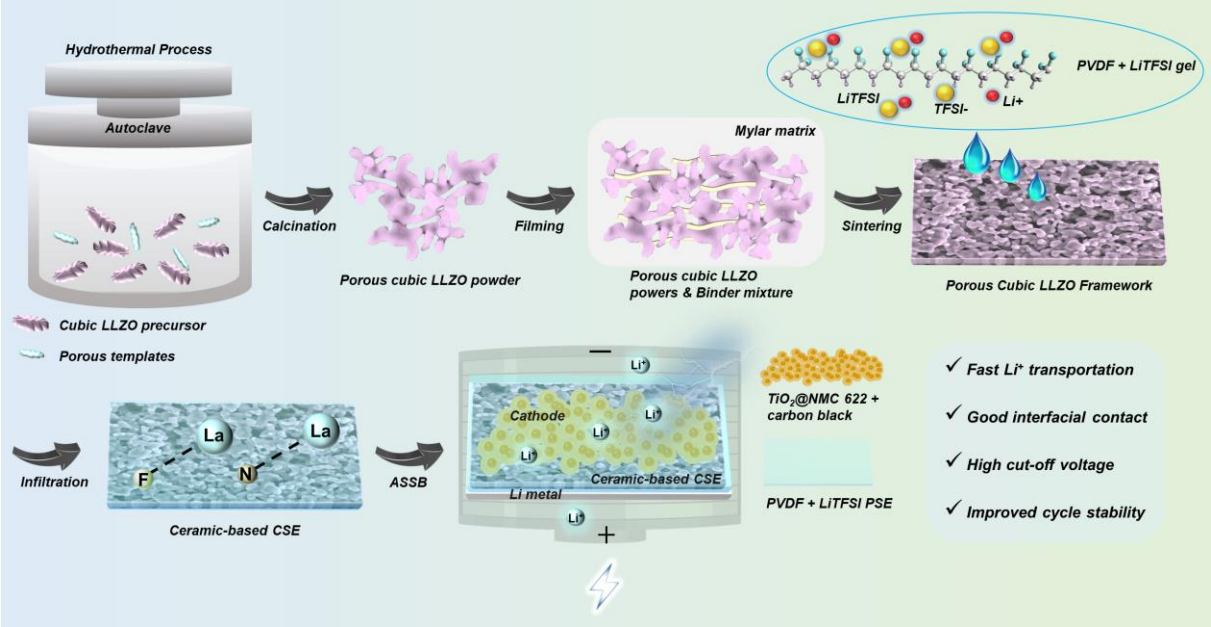

Figure 6. 1. Illustration of the ceramic-based CSE and the Li/ceramic-based CSE/TiO_2@NCM622 solid-state battery.

6.3. Results and Discussions

6.3.1. Characterization of Porous Cubic LLZO Powders

Figure 6.1 illustrates the synthesis process of the ceramic-based CSE and the schematic diagram of the all-solid-state lithium metal battery (ASSB) built with the ceramic-based CSE, Li metal anode, and the high-voltage cathode TiO_2@NCM622. To form porous c-LLZO particles, our earlier reported crystallization of cubic LLZO method[31] was modified by making use organic additives, namely PEG as template and PG as plasticized. The organics were added in four different formulations as described in appendixes A.3. (supplemental information for Chapter 6). Characterization (XRD, SEM, and BET) of the samples obtained from the different formulations is presented in Figures A.3.2-A.3.10. Among the four formulations, the one (No. 4) employing PEG with 20,000 molecular weight and PG at a molar ratio of 2: 0.5 was found to exhibit the pure cubic garnet phase as well as a 3D-continuous porous structure. Thus, it was selected as the porous cubic LLZO powder for further research.

Specifically, the selected porous cubic LLZO powders were prepared through a three-step method including co-precipitation, hydrothermal aging, and calcinations at 300 and 800 ℃ subsequently. As the XRD patterns in Figure 6.2a show, after the hydrothermal step, the precursor powders are

composed of $La(OH)_3$ crystals, along amorphous Zr / Al hydroxides (as discussed in our previous paper)[31] plus the polymer template (PEG MW = 20000 g/mol) and the plasticizer (PG) components. The first calcination step was conducted at 300 ℃ for 2 h under an air atmosphere to burn out the organic components. According to the XRD profile (Figure 6.2a) no crystalline transition occurred during this step as still it exhibits the characteristic peaks of $La(OH)_3$. Lastly, the final calcination was conducted at 800 ℃ for 6 h to promote the crystallization of the cubic LLZO phase, as confirmed by XRD (Figure 6.2a). To evaluate the porous structure of the as-prepared cubic LLZO powders, BET surface area and BJH pore size analysis were employed. As shown in Figures 6.2b and 6.2c, the N_2 adsorption/desorption isotherm curve is classified as the type IV characteristic of mesoporous materials. Moreover, the BJH curve inserted in Figure 6.2b exhibits an infinitely increasing trend suggesting the prepared porous powder is not a close-packed spatial structure, but a 3D-continuous structure with open space, which could be revealed further through the SEM images of the as-prepared porous cubic LLZO powders presented in Figure 6.2d. The EDS results show that the elements are uniformly dispersed in porous cubic LLZO powder (Figure 6.2e).

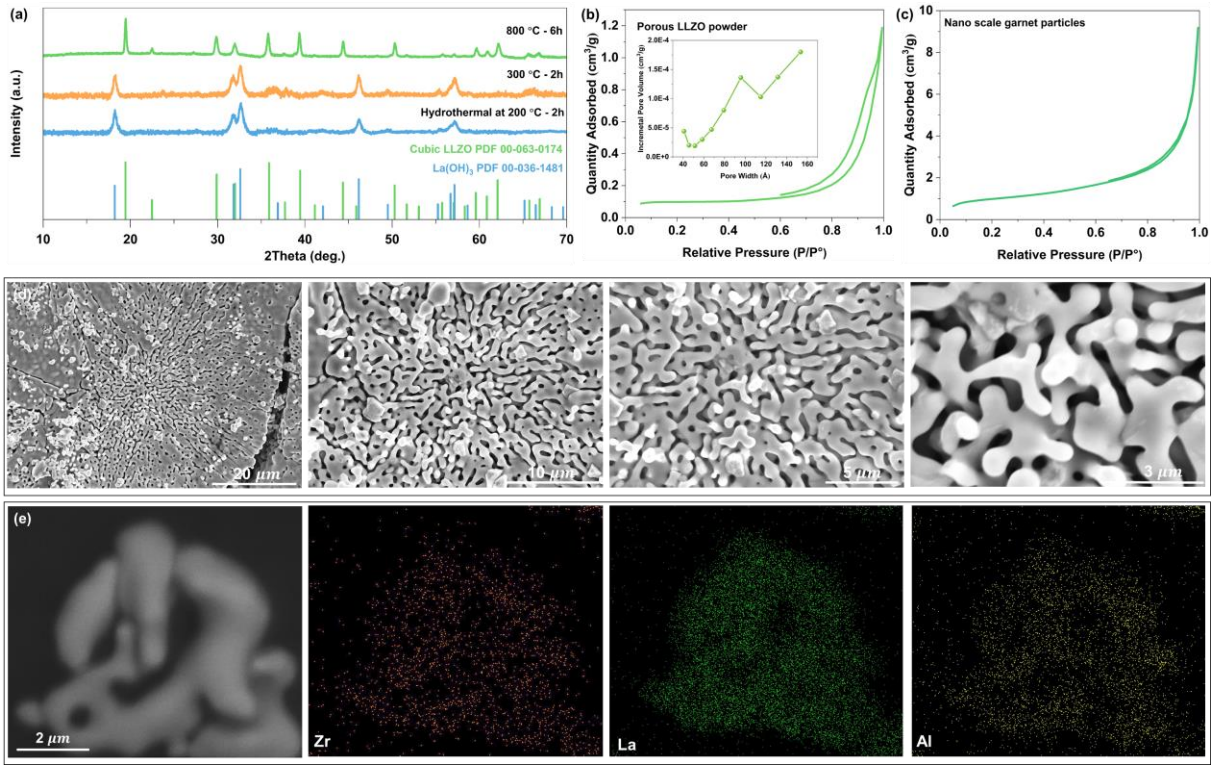

Figure 6. 2. Crystallinity, porous structure, and morphology characterizations of porous cubic LLZO powder. (a) XRD patterns under different synthesis processes, (hydrothermal, initial calcination at 300 ℃ for 2h, and the calcination at 800 ℃ for 6h); (b and c) N_2

adsorption/desorption isotherms of the porous and nano-scale cubic LLZO powders with BJH desorption pore size distribution curve in inset; (d) top-view SEM image; and (e) SEM/EDS mapping.

6.3.2 Characterization of thin porous cubic LLZO framework

As shown by the XRD pattern in Figure 6.3a, the porous LLZO framework is a cubic garnet-type single-phase without other impurities present. SEM images (overview, top-surface, and cross-section) of the porous cubic LLZO framework are shown in Figures 6.3 (b-d) with a digital picture of the ceramic framework disk (8 mm diameter) in inset. The porous structure is seen to be homogeneously dispersed into a solid cubic LLZO membrane. According to the high magnification SEM image of the cross-section (Figure 6.3e) the ceramic skeleton forms a 3D conductive network (yellow dotted line). The porous channels formed are micron-scale conducive to the infiltration of solubilized PSE. The thickness of the porous LLZO skeleton is about 122 μm, which is a very competitive thickness for CSE and could possess higher energy density in practical all-solid-state lithium metal batteries. The EDS results (Figure 6.3f) confirm the even distribution of all garnet constituent elements within the porous cubic LLZO framework.

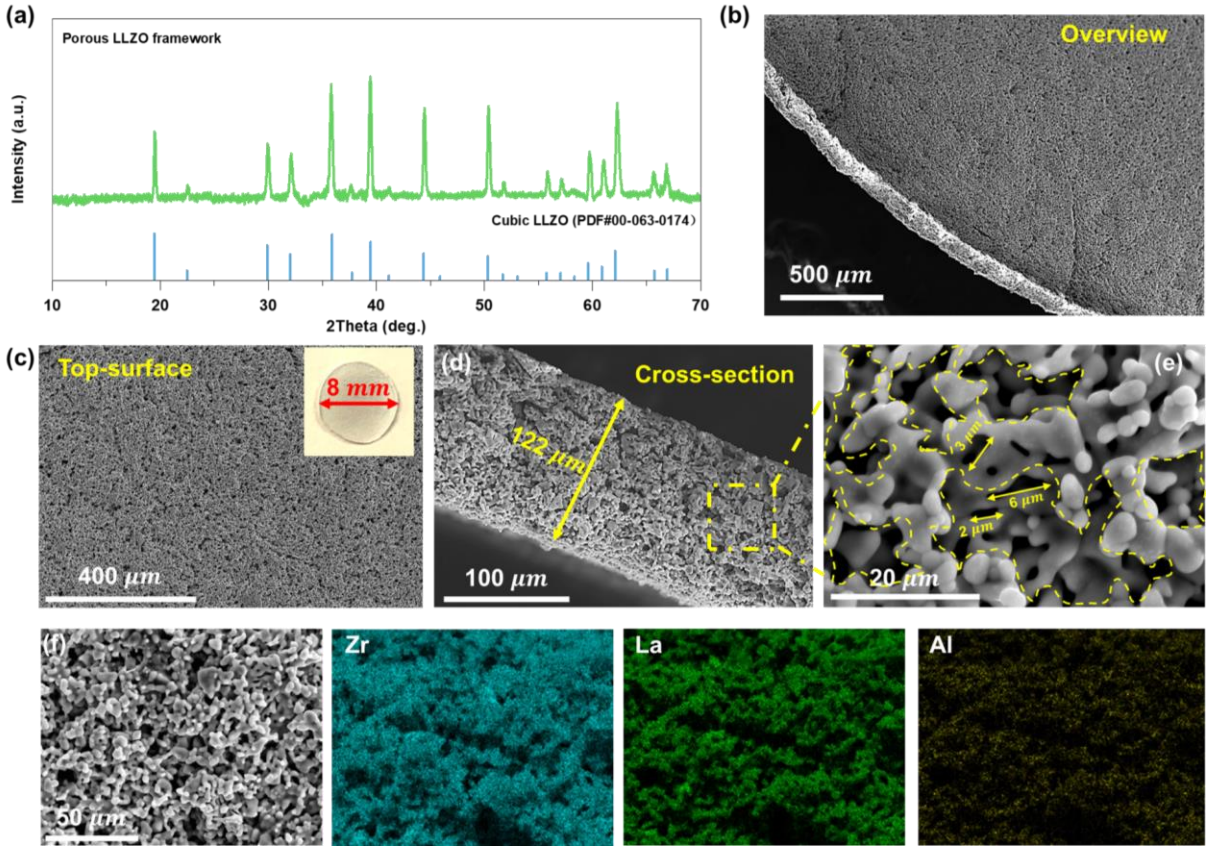

Figure 6. 3. Crystallinity, porous structure, and morphology of 3D cubic LLZO porous framework. (a) XRD pattern and PDF reference of cubic LLZO phase; SEM images (b) overview, (c) top surface with digital picture inset, (d) cross-section, and (e) enlarged view of the selected region; (f) EDS elemental maps.

6.3.3. Characterization of the ceramic-based CSEs

The so-formed porous cubic LLZO framework was infiltrated with PVDF-LiTFSI PSE to engineer the ceramic-based CSE, the XRD patterns of which are shown in Figure 6.4a. As it can be deduced the crystal structure of the cubic-garnet single-phase was not impacted by the polymer infiltration. Thermogravimetric analysis (TGA) results in Figure 6.4b, indicate that the weight percentage of ceramic in CSE is about 93%, ensuring high Li-ion conductivity safety owed to very good mechanical and thermal stability when employed in all-solid-state batteries. As such it could offer efficient suppression of Li dendrites compared to polymer-based hybrid solid electrolytes.

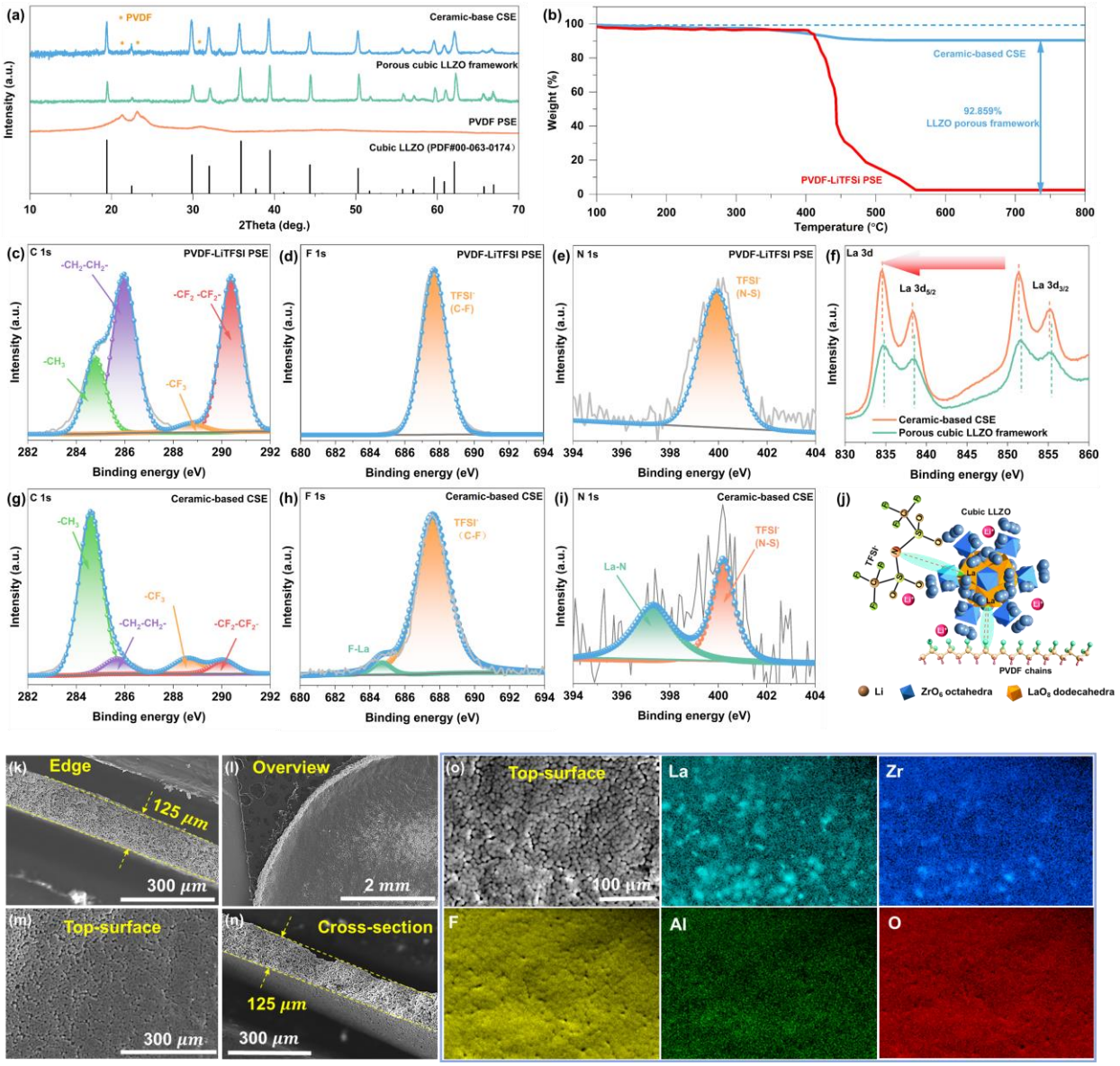

Figure 6. 4. Characterization of thin ceramic-based CSE. (a) XRD patterns of PVDF, 3D continuous porous LLZO framework, and the ceramic-based CSE; (b) TGA curves of the PVDF-LiTFSI PSE film and the ceramic-based CSE; (c-i) XPS spectra of PVDF-LiTFSI PSE and the ceramic-based CSE including C 1s, F 1s, N 1s, and La 3d; (j) the schematic of the interaction between infiltrated PVDF-LiTFSI PSE and porous LLZO framework; (k-n) SEM images of the edge, overview, top-surface, and cross-section, of the ceramic-based CSE; (o) EDS elemental maps.

To determine/reveal the chemical coupling between infiltrated PVDF-LiTFSI PSE and 3D-continuous porous LLZO framework, XPS analysis was performed on cubic LLZO particles, PSE (PVDF-LiTFSI) film, and the cross-section of the ceramic-based CSE (PVDF-LiTFSI in porous LLZO scaffold). In Figure 6.4c, the C 1s spectrum of PSE shows that the peaks are located at

284.78, 285.98, 288.68, and 290.38 eV which are attributed respectively to (-CH_3), (-CH_2-CH_2-), and (-CF_3), (-CF_2-CF_2-). But in CSE (Figure 6.4g), the four peaks shift to lower binding energy by 0.2, 0.4, 0.2, and 0.4 eV respectively, as well as the intensity of peaks attributed to -CH_2-CH_2- and -CF_2-CF_2- decrease while peaks attributed to -CH_3 and -CF_3 increase, indicating chemical surface interaction of some groups in PSE with some metal atoms in porous LLZO skeleton. To elucidate this interaction, XPS is conducted on F 1s and N 1s as presented in Figures 6.4 (d, h) and 6.4 (e, i). The F 1s and N 1s spectra of PSE only exhibit one peak each located at 687.68 eV and 399.88 eV, respectively; these peaks represent -CF_3 and N-S moieties in the $TFSI^-$ group. But in CSE, the corresponding F 1s and N 1s spectra show new peaks appearing at 684.68 eV and 397.28 eV corresponding to La-F and La-N bonding, respectively.[35,36] These new peaks provide clear indicators of strong chemical anchoring of PVDF-LiTFSI PSE onto LLZO porous scaffold. Specifically, the La-N bonding forms between La atoms in LLZO and N from $TFSI^-$ group, while the La-F bonding forms between La atoms and F from PVDF chains. Additionally, Figure 6.4f shows the La 3d spectrum of the CSE to display two sets of peaks located at 855.18, 851.38 eV (La $3d_{3/2}$), and 838.48, 834.48 eV (La $3d_{5/2}$), which shift to low binding energy by 0.2, 0.1, 0.2, and 0.1 eV compared with the peaks of porous LLZO framework itself, providing another proof of the bonding of the La atoms. Thus, it is proposed that the robust La-F and La-N bonding between the infiltrated PSE and 3D-continuous porous LLZO framework results in strong and homogeneous contact of PSE inside/outside the porous structure as presented in Figure 6.4j. Supplementary XPS surveys of the porous LLZO framework, PSE film, and the ceramic-based CSE are shown in Figure A.3.12. SEM images of the ceramic-based CSE are shown in Figures 6.4 (k-n). The results show that the thickness of the ceramic-based CSE is about 125 μm which is exceptional for ceramic-based (over 93%) composite solid-state electrolytes and very competitive for improved energy density of all-solid-state batteries. The EDS results shown in Figure 6.4o further confirm the homogeneous (intimate) composition of the polymer-in porous ceramic composite solid electrolyte.

6.3.4. Synergetic Li^+ migration capability

Ionic conductivity is the key property for a good solid electrolyte. This was evaluated for the as-designed ceramic-based CSEs employing electrochemical impedance spectroscopy (EIS). The ionic conductivity results under various temperatures of four types of electrolytes: the ceramic-

based CSE, the polymer-based CSE (LLZO particles in PVDF matrix), pure cubic LLZO SE, and pure PVDF-LiTFSI PSE are shown in Figures 6.5 (a and b). Based on equations (A.3.2 and A.3.3), the ceramic-based CSE has the highest ionic conductivity, reaching 0.437 mS cm^{-1} at 25 ℃ and has the lowest activation energy of 0.1905 eV, demonstrating very good capability for Li^+ transport and low temperature dependence. In contrast, the PVDF-LiTFSI and polymer-based CSE (cubic LLZO particles in PVDF matrix) have a relatively high E_a (0.3158 and 0.2258 eV), suggesting that the polymer matrix has a high Li-ion migration barrier. Interestingly, the E_a values obtained in other LLZO-PVDF composite solid electrolyte systems are higher than the value of the as-designed ceramic-based CSE here.[37-40] This good capability for Li^+ migration in the ceramic-based CSE is on one part due to the defect-free porous cubic LLZO skeleton that possesses high intrinsic ionic conductivity and promotes the dissociation of lithium salt; and on the other part the molecular bonding of La with $TFSI^-$ groups and PVDF chains that ensures a 3D-continuous two-phase with low interface impedance, providing fast migration pathways for Li-ion even faster than in LLZO alone (Figure 6.5b).

Li-ion transference number (t_{Li^+}) is also crucial for the development of practical all-solid-state lithium batteries. The t_{Li^+} of three types of prepared SEs was determined using equation (S4) in SI and presented in Figure 6.5c and Figures A.3.13 and A.3.14. The as-prepared ceramic-based CSE exhibits a very high t_{Li^+} of 0.72, which is much higher than the PVDF-LiTFSI PSE (~0.25) (Figure A.3.13) and polymer-based CSE (cubic LLZO particles in PVDF matrix) (~0.31) (Figure A.3.14). A comparison of lithium-ion transference number and ionic conductivity is presented in Figure 6.5d (four different types of SE). Among them, the as-designed ceramic-based CSE demonstrates the highest performance. This is mainly due to the fact that the PSE does not have ion transport selectivity, as opposed to garnet ceramic electrolyte that is single ion conductor. Moreover, in the composite structure, the high symmetry of the PVDF ($-CH_2-CF_2-$) chains which yields a highly crystalline structure restricting segment movement and as such the migration of Li^+, is not favoured due to the molecular bonding of PVDF-LiTFSI PSE with porous LLZO structure. In other words, it is postulated the interfacial polymer-ceramic bonding to break the high symmetry of the polymer thus facilitating the transport of Li^+. This increased t_{Li^+} enables lower concentration polarization as well as a reducing in the driving force for Li dendrite growth.

The electrochemical window (EW) of the as-designed CSE was evaluated using linear sweep voltammetry (LSV) form 3 – 6 V *vs.* Li/Li^+ with Li / ceramic-based CSE / SS cells. The stable window extends to 5.08 V (Figure 6.5f), which is higher than the pure PVDF-LiTFSI PSE (4.4 V).[41] The high-voltage stability exhibited by the ceramic-based CSE is mainly due to (i) electrochemical stability of the porous cubic LLZO framework (high concentration of ceramic in the CSE system), (ii) the formed molecular bonding of the polymer-ceramic two-phase composite, (iii) the good electrochemical stability of cubic LLZO itself with lithium metal that avoids early-stage oxidation. Figure 6.5g summarizes the ionic conductivity, Li^+ transference number and electrochemical window of LLZO-PVDF composite solid electrolyte systems (with different ratios of each component) reported in previous research works. It could be seen that the present ceramic-based CSE exhibits remarkable electrochemical properties. Therefore, the as-designed ceramic-based CSE is endowed with fast Li^+ transport and good electrochemical stability that warrantees its further application in ASSBs with advanced performance.

6.3.5. Interfacial stability and lithium dendrite suppression

To evaluate the interfacial stability and dendrite inhibition ability against lithium metal anode of the ceramic-based CSE, Li / ceramic-based CSE / Li symmetric cells were assembled and tested. The schematic diagram of the Li symmetric cell is shown in Figure 6.5h. Long-term interfacial stability is critical for the stable operation of solid-state batteries, and this can be analyzed by constant current cycling tests as shown in Figures 6.5e. The results indicate that the ceramic-based CSE did not short-circuit at current densities of 0.1 and 0.5 mA cm^{-2} for 1000 h. The magnification of the galvanostatic curves from 995 to 1000 hours is presented in Figure A.3.15. Even at the higher current density of 0.5 mA cm^{-2}, the symmetric cell still recovers to stable cycling after a short-term slight polarization. The SEM images and EDS results of the cycled (after 1000 h) interface at 0.5 mA cm^{-2} between the ceramic-based CSE and Li metal as presented in Figure 6.5 (i-l), exhibit good interfacial contact with no signs of physical cracking or element transition. Therefore, the ceramic-based CSE has excellent stability against Li metal, and this is due mainly to fast ionic transport and uniform electric field stemming from the CSE architecture and microstructure, lower interfacial impedance, and good chemical/electrochemical stability. Moreover, since the cumulative cycling capacity is the product of cycling current and time in a symmetric cell, it is deduced the ceramic-based CSE structure to resist lithium dendrite penetration.

On this basis, the as-designed ceramic-based CSE is judged highly promising for building ASSBs with increased energy density and safety.

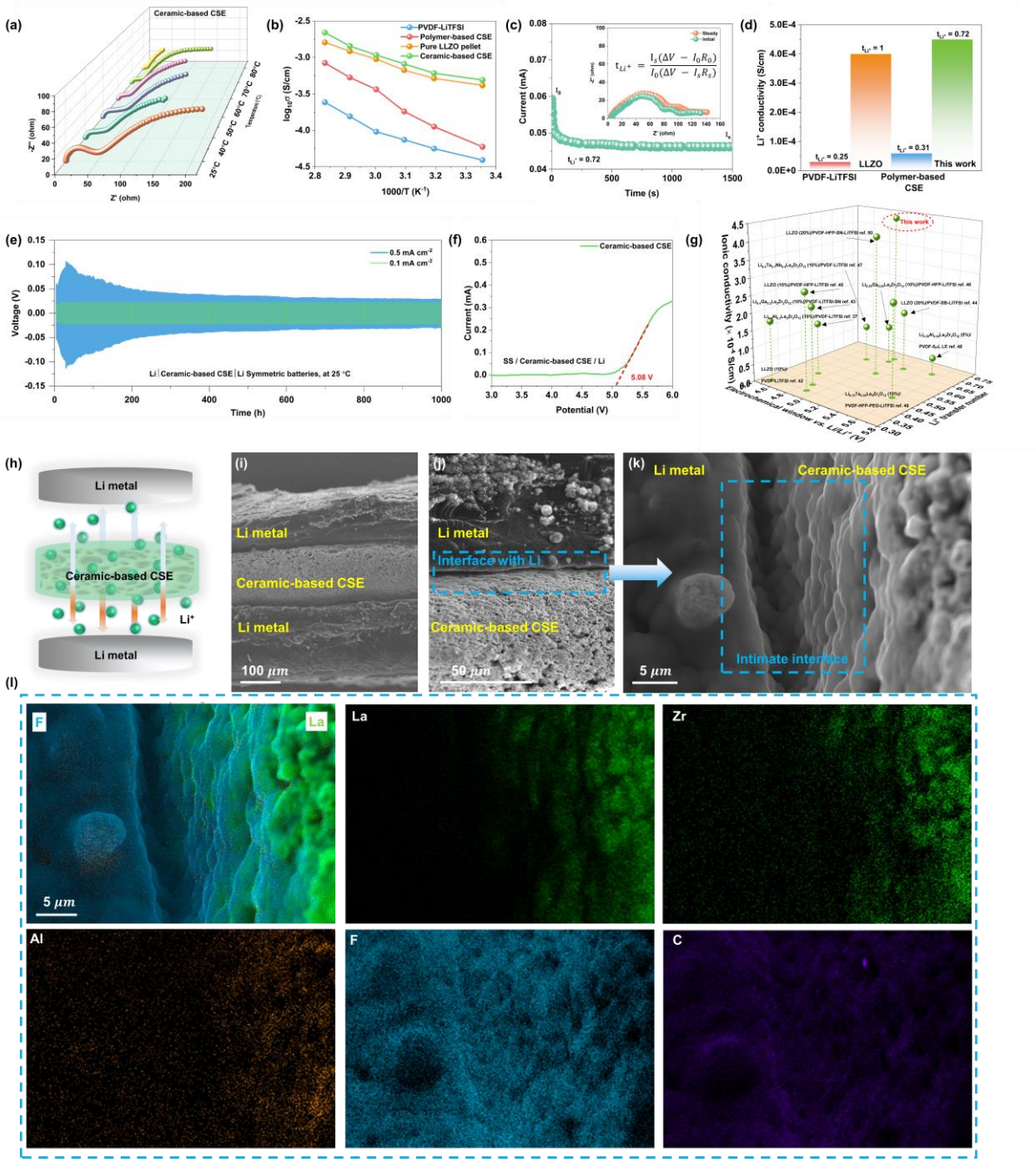

Figure 6. 5. Electrochemical characterizations of the ceramic-based CSE. (a) The EIS plots from 25 ℃ to 80 ℃); (b) Arrhenius plots of the ceramic-based CSE, cubic LLZO, PVDF-LiTFSI film, and polymer-based CSE (cubic LLZO in PVDF matrix); (c) polarization curve and EIS of the symmetric battery before and after polarization at 25 ℃; (d) comparison of Li^+ transference numbers and ionic conductivities; (e) galvanostatic curves of the Li symmetric cells at 0.1 and 0.5 mA cm^{-2}; (f) LSV curve at room temperature with scan rate 10 mV s^{-1} from 3 to 6 V; (g)

comparative Li^+ transport capacity and electrochemical window of (LLZO-PVDF)-based composite solid-electrolytes from different refs;[37, 42-50] (h) schematic diagram of Li symmetric battery; (i-k) SEM images of the interface between the ceramic-based CSE and Li; (l) EDS mappings of the cycled interface between Li metal and the ceramic-based CSE.

6.3.6. Full battery Performance

To demonstrate the applicability of the ceramic-based CSE in practical high-voltage ASSBs, we utilized TiO_2-coated $LiNi_{0.6}Co_{0.2}Mn_{0.2}O_2$ (TiO_2@NCM622) as cathode and Li metal as anode to fabricate coin-type garnet-based ASSBs (Figure 6.6a). The characterization of the TiO_2@NCM622 cathode (crystalline structure and particle morphology) is presented in Figures A.3.16 to A.3.18. The structural integrity of the as-assembled TiO_2@NCM622 / ceramic-based CSE / Li ASSB (before cycling) is evaluated with the SEM and EDS mapping images presented in Figure 6.6b, which clearly show tight contact of the interfaces between CSE and cathode or Li metal. The interfacial boundaries are clear without elemental transitions before charge-discharge cycling. Specifically, as seen from the morphologies and elemental distribution (C and F) at cathode / ceramic-based CSE interface (Figure A.3.19), the conductive PVDF-LiTFSI PSE from both cathode and CSE components forms a homogeneous interfacial layer that provides integrity and unimpeded interfacial Li-ion conduction.

The charge-discharge cycling results of the as-assembled TiO_2@NCM622 / ceramic-based CSE / Li ASSBs from 3 - 4.5 V at 0.1C and 25 ℃ are shown in Figures A.3.21 (a and b), where it can be observed that the capacity is 132.6 mAh g^{-1} after 50 cycles, with a capacity retention of 82% and an average Coulombic efficiency of more than 99%. The capacity fade is similar to the conventional NCM batteries with liquid electrolyte as demonstrated in Figure A.3.20. To further explore the stability of the as-designed ASSBs under high cycling rates, Figures A.3.21 (c and d) show the results of rate performance tests at 0.1, 0.2, 0.5, 1, and 2 C. The specific discharge capacities are 161.36, 153.33, and 95.33 mAh g^{-1} at 0.1, 0.2, and 0.5 C respectively and remain stable, while the specific capacity dropped significantly at 1C and 2 C. However, when the charge/discharge rate is restored to 0.1 C after experiencing the failure at 2 C charge/discharge, the specific discharge capacities can still recover to 157.57 mAh g^{-1}, which indicates the as-designed ASSBs built with the ceramic-based CSE have good reversibility and capacity. With respect to the severe capacity decline exhibited by the ASSB at 1 C and 2 C cycling, this is attributed to limited

lithium-ion conductivity of the PVDF-LiTFSI polymer electrolyte used in the cathode composite and not to the ceramic-based CSE or interfacial degradation.

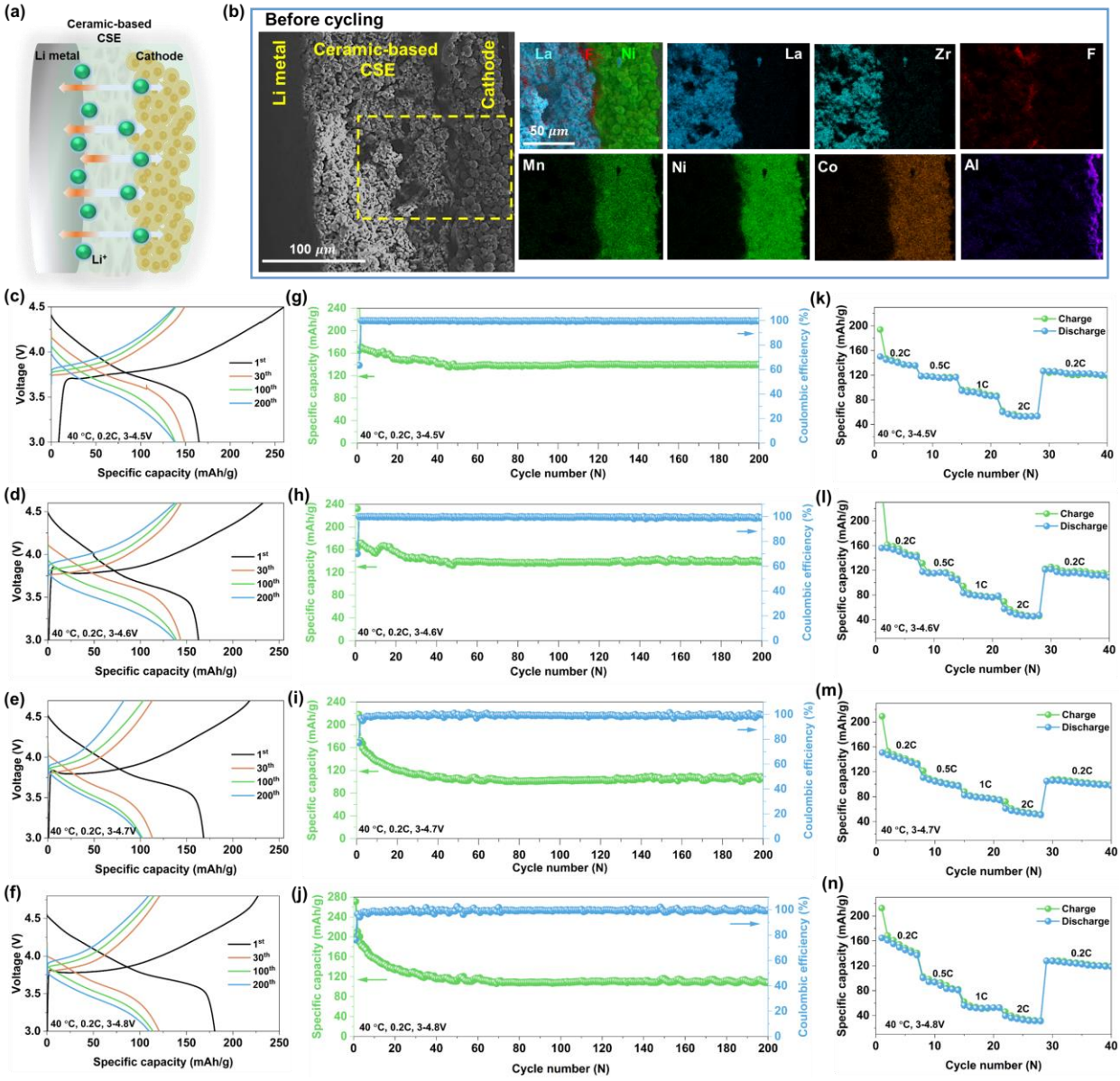

Figure 6. 6. Full all solid-state battery performance at different cut-off voltages. (a) schematic of the as-assembled TiO_2@NCM622 / ceramic-based CSE / Li ASSB; (b) SEM and EDS images of the as-assembled ASSB's cross-section before cycling; (c-f) charge-discharge voltage profiles; (g-j) cycling stability; (k-n) rate performance plots.

To enhance the ionic conductivity of the PVDF-LiTFSI polymer electrolyte of the cathode hence the rate capability of the ASSB made with the as-designed ceramic-based CSE, the charge-discharge cycling of the as-assembled TiO_2@NCM622 / ceramic-based CSE / Li ASSB was

conducted next at 40 ℃ in the voltage range of 3 to 4.5, 4.6, 4.7, and 4.8 V (vs. Li / Li^+) respectively. Figures 6.6 (c–f) depict the charge-discharge profiles of the full cell in the first 200 cycles at a rate of 0.2 C. Stable reversible specific discharge capacities of 139.08, 139.80, 105.84, and 108.04 mAh g^{-1} are achieved from each cut-off voltage (4.5 to 4.8 V) with a high Coulombic efficiency over 99%. The corresponding energy densities at 100 and 200 cycles and 0.2C are 398.3 and 376.1 Wh kg^{-1} respectively, higher than the current United State Advanced Battery Consortium LLC (USABC) goals for advanced high-performance batteries for electric vehicle applications (350 Wh kg^{-1})[30]. The cyclic voltammetry (CV) and accompanied EIS measurements before and after CV tests for the as-assembled ASSBs was conducted from 3 to 4.8 V at a scan rate of 0.1 mV s^{-1} and reported in Figure A.3.22, showing highly reversible lithiation and de-lithiation functioning. Additionally, the cycling stabilities of the as-assembled ASSBs of each voltage range are depicted in Figure 6.6 (g–j). It becomes clearly evident from these results that the cycling stability of the ASSBs is remarkably improved in comparison with the batteries tested at RT even with the LE. The reversible specific discharge capacities slightly drop at first 40 cycles (due to the NCM622 cathode intrinsic property of capacity decay).[51,52] After the initial 40 cycles, the reversible capacities remain stable at least up to 200 cycles. Notably, the average Coulombic efficiency of the ASSBs tested from 3 to 4.8 V reaches 99.76 % after 200 cycles, confirming the highly reversible and stable Li^+ intercalation / de-intercalation behavior. Furthermore, the rate performance of the as-assembled ASSBs with various cut-off voltages (4.5 to 4.8 V) is also evaluated at 40 ℃ (Figure 6.6 k-n). The specific discharge capacity decreases with increasing current density, but the ASSBs tested at 40 ℃ can provide higher discharge capacity when compared to that tested at RT. Specifically, the as-assembled ASSB tested from 3 to 4.8 V achieves reversible capacities of approximately 52.72 and 46.34 mAh g^{-1} at high discharge rate of 1 and 2 C, respectively. The results illustrate that the as-assembled TiO_2@NCM622 / ceramic-based CSE / Li ASSBs have excellent rate recovery. Therefore, the fast Li^+ transport and good interfacial stability with electrodes comes from the as-designed ceramic-based CSE that enables stable cycling ASSB performance at high cut-off voltage. Further enhancement in rate performance should be attained with co-optimization of the conductivity of the cathode composite itself.

6.3.7. Mechanism behind high-voltage stability

Stable solid-state electrolytes are essential for applications with high-voltage cathodes. In such conditions, solid-state electrolytes may experience severe oxidation, decomposition, and

deactivation during charging at high voltage, leading to inadequate cycling performance and even failure. The as-assembled TiO_2@NCM622 / ceramic-based CSE / Li ASSBs exhibit excellent stability with high-voltage cathode even under high cut-off voltage at 4.8 V. To figure out the mechanism of behind this high-voltage stability, the interface between TiO_2@NCM622 cathode and ceramic-based CSE was studied. The cross-sectional SEM and the corresponding EDS images of the TiO_2@NCM622 / ceramic-based CSE / Li ASSB after 200 cycles in the voltage range of 3 to 4.8 V at 0.2 C (40 ℃) (Li foil was removed) are presented in Figure 6.7 (a and b). Intimate contact between cathode and ceramic-based CSE can be observed. Besides, the elemental mappings show that Ni, Co, Mn, La, and Zr have created an intra diffused fine zone. To furtherly investigate the interface, FIB technique was employed to cut the smooth interface in Figure 6.7 (c and d). Figure A.3.23 shows the quantitative EDS spectra of three regions (cathode, interface and ceramic-based CSE) before and after cycling. Specifically, the concentration of Ni, Co, and Mn increases in the interface region of the cycled battery compared to the fresh one. Figure A.3.24 shows a cross section SEM image of ceramic-based CSE/TiO_2@NCM622 interfacial area after cycling and details of the morphology and size (particle size ~ 9 μm) of the TiO_2@NCM622 active material. No delamination or cracking at the interfacial zone or particles is evident. Meanwhile, the corresponding EDS mappings of the FIB-cut surface exhibits a F- and N-rich interphase formed between cathode and ceramic-based CSE as shown in Figure 6.7 (e and f). The X-ray photoelectron spectra (XPS) of F 1s, N 1s, and Li 1s for the uncycled and cycled interface between cathode and ceramic-based CSE are shown in Figure 6.7g. Compared to the fresh/uncycled interface, the intensity of the peak at 684.95 eV in F 1s spectra increased as a result of the formation of LiF in the interface rendering it F-rich; in the N 1s spectra, there is a new peak appearing at 402.35 eV which is ascribed to newly formed Li_3N; the formation of these Li salts is manifested also in the Li 1s spectra with the appearance of a new peak at 55.22 eV corresponding to LiF & Li_3N after long delithiation and lithiation cycling. The formation of LiF and Li3N at the interphase mainly comes from the decomposition of PVDF in cathode and PVDF-LiTFSI PSE in ceramic-based CSE as evident by comparing C 1s spectra before and after cycling, where the intensity of peak $–CF_3$ increases and peak $–CF_2$-CF_2- decreases. Thus, the N- & F-rich interphase (Li_3N and LiF) formed at the interface between the TiO_2@NCM622 cathode and ceramic-based CSE stabilizes the NCM particles against capacity decay under high cut-off voltage (4.8 V) as well as ensures an active face-to-face contact of two components (cathode and CSE) during the long delithiation and

lithiation cycling. Compared to other stabilized high-voltage lithium metal batteries enabled by introduction of LiF & Li_3N interphase in other research works,[53-56] our work produces LiF-Li_3N-rich interphase between ceramic-based CSE and electrodes via an in-situ topotactic reaction during cycling. This in-situ formed LiF-Li_3N-rich interphase provides a highly promising superior stabilizing tool in our pursuit for robust high-voltage all-solid-state lithium metal battery designs.

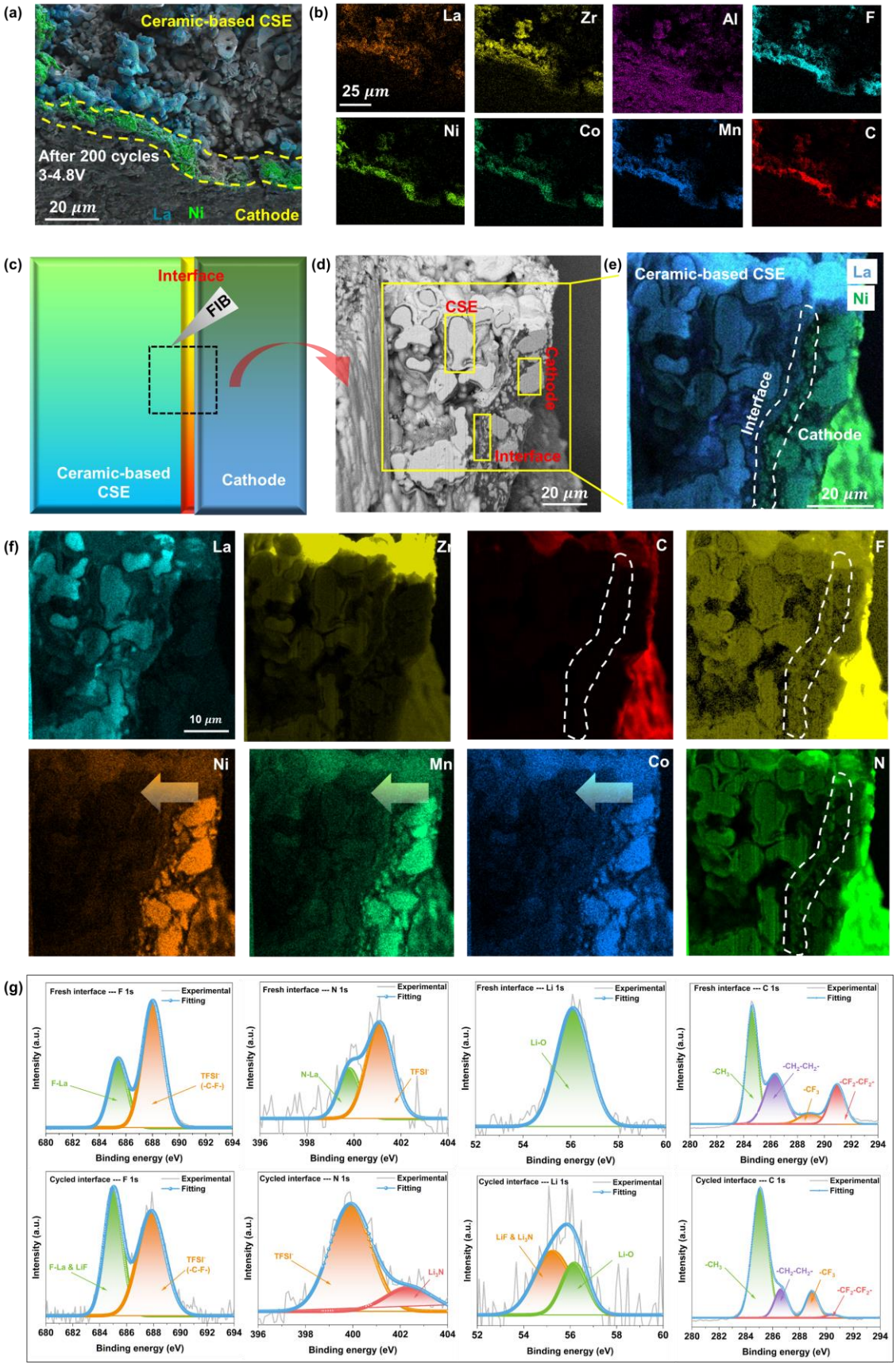
(a)
Ceramic-based CSE
After 200 cycles
3-4.8V
20 μm
La
Ni
Cathode
(b)
La
Zr
Al
F
25 μm
Ni
Co
Mn
C
(c)
Interface
FIB
Ceramic-based CSE
Cathode
(d)
CSE
Cathode
Interface
20 μm
(e)
Ceramic-based CSE
La
Ni
Interface
Cathode
20 μm
(f)
La
Zr
C
F
10 μm
Ni
Mn
Co
N
(g)
Fresh interface --- F 1s
Experimental
Fitting
F-La
TFSI⁻ (-C-F-)
Fresh interface --- N 1s
N-La
TFSI⁻
Fresh interface --- Li 1s
Li-O
Fresh interface --- C 1s
-CH3
-CH2-CH2-
-CF3
-CF2-CF2-
Cycled interface --- F 1s
F-La & LiF
TFSI⁻ (-C-F-)
Cycled interface --- N 1s
TFSI⁻
Li3N
Cycled interface --- Li 1s
LiF & Li3N
Li-O
Cycled interface --- C 1s
Intensity (a.u.)
Binding energy (eV)

Figure 6. 7. Interfacial analysis of cycled high-voltage ASSB over the voltage range 3 – 4.8 V. (a and b) Cross-sectional SEM and corresponding EDS mappings of the cycled ASSB; (c) illustration of FIB cutting area; (d and e) SEM and zonal EDS mapping of the FIB-cut smooth surface and selected regions subjected to quantitative analysis; (f) EDS mappings of the FIB-cut surface; (g) XPS spectra of F 1s, N 1s, Li 1s, and C 1s of the interface between cathode and ceramic-based CSE before and after cycling.

6.4. Conclusion

We developed a highly conductive and interface-robust garnet-based composite solid electrolyte (CSE) with high ionic conductivity by coupling PVDF-LiTFSI and porous cubic LLZO framework with 3D-continuous Li^+ transport channels. The newly engineered polymer-in-ceramic scaffold CSE does not only facilitate the dissociation of the Li salt into highly movable Li^+ ions, but also forms a (LiF and Li_3N rich) interphase with the TiO_2@NCM622 cathode which stabilizes the cathode against capacity fade under high cut-off voltage of 4.8 V. The polymer-in-ceramic CSE exhibits fast Li^+ migration at 25 ℃ of 0.437 mS cm^{-2} and t_{Li^+} = 0.72 and have a wide electrochemical stability window (5.08 V vs. Li^+ / Li). Li-Li symmetric cells based on the ceramic-based CSE can cycle stably for 1000 h at 0.1 and 0.5 mA cm^{-2} indicating an excellent electrochemical stability against Li metal and even Li^+ deposition (dendrite suppression). As-assembled TiO_2@NCM622 / ceramic-based CSE / Li all-solid-state batteries exhibit good long cycling stability at high cut-off voltages (up to 4.8 V for over 200 cycles) and rate performance. Our study opens new robust pathways for designing and building highly efficient high-throughput Li^+ conducting CSEs for scalable advanced all-solid-state lithium metal batteries.

6.5. References

1. Y. Ding, Z. P. Cano, A. Yu, J. Lu, Z. Chen, Automotive Li-ion batteries: current status and future perspectives. *Electrochem. Energy Rev.* **2019**, *2* (1), 1-28.
2. J.-M. Tarascon, M. Armand, Issues and challenges facing rechargeable lithium batteries. *Nature* **2001**, *6861*, (414), 359-367.
3. M. Li, J. Lu, Z. Chen, K. Amine, 30 Years of lithium-ion batteries. *Adv. Mater.* **2018**, *30* (33), 1800561.
4. B. Liu, J.-G. Zhang, W. Xu, Advancing lithium metal batteries. *Joule* **2018**, *2* (5), 833-845.
5. X. Cheng, R. Zhang, C. Zhao, Q. Zhang, Toward safe lithium metal anode in rechargeable batteries: a review. *Chem. Rev*. **2017**, 117 (15), 10403-10473.

6. D. Lin, Y. Liu, Y. Cui, Reviving the lithium metal anode for high-energy batteries. *Nat. Nanotechnol.* **2017**, *12* (3), 194-206.

7. C. Yang, K. Fu, Y. Zhang, E. Hitz, L. Hu, Protected lithium-metal anodes in batteries: from liquid to solid. *Adv. Mater.* **2017**, *29* (36), 1701169.

8. J. C. Bachman, S. Muy, A. Grimaud, H. Chang, N. Pour, S. F. Lux, O. Paschos, F. Maglia, S. Lupart, P. Lamp, L. Giordano, Y. Shao-Horn, Inorganic solid-state electrolytes for lithium batteries: mechanisms and properties governing ion conduction. *Chem. Rev.* **2016**, *116* (1), 140-162.

9. F. Han, J. Yue, C. Chen, N. Zhao, X. Fan, Z. Ma, T. Gao, F. Wang, X. Guo, C. Wang, Interface engineering enabled all-ceramic lithium battery, *Joule* **2018**, 2, 497-508.

10. A. Banerjee, X. Wang, C. Fang, E. Wu, Y. Meng, Interfaces and interphases in all-solid-state batteries with inorganic solid electrolytes. *Chem. Rev.* **2020**, *120* (14), 6878-6933.

11. C. Wang, K. Fu, S. P. Kammampata, D. W. McOwen, A. J. Samson, L. Zhang, G. T. Hitz, A. M. Nolan, E. D. Wachsman, Y. Mo, V. Thangadurai, L. Hu, Garnet-type solid-state electrolytes: materials, interfaces, and batteries. *Chem. Rev.* **2020**, *120* (10), 4257-4300.

12. T. Krauskopf, R. Dippel, H. Hartmann, K. Peppler, B. Mogwitz, F.H. Richter, W.G. Zeier, J. Janek, Lithium-metal growth kinetics on LLZO garnet-type solid electrolytes, *Joule* **2019**, 3, 2023-2049.

13. K. Lee, E. Kazyak, M.J. Wang, N.P. Dasgupta, J. Sakamoto, Analyzing void formation and rewetting of thin in situ-formed Li anodes on LLZO, Joule 2022, 6, 2547-2565.

14. L. Xu, J. Li, W. Deng, H. Shuai, S. Li, Z. Xu, J. Li, H. Hou, H. Peng, G. Zou, X. Ji, Garnet solid electrolyte for advanced all-solid-state Li batteries. *Adv. Energy Mater.* **2020**, *11* (2), 2000648.

15. Y. Yu, Z. Wei, H. Wang, H. Huang, Y. Jiang, X. Wu, X. Yao, Z. Wu, Y. Yu. Toward high energy density all solid-state sodium batteries with excellent flexibility. *Adv. Energy Mater.* **2020**, *10* (12), 1903698.

16. J. Wu, L. Yuan, W. Zhang, Z. Li, X. Xie, Y. Huang. Reducing the thickness of solid-state electrolyte membranes for high-energy lithium batteries. *Energy Environ. Sci.* **2021**, *14* (1), 12-36.

17. K. Xu, Electrolytes and interphases in Li-ion batteries and beyond. *Chem. Rev.* **2014**, 114 (23), 11503-11618.

18. Y. Huang, G. Tian, G. Rui, P. Shi, W. Fu, L. Chen, X. Liu, J. Zeng, B. Kang, Z. Yan, F. J. Stadler. A relaxor ferroelectric polymer with an ultrahigh dielectric constant largely promotes the dissociation of lithium salts to achieve high ionic conductivity. *Energy Environ. Sci.* **2021**, 14 (11), 6021-6029.

19. D. Lei, Y. He, H. Huang, Y. Yuan, G. Zhong, Q. Zhao, X. Hao, D. Zhang, C. Lai, S. Zhang, J. Ma, Cross-linked beta alumina nanowires with compact gel polymer electrolyte coating for ultra-stable sodium metal battery. *Nat. Commun.* **2019**,*10* (1), 4244.

20. L. Chen, Y. Li, S. Li, L. Fan, C. Nan, J. B. Goodenough, PEO/garnet composite electrolytes for solid-state lithium batteries: From "ceramic-in-polymer" to "polymer-in-ceramic". *Nano Energy*, **2018***, 46*, 176-184.

21. J. Zheng, P. Wang, H. Liu, Y. Hu, Interface-enabled ion conduction in $Li_{10}GeP_2S_{12}$–poly (ethylene oxide) hybrid electrolytes. *ACS Appl. Energy Mater.* **2019**, *2* (2), 1452-1459.

22. Y. Zheng, Y. Yao, J. Ou, M. Li, D. Luo, H. Dou, Z. Li, K. Amine, A. Yu, Z. Chen, A review of composite solid-state electrolytes for lithium batteries: fundamentals, key materials and advanced structures. *Chem. Soc. Rev.* **2020**, *49* (23), 8790-8839.

23. Z. Cheng, T. Liu, B. Zhao, F. Shen, H. Jin, X. Han, Recent advances in organic-inorganic composite solid electrolytes for all-solid-state lithium batteries. *Energy Storage Mater.* **2021**, *34*, 388-416.

24. X. Zhang, T. Liu, S. Zhang, X. Huang, B. Xu, Y. Lin, B. Xu, L. Li, C. Nan, Y. Shen, Synergistic coupling between $Li_{6.75}La_3Zr_{1.75}Ta_{0.25}O_{12}$ and poly (vinylidene fluoride) induces high ionic conductivity, mechanical strength, and thermal stability of solid composite electrolytes. *J. Am. Chem. Soc.* **2017**, *139* (39), 13779-13785.

25. L. Fan, H. He, C. Nan, Tailoring inorganic–polymer composites for the mass production of solid-state batteries. *Nat. Rev. Mater.* **2021**, *6* (11), 1003-1019.

26. T. Famprikis, P. Canepa, J. A. Dawson, M. S. Islam, C. Masquelier. Fundamentals of inorganic solid-state electrolytes for batteries. *Nat. Mater.* **2019**,*18* (12), 1278-1291.

27. Z. Zou, Y. Li, Z. Lu, D. Wang, Y. Cui, B. Guo, Y. Li, X. Liang, J. Feng, H. Li, C. Nan, Mobile ions in composite solids. *Chem. Rev.* **2020**.*120* (9), 4169-4221.

28. J. Maier, Space charge regions in solid two phase systems and their conduction contribution—II Contact equilibrium at the interface of two ionic conductors and the related conductivity effect. *Berichte der Bunsengesellschaft für physikalische Chemie* **1985**, *89* (4), 355-362.

29. N. J. J. de Klerk, M. Wagemaker. Space-charge layers in all-solid-state batteries; important or negligible? *ACS Appl. Energy Mater.* **2018**, *1* (10), 5609-5618.

30. USABC Goals for Advanced High-Performance Batteries for Electric Vehicle (EV) Applications (United States Council for Automotive Reserach LLC, 2021); https://uscar.org/wpfd_file/goals-for-advanced-high-performance-batteries-for-electric-vehicle-ev-applications/.

31. S. Wang; H-c. Chiu; G. P. Demopoulos, Tetragonal phase-free crystallization of highly conductive nanoscale cubic garnet ($Li_{6.1}Al_{0.3}La_3Zr_2O_{12}$) for all-solid-state lithium-metal batteries. *J. Power Sources* **2024**, *595*, 234061.

32. Q. Fan, K. Lin, S. Yang, S. Guan, J. Chen, S. Feng, J. Liu, L. Liu, J. Li, Z. Shi, Constructing effective TiO_2 nano-coating for high-voltage Ni-rich cathode materials for lithium ion batteries by precise kinetic control, *J. Power Sources* **2020**, *477*, 228745.

33. J. Yan, H. Huang, J. Tong, W. Li, X. Liu, H. Zhang, H. Huang, W. Zhou, Recent progress on the modification of high nickel content NCM: coating, doping, and single crystallization. *Interdiscip. Mater.* **2022**; *1* (3), 330-353.

34. Y. Li, X. Liu, D. Ren, H. Hsu, G. Xu, J. Hou, L. Wang, X. Feng, L. Lu, W. Xu, Y. Ren, R. Li, X. He, K. Amine, M. Ouyang, Toward a high-voltage fast-charging pouch cell with TiO_2 cathode coating and enhanced battery safety, *Nano Energy* **2020**, *71*, 104643.

35. H. L. Nguyen, V. T. Luu, M. C. Nguyen, S. H. Kim, Q. H. Nguyen, N. I. Nungu, Y-S. Jun, W. Ahn, Nb/Al-co-doped $Li_7La_3Zr_2O_{12}$ composite solid electrolyte for hig-performance all-solid-state batteries. *Adv. Funct. Mater*. **2022**, 32 (45), 2207874.

36. C. J. Wagner, A. V. Naumkin, A. Kraut-Vass, J. W. Allison, C. J Powell, J. R. Rumble JR, *The Nist X-Ray Photoelectron Spectroscopy (XPS) Database* **1989**.

37. M. Wu, D. Liu, D. Qu, Z. Xie, J. Li, J. Lei, H. Tang, 3D Coral-like LLZO/PVDF composite electrolytes with enhanced ionic conductivity and mechanical flexibility for solid-state lithium batteries, *ACS Appl. Mater. Interfaces* **2020**, *12* (47), 52652-52659.

38. C. D. Robitaille, D. Fauteux, Phase Diagrams and Conductivity Characterization of Some PEO-LiX Electrolytes *J. Electrochem. Soc.* **1986**, *133* (2), 315.

39 Y. Zhao, J. Yan, W. Cai, Y. Lai, J. Song, J. Yu, B. Ding, Elastic and well-aligned ceramic LLZO nanofiber based electrolytes for solid-state lithium batteries, *Energy Storage Mater.* **2019**, *23*,3 06-313.

40. J. H. Kim, K. Go, K. J. Lee, H.-S. Kim, Improved performance of all-solid-state lithium metal batteries via physical and chemical interfacial control. *Adv. Sci.* **2022**, *9*, 2103433.

41. L. Zou, K. Shi, Z. Xu, Z. Yang, W. Zhang, Double-layer solid composite electrolytes enabling improved room-temperature cycling performance for high-voltage lithium metal batteries. *ACS Omega.* **2022**, *7* (1), 994-1002.

42. F. Chen, M. Jing, H. Yang, W. Yuan, M. Liu, Y. Ji, S. Hussain, X. Shen, Improved ionic conductivity and Li dendrite suppression of PVDF-based solid electrolyte membrane by LLZO incorporation and mechanical reinforcement. *Ionics* **2021**, *27*, 1101-1111.

43. S. Cao, F. Chen, Q. Shen, L. Zhang, Dual-coordination-induced poly(vinylidene fluoride)/$Li_{6.4}Ga_{0.2}La_3Zr_2O_{12}$/Succinonitrile composite solid electrolytes towards enhanced rate performance in all-solid-state lithium batteries, *ACS Appl. Mater. Interfaces* **2023**, *15* (31), 37422-37432.

44. H. Hou, B. Hunag, X. Yu, J. Lan, S. Ming, J. Rong, X. Liu, F. Chen, Compatible composite electrolyte membrane $Li_7La_3Zr_2O_{12}$/SB-PVDF for solid-state lithium ion battery, *J. Energy Storage* **2023**, *68*, 107680.

45. H. K. Tran, B. T. Truong, B. Zhang, R. Jose, J. Chang, C. Yang, Sandwich-structured composite polymer electrolyte based on PVDF-HFP/PPC/Al-doped LLZO for high-voltage solid-state lithium batteries, *ACS Appl. Energy Mater.* **2023**, *6*, 1475-1487.

46. J. Cai, T. Liu, C. Liu, G. Liu, PVDF-HFP/LiTFSI based composite solid state electrolyte with different micromorphology of $Li_{6.25}Ga_{0.25}La_3Zr_2O_{12}$ doping, *J. Alloys Compd.* **2023**, *968*, 171872.

47. X. Song, T. Zhang, S. Huang, J. Mi, Y. Zhang, J. Travas-Sejdic, A. P. Turner, W. Gao, P. Cao, Constructing a PVDF-based composite solid-state electrolyte with high ionic conductivity $Li_{6.5}La_3Zr_{1.5}Ta_{0.1}Nb_{0.4}O_{12}$ for lithium metal battery, *J. Power Sources* **2023**, *564*, 232849.

48. O. V. Sreejith, S. E. Abraham, M. Ramaswamy, Free-standing and flexible garnet-PVDF ceramic polymer electrolyte membranes for solid state batteries, *Energy Fuels* **2023**, *37*, 2401-2409.

49. H. Gan, J. Sun, Y. Xia, P. Qiu, L. Li, W. Zhu, PEO/PVDF-HFP/LLZTO composite solid polymer electrolyte for high-performance all-solid-state lithium metal batteries, *J. Phys. Chem. C.* **2023**, *127*, 21015-21021.

50. Z. Fang, M. Zhao, Y. Peng, S. Guan, Combining organic plastic salts with a bicontinuous electrospun PVDF-HFP/$Li_7La_3Zr_2O_{12}$ membrane: LiF-rich solid-electrolyte interphase enabling stable solid-state lithium metal batteries, *ACS Appl. Mater. Interfaces* **2022**, *14*, 18922-18934.

51. X. Lu, N. Zhang, M. Jahn, W. Pfleging, H. J. Seifert, Improved capacity retention of SiO_2-coated $LiNi_{0.6}Mn_{0.2}Co_{0.2}O_2$ cathode material for lithium-ion batteries. *Appl. Sci.* 2019, 9 (18), 3671.

52. R. Gauthier, A. Luscombe, T. Bond, M. Bauer, M. Johnson, J. Harlow, A. Louli, J. R. Dahn, How do depth of discharge, C-rate and calendar age affect capacity retention, impedance growth, the electrodes, and the electrolyte in Li-ion cells? *J. Electrochem. Soc.* **2022**, *169* (2), 020518.

53. K. Shi, Z. Wan, L. Yang, Y. Zhang, Y. Huang, S. Su, H. Xia, K. Jiang, L. Shen, Y. Hu, S. Zhang, J. Yu, F. Ren, Y. He, F. Kang, In situ construction of an ultra-stable conductive composite interface for high-voltage all-solid-state lithium metal batteries. *Angew. Chem. Int. Ed.* **2020**, *59*, 11784-11788.

54. S. Zhang, F. Zhao, S. Wang, J. Liang, J. Wang, C. Wang, H. Zhang, K. Adair, W. Li, M. Li, H. Duan, Y. Zhao, R. Yu, R. Li, H. Huang, L. Zhang, S. Zhao, S. Lu, T.-K. Sham, Y. Mo, X. Sun, Advanced high-voltage all-solid-state Li-ion batteries enabled by a dual-Halogen solid electrolyte. *Adv. Energy Mater.* **2021**, *11*, 2100836.

55. B. Zhang, Z. Lin, H. Chen, L.-W. Wang, F. Pan, The stability and reaction mechanism of a LiF/electrolyte interface: insight from density functional theory. *J. Mater. Chem. A* **2020**, *8*, 2613-2617.

56. Z. Zhang, J. Wang, S. Zhang, H. Ying, Z. Zhuang, F. Ma, P. Huang, T. Yang, G. Han, W. Han, Stable all-solid-state lithium metal batteries with Li_3N-LiF-enriched interface induced by lithium nitrate addition. *Energy Storage Mater.* **2021**, *43*, 229-237.

Chapter 7: Global Discussion

7.1. Thesis Overview

As detailed in **Chapters 1 and Chapter 2**, all-solid-state lithium batteries (ASSLBs) have emerged as a promising next-generation energy storage technology, offering potentially enhanced safety, higher energy density, and longer lifespan compared to conventional liquid lithium-ion batteries.[1-3] The key component of ASSLBs is the solid-state electrolyte, which plays a critical role in enabling fast ion transport within the battery while preventing undesirable reactions at the electrode-electrolyte interfaces.[4-5] At this stage, solid inorganic electrolytes become highly attractive because they enable the use of high-capacity electrode materials (e.g. sulphur,[6] manganese,[7] and vanadate-based cathodes[8]) that are not particularly stable or safe to utilize in liquid organic electrolytes for current Li^+ battery technology. By avoiding the damage caused by dendritic Li development,[9] the use of metallic Li anodes, hence increasing realistic energy densities, may also be achievable with ceramic electrolytes.[5] Additional advantages of solid inorganic electrolytes include improved thermal and chemical stability and the removal of liquids and separators in electrochemical cells.[10] Here, the development of fast Li-ion SSE materials may also be viewed as a catalyst for the development of novel types of all-solid-state thin-film micro-batteries for electronics or for other applications.[11-12]

Among a variety of inorganic SSEs, the Li-stuffed garnet-type oxide $Li_7La_3Zr_2O_{12}$ (LLZO) has generated considerable interest as a potential solid electrolyte for SSBs due to its high ionic conductivity at room temperature, good electrochemical stability against lithium metal anode, and high-voltage electrochemical window.[13-14] LLZO comprises two polymorphs: tetragonal (t-LLZO, $I4_1/acd$)[15] and cubic (c-LLZO, $Ia\bar{3}d$)[16] phases, the latter of which presents two orders of magnitude higher ionic conductivity compared to the tetragonal phase. To avoid the formation of the thermodynamically advantageous tetragonal phase, aliovalent doping of metal cations either at Li^+ sites with Al^{3+},[17] Ga^{3+} [18]or the Zr sites with Ta^{5+} [19]or Nb^{5+} [20] are employed,[21] through which c-LLZO can be stabilized over its tetragonal counterpart. Al-doped LLZO is an appealing candidate among all the doped derivatives, due to its excellent sinterability and cost competitiveness.

Conventionally, to obtain a conductive cubic phase, LLZO is synthesized through solid-state reaction, which requires multiple milling-calcination cycles and high calcination temperatures

above 1100 ℃.[22-24] Meanwhile, the high-temperature procedure yields micron-sized particles with significant aggregates, rendering electrode-electrolyte assembly challenging.[25] Furthermore, although wet chemical routes like sol-gel, Pechini, co-precipitation, and spray pyrolysis produce fine LLZO particles at lower temperatures (900 °C), they require expensive precursors, multiple drying/calcination steps to remove water and organic solvents, and long annealing times to achieve phase pure conductive c-LLZO.[26-28] Hence, synthesizing submicron LLZO powders at low temperature (<800 °C) is critical for preparing dense pellets and allowing a stable interface to develop between LLZO/electrodes in SSBs fabrication.[25] This objective was addressed in **Chapter 4**, where a novel synthesis method of low-temperature crystallization of nanoscale cubic garnet solid-state electrolytes was proposed. Based on a dual-reaction mechanism (Figure 7.1), cubic garnet nanocrystals were synthesized from a hydrothermal precursor containing $La(OH)_3$(cr) and amorphous La-Al hydroxides converted to intermediate phase $La_2Zr_2O_7$ before crystallization was completed at a temperature as low as 600 ℃. The as-synthesized nano cubic garnet, after pellet compression and sintering, exhibits fast lithium-ion migration at 0.42 mS cm^{-1} conductivity at 21 ℃ with activation energy 0.17 eV (half of previously reported values) thanks to favourable grain microstructure, but also excellent interfacial stability against lithium metal in symmetric cell tests (Figure 7.2).

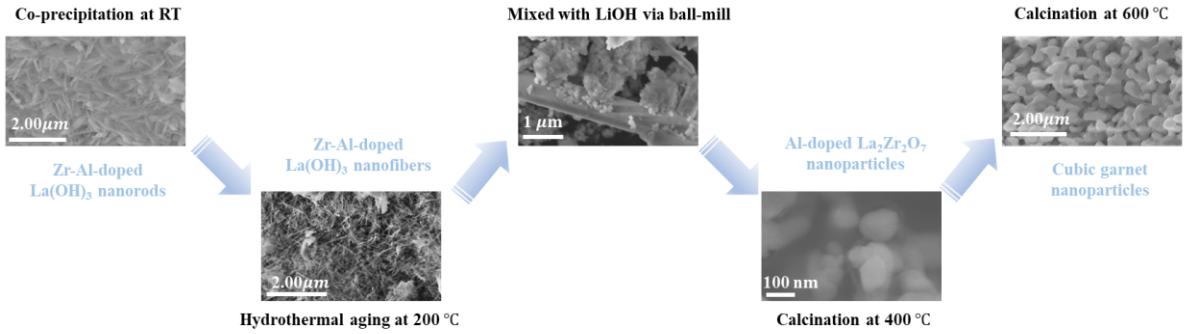

$$(a)\ 2La(OH)_{3\,(cr)} + 2Zr(OH)_{4\,(am)} \rightarrow La_2Zr_2O_{7\,(cr)} + 7H_2O$$

$$(b)\ La_2Zr_2O_{7\,(cr)} + La(OH)_{3\,(cr)} + 0.3Al(OH)_{3\,(am)} + 6.1LiOH_{(cr)} \rightarrow Li_{6.1}Al_{0.3}La_3Zr_2O_{12\,(cr)} + 5H_2O$$

Figure 7. 1. The dual-reaction mechanism of the low-temperature crystallization of nanoscale cubic LLZO advanced in Chapter 4.

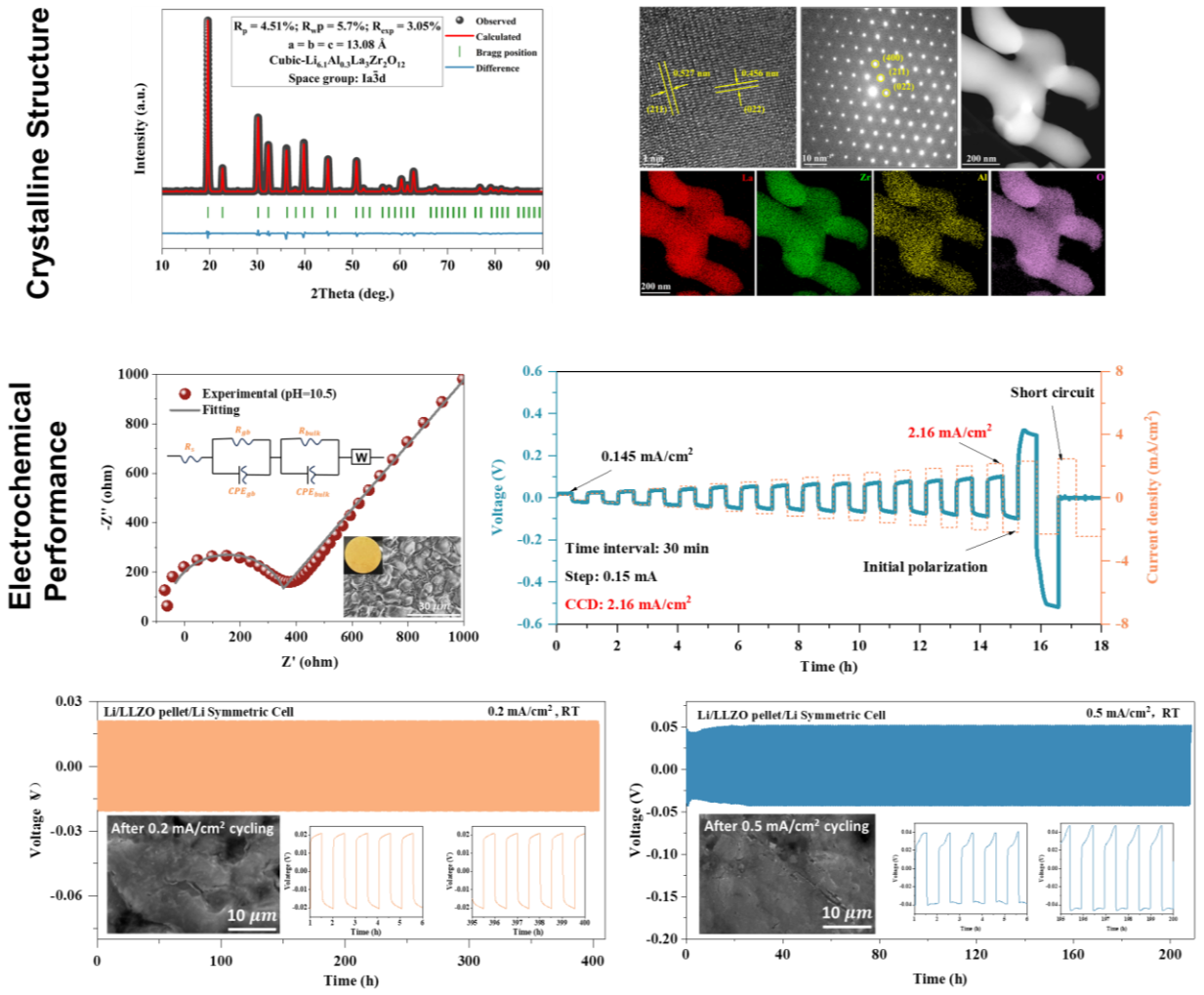

Figure 7. 2. Crystalline structure characterization and electrochemical performance of the nanostructured synthesized cubic LLZO.

Next the challenge of obtaining low impedance and stable interfaces of the ceramic solid-state electrolyte with th Li metal anode and composite cathode was addressed in Chapter 5 via construction of polymer-infiltrated porous garnet ceramic hybrid solid-state electrolytes (HSEs). The innovative aspect here was the rendering of the synthesized cubic garnet material into a porous ceramic scaffold as opposed to use it as densified pellet. In this way, the conductive polymer solid electrolyte (SPE) was hypothesized that upon infiltration and coating of the exterior surface would provide a robust structure with much better compatibility with the electrode materials, as well as manufacturing simplicity.[29-31] By employing the PSEs in small quantity (< 10 wt.%) into the ceramic scaffold, their crystallization at room temperature is hindered hence preserving their conductivity due to non-crystalline state for low impedance interfacing, while the >90wt.%

ceramic scaffold provides mechanical strength suppressing the growth of lithium dendrites. The HSE advanced in Chapter 5 featuring PEO-LiTFSI-in-porous cubic garnet scaffold differs from other hybrid/composite solid electrolytes as they are based predominantly on ceramic rather on polymer matrix. [32-33] The hybrid SSEs based predominantly on polymers, typically feature ceramic fillers in the polymer matrix, which are known to reduce the polymer's crystallinity and weaken the interactions between lithium ions and polymer chains, increasing Li-ion conductivity. However, the fillers' propensity to aggregate, limits their effectiveness for Lewis acid-base interaction, and the resulting ionic conductivity is insufficient for practical battery kinetics unless operated at elevated temperature.[34-35] Furthermore, the fillers do not successfully form an interconnected reinforcement to improve the mechanical properties of the composites due to the limited amount of ceramic fillers in polymer-based hybrid SEs.[36] Wen et al. reported an ultra-thin garnet-based hybrid SE with a thickness of 12 μm that had improved mechanical strength vis-à-vis polymer-based HSEs, but still contained a high amount of polymer,[37] as such the obtained ionic conductivity and mechanical strength were insufficient to fulfill commercial requirements. Nan et al. utilized the catalysis of La in dehydrochlorination and prepared poly(vinylidenefluoride) (PVDF) with LLZTO hybrid SE, whose ionic conductivity was as high as 5×10^{-4} S cm^{-1} at 25 °C, but still with relied on polymer matrix.[38] In other studies, suppression of Li dendrite growth was sought by modifying the morphology of the fillers in order to obtain homogeneous Li-ion migration and deposition. Ci et al. synthesized a sheet-like garnet SSE and prepared a hybrid SSE by immersing it in a Poly(ethylene oxide) (PEO) polymer matrix, resulting in improved interfacial stability against Li metal.[39] Another approach investigated involves the addition of plasticizers to Li salt/polymer blends to boost ionic conductivity to feasible levels, however, this sacrifices rigidity and increases flammability.[40-41] In another recent technique, blends of polymer electrolytes and inorganic ion conductors were used demonstrating enhanced ionic conductivity, but not the required mechanical strength. In reality, there is a contradiction between ionic conductivity and elastic modulus in hybrid SSEs. For high ionic conductivity,[42] low crystallinity, and more mobility polymer chains are required, resulting in mechanically softer polymers. Given, these limitations of polymer-based hybrid solid electrolytes, it was decided in this work to design ceramic-based hybrid SSEs capable of suppressing Li dendrites while delivering high power.

To this end, the approch taken is the engineering of a ceramic (garnet) skeleton that pprovides most ionic transport capability, other than high mechanical strength, while a secondary conductive

polymer molecularly bonded to ceramic addresses the interfacial issues. The first take at this is described in **Chapter 5**, where a novel HSE structure is designed featuring a polymer-infiltrated porous ceramic cubic $Li_{6.1}Al_{0.3}La_3Zr_2O_{12}$ (c-LLZO) scaffold fabricated by an integrated sintering method. The HSE structure exhibits high intrinsic ionic conductivity as well as good mechanical strength with even distribution of the polymer phase (LiTFSI-doped PEO) within the network of open pores resulting in uniform Li-ion migration flux. The infiltrated polymer solid electrolyte (PSE) forms strong molecular bonding on the interior and exterior surface of the ceramic skeleton via La-N bonds effectively lowering the interfacial impedance between two phases. Moreover, this continuous two-phase interface provides a fast pathway for Li-ion transport. Thus, the as-designed ceramic-based HSE exhibits high Li-ion transference number (0.71) and ionic conductivity (0.547 mS cm^{-1}) at 25 ℃. To demonstrate the suitability of the designed HSE (PEO-LiTFSI infiltrated into porous cubic garnet scaffold) in an all-solid-state lithium battery (ASSLB), it was assembled into a cell wih Li metal as anode and $LiFePO_4$/PEO-LiTFSI/Carbon composite cathode. The Li/HSE/LFP ASSLB exhibited high discharge specific capacity of 163 mAh g^{-1} at 0.1 C and average coulombic efficiency greater than 99 % after 50 cycles. This novel design opens new possibilities in our pursuit for next generation high-performance ASSLBs as shown in Figure 7.3.

The HSE developed and described in Chapter 5 constitutes a new proof-of-concept of porous ceramic scaffold-based hybrid solid-state electrolyte, which however is characterized by two major limitations; a thick SSE (~1 mm) that needs to be reduced by a factor of 10 in order to meet the requirement for enhanced energy density and on the other is limited to the use of a low voltage cathode (LFP) as PEO-LiTFSI polymer component is unstable above than 4.0 V. As such in its present structure, it is incompatible with high-voltage cathode materials or high-power operation (due to low polymer conductivity in cathode composite).

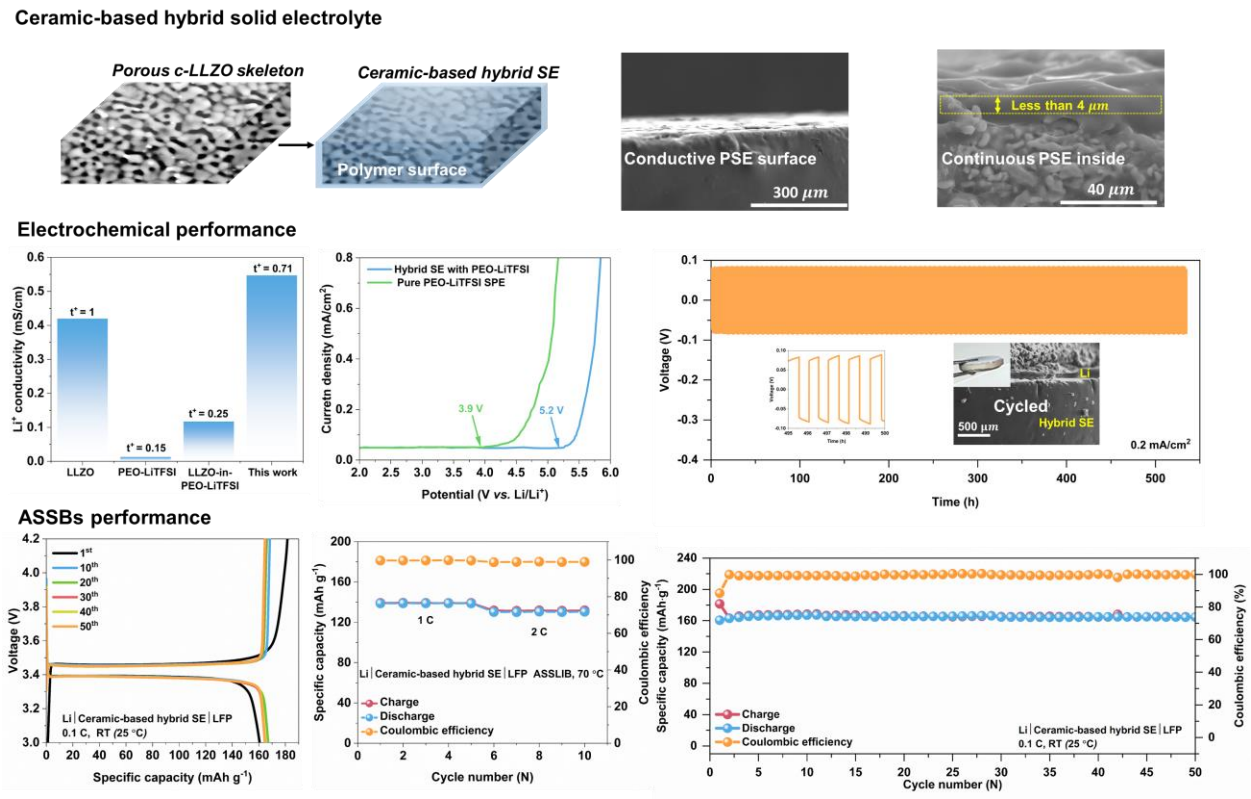

Figure 7. 3. Schematic and SEM images of the ceramic-based hybrid SE; electrochemical performance of HSE (LSV and symmetric cells; and ASSLB (Li/HSE/LFP) performance.

The above realization led to the work described in **Chapter 6**, where a porous (again) ceramic-based HSE is developed via modification of the formulation protocol yielding this time an ultra-thin framework (130 µm) that is infiltrated with conductive PVDF-LiTFSI PSE that has high voltage stability. The new type of 3D HSE is endowed with continuous ion-conductive channels permitting high Li^+ conductivity, and characterized by a wide electrochemical window (5.08 V) permitting pairing with high-voltage cathode materals. The novel-designed porous cubic garnet ($Li_{6.1}Al_{0.3}La_3Zr_2O_{12}$, LLZO) scaffold possesses high ceramic-content (~ 93%) while still has substantial porosity (45.74 %), achieving simultaneously excellent interfacing thanks to embedded polymer phase and mechanical strength in suppressing Li dendrites. The LLZO framework and PVDF-LiTFSI form a robust structure thanks to molecular engineering involving two types of metal-atom bondings specifically, La from the LLZO framework with N from $TFSI^-$ groups, and F from the PVDF polymer chains, respectively. The coupled LLZO-$TFSI^-$ facilitates the dissociation of the Li salt into fast moving liberated Li^+ ions that reduce the interfacial impedance between ceramic and polymer contributing to a high ionic conductivity and Li transfer number of

(0.437 mS cm^{-1}, and 0.72 at 25 ℃). An ASSLB made of Li metal, the new HSE (PVDF-LiTFSI-in-porous LLZO) and TiO_2-coated $LiNi_{0.6}Co_{0.2}Mn_{0.2}O_2$ cathode (TiO_2@NCM622-PVDF-LiTFSI-C) was built and electrochemically tested demonstrating uniform Li^+ transport enabling dendrite-free homogeneous Li stripping and deposition. The ASSLB delivered stable cycling for 200 times at 0.2C from 3 to 4.8 V. Post-mortem analysis of the ceramic-based HSE/cathode interphase showed no visible signs of mechanochemical debris or inhomogeneities suggesting the new ceramic-based HSE deserves further development. Representative results are graphically summarized in Figure 7.4.

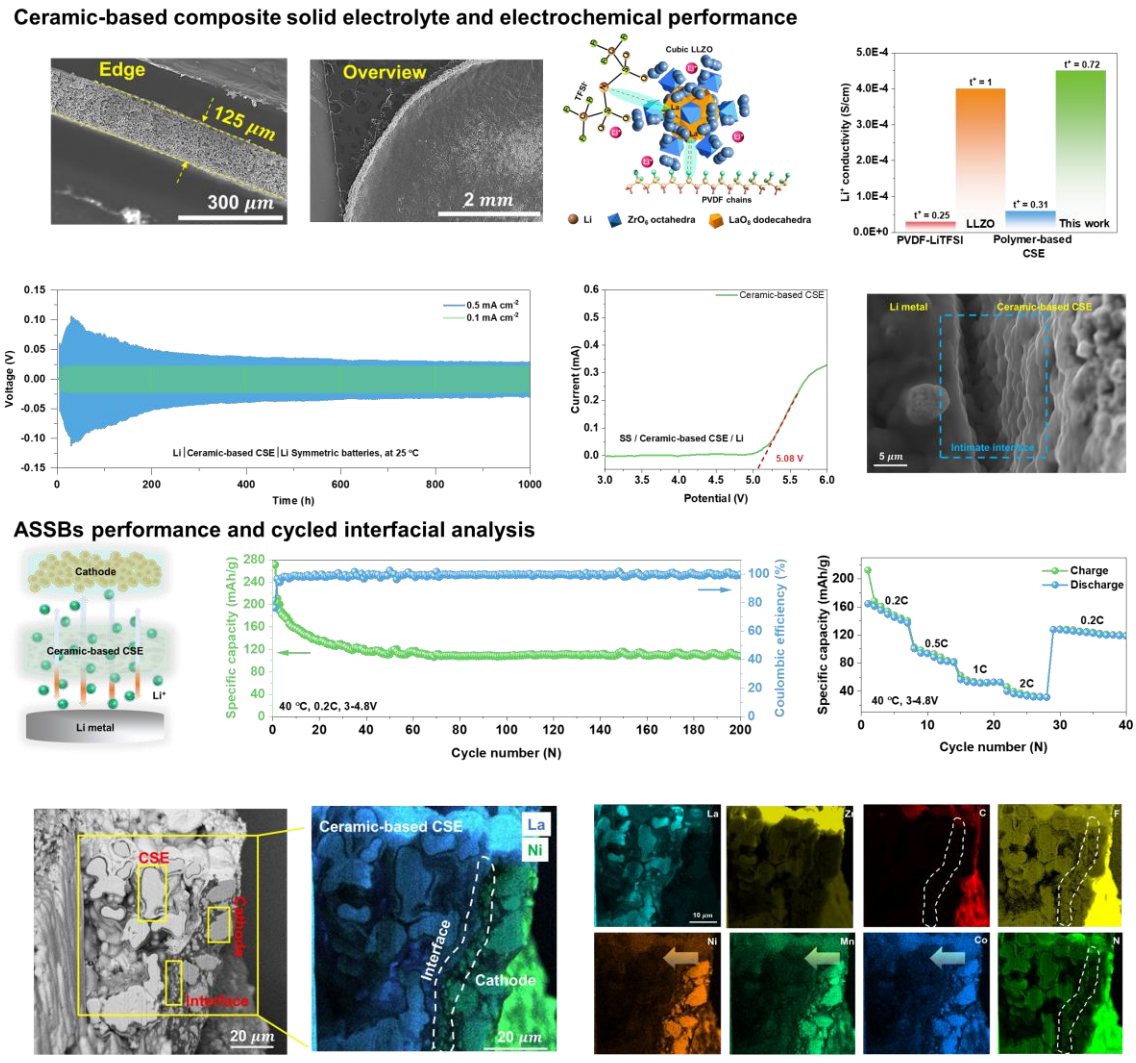

Figure 7. 4. The ultra-thin porous ceramic-based hybrid solid electrolyte (PVDF-LiTFSI-in-porous c-Al-LLZO); electrochemical performance of HSE (LSV and symmetric cell); ASSLB (Li/HSE/TiO_2-NMC622/PVDF-LiTFSI-C) performance; and post-cycled HSE/Cathode interface characterization.

7.2. References

1. J. B. Goodenough; K. S. Park, The Li-ion rechargeable battery: a perspective. *J. Am. Chem. Soc.* **2013,** *135* (4), 1167-76.

2. M. Li; J. Lu; Z. Chen; K. Amine, 30 Years of Lithium-Ion Batteries. *Adv. Mater.* **2018**, 30 (33), 1800561.

3. A. Masias; J. Marcicki; W. A. Paxton, Opportunities and Challenges of Lithium Ion Batteries in Automotive Applications. *ACS Energy Lett.* **2021,** *6* (2), 621-630.

4. J. Janek; W. G. Zeier, A solid future for battery development. *Nat. Energy* **2016,** *1* (9), 1-4.

5. J. Chen; J. Wu; X. Wang; A. Zhou; Z. Yang, Research progress and application prospect of solid-state electrolytes in commercial lithium-ion power batteries. *Energy Storage Mater.* **2021,** *35*, 70-87.

6. X. Ji; K. T. Lee; L. F. Nazar, A highly ordered nanostructured carbon-sulfur cathode for lithium-sulphur batteries. *Nat. Mater.* **2009,** *8* (6), 500-6.

7. A. Semih; N. Reinhard, A Lithium-Rich Compound $Li_7Mn(BO_3)_3$ Containing Mn^{2+} in Tetrahedral Coordination: A Cathode Candidate for Lithium-Ion Batteries. *Angew. Chem. Int. Ed.* **2013,** *125* (48), 12773-12776.

8. S. Afyon; F. Krumeich; C. Mensing; A. Borgschulte; R. Nesper, New high capacity cathode materials for rechargeable Li-ion batteries: vanadate-borate glasses. *Sci. Rep.* **2014,** *4* (1), 7113.

9. A. Jana; S. I. Woo; K. S. N. Vikrant; R. E. García, Electrochemomechanics of lithium dendrite growth. *Energy Environ. Sci.* **2019,** *12* (12), 3595-3607.

10. B. Zhang; R. Tan; L. Yang; J. Zheng; K. Zhang; S. Mo; Z. Lin; F. Pan, Mechanisms and properties of ion-transport in inorganic solid electrolytes. *Energy Storage Mater.* **2018,** *10*, 139-159.

11. H. Liu; X. Cheng; J. Huang; H. Yuan; Y. Lu; C. Yan; G. Zhu; R. Xu; C. Zhao; L. Hou; C. He; S. Kaskel; Q. Zhang, Controlling Dendrite Growth in Solid-State Electrolytes. *ACS Energy Lett.* **2020,** *5* (3), 833-843.

12. Y. Chen; Y. Jiang; S. Chi; H. J. Woo; K. Yu; J. Ma; J. Wang; C. Wang; Y. Deng, Understanding the lithium dendrites growth in garnet-based solid-state lithium metal batteries. *J. Power Sources* **2022,** *521*.

13. L. Xu; J. Li; W. Deng; H. Shuai; S. Li; Z. Xu; J. Li; H. Hou; H. Peng; G. Zou; X. Ji, Garnet Solid Electrolyte for Advanced All-Solid-State Li Batteries. *Adv. Energy Mater.* **2020,** *11* (2), 2000648.

14. T. Krauskopf; R. Dippel; H. Hartmann; K. Peppler; B. Mogwitz; F. H. Richter; W. G. Zeier; J. Janek, Lithium-Metal Growth Kinetics on LLZO Garnet-Type Solid Electrolytes. *Joule* **2019,** *3* (8), 2030-2049.

15. J. Awaka; N. Kijima; H. Hayakawa; J. Akimoto, Synthesis and structure analysis of tetragonal $Li_7La_3Zr_2O_{12}$ with the garnet-related type structure. *J. Solid State Chem.* **2009,** *182* (8), 2046-2052.

16. J. Awaka; A. Takashima; K. Kataoka; N. Kijima; Y. Idemoto; J. Akimoto, Crystal Structure of Fast Lithium-ion-conducting Cubic $Li_7La_3Zr_2O_{12}$. *Chem. Lett.* **2011,** *40* (1), 60-62.

17. E. Rangasamy; J. Wolfenstine; J. Sakamoto, The role of Al and Li concentration on the formation of cubic garnet solid electrolyte of nominal composition $Li_7La_3Zr_2O_{12}$. *Solid State Ionics* **2012,** *206*, 28-32.

18. C. Li; Y. Liu; J. He; K. S. Brinkman, Ga-substituted $Li_7La_3Zr_2O_{12}$: An investigation based on grain coarsening in garnet-type lithium ion conductors. *J. Alloys Compd.* **2017,** *695*, 3744-3752.

19. A. Gupta; R. Murugan; M. P. Paranthaman; Z. Bi; C. A. Bridges; M. Nakanishi; A. P. Sokolov; K. Han; E. W. Hagaman; H. Xie; C. B. Mullins; J. B. Goodenough, Optimum lithium-ion conductivity in cubic $Li_{7-x}La_3Hf_{2-x}Ta_xO_{12}$. *J. Power Sources* **2012,** *209*, 184-188.

20. S. Ohta; T. Kobayashi; T. Asaoka, High lithium ionic conductivity in the garnet-type oxide $Li_{7-x}La_3(Zr_{2-x}, Nb_x)O_{12}$ (x= 0 - 2). *J. Power Sources* **2011,** *196* (6), 3342-3345.

21. L. J. Miara; W. D. Richards; Y. Wang; G. Ceder, First-Principles Studies on Cation Dopants and Electrolyte|Cathode Interphases for Lithium Garnets. *Chem. Mater.* **2015,** *27* (11), 4040-4047.

22. R. Murugan; V. Thangadurai; W. Weppner, Fast lithium ion conduction in garnet-type $Li_7La_3Zr_2O_{12}$. *Angew. Chem. Int. Ed. Engl.* **2007,** *46* (41), 7778-81.

23. C. Deviannapoorani; S. Ramakumar; N. Janani; R. Murugan, Synthesis of lithium garnets from $La_2Zr_2O_7$ pyrochlore. *Solid State Ionics* **2015,** *283*, 123-130.

24. I. Kokal; M. Somer; P. H. L. Notten; H. T. Hintzen, Sol–gel synthesis and lithium ion conductivity of $Li_7La_3Zr_2O_{12}$ with garnet-related type structure. *Solid State Ionics* **2011,** *185* (1), 42-46.

25. M. Balaish; J. C. Gonzalez-Rosillo; K. J. Kim; Y. Zhu; Z. D. Hood; J. L. M. Rupp, Processing thin but robust electrolytes for solid-state batteries. *Nat. Energy* **2021,** *6* (3), 227-239.

26. N. Janani; C. Deviannapoorani; L. Dhivya; R. Murugan, Influence of sintering additives on densification and Li^+ conductivity of Al doped $Li_7La_3Zr_2O_{12}$ lithium garnet. *RSC Adv.* **2014,** *4* (93), 51228-51238.

27. Y. Shimonishi; A. Toda; T. Zhang; A. Hirano; N. Imanishi; O. Yamamoto; Y. Takeda, Synthesis of garnet-type $Li_{7-x}La_3Zr_2O_{12-1/2x}$ and its stability in aqueous solutions. *Solid State Ionics* **2011,** *183* (1), 48-53.

28. Q. Liu; Z. Geng; C. Han; Y. Fu; S. Li; Y. He; F. Kang; B. Li, Challenges and perspectives of garnet solid electrolytes for all solid-state lithium batteries. *J. Power Sources* **2018,** *389*, 120-134.

29. Y. An; X. Han; Y. Liu; A. Azhar; J. Na; A. K. Nanjundan; S. Wang; J. Yu; Y. Yamauchi, Progress in Solid Polymer Electrolytes for Lithium-Ion Batteries and Beyond. *Small* **2022,** *18* (3), 2103617.

30. W. Li; Y. Pang; J. Liu; G. Liu; Y. Wang; Y. Xia, A PEO-based gel polymer electrolyte for lithium ion batteries. *RSC Adv.* **2017,** *7* (38), 23494-23501.

31. Y. Jung; M. S. Park; D. H. Kim; M. Ue; A. Eftekhari; D. W. Kim, Room-Temperature Performance of Poly(Ethylene Ether Carbonate)-Based Solid Polymer Electrolytes for All-Solid-State Lithium Batteries. *Sci. Rep.* **2017,** *7* (1), 17482.

32. X. Yu; A. Manthiram, A review of composite polymer-ceramic electrolytes for lithium batteries. *Energy Storage Mater.* **2021,** *34*, 282-300.

33. S. Li; S. Zhang; L. Shen; Q. Liu; J. Ma; W. Lv; Y. He; Q. Yang, Progress and Perspective of Ceramic/Polymer Composite Solid Electrolytes for Lithium Batteries. *Adv. Sci. (Weinh)* **2020,** *7* (5), 1903088.

34. Y. M. Jeon; S. Kim; M. Lee; W. B. Lee; J. H. Park, Polymer-Clay Nanocomposite Solid-State Electrolyte with Selective Cation Transport Boosting and Retarded Lithium Dendrite Formation. *Adv. Energy Mater.* **2020,** *10* (47), 2003114.

35. J. Zhang; N. Zhao; M. Zhang; Y. Li; P. Chu; X. Guo; Z. Di; X. Wang; H. Li, Flexible and ion-conducting membrane electrolytes for solid-state lithium batteries: Dispersion of garnet nanoparticles in insulating polyethylene oxide. *Nano Energy* **2016,** *28*, 447-454.

36. L. Chen; Y. Li; S. Li; L. Fan; C. Nan; J. B. Goodenough, PEO/garnet composite electrolytes for solid-state lithium batteries: From "ceramic-in-polymer" to "polymer-in-ceramic". *Nano Energy* **2018,** *46*, 176-184.

37. C. Bao; C. Zheng; M. Wu; Y. Zhang; J. Jin; H. Chen; Z. Wen, 12 μm-Thick Sintered Garnet Ceramic Skeleton Enabling High-Energy-Density Solid-State Lithium Metal Batteries. *Adv. Energy Mater.* **2023,** *13* (13), 2204028.

38. X. Zhang; T. Liu; S. Zhang; X. Huang; B. Xu; Y. Lin; B. Xu; L. Li; C. Nan; Y. Shen, Synergistic Coupling between $Li_{6.75}La_3Zr_{1.75}Ta_{0.25}O_{12}$ and Poly(vinylidene fluoride) Induces High Ionic Conductivity, Mechanical Strength, and Thermal Stability of Solid Composite Electrolytes. *J. Am. Chem. Soc.* **2017,** *139* (39), 13779-13785.

39. J. Cheng; G. Hou; Q. Chen; D. Li; K. Li; Q. Yuan; J. Wang; L. Ci, Sheet-like garnet structure design for upgrading PEO-based electrolyte. *J. Chem. Eng.* **2022,** *429,* 132343.

40. L. Li; Y. Deng; G. Chen, Status and prospect of garnet/polymer solid composite electrolytes for all-solid-state lithium batteries. *J. Energy Chem.* **2020,** *50*, 154-177.

41. G. Xi; M. Xiao; S. Wang; D. Han; Y. Li; Y. Meng, Polymer-Based Solid Electrolytes: Material Selection, Design, and Application. *Adv. Funct. Mater.* **2020,** *31* (9), 2007598.

42. B. Jinisha; K. M. Anilkumar; M. Manoj; V. S. Pradeep; S. Jayalekshmi, Development of a novel type of solid polymer electrolyte for solid state lithium battery applications based on lithium enriched poly (ethylene oxide) (PEO)/poly (vinyl pyrrolidone) (PVP) blend polymer. *Electrochim. Acta* **2017,** *235*, 210-222.

Chapter 8: Synopsis

8.1. Global Conclusions

The major conclusions from the works conducted in Chapter 4 to Chapter 6 are:

Cubic garnet nanocrystals were synthesized through the development of a novel crystallization process consisted of three steps: co-precipitation, hydrothermal aging, and calcination. The hydrothermal formation of a precursor containing $La(OH)_3$(cr) and amorphous La-Al hydroxides opened a new calcination-driven crystallization pathway for cubic phase Al-doped $Li_{6.1}Al_{0.3}La_3Zr_2O_{12}$ (Al-LLZO) via $La_2Zr_2O_7$ at a temperature as low as 600 ℃.

The as-synthesized nanoscale cubic LLZO, after pellet compression and sintering, exhibited a high ionic conductivity (0.42 mS cm^{-1} at 25 ℃) and low activation energy 0.17 eV (half of previously reported values) due to favourable grain microstructure, plus good interfacial stability against Li metal (Li-ion stripping-platting cycling at a current density of 0.5 mA cm^{-2} for 400 h at ambient temperature).

A new approach to construction of hybrid (polymer-in-ceramic) solid-state electrolytes was proposed that is based on the development of a robust porous cubic-garnet scaffold (1 mm thick with a porosity of 30.56%), which is infiltrated with conducting polymer. The infiltrated polymer solid electrolyte (PEO-LiTFSI) forms strong molecular bonding on the interior and exterior surface of the ceramic skeleton via La-N bonds effectively lowering the interfacial impedance between the two phases.. Ceramic-based hybrid SSE was shown to exhibit fast Li-ion migration (0.547 mS cm^{-1} at 25 ℃) and high mechanical strength.

The interfacial stability of the newly designed ceramic-based HSE was demonstrated by assembling Li | PEO-LiTFSI-in-porous LLZO HSE | $LiFePO_4$ all-solid-state lithium batteries, which delivered a stable specific discharge capacity of 163 mAh g^{-1} at C/10 for 50 cycles at RT. The ASSLB could be operated even at 2C rate without sign of interfacial instability.

Via modification of the formulation protocol for the fabrication of the porous garnet scaffold and replacement of PEO-LiTFSI with PVDF-LiTFSI ultra thin (130 μm) HSE was engineered suitable for high-V (5 V vs. Li^+ / Li) operation. The novel-designed porous cubic garnet ($Li_{6.1}Al_{0.3}La_3Zr_2O_{12}$, LLZO) scaffold possesses high ceramic-content (~ 93%) while still has

substantial porosity (45.74 %), achieving simultaneously excellent interfacing thanks to embedded polymer phase and mechanical strength in suppressing Li dendrites. Its superior properties were attributed to molecular level interfacing through strong La-N and La-F bonds and the robust ceramic scaffold.

The ultra-thin HSE proved very stable in Li/HSE/Li symmetric cells (over 1000 hours at a current density of 0.5 mA cm^{-2}) and ASSLB assembled with TiO_2-coated $LiNi_{0.6}Co_{0.2}Mn_{0.2}O_2$ cathode and Li metal anode for over 200 cycles from 3 to 4.8 V with no signs of mechanochemical alteration.

8.2. Contributions to the Original Knowledge

The major contributions to original scientific knowledge achieved by the studies in Chapter 4 to Chapter 6 of this thesis, are listed below:

For the first time, the synthesis of cubic garnet phase at a calcination temperature as low as 600 ℃, as well as keeping the particle size around 100 – 200 nm is achieved. The elaboration of the low-temperature cubic-LLZO phase crystallization mechanism without the intermediate formation of tetragonal phase is also novel.

The concept of porous garnet scaffolds as framework for polymer-in-ceramic hydrid solid electrolytes and their application to ASSLBs is considered novel.

The development and analysis of the PEO-LiTFSI-in-porous cubic-garnet scaffold as hybrid solid-state electrolyte (HSE) in ASSLB is novel.

The engineering and analysis of the ultra-thin, molecularly bound together through strong La-N and La-F bonds, PVDF-LiTFSI-in-porous cubic-garnet HSE is novel.

8.3. Future Research Direction

For future research, firstly, in Chapter 4, the dual-reaction mechanism of the low-temperature crystallization of nanoscale cubic LLZO was only demonstrated in the experimental aspect. More theoretical computational simulations should be conducted on this reaction mechanism to develop a first-principles insight and understanding. Moreover, the advantages of the nanoscale cubic LLZO particles in all-solid-state lithium battery application could be further demonstrated, especially, as the electrolyte component in composite cathodes.

Secondly, in Chapter 5, a synergistic effect was demonstrated within the ceramic-based HSEs. The enhanced ionic conductivity of the designed ceramic-based HSEs should be explained on the basis of theoretical computational simulation. In addition, in-situ/operando characterization should be employed on selected all-solid-state lithium batteries enabled by the designed ceramic-based hybrid SSEs during cycling, to capture the interfacial evolution as well as elucidate the behavior of lithium migration and associated machanochemical changes.

Thirdly, in Chapter 6, an in-situ formed interphase (LiF & Li_3N) between cathode and ceramic-based CSE was detected, and demonstrated that it stabilizes the interface during the delithiation-lithiation process. In the future, the in-situ observation as well as the mechanism of the interphase formation should be studied.

Beyond the three chapters, future work on further optimizing the HSE and testing other conductive polymers is recommended.

Appendixes: Supplementary Information for Chapters 4, 5 and 6

A.1. Supplementary Information – Chapter 4

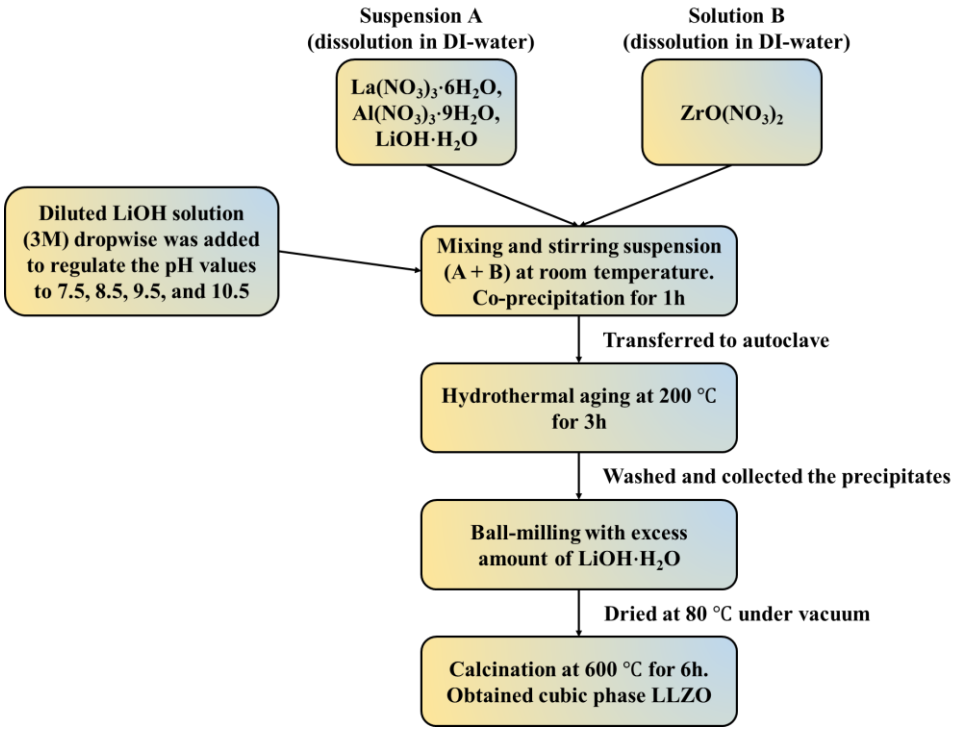

Figure A.1. 1. The flowchart of the low-temperature synthesis of cubic phase $Li_{6.1}Al_{0.3}La_3Zr_2O_{12}$ (c-Al-LLZO) at 600 ℃.

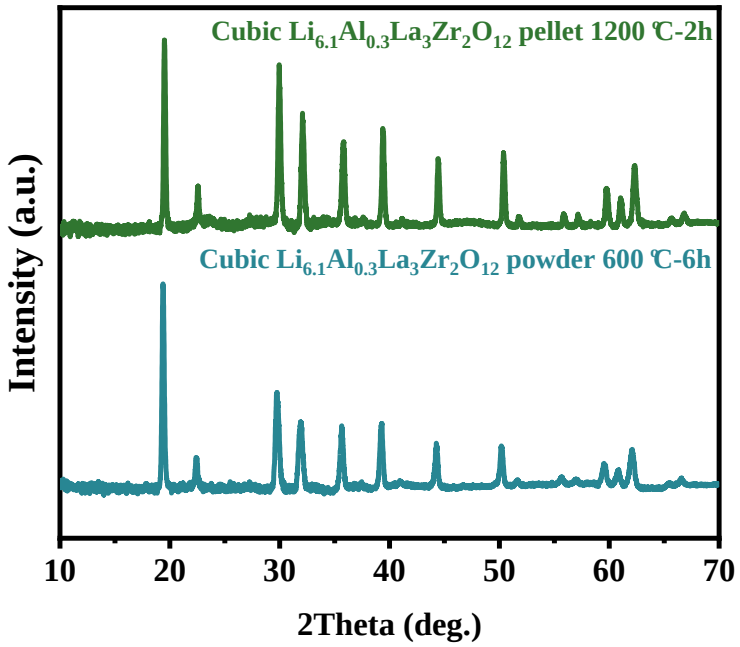

Figure A.1. 2. XRD patterns of c-Al-LLZO (pH 10.5) after 600 ℃ for 6 h and its pellet after 1200 ℃ 2 h heat treatment.

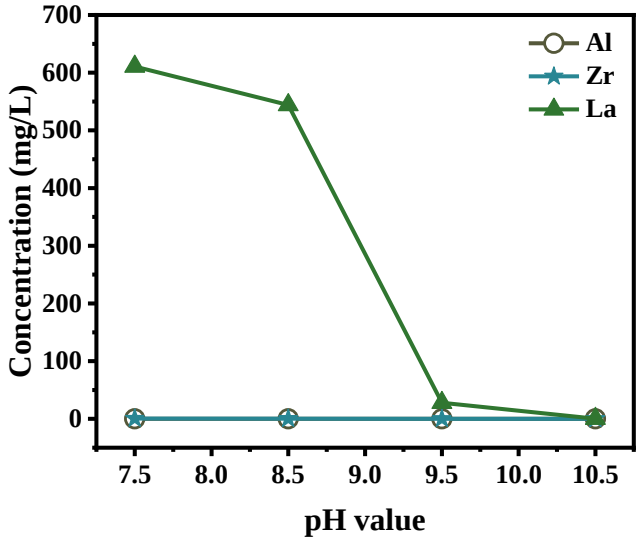

Figure A.1. 3. ICP solution analysis results of the supernatants collected after co-precipitation at room temperature at various pH values.

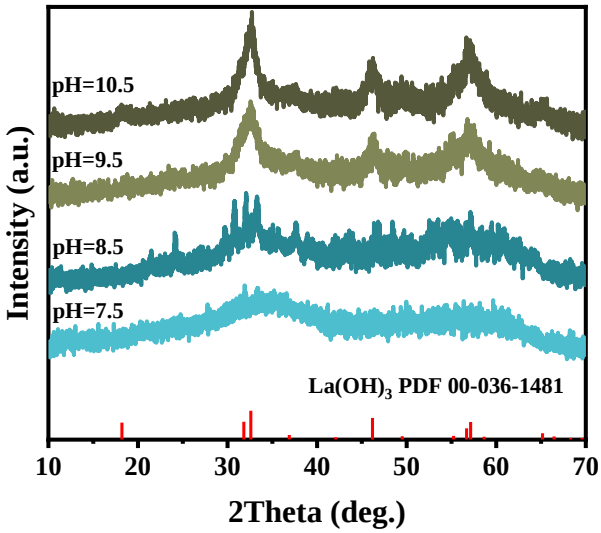

Figure A.1. 4. XRD (Cobalt Kα radiation, λ = 1.788892 Å) patterns of the powders obtained after the co-precipitation process. Bragg peak position of $La(OH)_3$ PDF 00-036-1481.

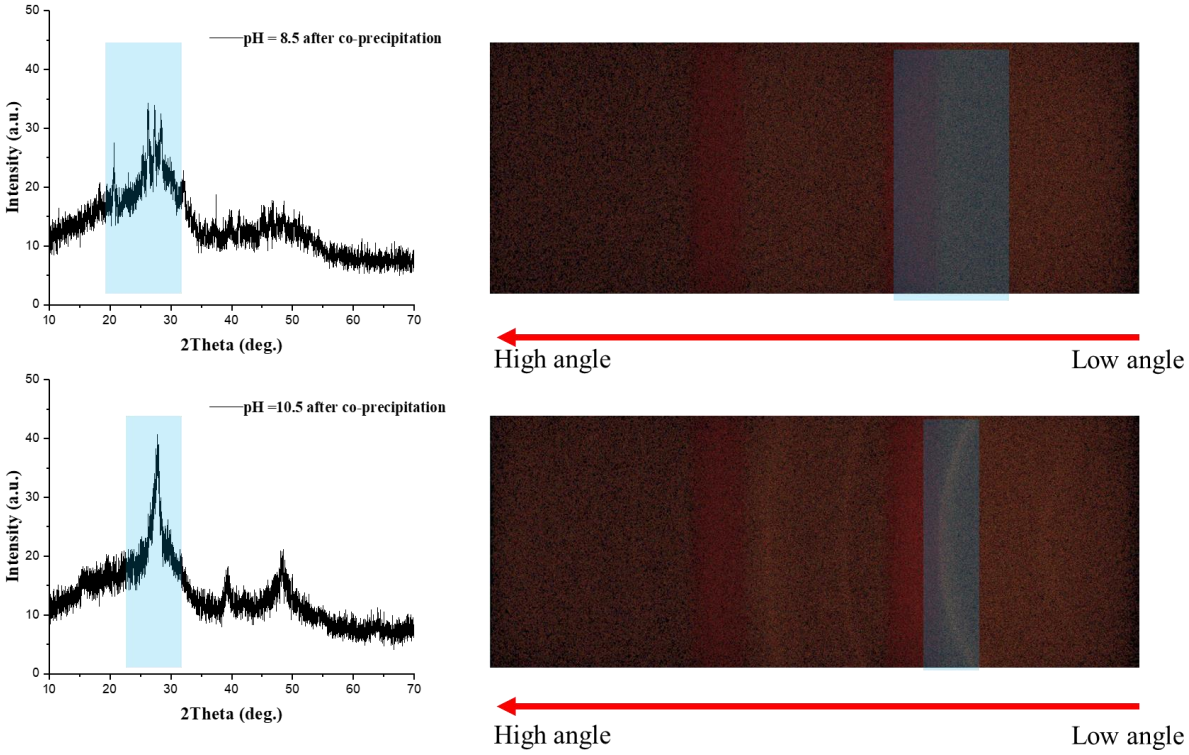

Figure A.1. 5. XRD (Cobalt Kα radiation, λ = 1.788892 Å) patterns of the powders obtained after the co-precipitation process (pH = 8.5 and 10.5) and the corresponding diffraction images.

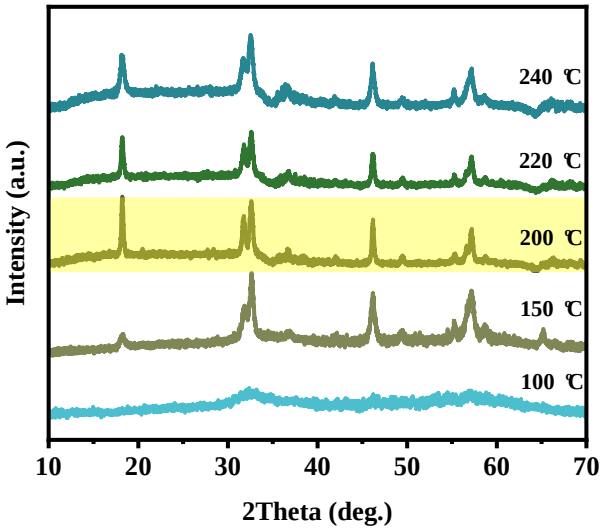

Figure A.1. 6. XRD (Cobalt Kα radiation, λ = 1.788892 Å) patterns of the intermediates obtained after hydrothermal aging at various temperatures for 3 h.

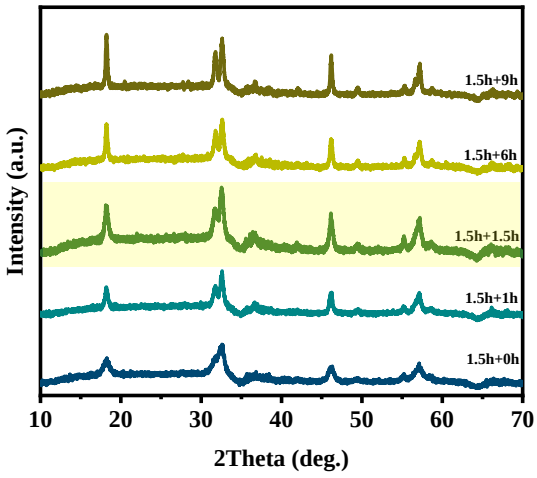

Figure A.1. 7. XRD (Cobalt Kα radiation, λ = 1.788892 Å) patterns of the intermediates obtained after hydrothermal aging at 200 ℃ for different holding periods.

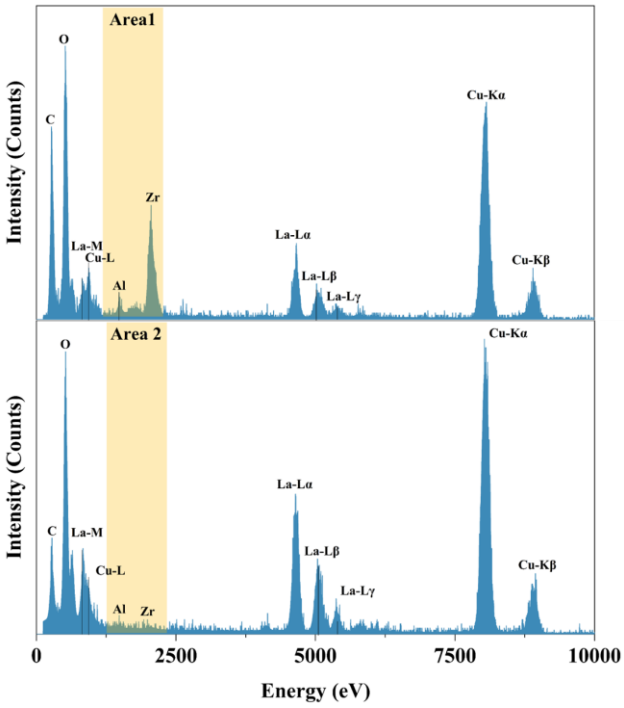

Figure A.1. 8. Energy dispersive X-ray spectroscopy (EDS) analysis of the different areas.

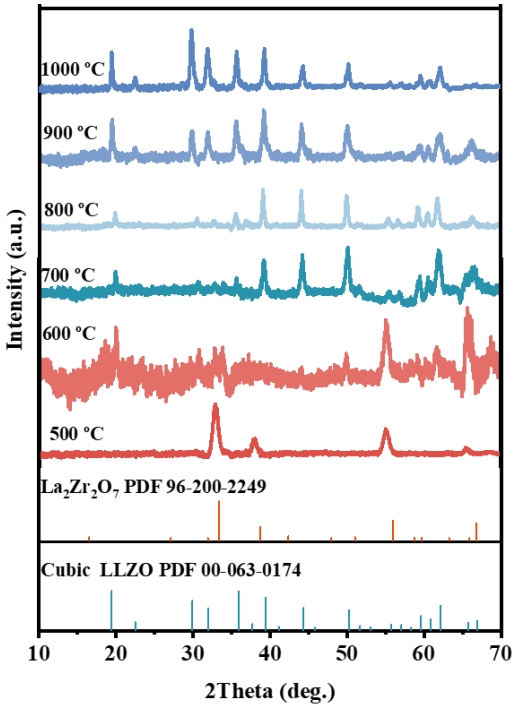

Figure A.1. 9. X-ray diffraction patterns of pH = 10.5 samples collected after calcination at different temperatures without the hydrothermal aging step.

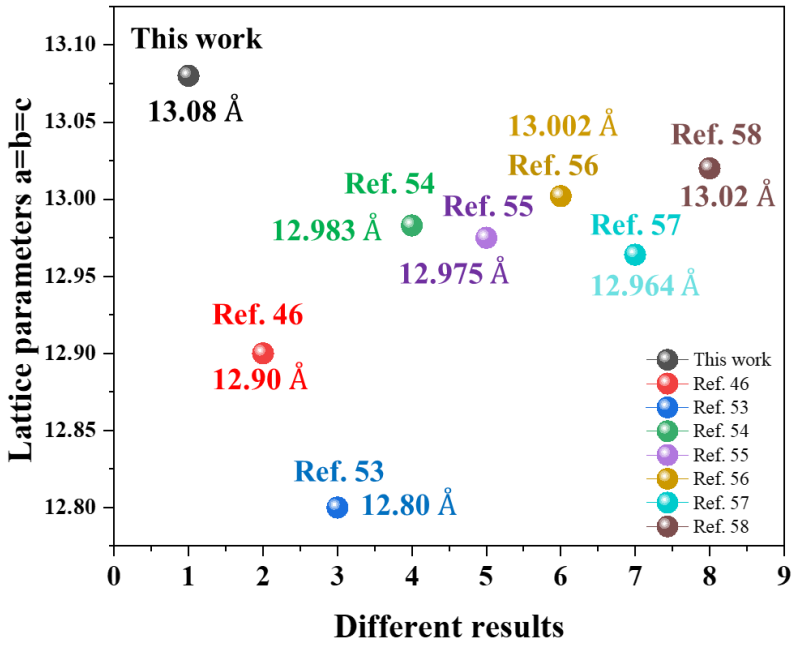

Figure A.1. 10. A summary of lattice parameters (a = b = c) comparison of this work with other published results.

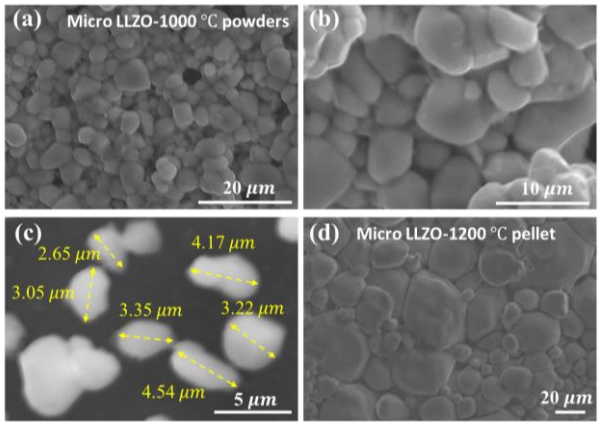

Figure A.1. 11. SEM images of the microscale c-Al-LLZO (a-c) powders obtained from the same synthesis process at 1000 ℃-6h, (d) the sintered pellet (1200 ℃-2h) of the microscale c-Al-LLZO.

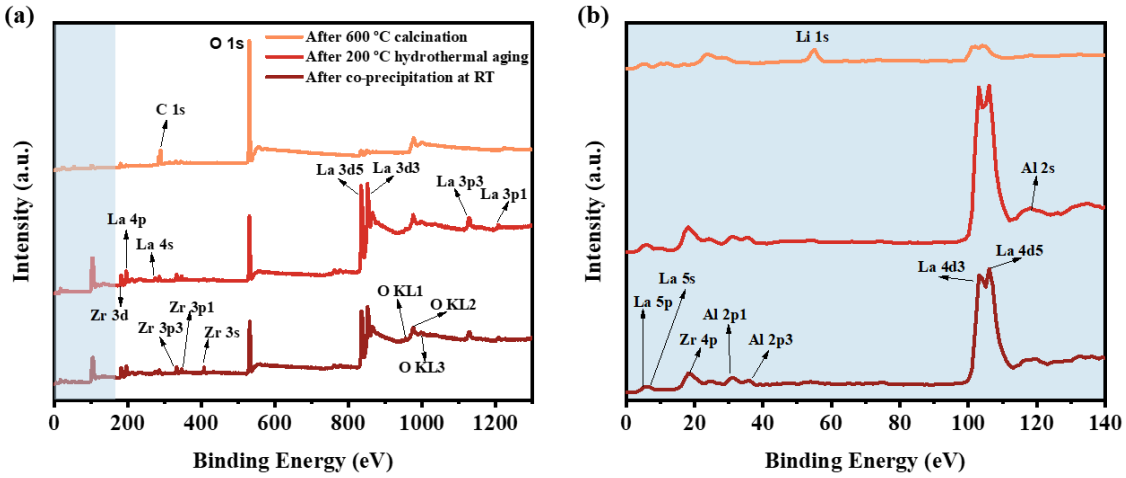

Figure A.1. 12. (a) The full survey of the products after co-precipitation, hydrothermal aging, and calcination process steps in terms of the presence of La, Zr, Al, Li, O, and C; (b) the amplification of the patterns between 0 to 140 eV.

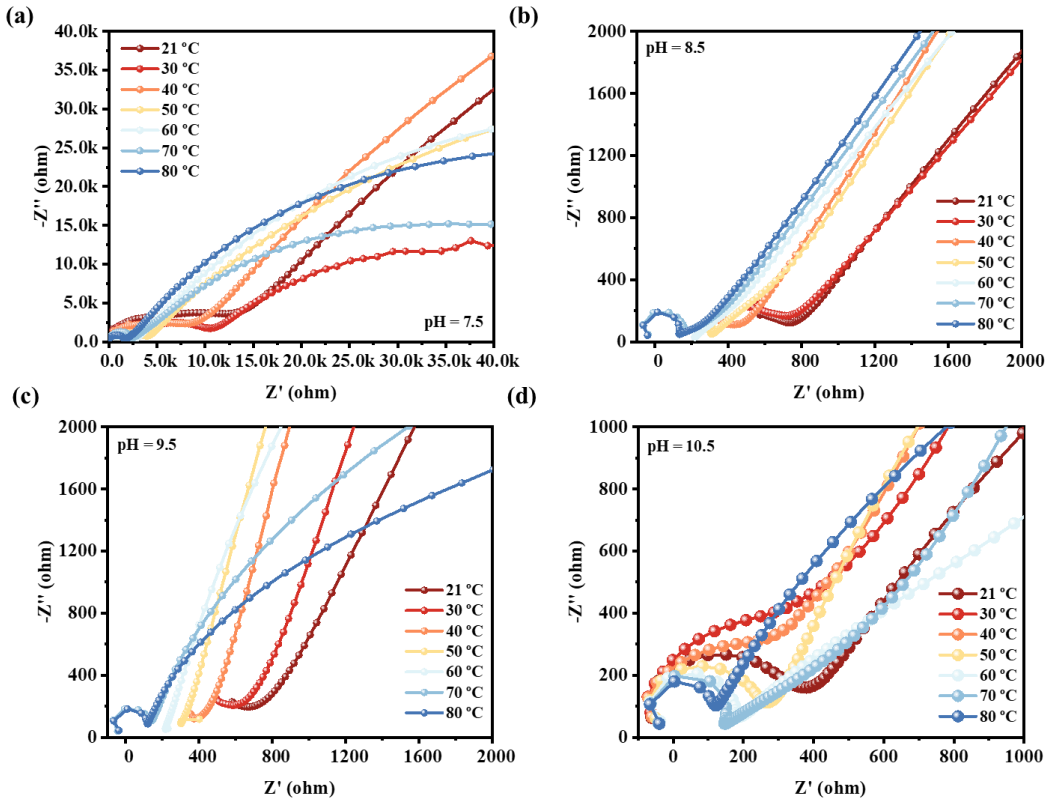

Figure A.1. 13. Nyquist plots of different c-Al-LLZO pellets measured at various temperatures from room temperature (21 °C) as well as from 30 to 80 °C with 10 °C temperature intervals (frequency range: 0.1 Hz to 1 MHz, amplitude: 10 mV).

Table A.1. 1. The Scherrer equation calculation data of the c-Al-LLZO (10.5) particle size.

Peak positions (2θ)	FWHM	Crystallites Sizes (nm)	Average Crystallites Size (nm)
19.38847	0.25571	36.60349601	29.37432606
22.40939	0.26772	35.13185722	
29.77405	0.37883	25.20039449	
31.89491	0.40848	23.49078815	
35.64025	0.33943	28.55136271	
39.23949	0.32052	30.55940047	
44.25331	0.31541	31.57706958	
50.18179	0.3477	29.29986153	
59.51897	0.42233	25.16483051	
60.78586	0.33969	31.48791079	
62.05945	0.41331	26.05061518	

Table A.1. 2. The Electrochemical Impedance Spectroscopy (EIS) data measured at room temperature (21 ℃) as well as from 30 to 80 ℃ with 10 ℃ temperature intervals.

c-Al-LLZO (7.5) pellet		
Temperature (℃)	**Total resistance (Ω)**	**Ionic conductivity σ (10^{-4} S*cm^{-1})**
21 ℃	11280	0.086
30 ℃	11076	0.087
40 ℃	8891.7	0.109
50 ℃	4103.2	0.236
60 ℃	2633.5	0.368
70 ℃	2310.6	0.419
80 ℃	1644.5	0.589

c-Al-LLZO (8.5) pellet		
Temperature (℃)	**Total resistance (Ω)**	**Ionic conductivity σ (10^{-4} S*cm^{-1})**
21 ℃	764.5	1.358
30 ℃	706.5	1.469
40 ℃	519.9	1.997
50 ℃	440.6	2.356
60 ℃	395.7	2.623
70 ℃	243.7	4.259
80 ℃	198.1	5.240

c-Al-LLZO (9.5) pellet		
Temperature (℃)	**Total resistance (Ω)**	**Ionic conductivity σ (10^{-4} S*cm^{-1})**
21 ℃	669.6	1.583
30 ℃	588.5	1.801
40 ℃	413.1	2.566
50 ℃	303.1	3.497
60 ℃	225.8	4.694
70 ℃	196.1	5.401
80 ℃	166.1	6.382

c-Al-LLZO (10.5) pellet		
Temperature (℃)	**Total resistance (Ω)**	**Ionic conductivity σ (10^{-4} S*cm^{-1})**
21 ℃	320.4	4.151
30 ℃	303.1	4.388
40 ℃	257.2	5.171
50 ℃	198.4	6.704
60 ℃	139.8	9.514
70 ℃	96.62	12.213
80 ℃	82.56	16.110

Equation A.1.1.:

The average size of the c-Al-LLZO (10.5) primary crystal was calculated with the Scherrer Equation:

$$D = K\lambda/\beta \cos\theta$$

Where, D is the crystallite size, (nm); K = 0.9, the Scherrer constant; λ = 1.78892 Å, the wavelength of the X-ray source Co; β is full width at half maximum (FWHM), and θ is the peak position.

Equation A.1.2.:

$$\sigma = L/(R \times S)$$

where σ is the ionic conductivity, L is the thickness of the solid electrolyte (cm), R is the resistance (ohm), and S is the area of the stainless steel (SS).

Equation A.1.3.:

$$\sigma T = Aexp(-\frac{E_a}{RT})$$

where σ ($S \cdot cm^{-1}$) is the ionic conductivity, T (K) is the absolute temperature, A is the pre-exponential constant, R is the Boltzmann constant, and E_a (eV) is the activation energy for the ionic conductivity. According to the Arrhenius equation, the total conduction activation energy is determined by the slope of the log 10 σ and 1/T plots.

A.2. Supplementary Information – Chapter 5

The porosity of the as-synthesized porous c-LLZO scaffolds was measured and calculated through the Archimedes method based on the following **Equation (A.2.1.)**:

$$Porosity = \left[\frac{m_{wet} - m_{dry}}{\rho_{liquid}}\right] / V_{pellet} \quad (1)$$

Where m_{wet} and m_{dry} are the weights of the scaffolds before and after immersion into liquid (n-butanol), ρ_{liquid} is the density of the liquid (0.811 g cm^{-3}), and V_{pellet} is the volume of the as-synthesized porous c-LLZO scaffolds.

Table A.2. 1. The porosity of the as-prepared LLZO scaffolds

	m_{dry}	m_{wet}	V_{pellet}	Porosity
Sample #1	**0.4499g**	**0.4945g**	**0.180 cm^3**	**30.55%**
Sample #2	**0.4497g**	**0.4957g**	**0.187 cm^3**	**30.33%**
Sample #3	**0.4511g**	**0.4973**	**0.185 cm^3**	**30.79%**
Average porosity: 30.56%				

The ionic conductivity (σ) was calculated based on the following **Equation (A.2.2.)**:

$$\sigma = L/(R \times S) \quad (2)$$

where σ is the ionic conductivity (S cm^{-1}), L is the thickness of the hybrid SE (cm), R is the resistance (ohm) of the SE, and S is the area of the stainless steel (SS).

The Li-ion transport activation energy (E_a) of the four SE types was calculated by the Arrhenius **Equation (A.2.3.):**

$$\sigma(T) = A \exp(-E_a/RT) \quad (3)$$

The lithium-ion transference number was calculated based on the following **Equation (A.2.4.):**

$$t_{Li^+} = \frac{I_S(\Delta V - I_0 R_0)}{I_0(\Delta V - I_S R_S)} \quad (4)$$

where ΔV, I_0, I_s, R_0 and R_s represent the polarization potential (10 mV), the initial current, steady current, initial interfacial resistance, and steady interfacial resistance, respectively.

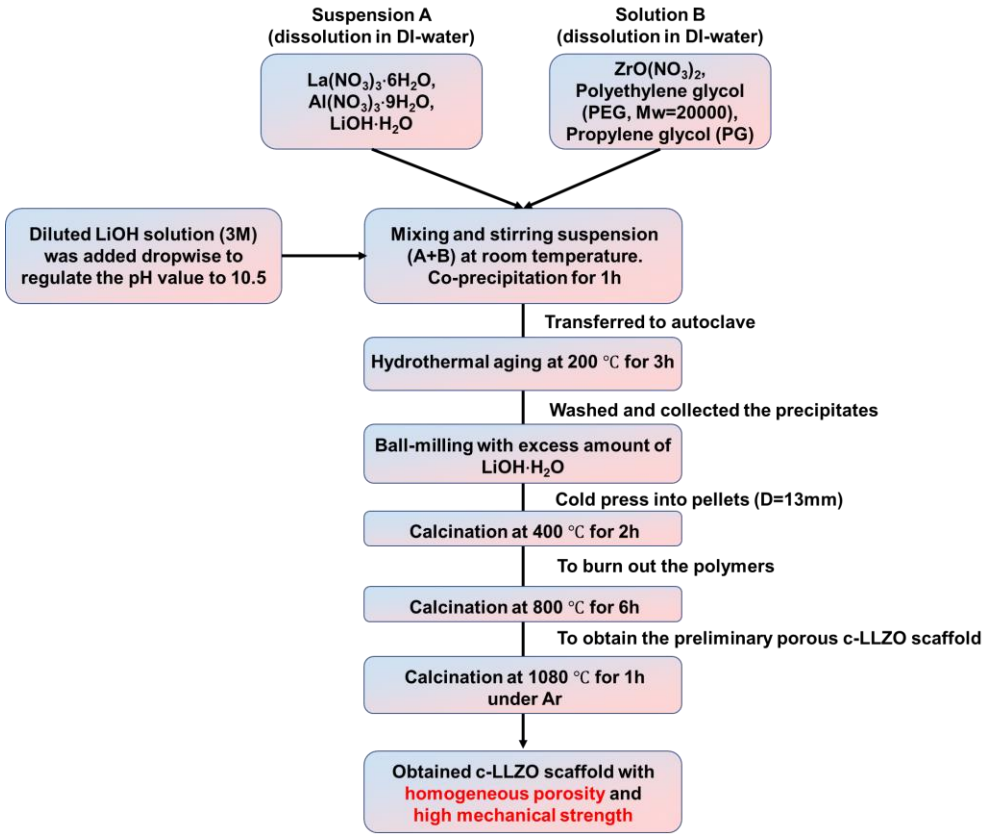

Figure A.2. 1. The flowchart of the synthesis process of the porous c-LLZO scaffold.

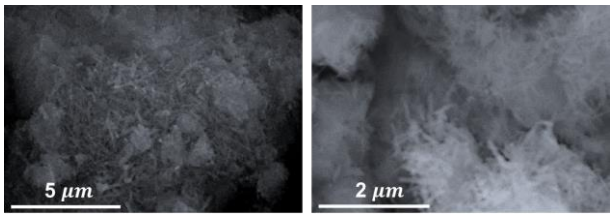

Figure A.2. 2. The SEM images of intermediate composites obtained from co-precipitation and hydrothermal aging.

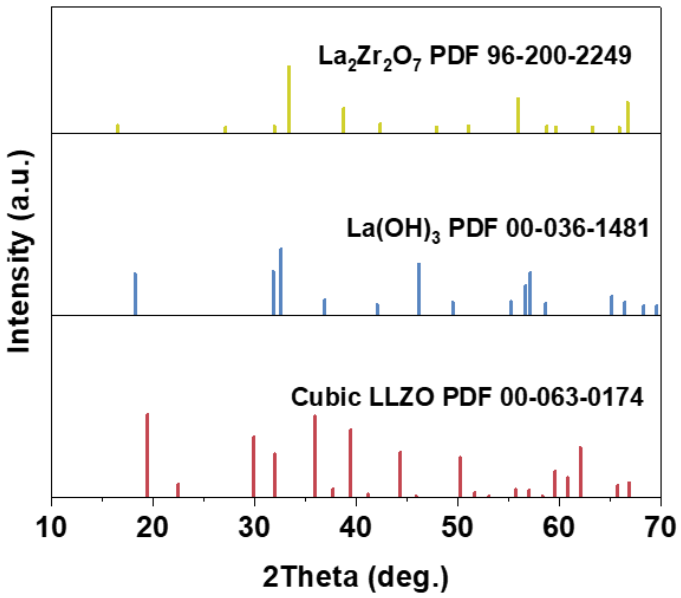

Figure A.2. 3. The Standard XRD peaks of $La(OH)_3$, $La_2Zr_2O_7$, and cubic-LLZO phase.

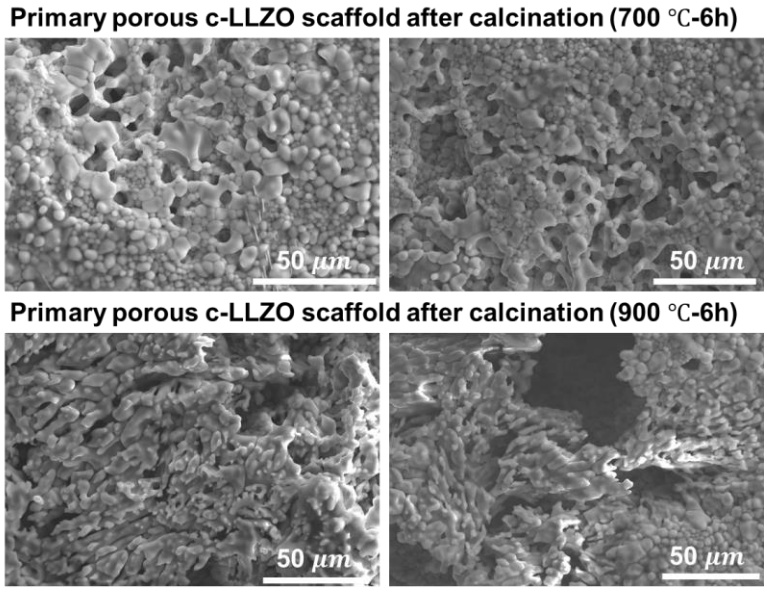

Figure A.2. 4. The SEM images of primary porous c-LLZO scaffold after calcination at 700 ℃ and 900 ℃ for 6h respectively.

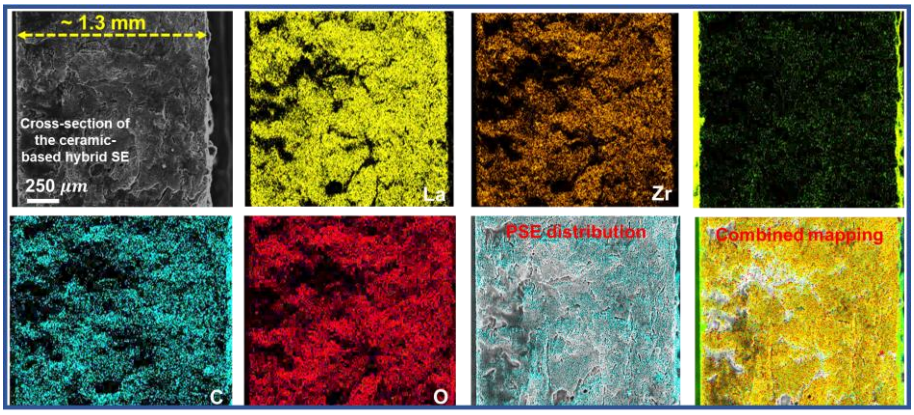

Figure A.2. 5. Cross-sectional SEM image and EDS results of the ceramic-based hybrid SE.

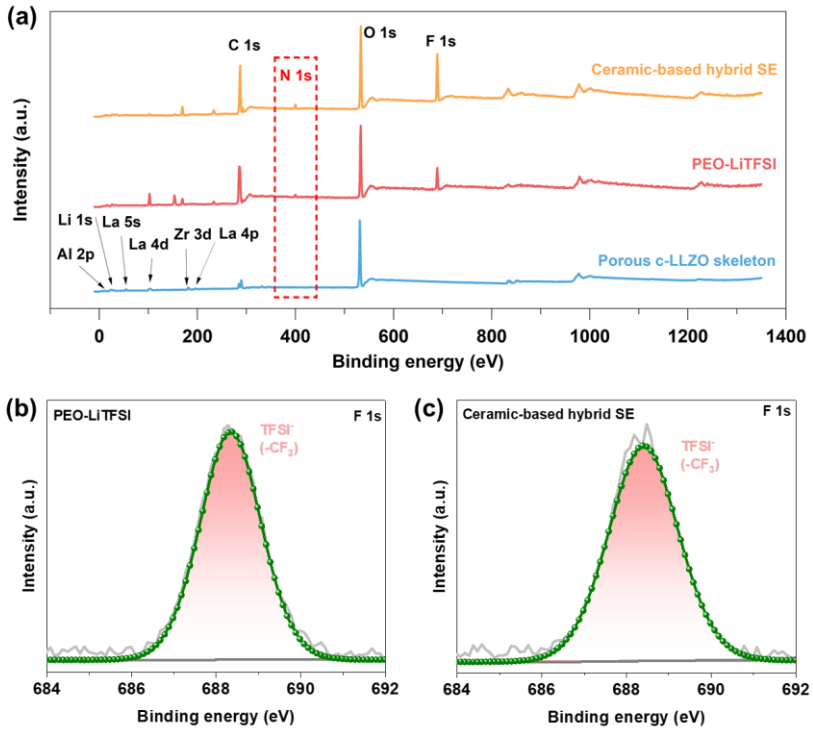

Figure A.2. 6. (a) XPS surveys of the porous c-LLZO skeleton, PEO-LiTFSI PSE and the ceramic-based hybrid SE; (b) and (c) F 1s spectra of the PEO-LiTFSI PSE and the ceramic-based hybrid SE.

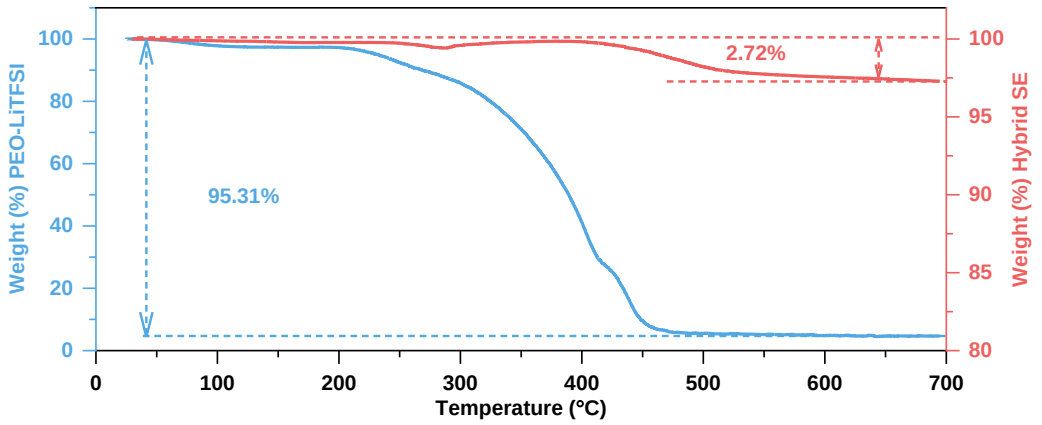

Figure A.2. 7. TGA results of PEO-LiTFSI PSE membrane and the ceramic-based hybrid SE.

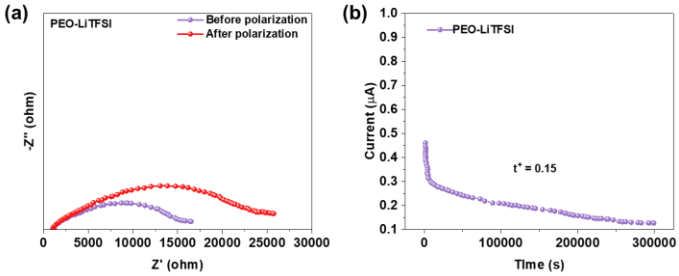

Figure A.2. 8. Li-ion transference number of PEO-LiTFSI PSE. (a) EIS of the symmetric battery before and after polarization; (b) polarization curve at 25℃.

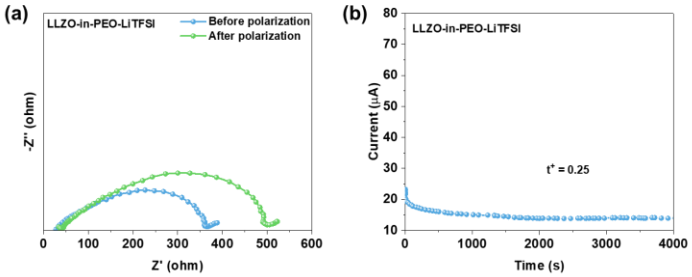

Figure A.2. 9. Li-ion transference number of polymer-based hybrid solid electrolyte (10 wt.% LLZO particles in PEO-LiTFSI). (a) EIS of the symmetric battery before and after polarization; (b) polarization curve at 25℃.

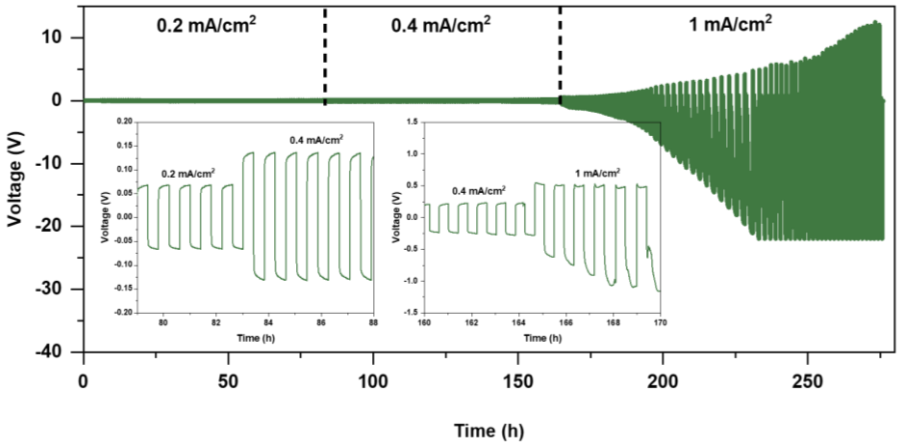

Figure A.2. 10. The galvanostatic curves of the Li / ceramic-based hybrid SE / Li symmetric batteries at different current densities.

A.3. Supplementary Information – Chapter 6

Supplemental notes

Note A.3.1: Equations

The porosity of the as-prepared porous cubic LLZO framework was measured and calculated through the Archimedes method based on the following Equation (A.3.1):

$$Porosity = \left[\frac{m_{wet}-m_{dry}}{\rho_{liquid}}\right]/V_{pellet} \quad (1)$$

Where m_{wet} and m_{dry} are the weights of the pellets before and after immersion into liquid, ρ_{liquid} is the density of the liquid (0.811 g/cm^3), and V_{pellet} is the volume of the as-prepared porous LLZO framework. The average porosity of the as-prepared porous LLZO framework is 45.74%.

The ionic conductivity (σ) was calculated based on the following Equation (A.3.2):

$$\sigma = L/(R \times S) \quad (2)$$

where σ (S cm^{-1}) is the ionic conductivity, L is the thickness of the hybrid SE (cm), R is the resistance (ohm), and S is the area of the stainless steel (SS).

The Li-ion transport activation energy (E_a (eV)) of the four types SEs were calculated by the Arrhenius Equation (A.3.3):

$$\sigma(T) = A\exp(-E_a/RT) \quad (3)$$

The lithium-ion transference number was calculated using the following Equation (A.3.4):

$$t_{Li^+} = \frac{I_s(\Delta V - I_0R_0)}{I_0(\Delta V - I_sR_s)} \quad (4)$$

where ΔV, I_0, I_s, R_0 and R_s represent the polarization potential (10 mV), the initial current (mA), steady current (mA), initial interfacial resistance (ohm), and steady interfacial resistance (ohm), respectively.

Note A.3.2: Alternative formulations for the synthesis of porous LLZO powders

Four different formulations based on modifications of the general synthesis route (five main steps) as presented in Figure A.3.1 and summarized below were followed.

Preparation of suspension A and solution B;

Co-precipitation;

Hydrothermal aging;

Mixing collected precipitates with Li source via ball milling;

Calcination Procedure.

The differences between four formulations are i) with/without plasticizer; ii) different MW of porous template employed; iii) different synthesis step where organics (template and plasticizer) introduced. Details are listed in Table A.3.1.

Note A.3.3: Mechanism of capacity decay.

It is noted that the liquid electrolyte ($LiPF_6$ in EC-DMC, LE) half-cell using the same high-voltage TiO_2@NCM622 cathode was also assembled for comparison purposes, and the cycling stability was evaluated as shown in Figure A.3.20. After 15 cycles the specific discharge capacity dropped from 183.77 to 163.75 mAh g^{-1}, and the capacity retention is 89%. This capacity fade is mainly attributed to NMC622 cathode, as at a highly delithiated state, the active Ni^{4+} ions are unstable and have a tendency to form NiO-like rock-salt phase on the material surface, which increases the ion transfer resistance due to its more compact structure. [1,2] (see Supplemental references)

Supplemental tables

Table A.3. 1. Different formulations for synthesis of porous LLZO powders

	Porous template	Plasticizer	Introduced step
Formulation 1 (sample a)	PEG (MW: 6000 g/mol)	Without	Suspension A
Formulation 1 (sample b)	PEG (MW: 6000 g/mol)	Without	Solution B
Formulation 1 (sample c)	PEG (MW: 6000 g/mol)	Without	Mixed with (collected precipitate and Li source) via ball milling

Formulation 2	PEG (MW: 6000 g/mol)	PEG (MW: 2000 g/mol)	Solution B (with different ratios between template and plasticizer)
Formulation 3	PEG (MW: 20000 g/mol)	PEG (MW: 2000 g/mol)	Solution B (with different ratios between template and plasticizer)
Formulation 4	PEG (MW: 20000 g/mol)	PG	Solution B (with different ratios between template and plasticizer)

Supplemental figures

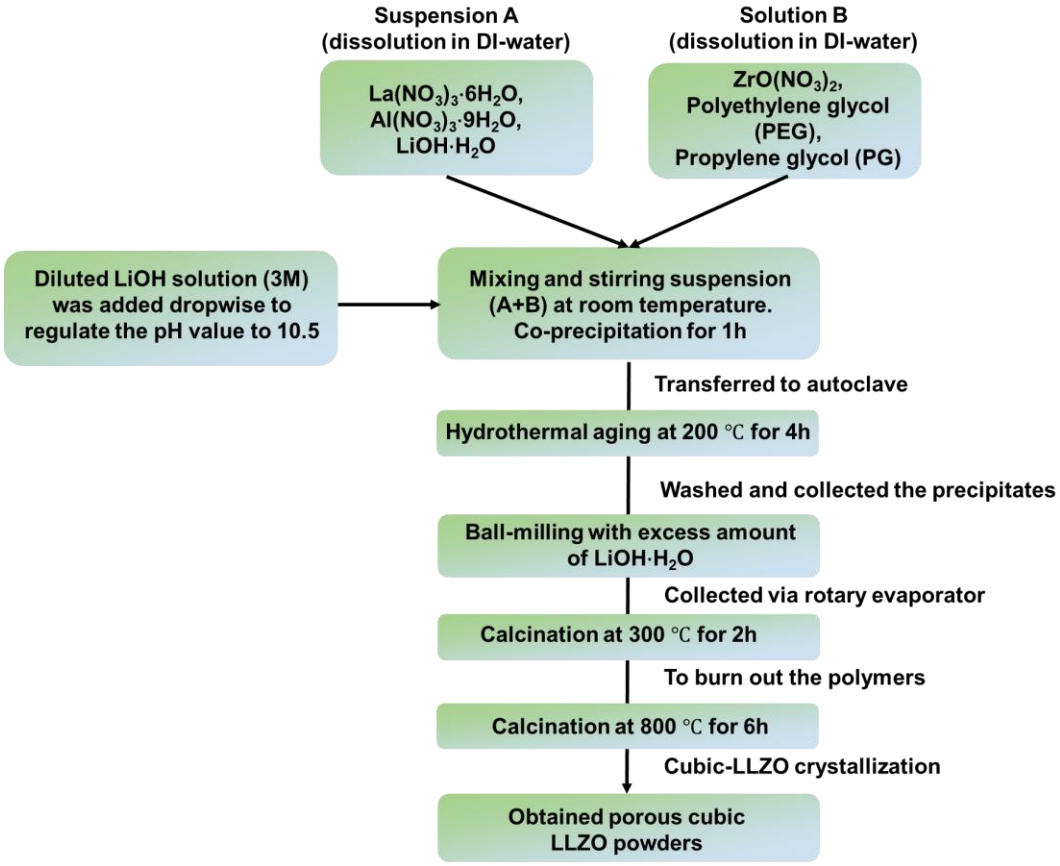

Figure A.3. 1. The flowchart of the synthesis process of the porous cubic LLZO powders.

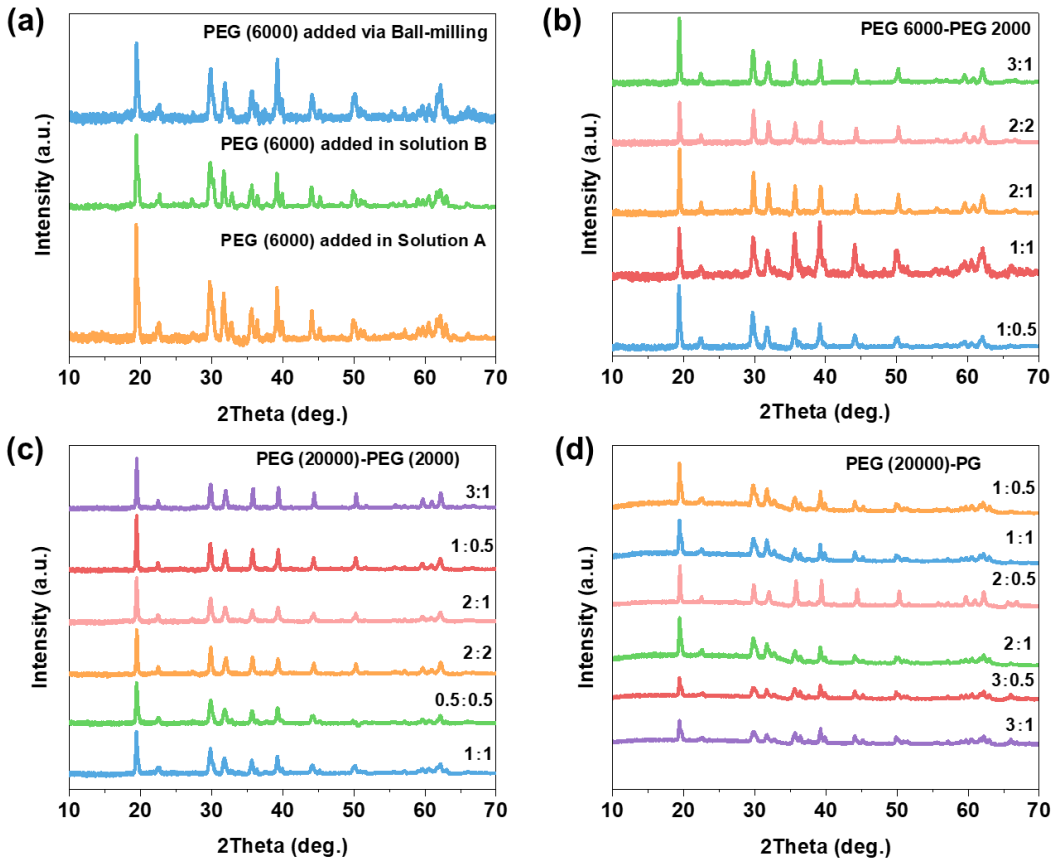

Figure A.3. 2. The XRD patterns of the porous cubic LLZO powders obtained through four different synthesis methods.

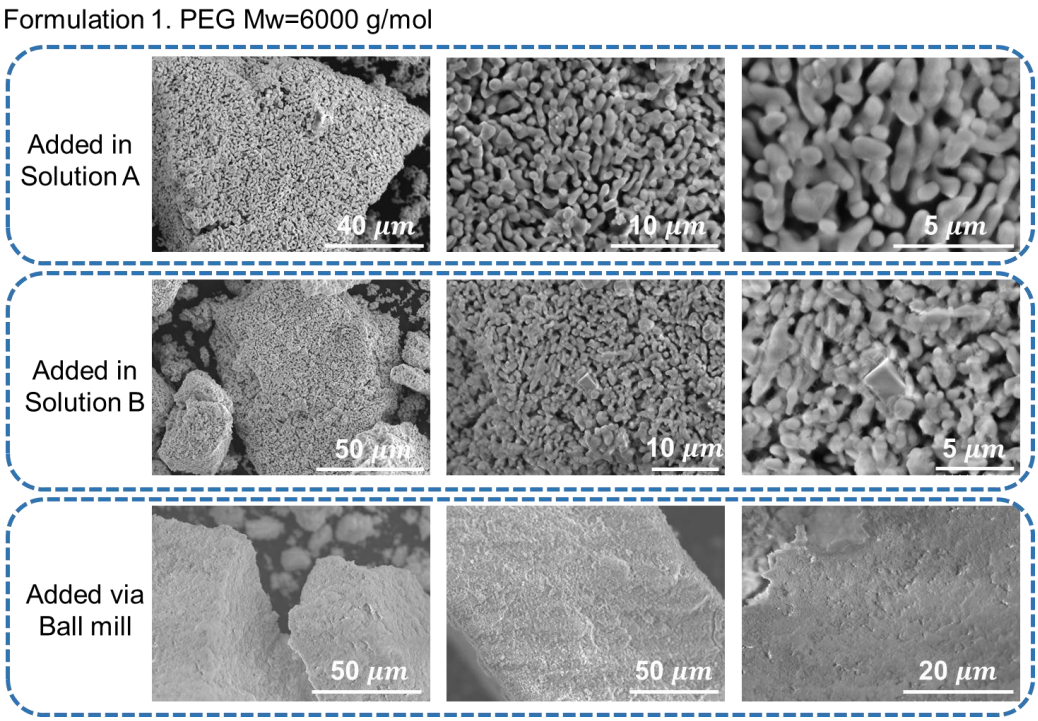

Figure A.3. 3. SEM images of the three types of porous LLZO powders based on the formulation 1.

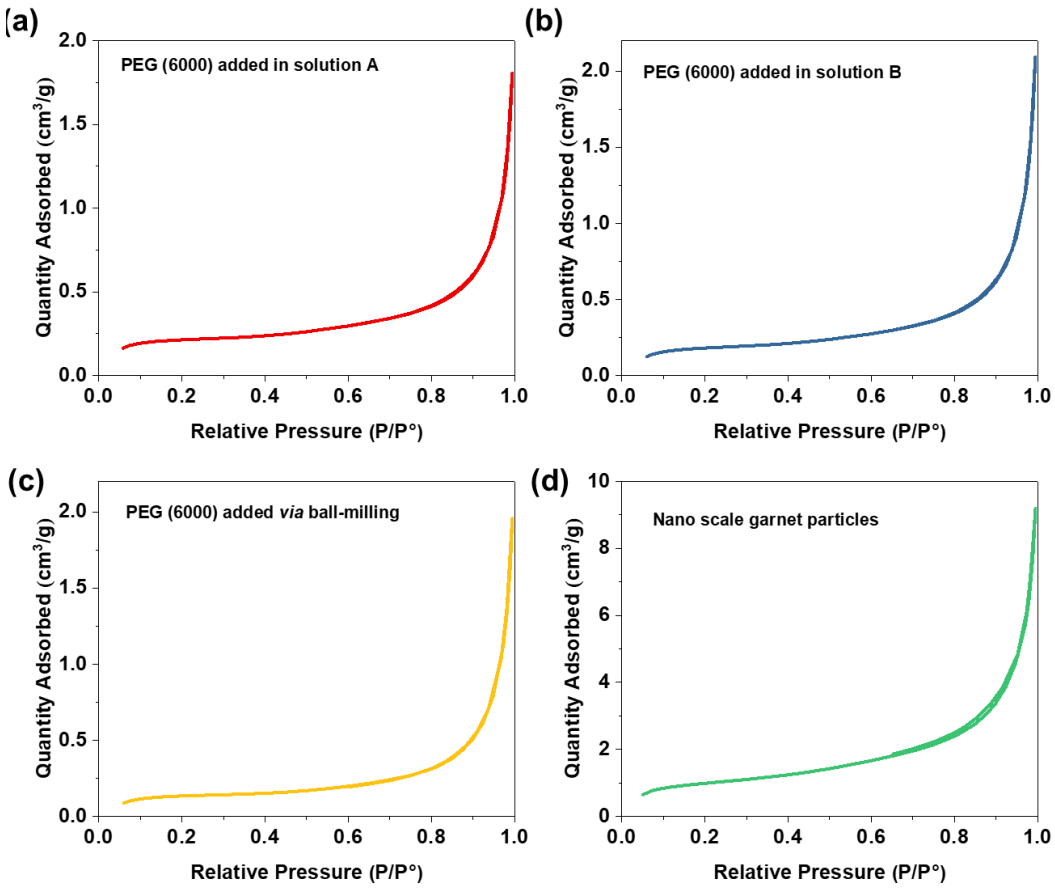

Figure A.3. 4. N_2 adsorption/desorption isotherms of the porous LLZO powders based on the formulation 1.

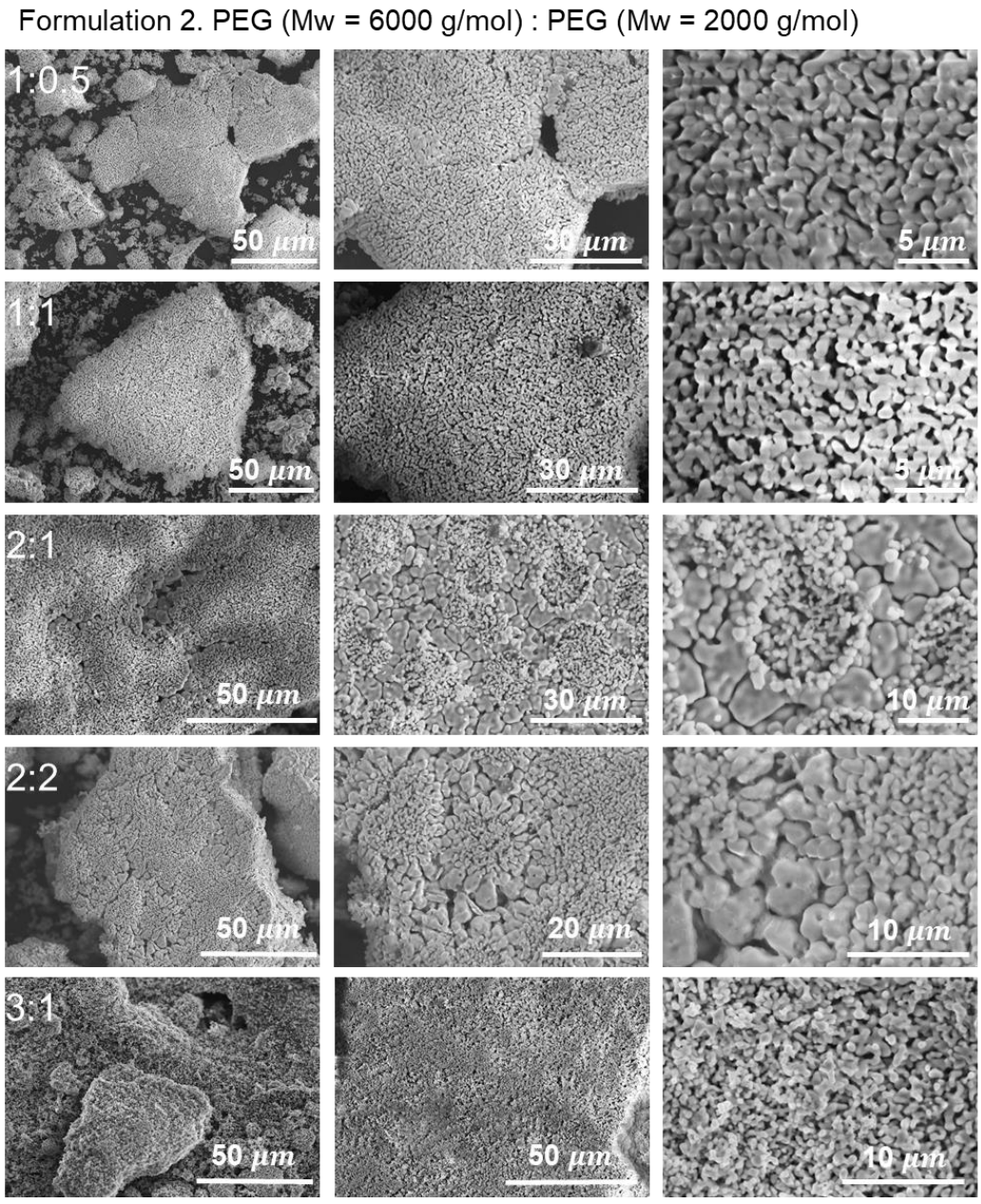

Figure A.3. 5. SEM images of the five types of porous LLZO powders based on the formulation 2.

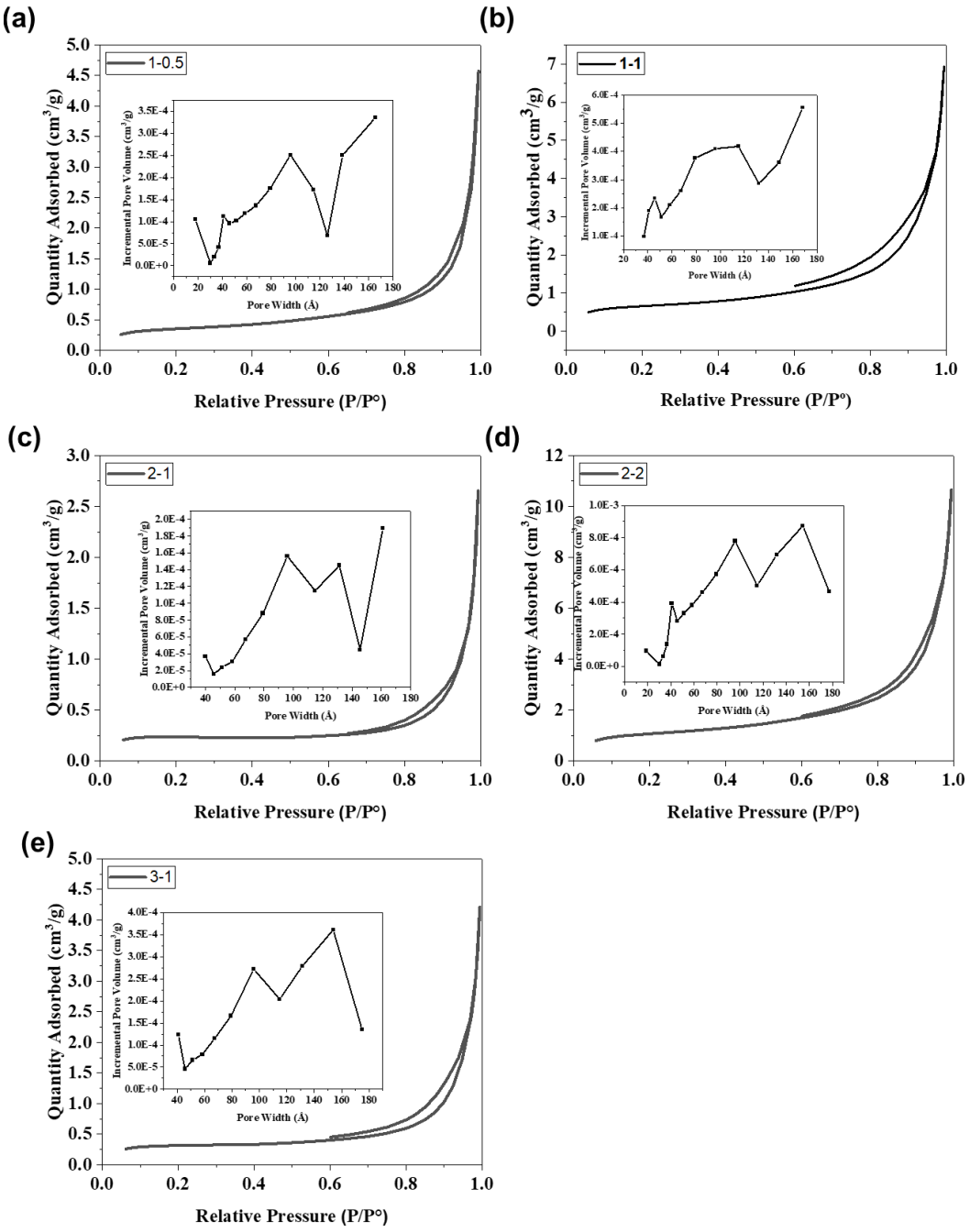

Figure A.3. 6. N_2 adsorption/desorption isotherms with BJH desorption pore size distribution curve as insets of the porous LLZO powders based on the formulation 2.

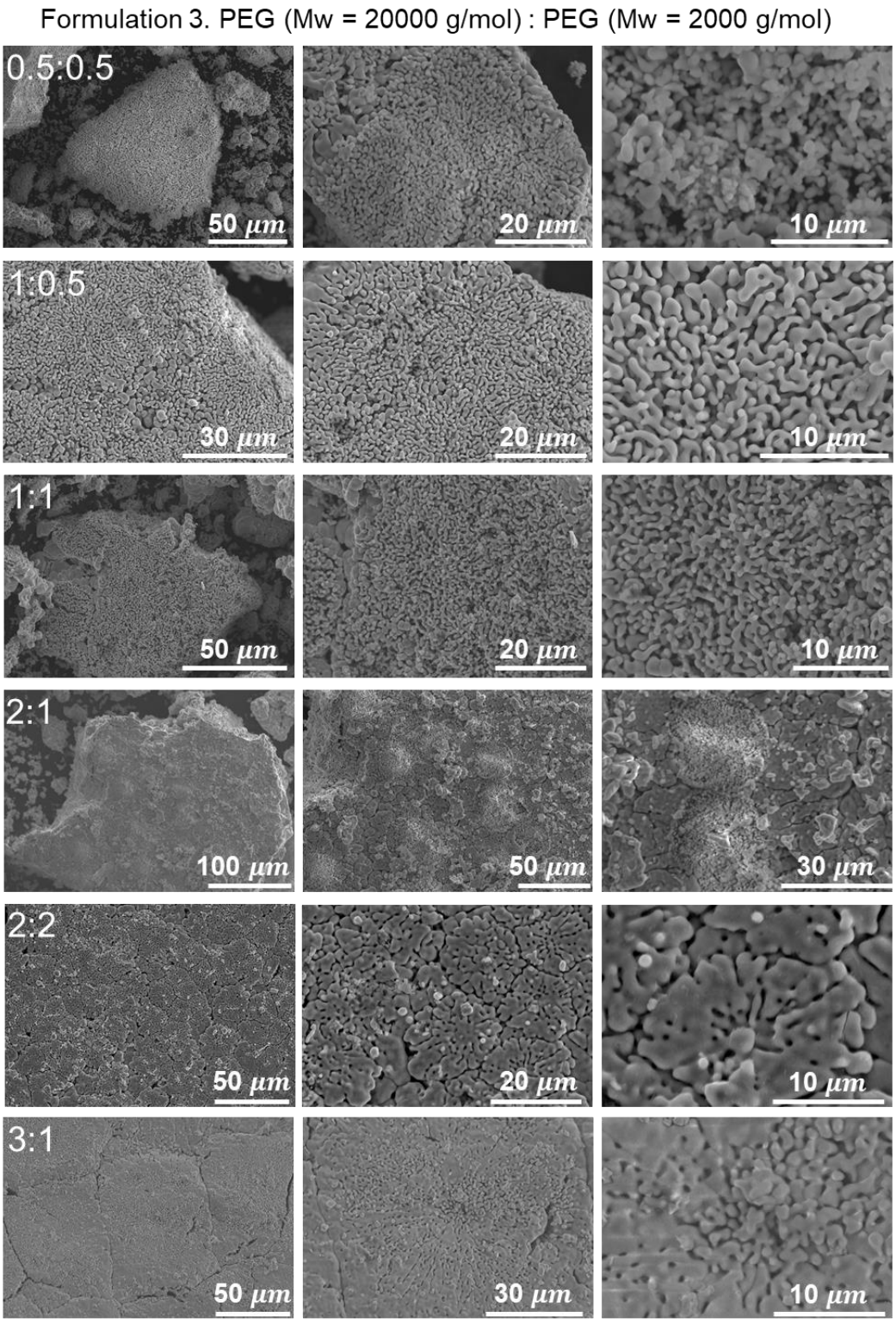

Figure A.3. 7. SEM images of the six types of porous LLZO powders based on the formulation 3.

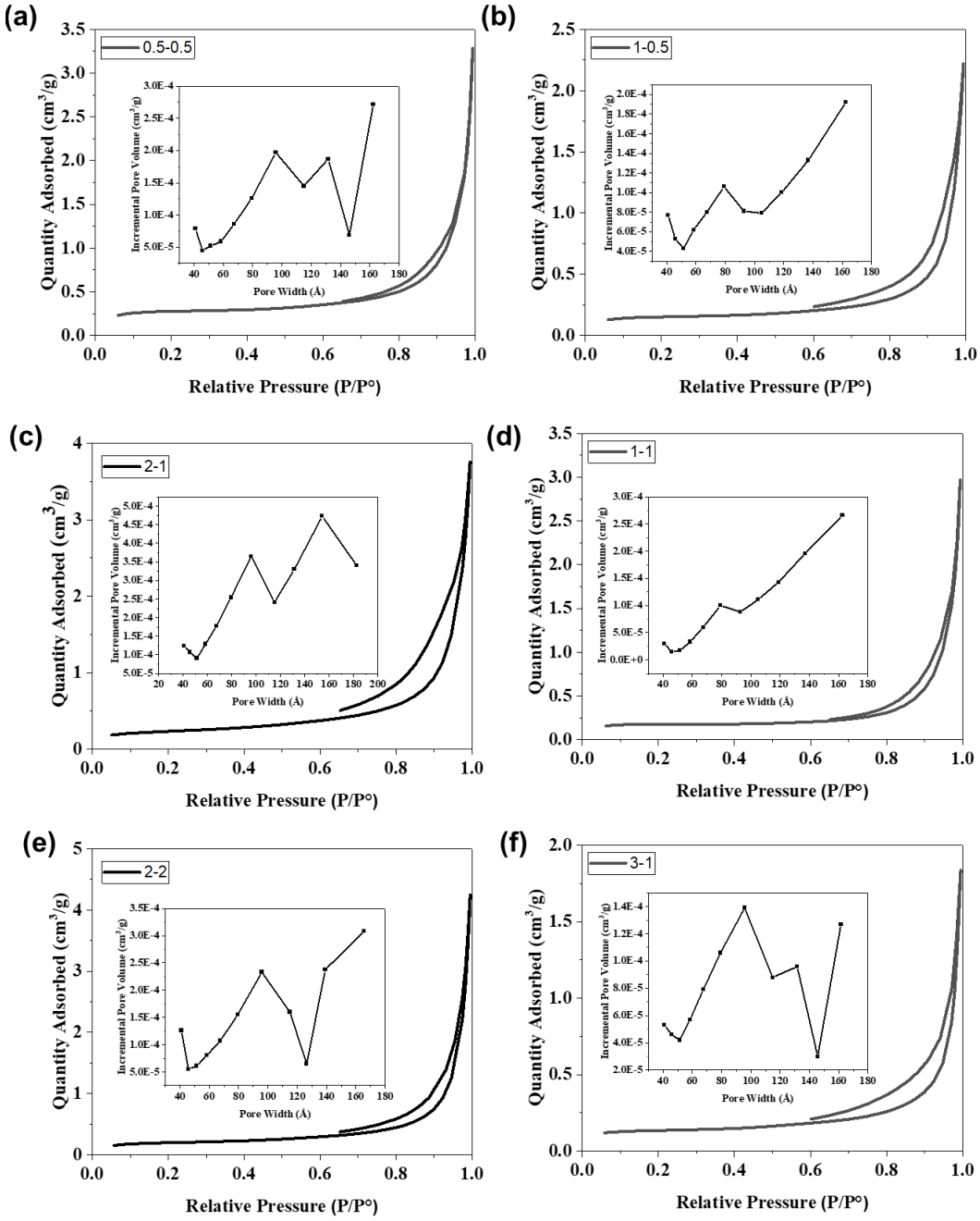

Figure A.3. 8. N_2 adsorption/desorption isotherms with BJH desorption pore size distribution curve as insets of the porous LLZO powders based on the formulation 3.

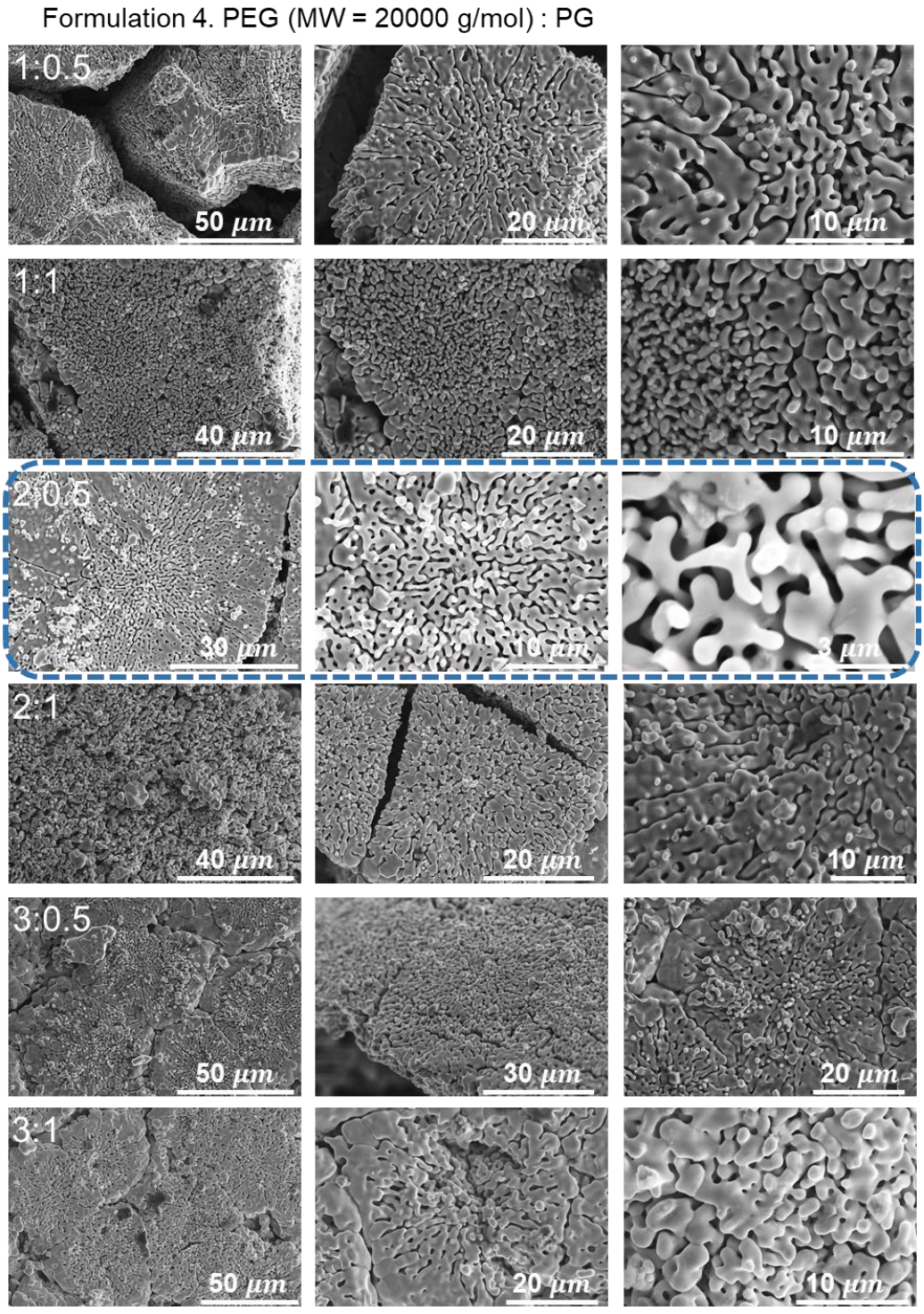

Figure A.3. 9. SEM images of the six types of porous LLZO powders based on the formulation 4.

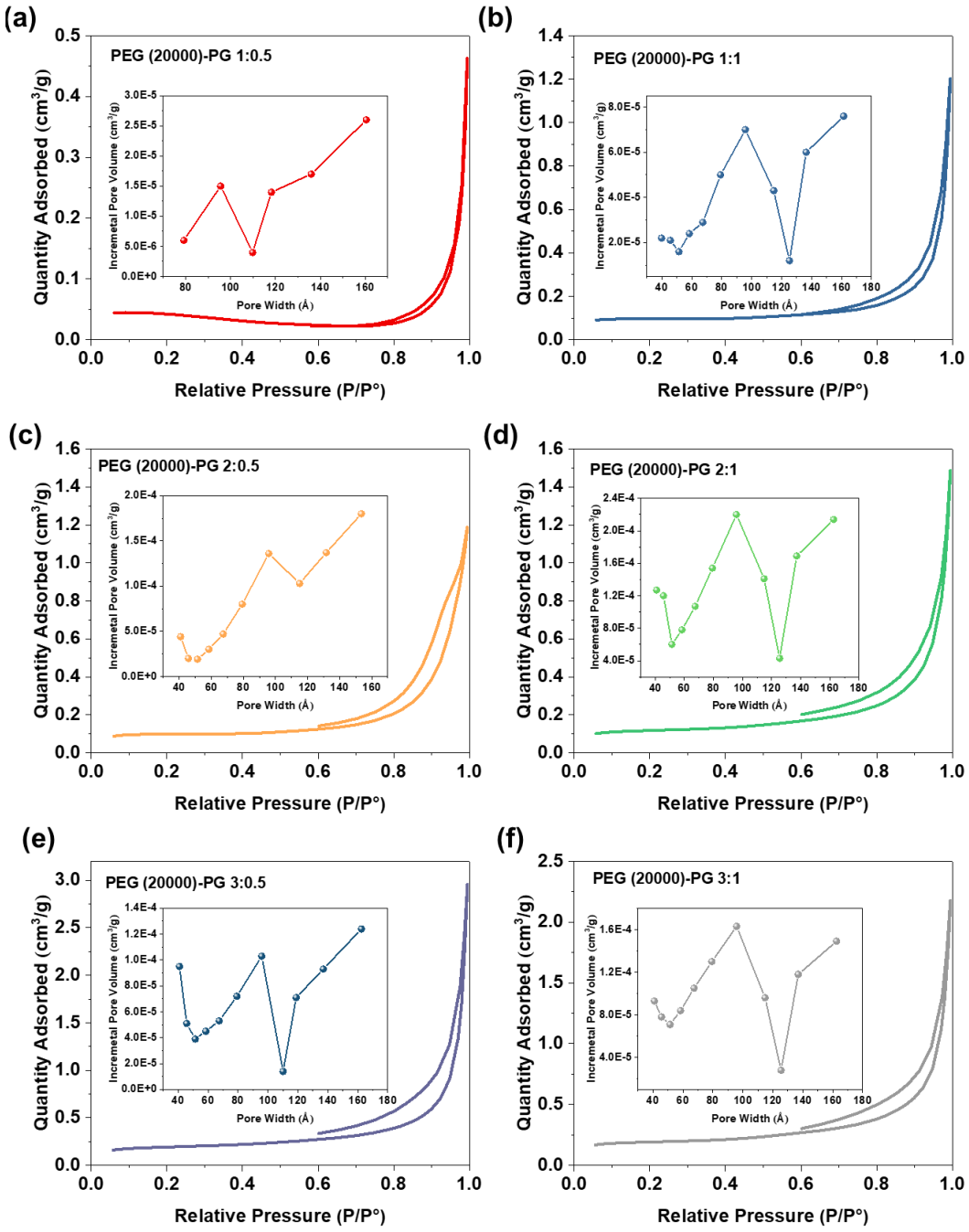

Figure A.3. 10. N_2 adsorption/desorption isotherms with BJH desorption pore size distribution curve as insets of the porous LLZO powders based on the formulation 4.

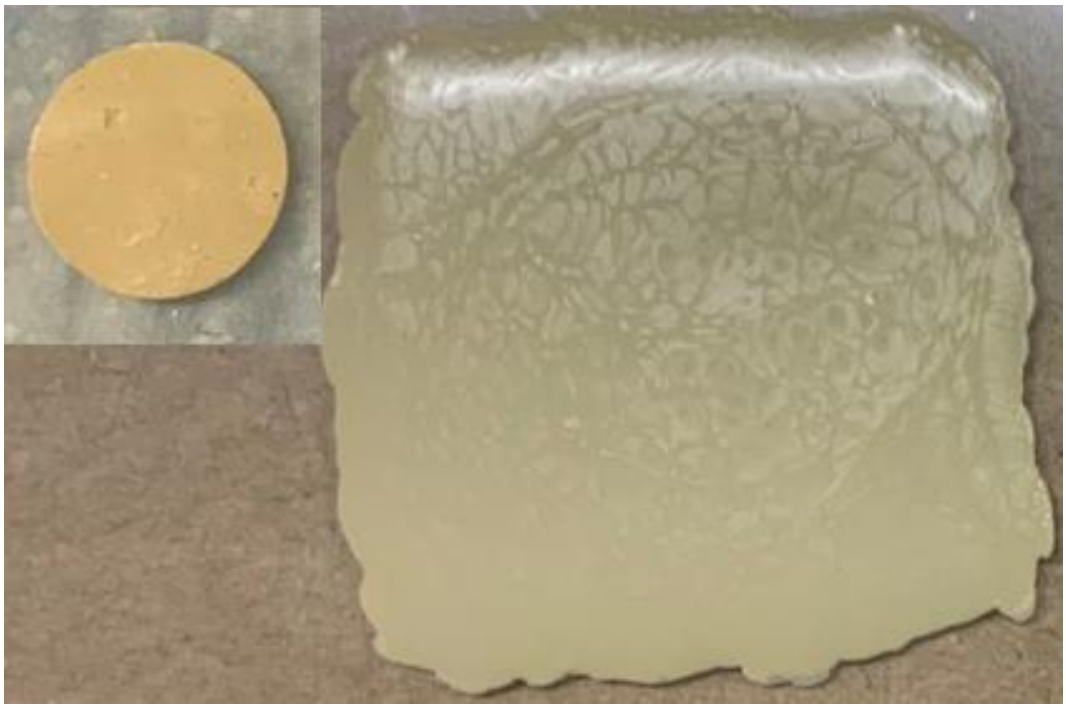

Figure A.3. 11. The digital images of dried and punched green film.

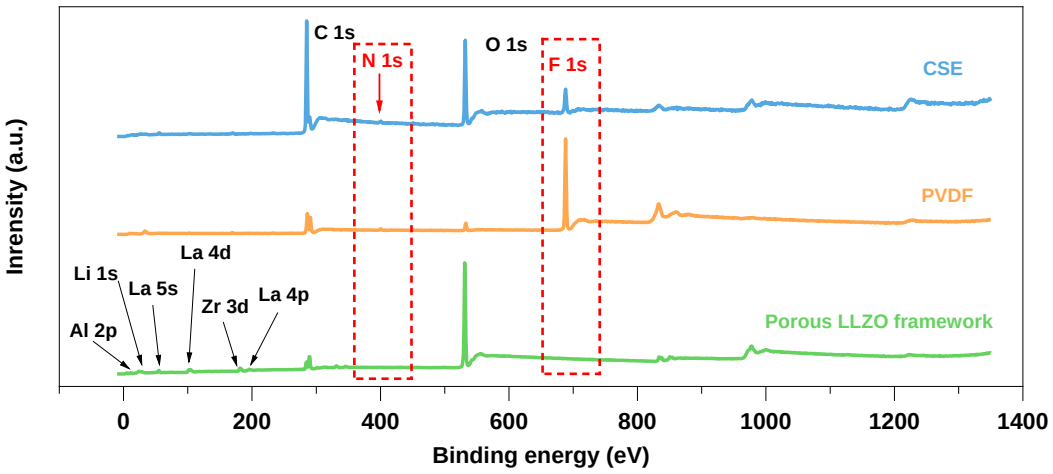

Figure A.3. 12. XPS surveys of porous LLZO framework, PVDF PSE, ceramic-based CSE.

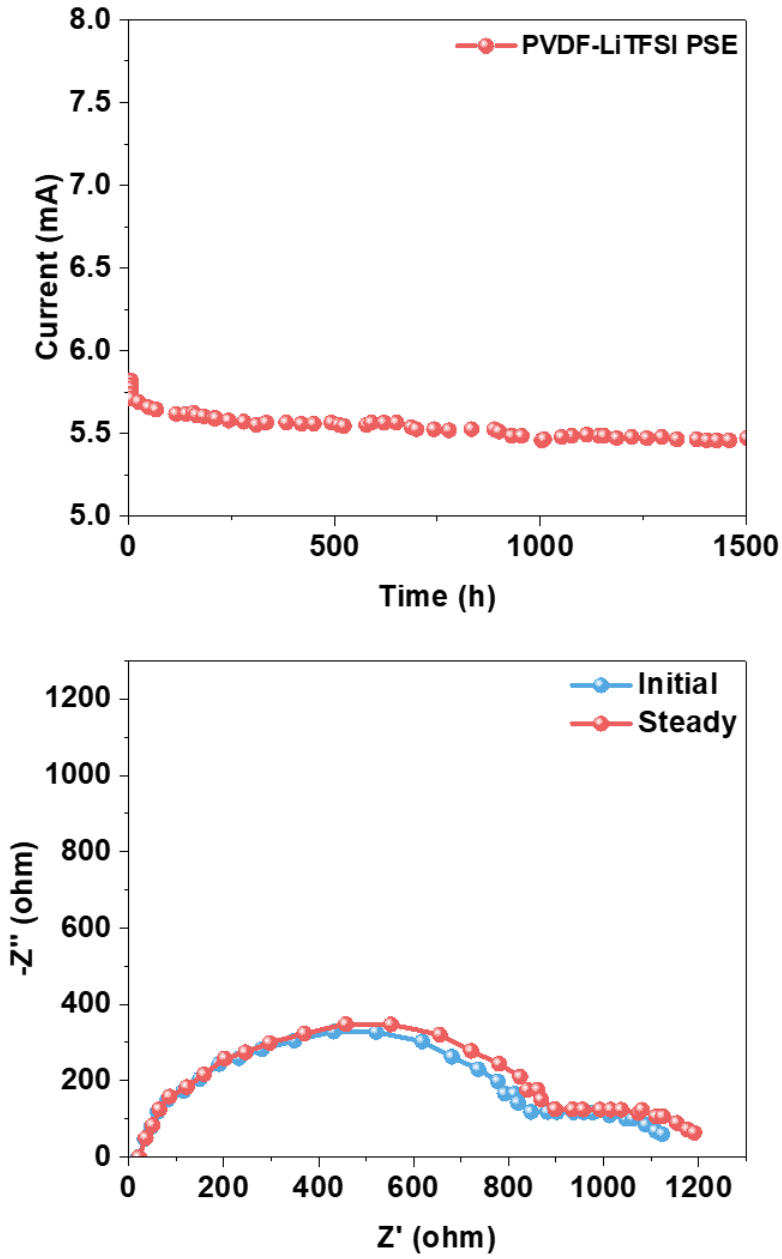

Figure A.3. 13. Polarization curve and EIS of the symmetric cell before and after polarization at 25 ℃ of PVDF-LiTFSI PSE.

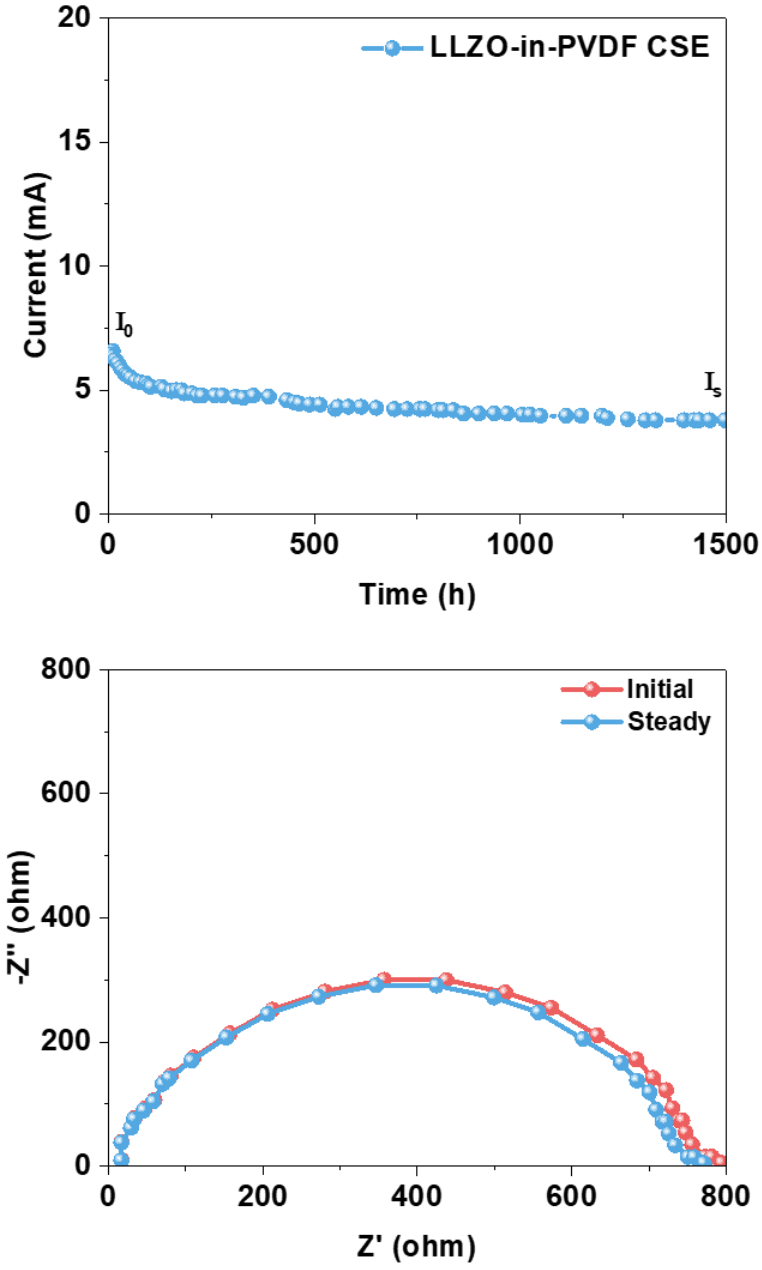

Figure A.3. 14. Polarization curve and EIS of the symmetric cell before and after polarization at 25 ℃ of LLZO-in-PVDF polymer based CSE.

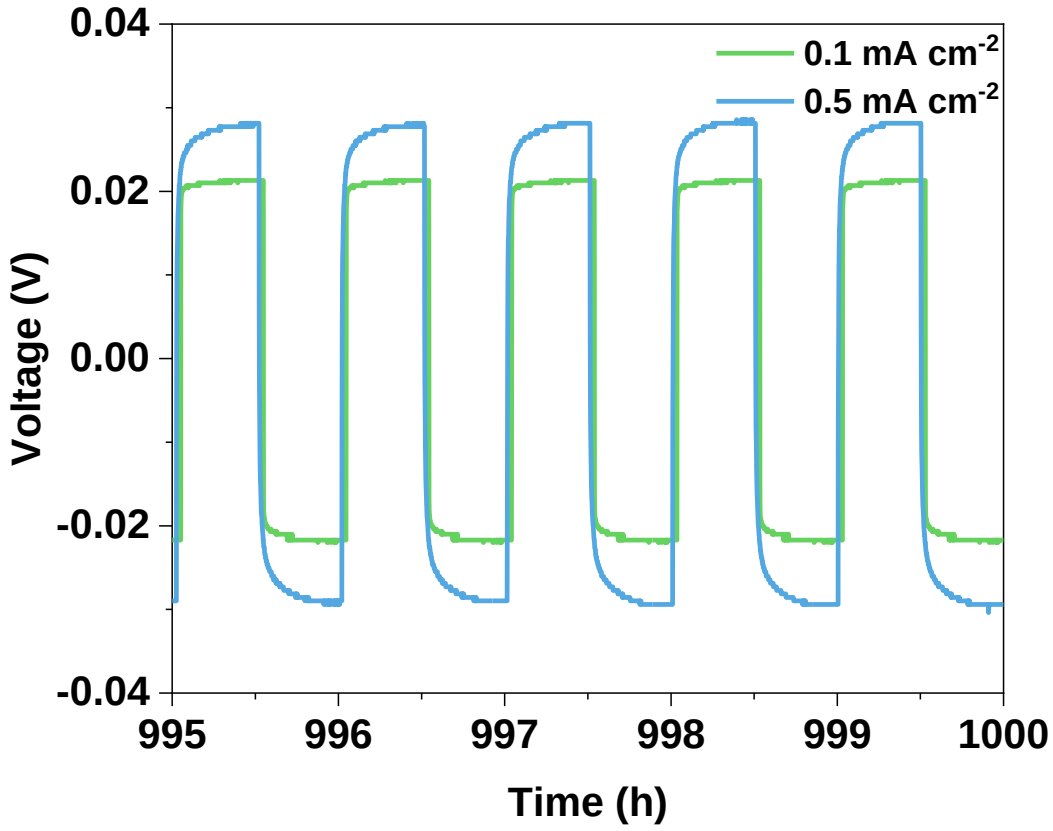

Figure A.3. 15. Magnification of the galvanostatic curves from 995 to 1000 hours.

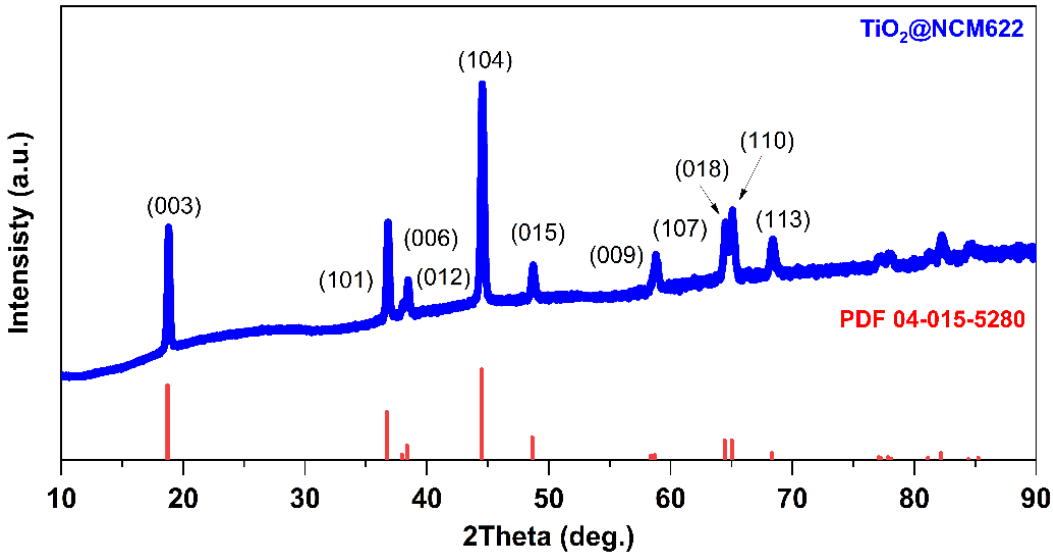

Figure A.3. 16. XRD pattern of the as-synthesized TiO_2-coated NCM622 cathode particles.

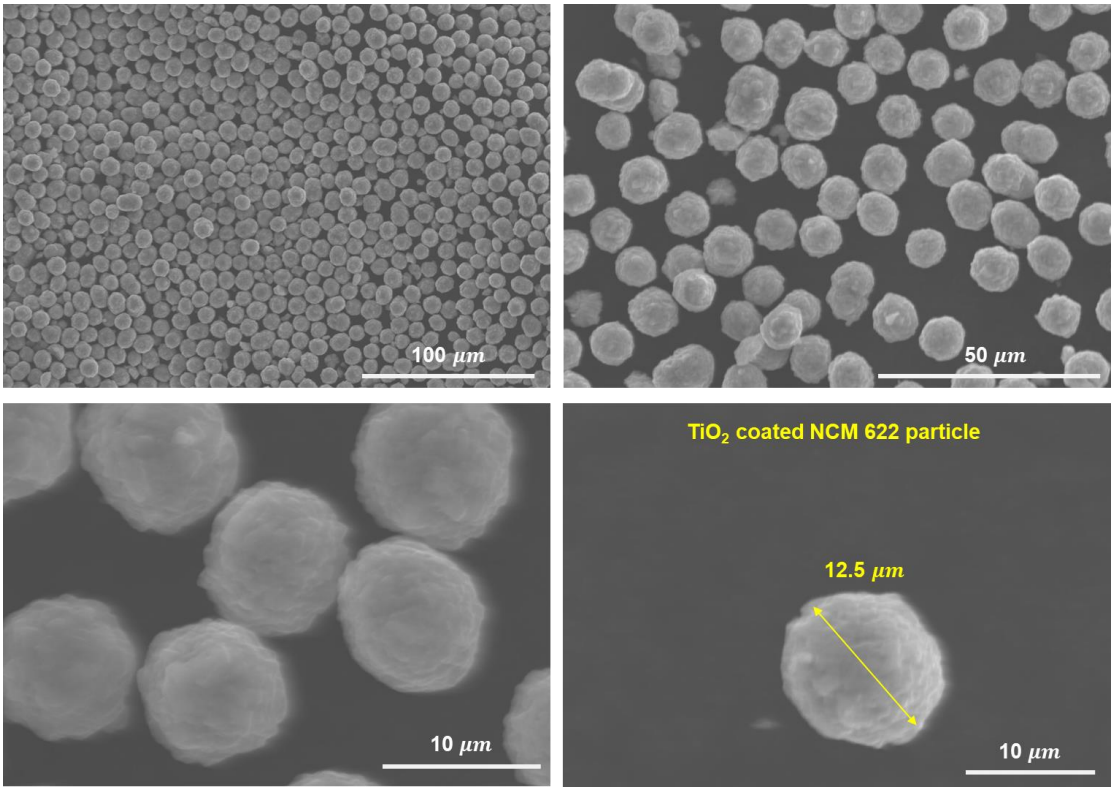

Figure A.3. 17. SEM images of the as-synthesized TiO_2-coated NCM622 cathode particles.

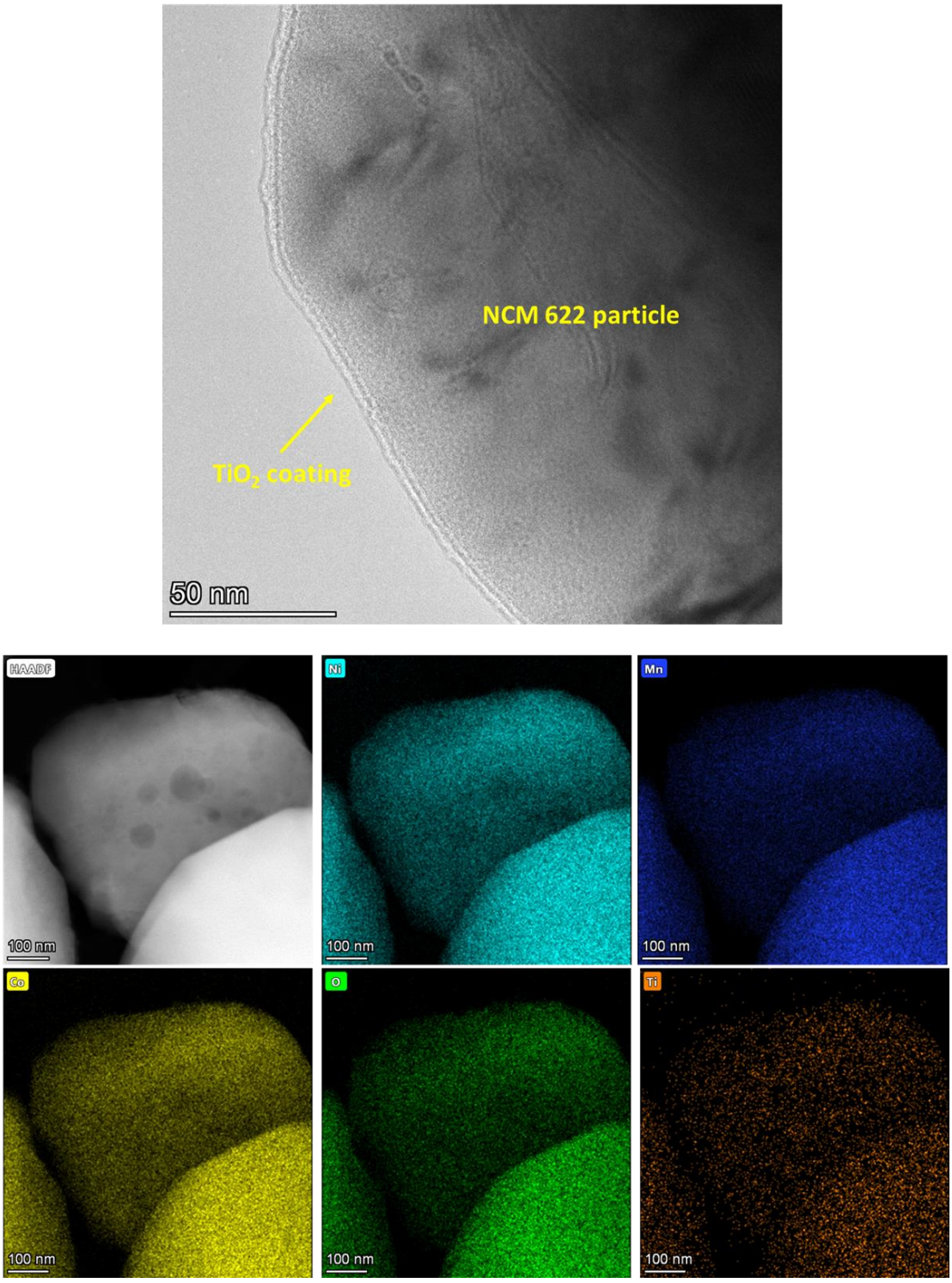

Figure A.3. 18. TEM images of the as-synthesized TiO_2-coated NCM622 cathode particles.

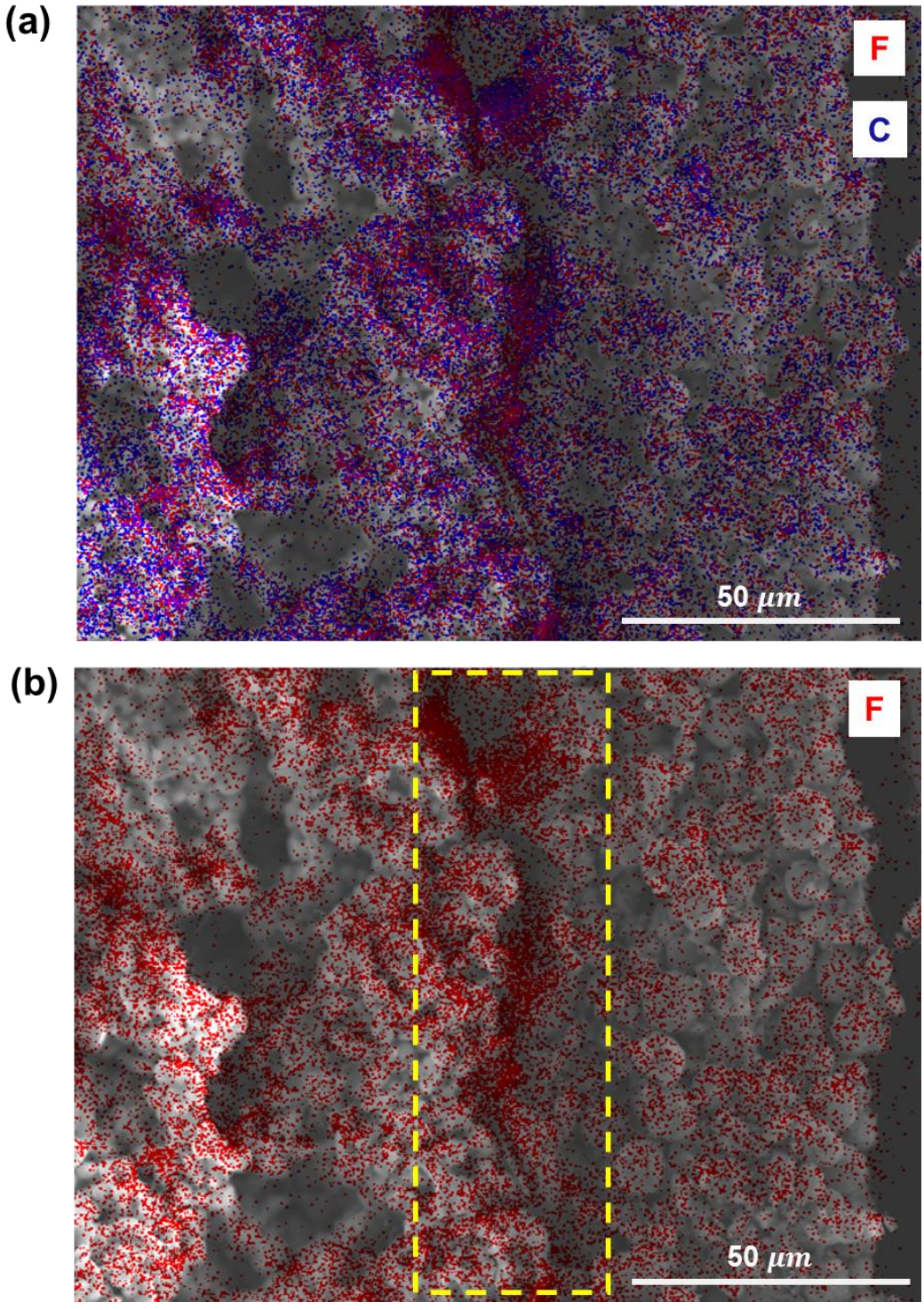

Figure A.3. 19. SEM and EDS (C and F) images of the interface between TiO_2-coated NCM622 cathode and ceramic-based CSE.

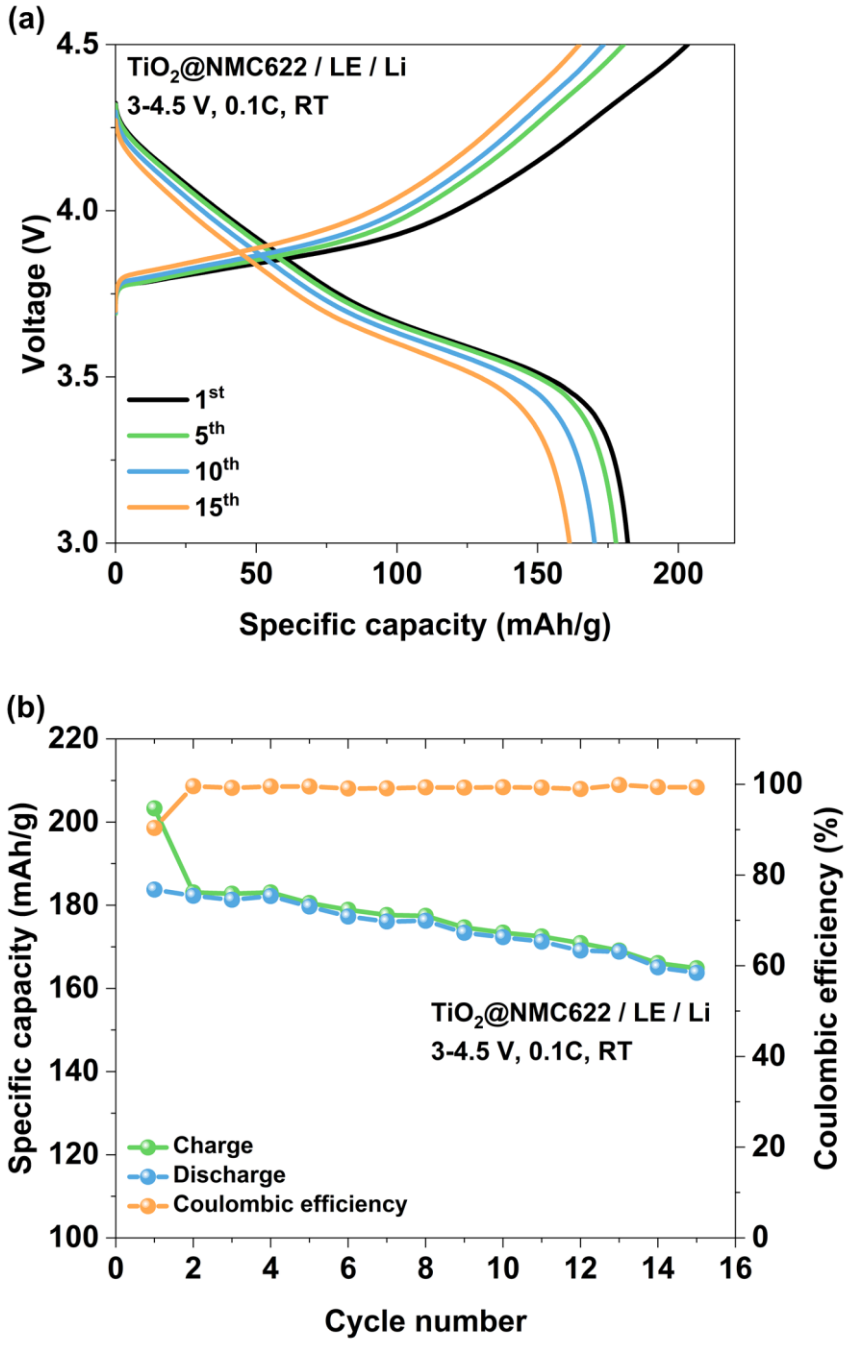

Figure A.3. 20. Conventional lithium-ion battery with liquid electrolyte. (a) charge-discharge voltage profiles of different cycles; (b) cycling stability at 0.1 C and 25 ℃.

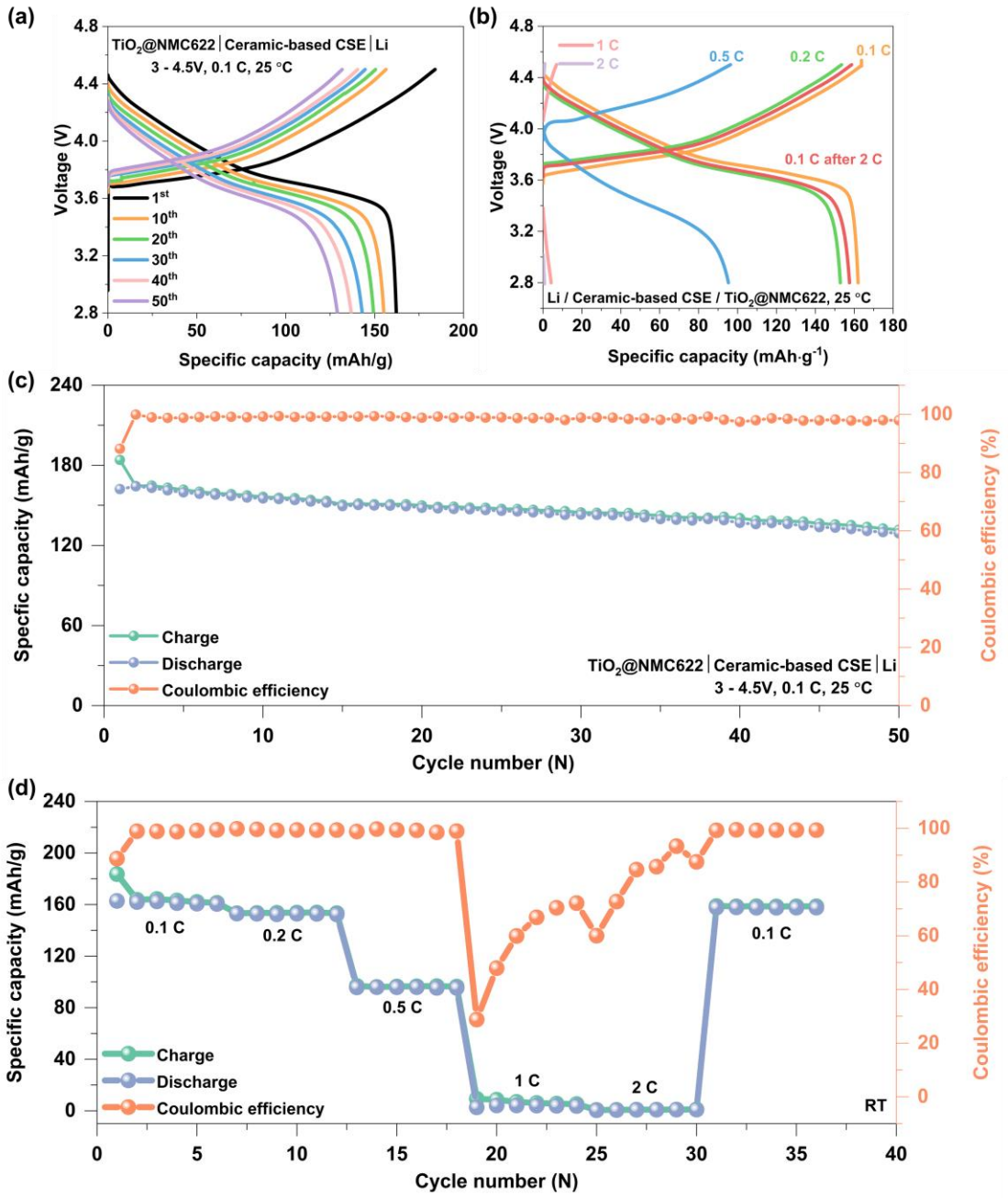

Figure A.3. 21. The electrochemical performance of the as-assembled ASSBs at 25℃. (a) charge-discharge voltage profiles of different cycles; (b) charge-discharge profiles at different rates; (c) cycling stability at 0.1 C; (d) the rate performance from 0.1 C to 2 C.

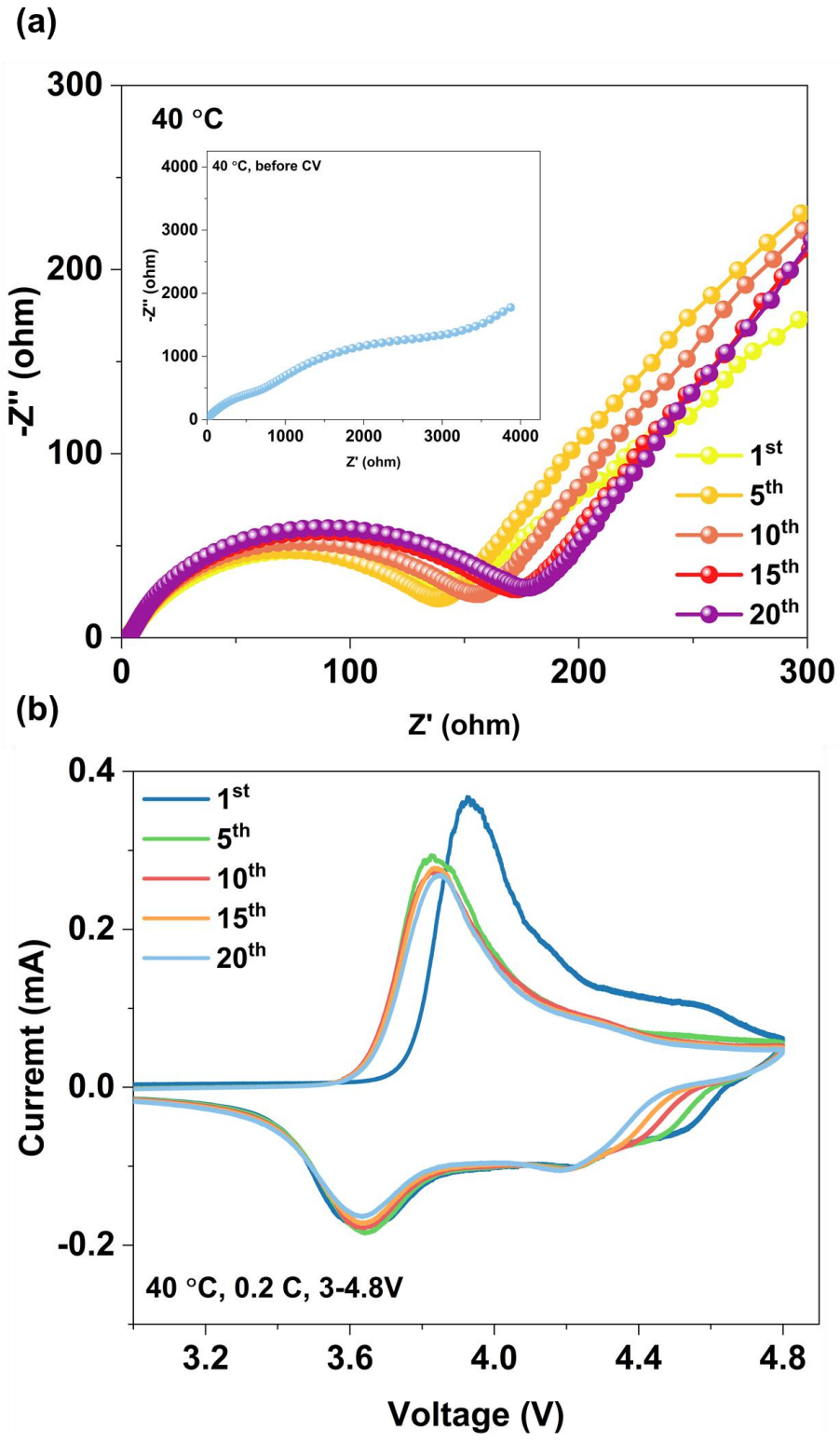

Figure A.3. 22. (a) EIS curves before (inset) and after CV tests and (b) CV profiles of the as-assembled TiO_2@NCM622 / ceramic-based CSE / Li ASSB from 3 to 4.8 V at a scan rate of 0.1 mV s^{-1}.

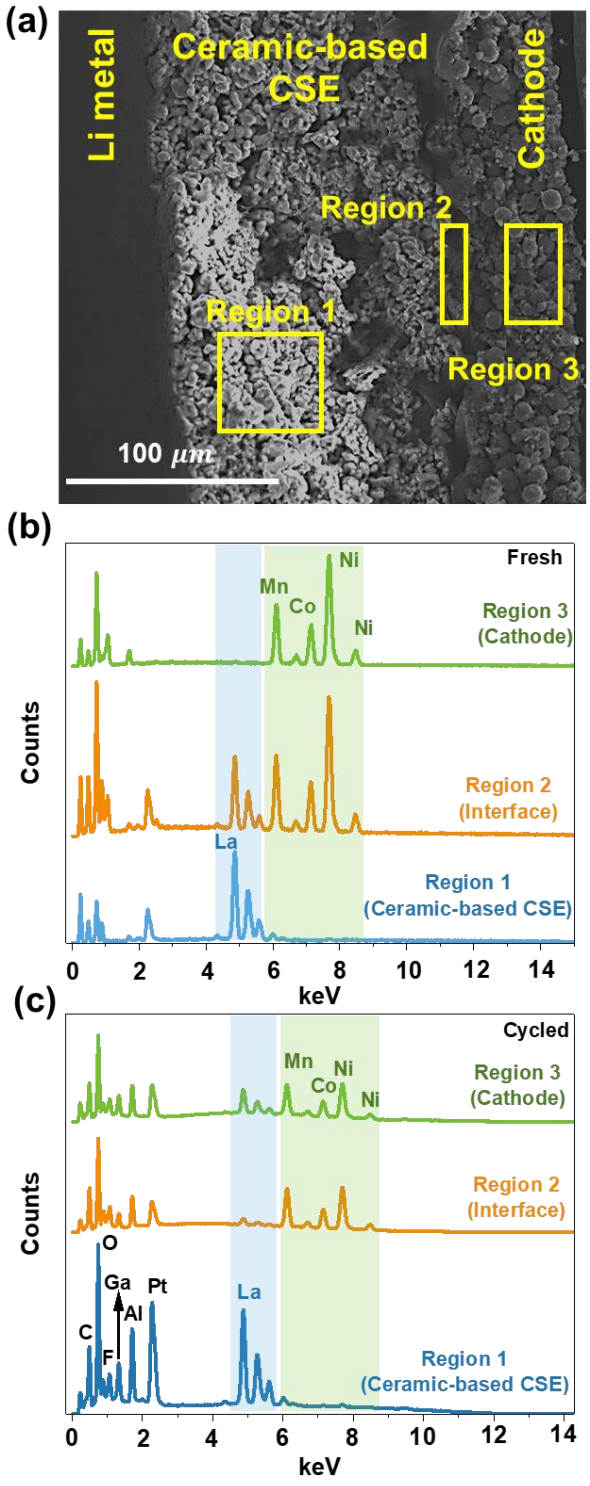

Figure A.3. 23. (a) SEM image of the as-assembled TiO_2@NCM622 / ceramic-based CSE / Li ASSB (before cycling) cross section and the EDS quantitative spectra of the ASSBs (before (b) and after (c) cycling from 3 to 4.8 V for 200 cycles).

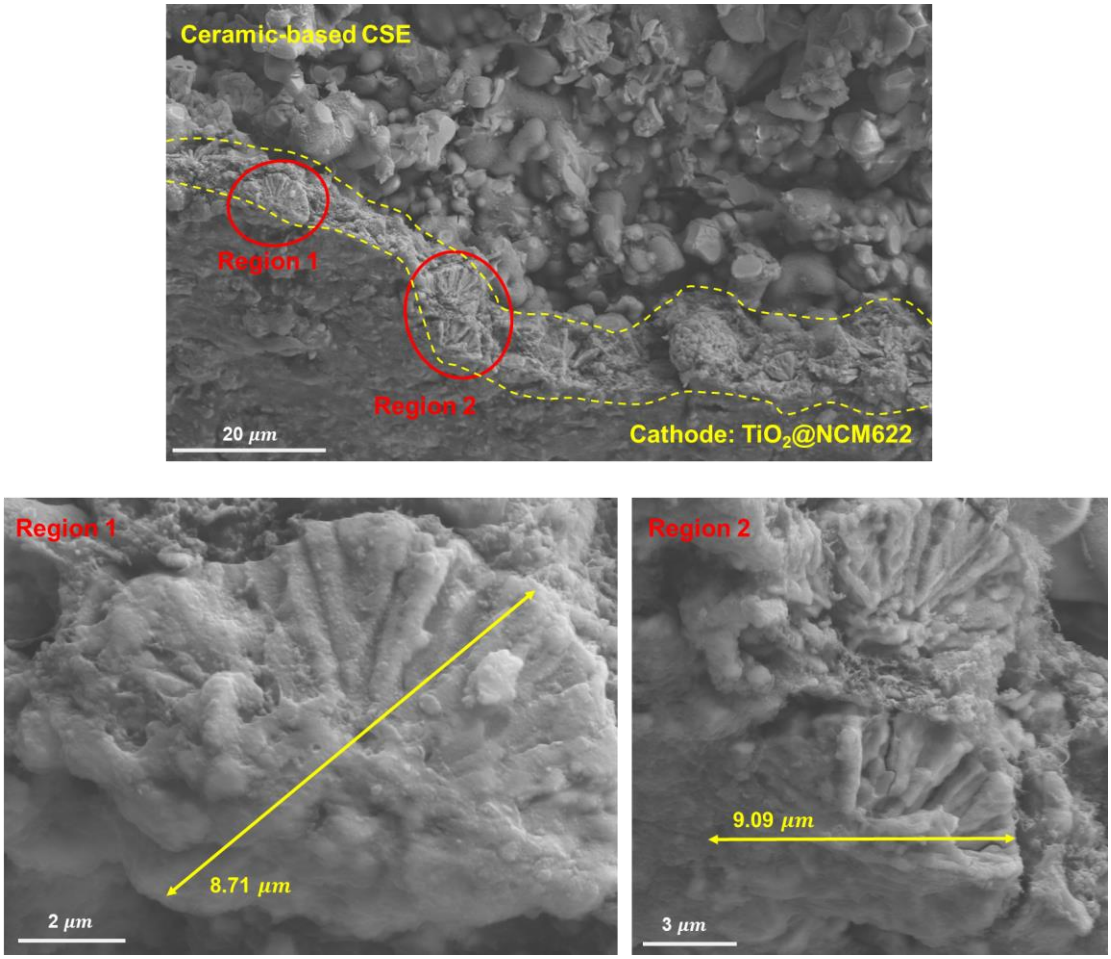

Figure A.3. 24. SEM images of the cycled as-assembled TiO_2@NCM622 / ceramic-based CSE / Li ASSB cross section and TiO_2@NCM622 cathode particle features after cycling.